Technical Report

TR-06-42

TRUE Block Scale Continuation Project

Final Report

Peter Andersson, Johan Byegård
Geosigma AB

Daniel Billaux, Itasca Consultants SA

Vladimir Cvetkovic, Royal Institute of Technology

William Dershowitz, Thomas Doe
Golder Associates Inc.

Jan Hermanson, Golder Associates AB

Antti Poteri, VTT

Eva-Lena Tullborg, Terralogica AB

Anders Winberg, Conterra AB (ed)

March 2007

Svensk Kärnbränslehantering AB
Swedish Nuclear Fuel
and Waste Management Co
Box 5864
SE-102 40 Stockholm Sweden
Tel 08-459 84 00
+46 8 459 84 00
Fax 08-661 57 19
+46 8 661 57 19

TRUE Block Scale Continuation Project

Final Report

Peter Andersson, Johan Byegård
Geosigma AB

Daniel Billaux, Itasca Consultants SA

Vladimir Cvetkovic, Royal Institute of Technology

William Dershowitz, Thomas Doe
Golder Associates Inc.

Jan Hermanson, Golder Associates AB

Antti Poteri, VTT

Eva-Lena Tullborg, Terralogica AB

Anders Winberg, Conterra AB (ed)

March 2007

Preface

This report constitutes the final report of the TRUE Block Scale Continuation project, run within the framework of the Tracer Retention Understanding Experiments at the SKB Äspö Hard Rock Laboratory, Sweden.

Funding organisations of the project are;

ANDRA (France)

JNC (Japan)

Posiva (Finland)

SKB (Sweden)

The work done has been accomplished with the active participation and efforts made by the in situ experiment and analysis teams from the organisations involved:

Posiva-VTT: Antti Poteri

ANDRA-Itasca: Daniel Billaux and Caroline Darcel

JNC-Golder: William Dershowitz, Aaron Fox, Thomas Doe, Mattaeus Ziegler, Shinji Takeuchi and Masahiro Uchida

SKB-GEOSIGMA: Peter Andersson, Johan Byegård, Henrik Widestrand, Magnus Holmqvist, Rune Nordqvist and Calle Hjerne

SKB-KTH/WRE: Vladimir Cvetkovic, Hua Cheng

SKB-Terralogica: Eva-Lena Tullborg

SKB-Golder: Jan Hermanson

The important contributions to realising the work presented in this report are hereby gratefully acknowledged.

Furthermore, the active guidance of the TRUE Block Scale Steering Committee (Aimo Hautojärvi (Posiva), Bertrand Vignal (ANDRA), Masahiro Uchida (JNC), and Jan-Olof Selroos (SKB) during the project is acknowledged, as well as the critical reviews provided by the TRUE Block Scale Continuation review panel: Jane C S Long, Ivars Neretnieks, Gunnar Gustafson and Wolfgang Kinzelbach.

Anders Winberg, Conterra AB

Project manager, TRUE Block Scale Continuation Project

Summary

Background and objectives

The TRUE Block Scale project was carried out during 1996–2002 /Winberg et al. 2002/. This project focused on site characterisation and building of hydrostructural and microstructural models /Andersson et al. 2002a/, sorbing tracer experiments in single structures and networks of structures over distances ranging between 15 and 100 m /Andersson et al. 2002b/ and also involved a unified application of various model approaches for modelling the in situ experiments. In 2002, ANDRA, Posiva, JNC and SKB decided to pursue some remaining issues in the so-called TRUE Block Scale Continuation project (TRUE BS2). The specific objectives of BS2 can be summarised as: "Improve understanding of transport pathways at the block scale, including assessment of effects of geology and geometry, macrostructure and microstructure". In order to cater to addressing the stated objective a series of hypotheses were formulated which explored the importance of geological information for predicting transport and retention and the possible differences between transport and retention between transport paths dominated by faults and those dominated by non-fault fractures (background fractures). In the process, prospects for carrying out experiments in fracture networks over longer distances (c 20–100 m) were explored. It was identified that experiments with sorbing tracers over these distances were prohibitive because of the time frames involved and the projected low mass recoveries. Instead the experimental locus was shifted to a geological structure previously not investigated by tracer tests in the TRUE Block Scale experiments.

Hydrostructural model and basic characterisation

The experimental site is located in the interior of the TRUE Block Scale rock block and is centred on Structure #19, known from the TRUE Block Scale Project in all exploration boreholes but one, variable in appearance from a singular fracture in the northwest to a more complex, multi-fracture structure in the southeast. Superimposed on the already existing hydrostructural model, two basic fracture types – Type 1 (Fault) and Type 2 (non-fault) – developed by /Dershowitz et al. 2003/ have been incorporated on the basis of the characteristics of existing intercepts.

The basic characterisation performed in BS1 has furthermore been complemented by hydraulic cross-hole interference tests (CPT-1 through CPT-3) involving tracer dilution tests with the purpose of selecting suitable tracer injection and pumping sections. The tests identified a suitable pumping section in Structure #19 in borehole KI0025F03 and suitable injection sections in Structure #19 (KI0025F02) and in a background fracture (KI0025F02) connected to Structure #19. The resulting flow paths represent a Type 1 flow path and a flow path dominated by Type 2 fractures, respectively. The transmissivity of Structure #19 is in the order of $1 \cdot 10^{-6}$ m^2/s whereas the transmissivity of the background fracture BG1 is in the order of $1 \cdot 10^{-9}$ m^2/s, i.e. some three orders of magnitude lower.

Microstructural models and their parameterisation

The microscopic characteristics of the geological materials collected from the available intercepts in Structure #19 and the sole intercept of background fracture BG1 are used to provide generalised descriptions of the two geological features. Using the basic stratigraphy of the Type 1 and Type 2 fracture type-based assignment is made of porosity, formation factor and sorption coefficients for the various geological materials and for the different tracers used. Typically, the diffusion and sorption properties are lower for the background fracture BG1 than for the fault type Structure #19.

Tracer tests

In order to obtain basic understanding of conservative tracer transport and to demonstrate sufficient tracer mass recovery a series of tracer injections (CPT-4a through CPT-4C were made using various flow field configurations (radially converging, weak dipole) in the injection sections in Structure #19 and in BG1 using the selected pumping section in Structure #19 (Q = 2.6–2.8 l/min). The results of the tests showed that employment of slight over-pressure in the injection sections were required to produce mass recoveries above 80% from the two injection sections. Typical peak arrival times of non-sorbing tracers for Flow path I (in Structure #19) and Flow path II (from BG1 to Structure #19) were found to be some 30 hours and 300 hours, respectively.

In the ensuing BS2B test, tracers of variable sorption strength were administered as a cocktail in each flow path. Based on the availability of isotopes, the following selection was made:

- Slightly sorbing tracers: $^{85}Sr^{2+}$ for Flow path I and $^{22}Na^{+}$ for Flow path II.
- Moderately sorbing tracers: $^{86}Rb^{+}$ for Flow path I and $^{133}Ba^{2+}$ for Flow path II.
- Strongly sorbing tracers: $^{137}Cs^{+}$ for Flow path I and $^{54}Mn^{2+}$ for Flow path II.

The sorbing tracers were also complemented by two non-sorbing tracers in each flow path:

- $^{131}I^{-}$ together with ^{160}Tb-DTPA (Flow path I).
- Tritiated water (HTO) together with ^{155}Eu-DTPA (Flow path II).

Similarly to the pre-tests the BS2B test was performed by establishing a radially converging flow field with a constant withdrawal rate in the selected sink in borehole section KI0025F03:R3 (Structure #19). Withdrawal was established using the maximum sustainable flow (2.5 l/min, decreasing to 2.3 l/min at the end of the test).

The tracer cocktails were injected as decaying pulses with simultaneous injection of water (unlabelled formation water) creating a slight excess pressure and thus, a weak dipole flow field. Samples were automatically withdrawn both in the injection and withdrawal sections and in addition on-line γ-detectors were used.

Predictions of tracer tests

Predictions were carried out by four independent modelling teams representing the partners of the TRUE Block Scale Continuation project. As a basis for the predictions, the modelling teams made use of all the accumulated geological information from the TRUE Block Scale (BS1 and BS2) and TRUE-1 projects. Specifically, the modellers were provided details on the intercepts of the injection and pumping sections and the results of the tracer pre-tests (CPT-1 through CPT-4). A close scrutiny of the predictions for Flow path I relative to the experimental outcome shows that most modelling teams provide equitable predictions of the least sorbing tracer (^{85}Sr), whereas differences become readily visible in the case of Caesium (^{137}Cs), where the predictions by the SKB-KTH/WRE team shows a very good correspondence with the measured breakthrough. The predictions for the background fracture Flow path II show a surprisingly large spread in the case of the weakly sorbing ^{22}Na. For the more strongly sorbing tracers, ^{133}Ba and ^{54}Mn, the predictions show a significantly larger spread, flanking the experimental breakthroughs.

Geometries of investigated flow paths

The geometries of the two investigated flow paths have been visualised using various techniques. Flow path I is a relatively simple flow path, some 20 m long and assumed essentially contained within the fault type Structure #19 with a mean travel time of some 10 hours /Andersson et al. 2005/. The modelled lengths are close to the Cartesian distance (mean length varying between 22 to 44 m).

The background fracture Flow path II is a network flow path involving one or more background fractures (including BG1) in combination with Structure #19. The Cartesian distance between

the source and the sink is about 22 metres and the mean travel time is some 200 hours /Andersson et al. 2005/. The modelled path lengths vary between 40 and 150 m between realisations, of which between 0–40 m is attributed to the leg in Structure #19.

Evaluation of retention properties

The assessment of the immobile zone retention properties along the two studied flow paths is based on the results of the four individual BS2B model evaluations available. The main emphasis in on the retention caused by matrix diffusion, which is dependent both on the properties of the flow field (hydrodynamic control parameter β, also referred to as the transport resistance F [T/L] and those of the corresponding immobile zones (material retention property group κ, accounting for both matrix diffusion and sorption). This means that the properties of immobile zones need always to be assessed in close conjunction with assumptions regarding the flow field and the flow path.

In the developed microstructural model of the immobile zones the Type 1 fractures are fault type and exhibit a high degree of heterogeneity and also include porous fault gouge. The Type 2 fractures are non-fault type and are not as heterogeneous as the Type 1 fractures. High porosity geological materials (fault gouge) are assumed not to exist in the Type 2 fractures.

Most of the developed transport models describe Flow path I by a few hours of advective residence time and the Flow path II as being characterised by about 150 hours mean advective residence time. All models show clear differences in the advective transport between the two flow paths. The Euclidian distance from the injection point to the sink is about the same for both flow paths, but the models indicate an order of magnitude longer advective water residence times in Flow path II compared to Flow path I. This suggests that Flow path II is geometrically much more complex than Flow path I.

The average values of the evaluated hydrodynamic control parameter β along the two flow paths, as obtained from the four evaluation models, is found, with two exceptions, to be fairly consistent amongst the models. Strikingly, the average level of β is close to two orders of magnitude higher (higher retention) for the Flow path II compared to Flow path I. The earlier described three order difference in transmissivity between the Structure #19 and BG1 would suggest an even larger difference in β. This circumstance may be explained additional fractures making up Flow path II together with BG1 exhibiting higher transmissivities than BG1.

The effective retention material properties along the two flow paths, and for most of the tracers, were calculated by SKB-KTH/WRE. Flow path I shows effective immobile zone retention properties that are close to the properties specified for cataclasite in the microstructural model (higher retention). Contrary to this, Flow path II shows effective immobile zone retention properties that are close to the properties of the altered zone. This finding is also supported by the nature of the flow paths since both the injection and extraction points of Flow path I are located in the Structure #19, being a fault type structure composed of multiple immobile zones including high porosity immobile zones (fault gouge). The injection point in Flow path II is located in a simple non-fault type fracture and the results of both numerical flow modelling and assessment of modelled advective water residence time distributions suggest that this flow path is geometrically more complex, expected to be dominated by the background fractures.

Assessment of the hydrostructural model

The hydrostructural model at Structure #19 is substantially confirmed by the results of BS2A and BS2B hydraulic and tracer tests performed between sections located at the interpreted locations of Structure #19. In particular:

- The hydraulic interference tests (pre-tests) clearly show evidence of Structure #19 acting as a planar effectively homogeneous conductive structure, featured by radial flow at intermediate distances, and is shown similar for the different tested borehole intersections.
- Non-sorbing tracer tests carried out between boreholes intersecting what is interpreted as Structure #19 show advective travel times and dispersion values consistent with flow in a single, planar structure.

- The magnitude of the effective solute retention values from the BS2B sorbing tracer experiments are consistent with those that would be expected for transport on a fracture plane in contact with the immobile zones as defined by the microstructural model and the given flow situation.

The background fracture BG1 was the point of injection for the BS2B injection in Flow path II. The designation "background fracture" is used because of the lack of direct evidence of this fracture in other boreholes. The evidence for its existence is limited to a single flow log and a BIPS log. Due to the single intercept it is not possible to definitively assign a fracture size. Furthermore, by project experience, local fracture intersections have orientations which are generally 10 to 30 degrees different from the average orientation of the interpreted fracture plane based on the individual intersections. Consequently, the hydrostructural model is very uncertain concerning BG1. The following select conclusions can be drawn:

- Only very small portions of Flow path II can be along Structure #19 due to its distinctly different immobile zone solute retention properties compared to background fractures. BG1 can therefore either be of the scale of greater than 20 m radius (to approach borehole KI0025F03), or Flow path II must be made up of a number of background fractures.
- Because the effective dispersion length back-calculated for Flow path II is relatively small, it is likely that Flow path II contains a small number of connected background fractures.
- The lower immobile zone retention properties observed in Flow path II supports the hypothesis that BG1 is a Type 2 fracture with limited or no high porosity immobile zones.

Conclusions

- The lower immobile zone retention material properties assigned to background fractures compared to those assigned to the fault-type Structure #19 have been verified by means of back-calculations. The evaluated Type 1 flow path (Structure #19, Flow path I) retention material properties, as expressed by κ parameter, are one order of magnitude higher than for the background fracture flow path. This finding is consistent with the developed micro-structural model. It is noted that the observed difference is applicable to experimental time scales while at longer time scales the retention capacity of the fault type fractures may become saturated.
- The overall retention (taking effects of both κ and β into account) in the background fracture Flow path II is found to be about one order of magnitude higher than for Flow path I. This finding is attributed to the fact that that the flow rate is significantly lower compared with Flow path I, resulting in longer residence times.
- The presented results are consistent with Flow path I being contained in a planar structure with immobile zones assigned according to the microstructural model. Similarly, the results suggest Flow path II is being made up of a set of background fractures, including BG1.
- The uncertainty associated with the analysis and interpretations has been evaluated quantitatively, demonstrating that the uncertainty in the hydrodynamic (pathway length and velocity) parameter group β is higher than that for the retention (physical and geochemical) parameter group κ. This analysis supports the development of more realistic hydrostructural models with uncertainty represented through discrete fracture network (DFN) simulations for radionuclide transport in crystalline rock.

The analysis (prediction and evaluation) made of the TRUE Block Scale Continuation tracer tests demonstrates clearly that a good geological basis (as expressed in the developed hydrostructural and microstructure models) is important for understanding sorbing tracer transport in fractured crystalline rock.The quantitative analysis pertaining to the background fracture Flow path II suggests that background fracture flow paths, although with poor material retention properties, may contribute significantly to retention because of the low flow rates expected in them. Given that the current results are based on one sole experimental result there exists a need to further substantiate the present findings.

Sammanfattning

Bakgrund och syften

Projektet TRUE Block Scale (BS1) genomfördes under åren 1996–2002 /Winberg et al. 2002/. Detta projekt fokuserade på platsbeskrivning och byggande av beskrivande hydrostrukturella och mikrostrukturella modeller /Andersson et al. 2002a/, spårförsök med sorberande spårämnen i enskilda sprickor och nätverk av strukturer över avstånd mellan 15 till 100 m /Andersson et al. 2002b/ och inkluderade en gemensam ansats på modellering av in situ försöken. ANDRA, Posiva, JNC och SKB bestämde 2002 att fortsatt studera några speciella frågeställningar inom projektet TRUE Block Scale Continuation (BS2). De specifika målen med BS2 kan sammanfattas med en övergripande inriktning att ”öka förståelsen av transportvägar i blockskala, inkluderande uppskattning av effekterna av geologi och geometri, makrostruktur och mikrostruktur”. För att effektivt förhålla sig till det övergripande målet formulerades att antal hypoteser som adresserade betydelsen av geologisk information för prediktion av transport och retention, och möjliga skillnader i transport- och retentionshänseende mellan flödesvägar som domineras av förkastningssprickor och de flödesvägar som domineras av icke-förkastningssprickor (här benämnda bakgrundssprickor). Därefter analyserades möjligheterna att genomföra experiment i nätverk av strukturer över längre avstånd (c 20–200 m). Det identifierades att experiment med sorberande spårämnen över dessa avstånd var näst intill omöjliga att genomföra på grund av de tidsskalor som är aktuella sammantaget med projicerade förluster av spårämnen. Istället försköts den experimentella inriktningen till en geologisk struktur som inte undersökts med spårförsök i de föregående in situ experimenten inom ramen för TRUE Block Scale.

Hydrostrukturell modell och grundläggande karakterisering

Den valda experimentplatsen är lokaliserad i det inre av TRUE Block Scale blocket och är centrerad på Struktur #19, känd från TRUE Block Scale i samtliga undersökningsborrhål sånär som ett, med ett uppträdande varierande från en enskild spricka i nordväst till en mer komplex struktur bestående av ett flertal sprickor i sydost. Den redan existerande hydrostrukturella modellen har överlagrats med två generaliserade spricktyper baserade på existerande borrhålsintercept – Typ1 (förkastningspricka) och Typ 2 (icke förkastning) – som beskrivs i detalj av /Dershowitz et al. 2003/.

Den grundläggande karakteriseringen utförd under BS1 har kompletterats med hydrauliska interferenstester (mellanhålstester CPT-1 till CPT-3) som inkluderade utspädningsmätningar, utförda med målet att välja ut lämpliga injicerings- och pumpsektioner för spårförsök. Dessa tester identifierade en lämplig injiceringssektion i Struktur #19 i borrhål KI0025F03 och lämpliga injiceringssektioner i Struktur #19 (KI0025F02) och i en bakgrundsspricka i KI0025F02 som är hydrauliskt konnekterad till Struktur #19. De resulterande flödesvägarna representerar en flödesväg Typ 1, respektive en som domineras av Typ 2 sprickor. Struktur #19:s transmissivitet är c $1 \cdot 10^{-6}$ m^2/s medan transmissiviteten hos bakgrundsprickan BG1 är c $1 \cdot 10^{-9}$ m^2/s, dvs en skillnad på tre storleksordningar.

Mikrostrukturella modeller och deras parameterisering

Den mikrostrukturella karakteristiken hos geologiskt material provtaget i tillgängliga intercept med Struktur #19 och det enda interceptet med bakgrundssprickan BG1 används för att skapa generaliserade beskrivningar av de två geologiska strukturerna. Genom att använda den grundläggande stratigrafin, definierade av Typ 1 och Typ 2 sprickor, tillskrivs egenskaper av porositet, formationsfaktor och sorptionskoefficienter för de geologiska beståndsdelar som bygger upp strukturerna i enlighet med de generaliserade modellerna och för de olika spårämnena som använts. Generellt är diffusions- och sorptionsegenskaperna lägre för bakgrundssprickan BG1 än för Struktur #19, den senare av förkastningstyp.

Spårförsök

För att få en grundläggande förståelse av transport av icke sorberande spårämnen och för att demonstrera en tillräcklig massbalans (*mass recovery*) genomfördes en serie spårämnes-injiceringar (CPT-4a till CPT-4c) med utnyttjande av olika flödeskonfigurationer (radiellt konvergerande och svag dipol) i de utvalda injiceringssektionerna i Struktur #19 och BG1 under pumpning i Struktur #19 med ett flöde varierande mellan 2.6–2.8 l/min. Resultaten av dessa försök visade att utnyttjande av ett svagt övertryck i injiceringssektionerna var nödvändigt för att erhålla över 80% massa i retur i pumpborrhålet från de två injiceringarna. Typiska ankomsttider för toppen av genombrottet av de icke-sorberande spårämnena för flödesväg I (i Struktur #19) och flödesväg II (från BG1 till Struktur #19) var c 30 respektive 300 timmar.

I det efterföljande BS2B-försöket injicerades cocktails av spårämnen med varierande sorptions-styrkor i de två flödesvägarna. Baserat på tillgängligheten av isotoper gjordes följande val:

- Svagt sorberande spårämnen: $^{85}Sr^{2+}$ för flödesväg I and $^{22}Na^{+}$ för flödesväg II.
- Moderat sorberande spårämnen: $^{86}Rb^{+}$ för flödesväg I and $^{133}Ba^{2+}$ för flödesväg II.
- Starkt sorberande spårämnen: $^{137}Cs^{+}$ för flödesväg I and $^{54}Mn^{2+}$ för flödesväg II.

De sorberande spårämnena kompletterades med två icke-sorberande spårämnen i vardera flödesvägen:

- $^{131}I^{-}$ tillsammans med ^{160}Tb-DTPA (flödesväg I).
- Tritierat vatten (HTO) tillsammans med ^{155}Eu-DTPA (flödesväg II).

På motsvarande sätt som för för-försöken genomfördes BS2B-försöket genom att etablera ett radiellt konvergerande flödesfält med konstant pumpflöde i den utvalda pumpsektionen i borrhål KI0025F03:R3 (Struktur #19). Pumpning genomfördes med det högsta möjliga flödet (2.5 l/min, som under försökets gång minskade till 2.3 l/min vid försökets slut).

Spårämneslösningarna injicerades som avklingande pulser med samtidig injicering av vatten (omärkt formationsvatten) som skapade ett svagt övertryck, och därmed ett svagt dipolfält. Prover samlades in automatiskt både från injicerings- och pumpsektioner och därutöver utnyttjades en gammadetektor för kontinuerlig mätning på befintliga slangar.

Prediktioner av genomförda spårförsök

Prediktioner (förutsägelser) av BS2B gjordes av de fyra oberoende modelleringsgrupperna som representerar de fyra deltagarorganisationerna i TRUE Block Scale Continuation. Som ett underlag för prediktionerna använde modelleringsgrupperna all den samlade geologiska informationen från TRUE Block Scale (BS1 och BS2) och TRUE-1 projekten. Specifikt delgavs modellörerna detaljer om de olika intercepten i injicerings- och pumpsektionerna och resultaten från för-försöken (CPT-1 till CPT-4). En detaljerad genomgång av prediktionerna för flödesväg I i jämförelse med de experimentella resultaten visar att majoriteten av modellgrupperna presenterar likvärdiga prediktioner av det svagsorberande spårämnet (^{85}Sr), medan skillnader blir tydliga för Cesium (^{137}Cs), där dock prediktionerna av modellgruppen SKB-KTH/WRE visar en mycket god överensstämmelse med mätt genombrott. Prediktionerna för flödesväg II uppvisar en förvånansvärd stor spridning i fallet med den svag-sorberande ^{22}Na. För de mer starkt sorberande spårämnena, ^{133}Ba och ^{54}Mn, visar prediktionerna väsentligt större spridning men flankerar de experimentella genombrottskurvorna.

Flödesvägarnas geometrier

De två flödesvägarnas geometrier har visualiserats med olika metoder. Flödesväg I är en i grunden relativt enkel flödesväg, c 20 m lång, antagen att vara huvudsakligen begränsad till Struktur #19, och med en medeltransporttid på c 10 timmar /Andersson et al. 2005/. Längden på modellerade flödesvägar är nära det kartesiska avståndet (medellängder mellan 22 till 44 m).

Flödesväg II är en flödesväg genom ett nätverk av bakgrundsprickor (inklusive BG1) som ansluter till Struktur #19. Det kartesiska avståndet mellan injicerings- och pumpsektion är 22 m med en medeltransporttid på c 200 timmar /Andersson et al. 2005/. De modellerade längderna

varierar mellan 40 och 150 m mellan olika realiseringar, av vilka 0–40 m tillskrivs transport i Struktur #19.

Utvärdering av retentionsparametrar

Den samlade utvärderingen av retentionsegenskaperna i de immobila zonerna längs de två studerade flödesvägarna baseras på de individuella resultaten från de fyra modellgrupperna.

Den huvudsakliga emfasen ligger på retentionen som orsakas av matrisdiffusion, som är beroende både av egenskaperna hos flödesfältet (genom den hydrodynamiska kontrollparametern β, också benämnd transportmotstånd F [TL^{-1}] och egenskaperna hos de immobila zonerna längs flödesvägen (givna av materialegenskapsgruppen κ, som innefattar både effekter av matrisdiffusion och sorption). Detta innebär att retentionsegenskaperna hos de immobila zonerna alltid måste utvärderas tillsammans med antaganden om flödesfält och flödesväg.

I den utvecklade mikrostrukturella modellen av de immobila zonerna, är Typ 1-sprickorna av förkastningskaraktär och uppvisar en hög grad av heterogenitet och innehåller också porösa, ibland leriga sprickfyllnader (*fault gouge*). Sprickorna av Typ 1 är av icke förkastningstyp och är inte så heterogena som sprickorna av Typ 1. Högporösa sprickfyllnader antas inte finnas i sprickor av Typ 2.

I de flesta av transportmodellerna av det studerade systemet beskrivs flödesväg I av ett fåtal timmar av advektiv transport medan flödesväg II karakteriseras av ungefär 150 timmar medeltransporttid. Samtliga modeller visar på tydliga skillnader i advektiv transport mellan de två flödesvägarna. Det euklidiska avståndet mellan injiceringspunkten och pumpsektionen är ungefär det samma mellan de två flödesvägarna, men modellerna indikerar en storleksordning längre residenstid i flödesväg II jämfört med flödesväg I.

Medelvärden av de utvärderade hydrodynamiska kontrollparametrarna β längs de två flödesvägarna, erhållna från de fyra utvärderingsmodellerna, är med två undantag, relativt konsistenta mellan modellerna. Medelvärdet på β är nära två storleksordningar högre (större retention) för flödesväg II jämfört med flödesväg I. Den tidigare redovisade tre tiopotenser stora skillnaden i transmissivitet mellan Struktur #19 och BG1 borde innebära till och med en större skillnad i β. Detta aktuella förhållande kan förklaras av att övriga sprickor som tillsammans med BG1 utgör del av flödesväg II har högre transmissivitet än BG1.

De effektiva retentionsegenskaperna längs de två flödesvägarna utvärderades av SKB-KTH/WRE för flertalet av de utnyttjade spårämnena. Flödesväg I uppvisar effektiva retentionsegenskaper för immobila zoner som motsvarar kataklasit i den mikrostrukturella modellen (större retention). I motsats uppvisar flödesväg II effektiva retentionsegenskaper för immobila zoner som ligger nära omvandlat sidoberg. Detta resultat understöds också av karaktären hos flödesvägarna, där både injicerings- och pumpsektion för flödesväg I är belägna i Struktur #19. Den senare är en förkastningsliknande struktur bestående av ett flertal immobila zoner, som också innefattar högporösa sprickfyllander (*fault gouge*). Injektionspunkten i flödesväg II är belägen i en något enklare spricka som inte är av förkastningstyp och resultaten både av numerisk modellering och bedömning av fördelningar av advektiva residenstider indikerar att denna flödesväg är geometriskt mer komplex, och förväntas domineras av bakgrundsprickor.

Utvärdering av den hydrostrukturella modellen

Den uppställda hydrostrukturella modellen i anslutning till Struktur #19 beläggs överlag av de samlade resultaten från hydrauliska försök och spårförsök inom ramen för BS2A och BS2B mellan sektioner i och i närheten av Struktur #19. Följande specifika resultat kan noteras:

- De hydrauliska interferenstesterna (för-försöken) visar tydliga bevis för att Struktur #19 fungerar som en plan, huvudsakligen homogen konduktiv struktur, som karakteriseras av radiellt flöde över intermediära avstånd, och med likartade hydrauliska responser från de olika intercepten med strukturen.
- Försök med icke sorberande spårämnen som utförts mellan borrhålen som tolkas skära Struktur #19 uppvisar advektiva transporttider och dispersionsvärden som är överensstämmande med flöde i en enskild plan struktur.

- Storleken på de effektiva retentionsegenskaperna från spårförsök med sorberande spårämnen (BS2B) är överensstämmande med vad som förväntas i termer av transport i ett sprickplan i kontakt med immobila zoner, så som de definieras av den mikrostrukturella modellen, och den givna flödessituationen.

Bakgrundssprickan BG1 utgjorde injiceringspunkt för BS2B-injiceringen i flödesväg II. Benämningen ”bakgrundsspricka” används därför att den aktuella sprickan saknar direkta bevis på intercept i de angränsande borrhålen. Bevisen för dess existens är begränsade till en enskild flödeslogg och en BIPS-logg. Beroende på att sprickan endast identifierats i ett borrhål är det svårt att tillskriva en storlek till sprickan. Vidare, baserat på erfarenheter inom projektet, så har enskilda sprickintercept en geometri som vanligtvis skiljer sig 10 till 30 grader från den medelorientering som kan beräknas för sprickplanet baserat på de enskilda intercepten. Som en följd av detta är osäkerheten i den hydrostrukturella modellen stor när det gäller BG1. Följande slutsatser kan dras:

- Endast en mindre del av flödesväg II kan vara belägen i Struktur #19 på grund av de väsentligt olika retentionsegenskaperna hos immobila zoner hos denna. BG1 kan därför antingen ha en storlek motsvarande en radie om 20 m (för att nå borrhål KI0025F03), eller så måste flödesväg II bestå av ett antal bakgrundssprickor.
- Då den effektiva dispersionslängden bakåtberäknad från flödesväg II är relativt liten, är det troligt att flödesväg II består av ett mindre antal konnekterade bakgrundssprickor.
- De lägre retentionsegenskaper för immobila zoner som observerats för flödesväg II stöder hypotesen att BG1 är en spricka av Typ 2 med inga eller begränsad andel av högporösa immobila zoner.

Slutsatser

- De lägre retentionsegenskaperna för immobila zoner som tillskrivs bakgrundssprickor jämfört med Struktur #19 (förkastningskaraktär) har verifierats genom bakåtberäkningar. Den utvärderade retentionsegenskaperna för flödesväg I (Struktur #19), uttryckta som parametern κ, är ungefär en storleksordning högre än för flödesvägen bestående av bakgrundssprickor (flödesväg II). Denna observation är i överstämmelse med den utvecklade mikrostrukturella modellen. Det kan noteras att den observerade skillnaden i egenskaper är tillämpbar för experimentella tidsskalor. Över längre tider kommer förmodligen retentionskapaciteten hos sprickor/strukturer av förkastningskaraktär att mättas.
- Den övergripande retentionen (med hänsyn både till både κ och β) i flödesväg II (dominerad av bakgrundsprickor) är ungefär en storleksordning större än i flödesväg I. Detta resultat tillskrivs i första hand längre residenstider (lägre flöde) jämfört med flödesväg I.
- De presenterade resultaten är i överensstämmelse med att flödesväg I avgränsas av en plan struktur med immobila zoner tilldelade och parameteriserade i enlighet med den mikrostrukturella modellen. På samma sätt indikerar resultaten att flödesväg II består av ett antal bakgrundsprickor (inklusive BG1).
- Osäkerheten i utförd analys och tolkningar har utvärderats kvantitativt, och har påvisat att osäkerheten i den hydrodynamiska parametern β (längden på flödesvägen och flödeshastighet) är högre än den för retentionsparametern κ (bestämd av fysiska och kemiska egenskaper). Den utförda analysen stöder utvecklingen av mer realistiska hydrostrukturella modeller med osäkerhet representerad av simuleringar av transport av radionuklider i diskreta spricknätverk (DFN).

Modellanalysen (prediktioner och utvärdering) av spårförsöken inom ramen för TRUE Block Scale Continuation visar tydligt att en god geologisk kunskap (i termer av utvecklade hydrostrukturella och mikrostrukturella modeller) är viktig för förståelsen av transport av sorberande spårämnen i sprickigt kristallint berg. Den kvantitativa analysen med fokus på flödesväg II i bakgrundssprickor indikerar, trots lägre retentionsegenskaper, att dessa kan bidra väsentligt till retention beroende på att de karakteriseras av lägre flöden och längre residenstider. Då de aktuella resultaten endast baserat på ett enskilt experimentellt resultat finns det ett behov att belägga detta förhållande ytterligare.

Contents

1 Introduction

1.1 Background

Concepts for deep geological disposal of spent nuclear fuel include multi-barrier systems for isolation of nuclear waste from the biosphere. Waste forms, and concepts for encapsulation of the waste and engineered barriers may vary between countries, but most concepts rely on a natural geological barrier which should provide a stable mechanical and chemical environment for the engineered barriers, and should also reduce and retard transport of radionuclides released from the engineered barriers. In case of early canister damage, the retention capacity of the host rock in relation to short-lived radionuclides such as Cs and Sr become important.

In planning the experiments to be performed during the Operating Phase of the Äspö Hard Rock Laboratory, the Swedish Nuclear Fuel and Waste Management Company (SKB) identified the need for a better understanding of radionuclide transport and retention processes in fractured crystalline rock. The needs of performance assessment included improved confidence in models to be used for quantifying transport of sorbing radionuclides. It was also considered important, from the performance assessment perspective, to be able to show that adequate transport data and parameters (distribution coefficients, diffusivity, parameters representing the "flow wetted surface area", etc) could be obtained from site characterisation (field experiments and associated modelling), and that laboratory results could be related to retention parameters obtained in situ. To answer these needs, SKB in 1994 initiated a tracer test programme named the Tracer Retention Understanding Experiments (TRUE).

The First Stage of TRUE /Winberg et al. 2000/ was performed in the detailed scale (0–10 m) and was focused on characterisation, experimentation and modelling of an interpreted single feature. Work performed included staged drilling of five boreholes, site characterisation, and installation of multi-packer systems to isolate interpreted hydraulic structures. Subsequent cross-hole hydraulic tests and a comprehensive series of tracer tests were used to plan a series of three tracer tests with radioactive sorbing tracers. The in situ tests were supported by a comprehensive laboratory programme performed on generic as well as on site-specific material from the studied feature. In addition techniques for characterisation of the pore space of the investigated flow paths using epoxy resin have been developed and successfully tested in situ.

The various phases of tracer testing performed as part of TRUE-1 were subject to blind model predictions and subsequent evaluation /Elert 1999, Elert and Svensson 2001, Marshall and Elert 2003/. The results of the TRUE-1 experiments showed clear evidence of diffusion, attributed by some researchers as diffusion into the rock matrix with associated sorption on inner pore surfaces /Cvetkovic et al. in manuscript, Widestrand et al. in manuscript/. Other researchers claimed that the observed retention could be attributed to diffusion/sorption in fine-grained fault gouge material /Mazurek et al. 2003, Jakob et al. 2003/. A clear distinction between alternative interpretations can only be achieved by fully implementation of the developed resin technology to the investigated feature. An interim step in this direction has been taken by the successful investigation of fault rock zones at Äspö HRL /Maersk Hansen and Staub 2004, Hakami and Wang in prep/.

The TRUE Programme identified early that the understanding of radionuclide transport and retention in the Block Scale (10–100 m) also required a separate experiment. Consequently the TRUE Block Scale project /Winberg 1997/ was devised. The experiment hosted in the southwestern parts of the experimental level is centred on the 450 m level. The investigated rock block (200×250×100 m) was investigated during the period 1996 through 1999, and was reported during 2003.

The TRUE Block Scale project was executed as an international partnership funded by ANDRA, ENRESA, JNC, Nirex, Posiva and SKB. The project was divided in a series of defined stages; Scoping Stage, Preliminary Characterisation Stage, Detailed Characterisation Stage, Tracer Test Stage and the Evaluation and Reporting Stage. The specific objectives were to; 1) increase understanding of tracer transport in a fracture network and improve predictive capabilities, 2) assess the importance of tracer retention mechanisms (diffusion and sorption) in a fracture network, and 3) assess the link between flow and transport data as a means for predicting transport phenomena. Characterisation in included drilling, core logging, borehole imaging, borehole radar, 3D seismic surveys, hydraulic tests (flow logging, single hole tests, cross-hole interference tests), tracer dilution tests, hydro-geochemical analyses of groundwater samples and various types of mineralogical, geochemical and petrophysical measurements on drill core samples. Drilling and characterisation of each new borehole was followed by analysis and decision with regards to need and geometry of a subsequent borehole. The main set of tools for determining the conductive geometry and the hydrostructural model was a combination of borehole television (BIPS), high resolution flow logging and pressure responses from drilling and cross-hole interference tests. The constructed hydrostructural model was made up of a set of deterministic subvertical structures mainly oriented northwest. Hydraulic features not part of the deterministic set were included in a stochastic background fracture population. Material properties and boundary conditions were also assigned to the developed model. Characteristics and properties measured in the laboratory were integrated in generalised microstructural models. Hypotheses formulated in relation to defined basic questions were addressed in the in situ radioactive sorbing tracer tests and in the subsequent evaluation using numerical models. Details on the characterisation process and construction of hydrostructural and microstructural models are provided by /Andersson et al. 2002a/. The in situ tracer test programme was crowned by four injections of cocktails of radioactive sorbing tracers in three different source-sink pairs over distances ranging between 15 and 100 m, as integrated along the deterministic structures of the hydrostructural model, defining flow paths of variable complexity /Andersson et al. 2002b, 2004a/. Numerical modelling using a variety of concepts/codes constituted an important and integrated component of the project. A major accomplishment in this context was the development of a common conceptual basis for transport and retention. The fractured crystalline rock volume was here conceptualised as a dual porosity medium (mobile-immobile). Model predictions of the sorbing tracer tests were followed by evaluation modelling where the various modelling results were used for elevating understanding of block scale transport and retention and relative role of processes. Diffusion to the immobile pore space, sorption in the immobile pore space and surface sorption on the fracture surfaces along the transport paths were interpreted as the main retention processes in the prediction and evaluation models applied. This interpretation was supported both by the characteristics of in situ breakthrough curves and modelling, where in the latter case the measured residence time distributions were reproduced more accurately with diffusional mass transfer invoked. Geological information from the site also provided support for the assumption of multiple immobile zones along the investigated flow paths. Details on implementation of the common conceptual basis, model predictions and evaluation are provided by /Poteri et al. 2002/.

At the termination of the TRUE Block Scale project it was recognised that a number of questions remained incompletely analysed and/or understood /Winberg et al. 2002/, and hence a continuation project was set up involving ANDRA, JNC, Posiva and SKB. The basic element of the TRUE Block Scale Continuation project, as further elaborated in this report, is application of the integrated knowledge base from TRUE to an untested part of the TRUE Block Scale rock volume. In this context special emphasis is put on the geological understanding and the distinction between fault structure retention as opposed to the retention seen in a background fracture (featured by lower transmissivity and projected lower retention capacity).

The TRUE Block Scale Continuation Project is organised in two different phases:

- BS2A – which involved scoping calculation by the four modelling groups involved in support for planed experiments; ANDRA-Itasca (unified analysis of geological structures of different sizes) /Darcel 2003/, JNC-Golder (Network aspects, distances, time frames and mass recovery), Posiva-VTT (discrimination of various types of fracture heterogeneity) /Poteri 2003/, and SKB-KTH-WRE (Significance of diffusion limitations and rim zone heterogeneity) /Cvetkovic 2003/. Furthermore, the experimental array was optimised in order to conduct a series of three cross-hole interference tests (CPT-1 through CPT-3) including tracer dilution /Andersson et al. 2004b/.
- BS2B – This included performance of three non-sorbing tracer tests /Andersson et al. 2004b/, performance of two injections of radioactive sorbing tracers /Andersson et al. 2005/, followed by predictive modelling, evaluation, and reporting. The individual modelling results of the four modelling teams involved are reported by /Billaux 2005, Fox et al. 2005, Poteri 2005, Cheng and Cvetkovic 2005/.

This current report presents the results of the TRUE Block Scale Continuation project which feature scooping modelling of network transport, in situ pre-tests (cross-hole interference including tracer dilution, non-sorbing tracer tests), model predictions, tracer tests with radioactive sorbing followed by integrated evaluation.

1.2 Rationale

One important contribution of the TRUE Block Scale project was the establishment of a common framework for Transport and retention. This enabled, despite the apparent differences in the type (site characterisation/performance assessment-related) and complexity (dimensionality, representation of conductive elements and whether analytical or numerical), a unified comparison of modelled retention. An important basis for the conducted analysis was the further developed conceptual microstructural models. The latter developed significantly as a result of the work conducted, which included detailed mineralogy/geochemistry, porosity determinations and polymer impregnation (PMMA) of (altered) wall rock and millimetre- to centimetre-sized breccia. Furthermore, the sorption characteristics of altered wall rock and fine-grained (clayey) fault gouge were estimated based on ambient water chemistry, cation exchange capacity (CEC) and mineralogy of the geological material and the selectivity coefficients of the tracers.

Significant progress has been made *en route* from the First TRUE Stage /Winberg et al. 2000/ through TRUE Block Scale /Andersson et al. 2002ab, Poteri et al. 2002, Winberg et al. 2002/. This applies both to establishing and refining representations of immobile zones in parameterised microstructural models of and to numerical modelling based thereon. However, it was concluded that in situ porosity determination of fault gouge in its natural state was high on the list of prioritised needs, this while the fault gouge is deemed to have strong influence on reactive mass transfer over experimental time scales. Furthermore, leaning only on estimated/calculated K_d values of relevant tracers/material was found to require verification, although estimates for K_d of intact rock have been found to compare well with experimental data. The address of these two issues, in situ characteristics and porosity of fault gouge and verification laboratory sorption measurements on altered wall rock and fault gouge, have been pursued as part of the TRUE-1 Continuation project /Maersk Hansen and Staub 2004, Hakami and Wang in prep, Byegård and Tullborg in prep/ (the TRUE-1 Continuation activities are separated from TRUE Block Scale organisation-wise, but are fully and mutually co-supportive).

It is noted that in situ tests and modelling of longer flow paths in single intermediate-sized structures within TRUE Block Scale Continuation is intimately connected to improving understanding transport of radionuclides from the network of fractures in the immediate vicinity of a deposition hole to, and within, an intermediate fracture zone (SKB nomenclature: small local deformation zone). Integration of available TRUE Block Scale (and Äspö HRL) information and data for model prediction, performance of an in situ test involving such a structure,

is considered a valuable contribution to understanding flow and transport in crystalline rock. To test the above hypotheses, alongside the necessary geometrical considerations of structure /fracture geometries, the project will integrate and use geologic data to interpret retention properties for prediction purposes. That is, given fracture mineralogy, spatial distribution of porosity, geometry and properties of fault gouge and other structural details (some information strategically imported), can one predict and evaluate in situ retention convincingly? If this is the case, then site selection and site characterisation programs, in their early stages, can make use of an early geologic description based on drill-cores to estimate retention properties applicable to experimental time scales long before in situ tracer tests can be performed.

Injection in (low-transmissivity) background fractures connecting to fracture/structure networks is a valuable contribution to understanding the other extreme, i.e. conductive elements which are likely to be connecting to, or being located in the close vicinity of a deposition borehole. The key issues here are pathway branching and mixing at fracture intersections. We will strive to identify background fracture pathways that can be used to characterise and test these processes.

The TRUE Block Scale Project /Andersson et al. 2002a, Poteri et al. 2002, Winberg et al. 2002/ identified diffusion/sorption to available immobile pore spaces as the main active retention mechanism in the case of the TRUE Block Scale Phase C tests. The particular part of the immobile pore space that contributes the bulk of the observed in situ retention was however not determined conclusively. It was further noted that the evaluated in situ retention parameters were increased compared to the available laboratory-derived retention parameters for the (unaltered intact) rock matrix. Critical issues were hence primary associated with the evaluated increased retention relative to available laboratory data. Can this effect be associated with high porosity immobile zones (fault gouge/wall rock rim zone) as stated by the project group, or is this in fact an effect of an underestimation of the area (normalised to flow) exposed to flow (transport) along the studied flow paths? Furthermore, can assessments be improved of the relative contributions of the available immobile zones assumed present along the flow paths, and their relative contribution to retention? It is noted that the TRUE Block Scale Continuation project may not fully "resolve" conclusively the issues put forward. The project will at any rate improve understanding of key issues identified within the project related to block scale transport issues related to geometry, hydrogeology and solute retention, including effects of microstructure.

1.3 Objectives

The general objectives of the Tracer Retention Understanding Experiments (TRUE) are to:

- develop an understanding of radionuclide migration and retention in fractured crystalline rock,
- evaluate to what extent concepts used in models are based on realistic descriptions of a rock volume and if adequate data can be collected in site characterisation,
- evaluate the usefulness and feasibility of different approaches to model radionuclide migration and retention,
- provide in situ data on radionuclide migration and retention.

The overall objective of the TRUE Block Scale Continuation Project can be summarised as:

"Improve understanding of transport pathways at the block scale, including assessment of effects of geology and geometry, macrostructure and microstructure".

In order to cater to addressing the overall objective a series of hypotheses were formulated as further elaborated in Section 1.4.

1.4 Assessment of premises for in situ experimentation

The TRUE Block Scale Technical Committee in February 2003 defined plans for the BS2A modelling. Supporting and scooping modelling was to be performed to analyse "longer flow paths" and flow paths involving low-transmissivity "background fractures". The possible needs for remediation of the KI0023B piezometer should also be explored. This latter concern was motivated by:

- The possible effect of the Structure #20-Structure #6 short circuit in section KI0023B:P7 on flow paths using sinks in the Structure #20 system in the vicinity of borehole KI0023B.
- The possibility of increasing the number of injection points in background fractures in KI0023B.
- The possibility of performing Posiva logging in KI0023B, was the downhole equipment to be removed, to bring its level of characterisation up to that of the KI0025F02 and KI0023F03 boreholes – particularly to define the extensions of Structures #22 and #23, or to identify other conductive features.

The simulations to explore the effects of the KI0023B short circuit and longer flow paths were carried out by JNC-Golder. The experimental team selected a series of potential test scenarios (source-sink alternatives). Among these alternative set ups 6 simulation source-sink pairs for background fracture flow paths (B2, B4, B8, B13, B18, B23) and 5 source-sink pairs involving longer flow paths (F4, F5, F10, F11, F15), the latter varying in Euclidean length between 50 m and 115 m.

The simulations were carried out using FracMan/PAWorks with Laplace Transform Galerkin (LTG) transport through a mapped pipe channel network, cf Section 4.3 and Appendix C2. The developed DFN model employed the TRUE Block Scale project reference hydrostructural model. The background fracture population was generated using the parameters presented by

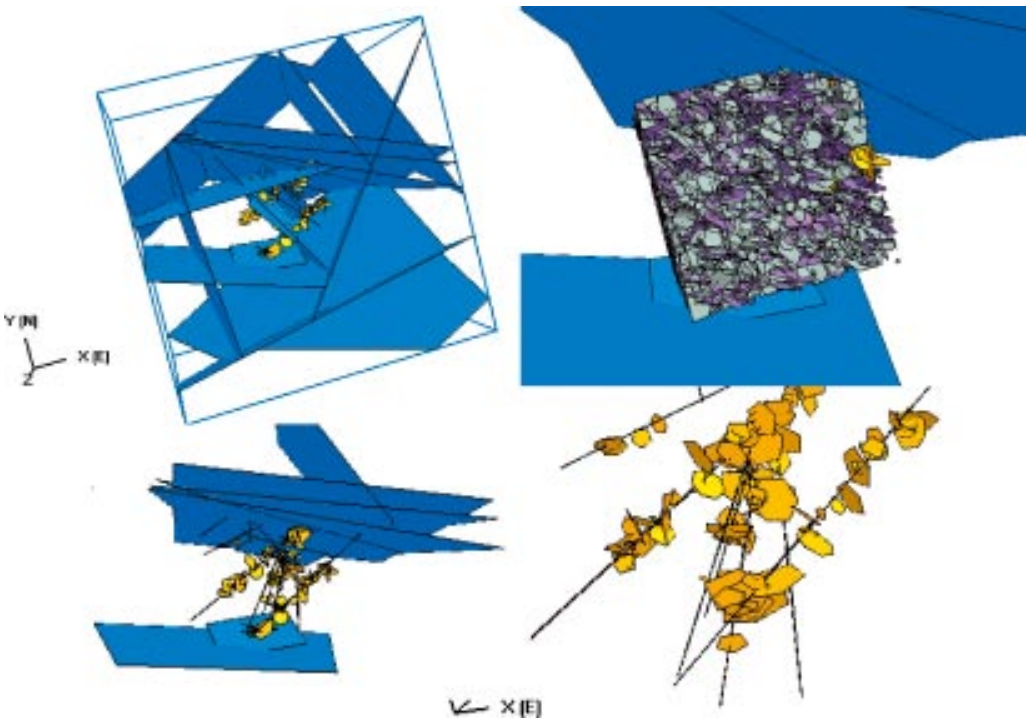

Figure 1-1. *Outline of JNC/Golder BS2A modelling: Upper left – model at 500 m to boundary conditions. Upper right – detailed region of background fractures (zoom view). Lower left – deterministic structures and Posiva flow low features (zoom view). Lower right – boreholes with Posiva flow log features (zoom view).*

/Andersson et al. 2002a/. The fracture transport and immobile zone properties were based on a correlation between fracture transmissivity and aperture, calibrated to the results of TRUE Block Scale tracer tests, Phase C /Dershowitz and Klise 2002/.

The KI0023B:P7 short circuit has a measured internal flux of 0.2 l/m. This was represented in the JNC/Golder modelling as a grouped flux of 0.05 l/m for a realistic case, and 2 l/m for an assumed extreme case. Remediation of the KI0023B piezometer was modelled by setting the leakage flux to zero l/m. This is considered as a fairly coarse approximation, but still considered adequate given schedule constraints.

DFN simulation results are shown in Tables 1-1 and 1-2 in terms of travel times and recovery and in Figures 1-2 and 1-3 in terms of cumulative recovery. The following general findings were noted:

a) The simulated F-series tests (long distances) produced flow paths to the boundaries of the block in addition to flow paths to tracer test sinks (based on David Holton's boundary conditions). As a result, there is considerable mass loss to the boundaries, rather than to the pumping well.

b) For the simulated F-series tests, using the extreme 2 litres/minute sink to represent the leak in KI0023B:P7, there is a significant improvement in tracer mass recovery for some set-ups with remediation of the KI0023B:P7 short circuit.

c) For one of the F-series simulation cases, the gradient is generally away from the desired sink. Adding 2 litres/minute sink at KI0023B:P7 moves the "groundwater divide" closer to the model boundaries, actually increasing recovery.

d) For the B-series (involving injection in background fractures) experiments, the recoveries are generally very good, since the distances are small and no other sinks are acting. These simulations do not show any improvement with KI0023B:P7 remediation.

e) The F-series simulations produce very long conservative-tracer travel times with t_5 in the range 4,500–12,000 hrs for the flow paths that make up networks. This equates to tests that have durations between 0.5–1.4 yrs. In this context it is noted that the BS2c test run between KA2563A:S1 and KI023B:P6 (L = 130 m) showed a travel time in the order of 3 months.

f) The simulated conservative tracer travel time (t_5) for the longest Structure #19 flow path (115 m between KA2563A and KI0025F, distance = 115 m) is 1,750 hrs (73 days or 2.4 months).

The overall conclusions given the simulation results were:

1) The low recoveries observed and long travel times for the long network pathways do not bode well for the planned long distance network tracer tests. This observation is reinforced by the field observation of geochemical contrast between the #19 system and the #20 system.

2) Tests in networks involving injection in background fractures are definitely feasible and can be expected to yield quite good recoveries. This is substantiated by our previous experience from testing other "background fractures", e.g. Structures #21, #22, #23.

3) Tests in fracture networks over long distances can be expected to show low, and possibly no recovery. This is a direct consequence of the pattern of connectivity in the rock block that has many different connections toward structures that ultimately drain to the tunnels.

4) Still, there is a reasonable chance that we can get breakthrough (t_5 at least) for conservative tracers for many of the network pathways considered within six months to one year of pumping. Strongly sorbing tracers, it seems, would be unlikely to show up in reasonable times.

5) Based on the simulations performed so far, there is considerably less risk if pathways in Structure #19 (i.e. F5, F2, F7 and F9) are pursued. However, there is still some risk. To quantify that risk, additional simulations of F5 will be run employing multiple realisations of stochastic "background fractures" and synthetic members of the "200-m scale" deterministic structure population.

6) The simulations clearly show that remediation of KI0023B does not produce significant changes in tracer recovery for the proposed flow paths. It should be pointed out that remediation of KI0023B would define better the locations of Structures #22 and #23 (and others), as well as provide additional points for sinks or sources.

Table 1-1. Simulation results from analysis of flow paths involving background fractures.

		Background tests					
		B2	**B4**	**B8**	**B13**	**B18**	**B23**
KI0023B:P7	**t5**	178.0	?	115.7	29.0	87.0	34.0
nodal group	**t50**	na	?	290.2	113.1	199.9	119.2
REMEDIATED	**t95**	na	?	1,902.2	na	1,095.8	na
	% Recovery	14.4%	?	95.4%	92.8%	98.6%	87.7%
KI0023B:P7	**t5**	178.0	?	114.8	29.0	87.0	34.0
nodal group	**t50**	na	?	290.1	114.8	199.9	114.8
P7 flux of 0.05 l/min	**t95**	na	?	1,797.0	na	1,095.8	na
	% Recovery	14.6%	?	95.4%	92.9%	98.6%	87.8%
KI0023B:P7	**t5**	163.1	?	90.3	27.9	81.0	27.9
nodal group	**t50**	999.3	?	210.4	93.8	184.1	80.0
P7 flux of 2 l/min	**t95**	na	?	na	na	1,200.9	na
	% Recovery	66.7%	?	92.0%	92.4%	97.8%	91.0%

Table 1-2. Simulation results from analysis of flow paths involving longer flow paths.

		Long distance tests				
		F4	**F5**	**F10**	**F11**	**F15**
KI0023B:P7	**t5**	12,000	1,750	4,500	12,000	4,500
nodal group	**t50**	na	5,000	Na	na	Na
REMEDIATED	**t95**	na	10,950	Na	na	Na
	% Recovery	41.5%	97.8%	23.6%	41.3%	25.2%
KI0023B:P7	**t5**	12,000	1,750	4,500	12,000	4,500
nodal group	**t50**	na	5,000	na	na	na
flux of 0.05 l/min	**t95**	na	10,950	na	na	na
	% Recovery	41.5%	97.8%	24.3%	41.8%	25.9%
KI0023B:P7	**t5**	10,000	2,000	2,950	9,000	2,950
nodal group	**t50**	na	6,000	17,000	28,000	14,025
flux of 2 l/min	**t95**	na	na	na	na	na
	% Recovery	35.4%	91.6%	51.9%	53.20%	53.2%

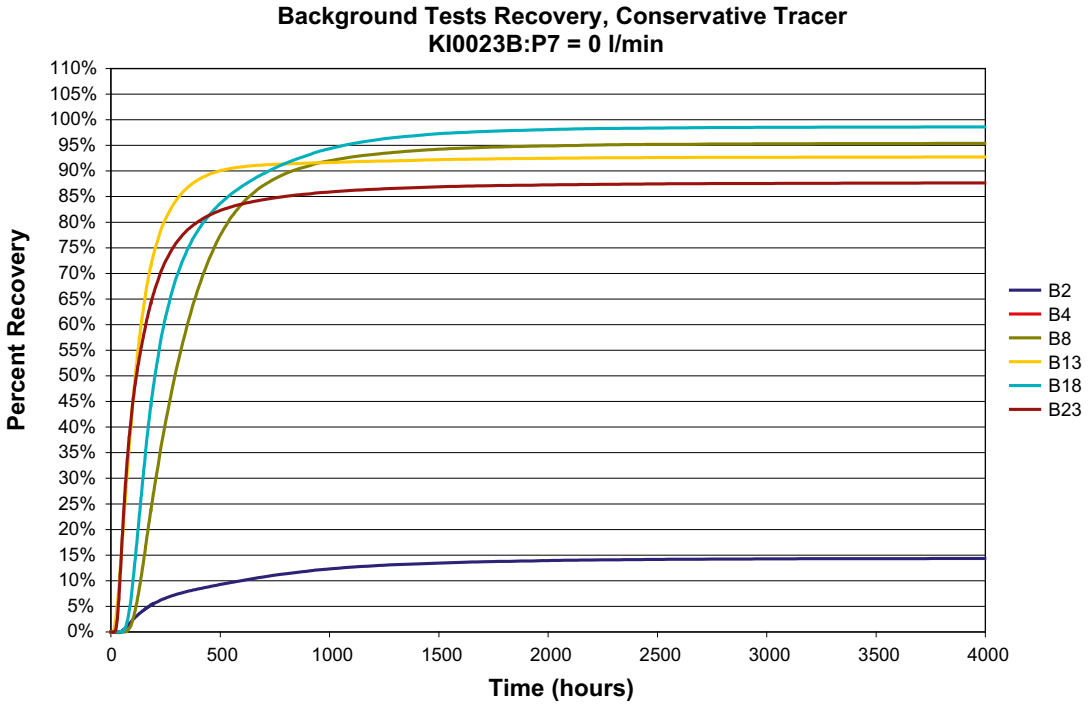

Figure 1-2a. *Simulation of flow paths involving injection in background fractures (no effect of short circuit in KI0023B:P7).*

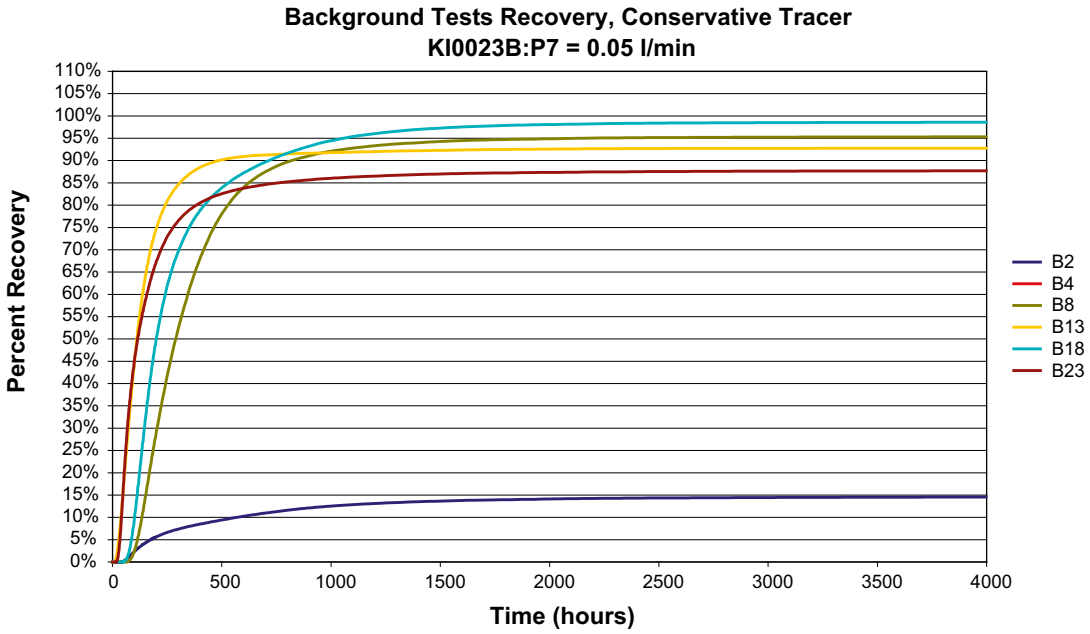

Figure 1-2b. *Simulation of flow paths involving injection in background fractures (effect of short circuit in KI0023B:P7 simulated as an additional sink with q = 0.05 l/min).*

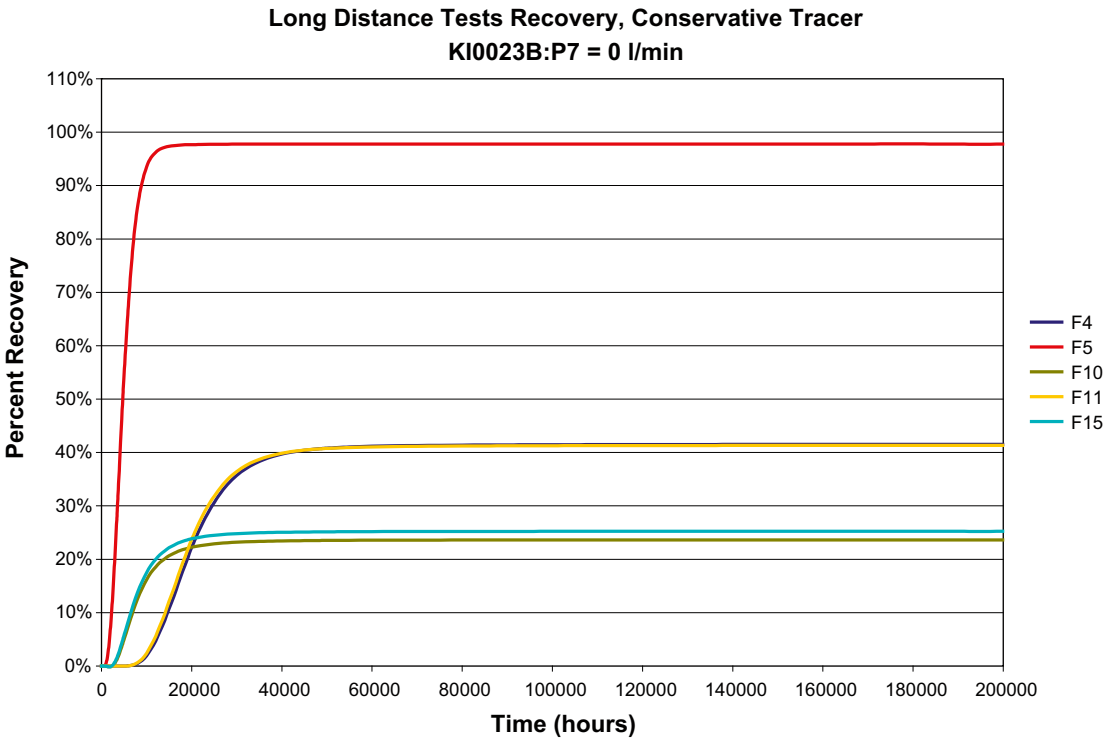

Figure 1-3a. *Simulation of longer flow paths (no effect of short circuit in KI0023B:P7).*

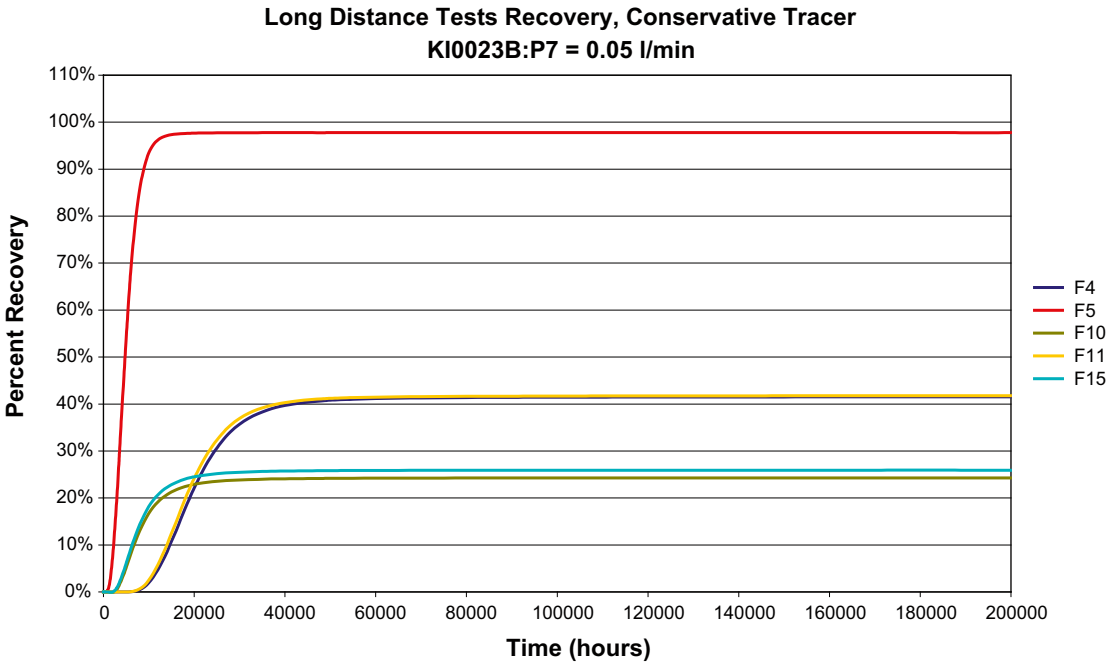

Figure 1-3b. *Simulation of longer flow paths (effect of short circuit in KI0023B:P7 simulated as an additional sink with q = 0.05 l/min).*

1.4.1 Summary

The investigation of the role of background fractures in transport of solutes over longer distances was a key element in the BS2A supporting modelling performed by JNC-Golder. The results of the modelling clearly showed that tests in "complex" fracture networks (involving injection in background fractures) would most likely result in transport times beyond the practical time frames set for BS2. In addition, mass recoveries would be too low to allow use of radioactive sorbing tracers. Instead, address of transport in an intermediate-sized conductive structure, including injections in associated background fractures, and even possible tests in a singled-out background fracture, was presented in a memorandum presented to the SC late Spring 2003. The project team proposed Structure #19 as the main target for the planned experiments. The address of effects of background fractures was given second priority, but ample opportunities are provided to inject tracer in sections with background fractures known, or believed, to be in hydraulic contact with Structure #19.

The underlying principal arguments for proposing Structure #19 are:

- It appears to be a well-defined single feature.
- It appears so have good hydraulic connectivity along its strike.
- It is intercepted by most of the boreholes penetrating the TRUE Block Scale rock volume. Intermediate injection and sampling points could be established in relation to a given test set-up.
- It is geochemically distinct from the #20 complex.
- Structure #19 has relatively few intersections with other known major structures.
- Tests with sink and source sections in Structure #19 would not be affected by the leakage in KI0023B.

1.5 Hypotheses

The a priori theme of TRUE Block Scale Continuation; "Tracer tests over long distances involving a single intermediate-sized structure and integrated evaluation modelling" entailed formulation of a priori hypotheses to be explored by the planned work.

The hypotheses for the BS2B experimental program were originally and tentatively divided in two basic groups related to; (I) the general nature of transport in fracture networks, and (II) transport involving background fractures with due consideration of differences between fault and joint microstructure and properties as identified by /Dershowitz et al. 2003/, branching and mixing phenomena in fracture networks;

- Hypothesis Ia) Microstructural (i.e. detailed geological, mineralogical and geochemical) information can provide significant support for predicting transport of sorbing solutes at experimental time scales.
- Hypothesis Ib) Transport at experimental time scales is significantly different for faults (significant alteration, brecciation and fault gouge) and joints (with or without alteration), due to differences in microstructure and associated properties.
- Hypothesis Ic) Longer distance pathways are dominated by fault rock zone behaviour, while shorter pathways (i.e. representative of fractures in the vicinity of a canister deposition hole) may be more likely to be dominated by joint fracture characteristics.
- Hypothesis IIa) Branching of transport pathways can be demonstrated to occur in networks of background fractures.
- Hypothesis IIb) Mixing at fracture intersection can be demonstrated to occur in networks involving background fractures.

- Hypothesis IIc) Fracture retention properties tend to be scale-dependent primarily due to differences in microstructure.

It is noted that given the outcome of BS2A and early results from borehole reinstrumentation indicated that proper address of Hypotheses Ic, IIa and IIc are likely to be associated with a high degree of uncertainty due to geometrical and mass recovery aspects. In the case of hypotheses Ic, IIc, as shown in Section 1.4, time frames and reduced control (projected low mass recovery) rules out long experimental distances. In the case of Hypothesis IIa we simply lack the in situ control and monitoring power to address this subhypothesis. Although the project has been forced to step back from full address of the originally stated hypotheses, they are retained above for accounting and future reference.

2 Geological setting

2.1 General

The Äspö Region is characterised by granitoids which belong to the Transscandinavian Igneous Belt (TIB). First order discontinuities at a regional scale include N-S and EW lineaments, mainly corresponding to deformation zones, extending some 20–30 kms. Second order discontinuities are reflected in NE- and NW lineaments, some 100–200 m wide and extending 1 to 20 kms. The dominant rocks on the Äspö island range in mineralogical composition from true granites (Ävrö granite) to granoidioritic to quartz monzodioritic composition (Äspö diorite) /Kornfält and Wikman 1988/. U-Pb dating shows these rocks to have intrusion ages around 1,800 Ma /Wahlgren et al. 2005/. These rock types are since early 2002 the focus for extensive investigation in conjunction with the site investigations and site modelling at Simpevarp/Laxemar /SKB 2006/. North and south of the Äspö island are found circular granitic intrusions, the Götemar and Uthammar massifs, which are of significantly younger age, c 1,450 Ma /Åhäll 2001/. Fine-grained granite exists throughout the island and its closest environs in the form of dykes or minor bodies, in some cases cutting granitoids of older age. A general description of the existing rock types including average mineralogical content is provided by /Wahlgren et al. 2005/.

The pattern of interpreted deformation zones at Äspö HRL fits into the general framework of regional scale lineaments/structures. The site investigations at Laxemar have shown that the Äspö island is affected by two regional deformation zones; the E-W Mederhult zone running along its northern shore and the Äspö Shear zone (EW-1) trending ENE across the island. The southern part of Äspö is mainly affected by the latter zone. Local mylonites and shear zones associated with EW-1 control the orientation of subsequent brittle deformation (increased fracturing and brecciation) /Rhén et al. 1997b/. Outcrop mapping on the island indicate that most deformation zones on the Äspö island strike E-W or correlate with the mylonites in the Äspö shear zone striking NE across the centre of the island. Fracturing and fault geometry is found to be strongly related to lithology, where similar characteristics are noted for the Ävrö granite and the Äspö diorite /Andersson et al. 2002a/ whereas the number of subparallel master faults and fracture density is significantly higher (factor 5–10) in the fine-grained granite bodies. Fracture orientations and developed fracture sets largely follow the most conspicuous lineament orientations. Based on the combined analysis of outcrop and borehole data three steeply dipping fracture sets (N-S, NNW and WNW) are identified. A fourth set is subhorizontal trending E-W. The indicated orientations are found in all the different lithologies. The hydraulically active fractures mainly belong to the WNW set, and to a lesser extent the NNW fracture sets. The former set is parallel with the in situ axis of maximum compressive stress, which is essentially horizontal.

2.2 Hydrostructural model

The characterisation of the TRUE Block Scale experimental volume /Andersson et al. 2002a/ involved application of various investigation techniques, e.g. triple-tube core drilling, borehole radar, cross-hole/3D seismics, various types of flow logging techniques (including Posiva flow logging), BIPS borehole imaging and BOREMAP core logging, assessment of hydraulic responses to drilling and various types of single-hole and cross-hole hydraulic tests. The basic geoscientific characterisation used to identify the geological and hydraulic context of the investigated rock volume was crowned by tracer dilution tests (to identify suitable source and sink sections for tracer tests) and multiple-hole tracer tests /Andersson et al. 2002b/ which were used to assess the transport and retention properties of the selected flow paths. The in situ characterisation work was complemented by various laboratory measurements, e.g. of porosity,

mineralogy and solid phase geochemistry and hydrogeochemistry. The various methods, the methodology for their application and their usefulness are described and reviewed in detail by /Andersson et al. 2002a/. While the investigations were staged, a sequence of hydrostructural models were produced over the duration of the TRUE Block Scale project, as described by /Andersson et al. 2002a/, reflecting the successive evolution of the understanding of the investigated rock volume. The final hydrostructural model (Tracer Test Stage), cf Figure 2-1, features 13 named deterministic structures which are interpreted in two or more boreholes, one structure being Structure #19, located in the far western part of the rock volume. This structure was not part of the tracer test work during TRUE Block Scale and was consequently only given marginal attention at the time. The structure was however known in all boreholes but KA2511A showing a gradual change from an essentially singular feature to a more complex structure in the southeast, cf Figure 2-1. Furthermore, the multi-packer isolation of Structure #19 in the various boreholes indicated that it was in contact with the Structure #20 network (including Structure #6, #23, #22, #13 and #21), either by way of Structure #13, or by way of background fractures of unknown geometry.

One way of describing the different structures in a simplified way suitable for modelling purposes is to use the subdivision into Type 1 and Type 2 features which was applied in the Äspö Task Force Task 6C modelling study, as illustrated in Figure 2-2 and Figure 2-3, respectively. The Type 1 fracture is characterised by a significant movement along the main fault plane. The structure typically contains a ductile precursor (mylonite) which has been reactivated forming a brittle fault filled with mineralisations, cataclasite and fault gouge. The wall rock around the structure has been altered by hydrothermal solutions. It is often accompanied by subparallel fractures in the mylonite and altered zone. The Type 2 fracture, in contrast, is characterised by a fracture without typical kinematic indicators. The fracture is formed without any plastic precursor and contains fracture mineralisations only. There is a significant zone of alteration around the open fracture plane and it is often accompanied by subparallel fractures of the same type.

In order to describe the structures within the TRUE Block Scale rock volume in a manner compatible with the model outlined in Task 6C /Dershowitz et al. 2003/ the term Complexity factor was introduced to be used together with the Type 1 and Type 2 concept. The Complexity

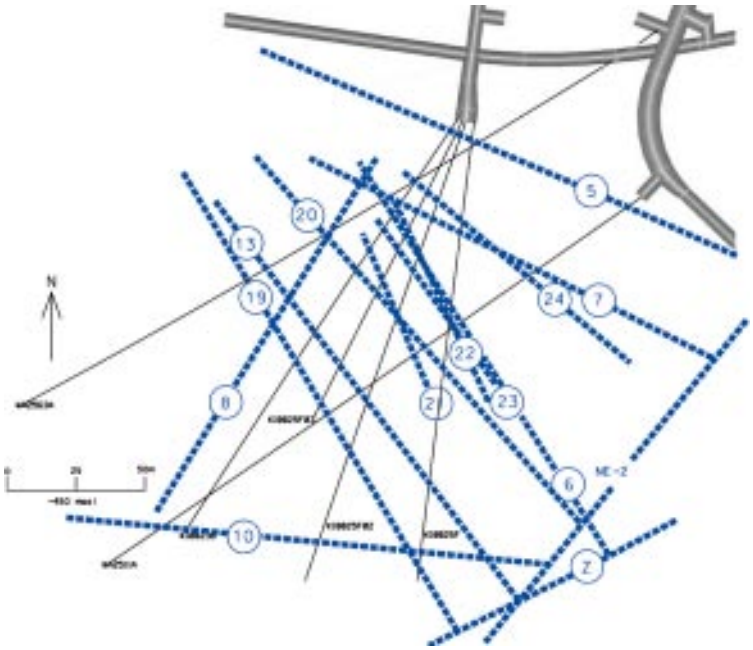

Figure 2-1. *Plan view of the Tracer Test Stage hydrostructural model of the TRUE Block Scale rock volume, cf /Andersson et al. 2002a/.*

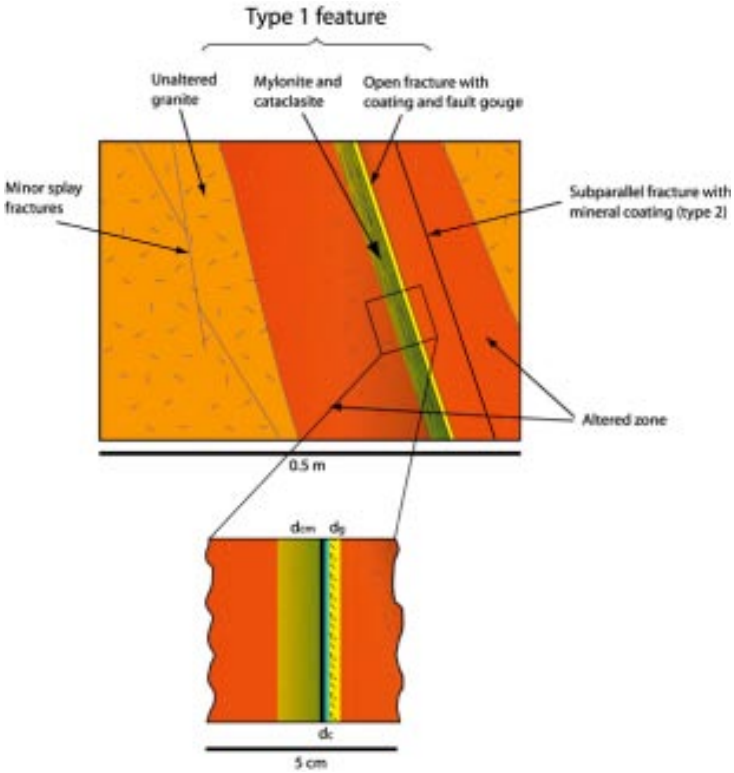

Figure 2-2. *Fracture type 1 represents a structure containing a ductile precursor (mylonite) which has been reactivated forming a brittle fault filled with mineralisations, cataclasite, fault gouge. The wall rock around the structure has been altered by hydrothermal solutions /cf Dershowitz et al. 2003/.*

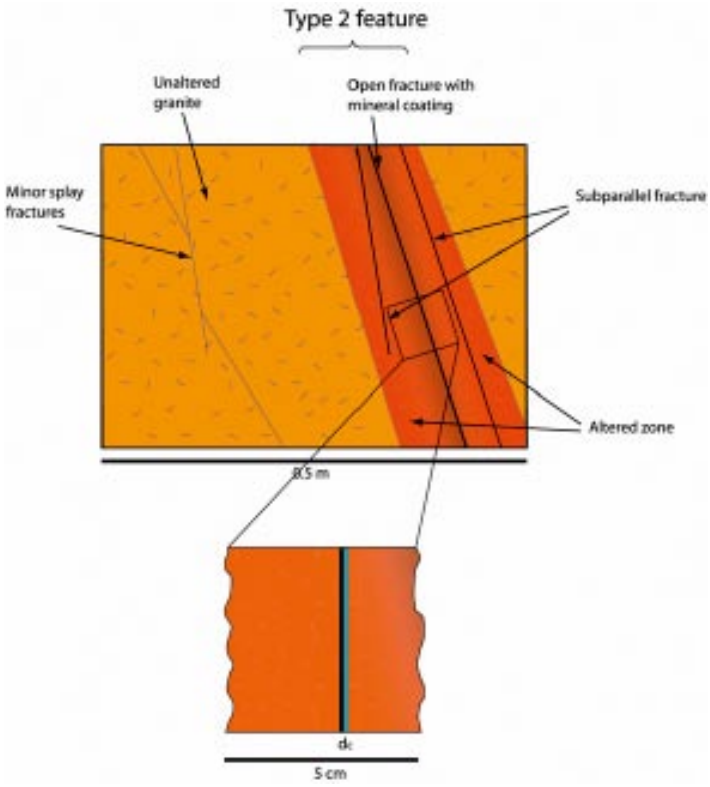

Figure 2-3. *Fracture Type 2 is a fracture without a ductile precursor containing fracture mineralisations only but usually with a significant zone of alteration around the open fracture plane /cf Dershowitz et al. 2003/.*

factor indicates the number of conducting features in the structure, i.e. at each structure intercept the fracture type and the Complexity factor is provided (for more details, see Appendix A). The result is shown in Figure 2-4, where it is evident that most of the structures vary in complexity over their entire length. Furthermore, it is common that a combination of both Type 1 and Type 2 fractures makes up any given structure.

The deterministic structure in focus for the BS2 phase of the TRUE Block Scale Continuation project, #19, varies considerably over its length with the more complex pattern (Type 2 structure with complexity factor 3 or more) in the SE part whereas in the NW part the fault reduces to a single fracture. Also a conductive splay fracture connected to #19 was detected in borehole KA2563A. The central parts of Structure #19 (described by intersections in boreholes KI0023B, KI0025F03 and KI0025F02) can be described as mainly two parallel features of Type 1 character cf Figure 2-5.

2.2.1 Structure #19

Structure #19 is steeply dipping NNW trending ductile deformation zone, 20 to 100 cm wide, which have subsequently been reactivated. This has resulted in faults with fault gouge and fault breccia present in its core. The length of the structure is at minimum l50 m.

This type of structure is very similar in character and composition to the earlier described and documented Structure #13 and Structure #20 in the TRUE Block Scale rock volume /cf Andersson et al. 2002a/. Based on tracer dilution tests it was decided that the main focus for the sorbing tracer tests should be the interceptions in boreholes KI0023B, KI0025F03 and KI0025F02 (encircled in Figure 2-5). For the description of the structure (analyses of fracture material etc) however, also samples from KI0025F were used, cf Table 2-1.

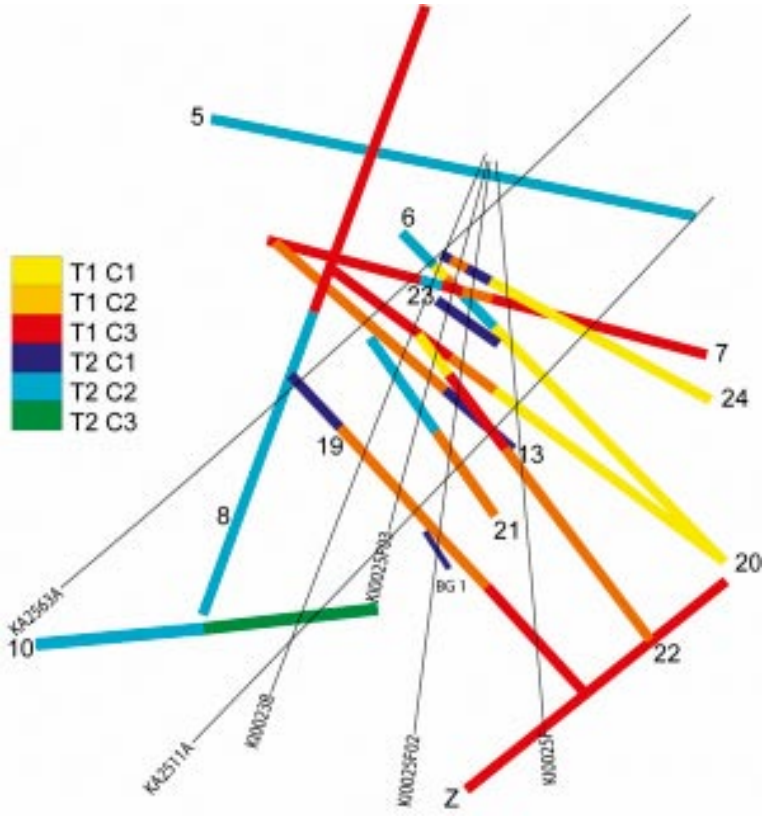

Figure 2-4. *Fracture types and complexity according to Äspö Task Force Task 6C /Dershowitz et al. 2003/ draped on the BS2 hydrostructural model.*

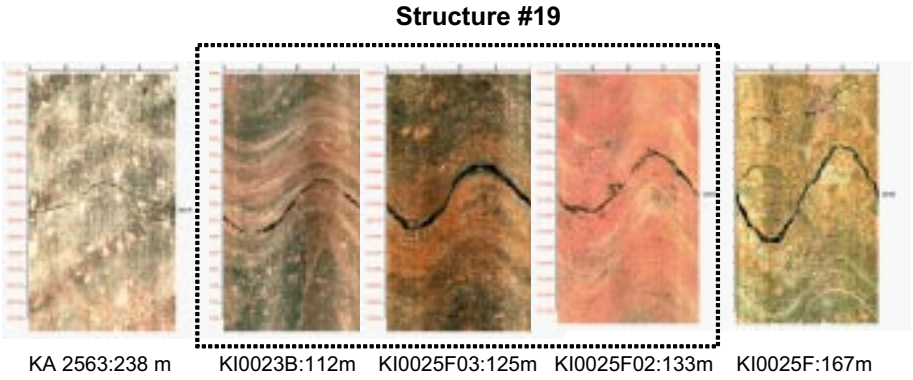

Figure 2-5. *Fracture intersections observed in BIPS logs, with similar orientations in several intersecting boreholes. Each BIPS image represents a borehole interval of approximately 30 cm. Encircled are the three central intersections of Structure #19 that are the main focus of the BS2 experiments.*

Table 2-1. Description of intercepts of Structure #19 in boreholes KA2563A, KI0023B, KI0025F02, KI0025F03 and KI0025F. The mineralogy is determined by X-ray diffractometry.

Borehole length (section)	Tectonic zone	Conductive zone	Mineralogy in fracture coating and infilling
KA2563A: 238 m	Weak alteration of host rock 2–4 cm	One single fracture	Calcite, chlorite, illite and mixed-layer clay
KI0023B: 111.45–111.86 m	Strong tectonisation including mylonites and cataclasite 50 cm wide	Section with breccia and probably gouge 1–2 cm wide	Adularia epidote, chlorite, calcite and probably clay minerals
KI0025F03: 124.65–124.75 m	Smaller tectonised zone hosting thin mylonites and cataclasites 20 cm wide	Looks like 2 parallel fractures ca 1 cm apart with breccia fragments and probably gouge in between 1–2 cm wide	Quartz, chlorite, K-feldspar, epidote, fluorite, calcite, corrensite
KI0025F02: around 133 m borehole length	A wide tectonised zone including small mylonites and cataclasites 100 cm wide	Two conductive features with one main conductor with breccia and fault gouge – some cm wide 2–3 cm wide	Quartz, K-feldspar, plagioclase, chlorite, calcite, epidote, smectite, mixed-layer clay
KI0025F: 166.45–166.9 m	Tectonised part including mylonites 20 cm wide	A small network of fractures probably with clay coatings running parallel with the tectonised zone but 15 cm apart	Calcite, Quartz, plagioclase, K-feldspar, chlorite, and mixed-layer clay with large illite components

From a mineralogical point of view the zone is hosted in Äspö diorite but, as mentioned above and also visible in Figure 2-5, the ductile deformation and hydrothermal alteration along the zone has changed the mineralogy of the wall rock to thin mylonites (consisting of fine-grained quartz, epidote, K-feldspar albite and chlorite) and cataclasic rock (quartz, K-feldspar, albite and chlorite). The fracture coatings and infillings are represented by chlorite, calcite, clay minerals and also altered rock fragments and grains of quartz and feldspar. The variability in mineralogy is described in Section 2.3.

2.2.2 Background fracture BG1

In an early phase of the BS2B programme two fractures in boreholes KI0025F02 and KI0025F03, southwest of Structure #19, were identified as hydraulically conductive, and potentially being the same structure, and a Structure #25 was proposed. However, later it was observed that no hydraulic response between the two fractures could be measured, although both features showed hydraulic connection with Structure #19. One of these, at 113.6 m in KI0025F02, was chosen to represent background fractures present within the rock block between major structures like Structures #19 and #20. This fracture was given the name BG1.

The BG1 fracture in KI0025F02 is situated between a thin (few mm wide) mylonite and a fracture sealed by calcite (cf Figure 2-6). Despite the closeness to the small mylonite the wall rock is relatively fresh and e.g. biotite is still present close to the fracture, although the plagioclase is saussuritisised. The feldspars also show some red-staining, cf Table 2-2.

Table 2-2. Characteristics of background fracture BG1 (based on the sole observation in borehole KI0025F02).

Borehole:section	Tectonic zone	Conductive zone	Mineralogy of fracture coating (non-continuous)
KI0025F02:138.6	A thin mylonite and a sealed fracture with calcite. Some red-staining observed in the wall rock	One small fracture sub parallel with the mylonite but mainly hosted in relatively fresh wall rock	Calcite, Chlorite and, small amounts of Prehnite/ Epidote K-feldspar, pyrite and clay minerals

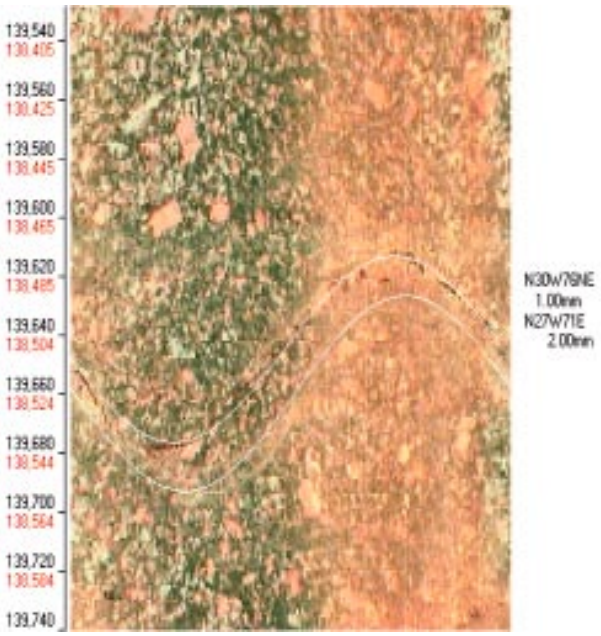

Figure 2-6. *Detail of BIPS borehole TV image of background fracture BG1 as seen borehole KI0025F02. The fracture is striking N30W and dipping steeply to the northeast.*

2.3 Microstructural models

The reason for establishing a microstructural model is to provide a conceptualised description of the mineralogy and textures, which thereafter is assign retention parameters to the different entities in the model as laid out by the parameterised geometry of fracture type involved. For the time frame of a tracer test most of the retention is assumed to take place in the very close rim in contact with the tracer flow path. Therefore the identification of the fracture infillings and coatings are highly important for the microstructural model. Good samples, which in this case implies samples undisturbed by flushing (maintaining integrity of unconsolidated fine-grained material) and without rotation of the core segments in the core barrel against one another during drilling, are of utmost importance. Unfortunately, although all boreholes apart from KA2563A and KA2511A are drilled using triple-tube core barrels the outcome, particularly with regards to flushing of clay material, is are not always successful. This means that amounts of clay minerals estimated based solely on the findings in the drill cores can be substantially underestimated.

Assignment of thicknesses and porosities to the different layers are important entities for the modelling. In Appendix A this is handled in accordance with the simplifications introduced in the Type 1 and Type 2 structures proposed in the Task 6C report /Dershowitz et al. 2003/.

2.3.1 Structure #19

The outcome of the pre-test using tracer dilution measurements (cf Chapter 3) put focus on the Structure #19 intercepts in boreholes KI0023B, KI0025F03, KI0025F02 for further use in in-situ tests. However, since the material available for analyses from these intercepts are limited also samples from the other two intercepts (KA2563A and KI0025F) are used in order to describe the in filling material.

Thin sections, X-ray diffractometry and chemical analyses were used. The fracture minerals identified by these methods are given in Table 2-1 and Table 2-2.

Material from the intercept in KI0025F02: 133 m was analysed already during the TRUE Block Scale characterisation phase /Andersson et al. 2002a/

For illustration two figures, showing thin sections and photos of fracture surfaces pf Structure #19, are provided, cf Figure 2-7 and Figure 2-8.

Intercept of KI0025F02:

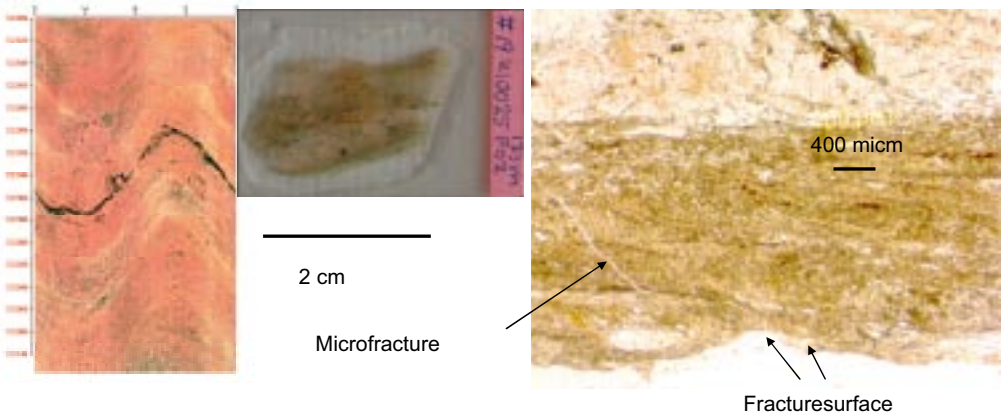

Figure 2-7. *Structure #19 intercept in borehole KI0025F02. The thin section microphotograph (to the right), illustrates the layered structure of the wall rock (rim zone). The ductile deformation zone hosting the water conducting fractures is built up of cataclastite interlayered with thin mylonites. The relatively denser (low porosity) mylonites are transversed by microfractures increasing the total porosity.*

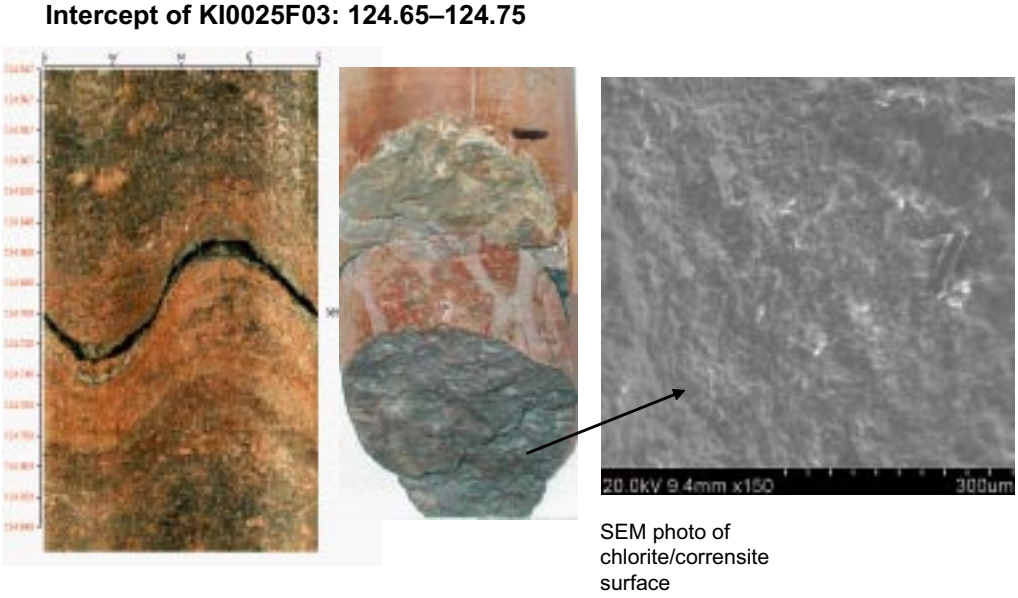

Figure 2-8. *Composite showing the SEM photo (to the right) of the chlorite/corrensite surface probably exposed to the flowing water in Structure #19 at the intercept in borehole KI0025F03.*

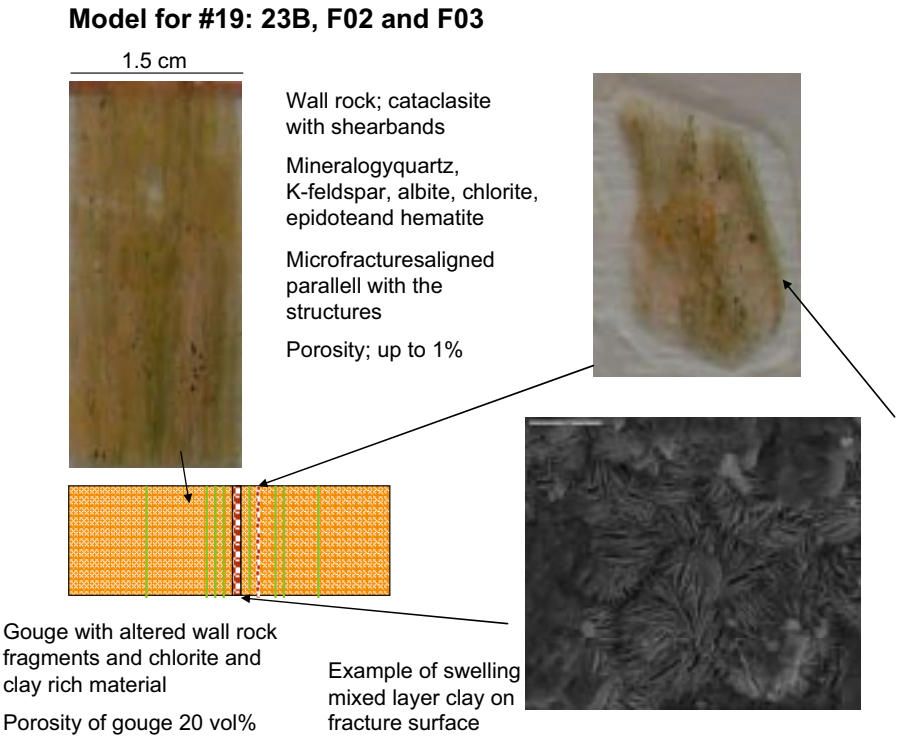

Figure 2-9. *The basic concept of the proposed simplified model of the central parts of Structure #19 as represented by the intercepts in KI0023B, KI0025F02 and KI0025F03.*

In summary, most of the fracture surfaces are coated by chlorite and clay minerals, some calcite and hydrothermal Al-silicates like prehnite and epidote. The fault gouge material is made up of altered rock fragments and grains of quartz, K-feldspar, albite, epidote, chlorite, calcite and clay minerals. The latter varies between the samples ranging from illite, mixed layer illite/smectite and corrensite (mixed layer chlorite/smectite) and pure smectite. The fault gouge material sampled from KI0025F02 consists to almost 50% of chlorite and smectite. This composition has

not been verified in samples from the other intercepts although clay minerals are indicated in all of them. It is believed that despite the use of the triple tube core barrel, disturbances during drilling may have caused flushing of the fault gouge whereby some clay minerals probably have been lost.

The Rim zone (the 1–2 cm close to the water conducting fractures) consists of cataclasite (tectonised and altered Äspö diorite) with interlayered mylonites.

Figure 2-9 visualises this information and Table 2-3 contains principal parameterisation of Structure #19.

For modelling retention along the flow paths a first step is to establish a microstructural model, which quantifies the thickness of each of the geometrically defined (immobile) zones, and to assign a porosity to each individual layer, either measured or estimated. Thereafter the different layers are assigned retention properties. No additional experimental investigations of porosity and diffusivity parameters have been performed since the TRUE Block scale initial phase /Andersson et al. 2002a/. Instead the values presented herein are based on the concept proposed and described for the Task 6C concept /Dershowitz et al. 2003/. Generic values of porosities applicable to TRUE Block Scale conditions are there proposed for the different materials. Formation factors are calculated using the combination of Archie's law and tabulated water diffusivities for the different tracers. Table B-5 in Appendix B shows proposed porosities and diffusivity values for the different geological materials and how these have been used in the present report.

Structure #19 is a complex structure composed of several parallel faults/features. It is noted that the given parameterisation is made per individual feature. Accounting of multiple parallel features is made through assignment of a Complexity factor, cf Section 2.2.

Retention is mainly provided my diffusion and sorption and in a time-wise short experiments like the BS2B tracer tests, sorption plays an important role. For simplification two entities have been defined, to which sorption capacities are assigned. These are; gouge (fracture infilling and fracture coatings) and rim zone (which is the 1–2 cm immediately adjacent to the conductive fracture/fault which comprise mylonites, catacalsites and altered rock). This concept is discussed in detail in Appendix B and also in the reporting of laboratory sorption measurements on gouge and rim zone material, which also include material from the TRUE Block Scale rock volume /Byegård and Tullborg in prep/.

Investigations of the different borehole intercepts with Structure #19 provided significant amount of gouge material only for the KI0025F02 intercept. As discussed above, high amounts of e.g. smectite (15%) and chlorite (30%) were identified in these samples /Andersson et al. 2002a/. However, fault gouge material in amounts sufficient to be used in laboratory measurements of sorption, was not found in the other intercepts with Structure #19, this probably due to events during drilling. This said – it has not been possible to confirm presence of smectite (even in trace quantities) in the other sampled intercepts although other clay minerals have been identified.

Table 2-3. Geometry, porosity and formation factor assigned to rock types making up Geological Structure Type 1 (Fault) representative of Structure #19.

Rock type	Thickness (cm)	Porosity (%)	Formation factor (−)
Intact wall rock	−	0.3	7.3E–5
Altered zone	15	0.6	2.2E–4
Cataclasite/Mylonite d_{cm}	1	1	4.9E–4
Fault gouge d_g	0.3	20	5.6E–2
Fracture coating d_c	0.05	5	6.2E–3

During the initial phase of the TRUE Block scale experiment, sorption capacities (K_d) for the fault gouge material were predicted based on mineralogy, literature data for CEC, selectivity coefficients and groundwater chemistry /Andersson 2002a/. The recently carried out laboratory measurements /Byegård and Tullborg in prep/ are compared with the before mentioned estimated values for fault gouge materials from Structures #19, #20 and #22 in Figure 2-10. A generally good agreement between the estimated/predicted and measured values is noted and it is also evident that the different fault gouge materials showed largely similar values. It is interesting to note that the smectite sample from Structure #19 showed lower K_d values than estimated. This may suggest that the importance of the smectite is over-estimated, or that the smecitite component was over-estimated in the mineralogical composition used for the prediction.

Smecitite has a very high CEC capacity and its presence/absence may have a significant effect on the total sorption capacity. Since we only have indication of smectite from one intercept, but the others showed some disturbances and are therefore less reliable, it was decided to use two different approaches, cf Appendix B for details and Table 2-4 for results.

It is further noted that the fracture coating in accordance with the Type 1 structure in /Dershowitz et al. 2003/ is assigned equivalent properties of the fault gouge material as described above.

Table 2-4. Assignment of volumetric sorption coefficient K_d according to two concepts A and B outlined in the text above.

Tracer	Concept A K_d (m^3/kg)	±	Concept B K_d (m^3/kg)	Interval
$^{85}Sr^{2+}$	6.0E–4	3E–5	1.3E–3	(6.0–21)E–4
$^{86}Rb^{+}$	2.7E–3	9E–4	1.5E–2	(2.7–27)E–3
$^{137}Cs^{+}$	4.0E–2	1E–3	1.0E–1	(4.0–14)E–2

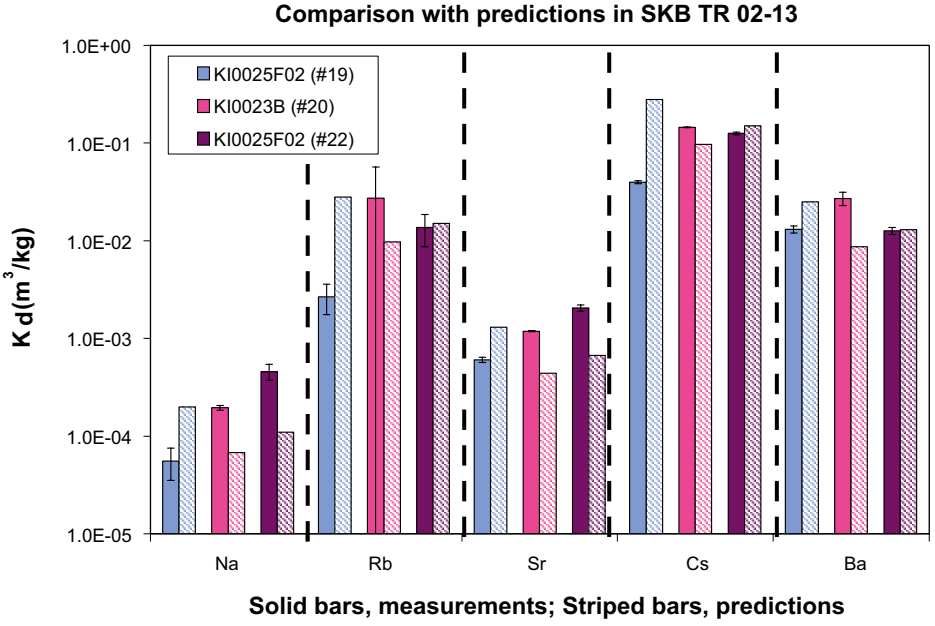

Figure 2-10. *Results from Kd measurements on fault gouge material from intercepts with TRUE Block Scale Structures #19, #20 and #22. The results are compared with predicted based on mineralogy, hydrogeochemistry and literature data for CEC and selectivity coefficients.*

The fracture rim zone of Structure #19 has been categorised to consist of ~ 80% of "strongly hydrothermally altered rock" (represented by the intercept in KI0023B) and ~ 20% of "mylonitic and cataclasitic wall rock, in Äspö diorite" (represented by the intercept in borehole KI0025F). These two rock materials have been subject to sorption experiments in the laboratory giving the following results for the tracers used in the TRUE Block Scale Continuation experiment /Byegård and Tullborg in prep/.

Assignment of surface sorption coefficients for the rim zone of Structure #19 is provided in Table 2-5, see Appendix B for details.

2.3.2 Background fracture BG1

The micro-scale characteristics of background fracture BG1, as observed in KI0025F02: 138.5 m, are shown in Figure 2-11. For identification of phases, very little material was available and the characterisation is based on one thin section studied for description of the rim zone and one fracture surface sample studied in SEM for identification of the fracture coating.

BG1 is an open fracture surrounded to the left by a calcite sealed fracture (2–10 mm apart from BG1) and to the right of a thin mylonite about 2–10 mm away from BG1 cf Figure 2-11. Biotite is preserved in the wall rock but the feldspars are altered and show some red staining due to micrograins of hematite close to the fracture edge.

Table 2-5. Assignment of surface sorption coefficient K_a relevant to fracture rim zone material of Structure #1.

	Strongly hydrothermally altered rock (80%)				Mylonitic and cataclasitic wall rock, in Äspö diorite (20%)			
Tracer	K_a (m)	±	K_d (m³/kg)	±	K_a (m)	±	K_d (m³/kg)	±
$^{85}Sr^{2+}$	1.5E–5	5E–6	2.6E–5	1.5E–5	2.2E–5	9E–6	1.4E–4	2E–5
$^{86}Rb^{+}$	< 1E–4		< 4E–4		< 8E–4		< 4E–3	
$^{137}Cs^{+}$	1.0E–3	4E–6	< 5E–4		9.8E–3	5E–4	< 3E–2	

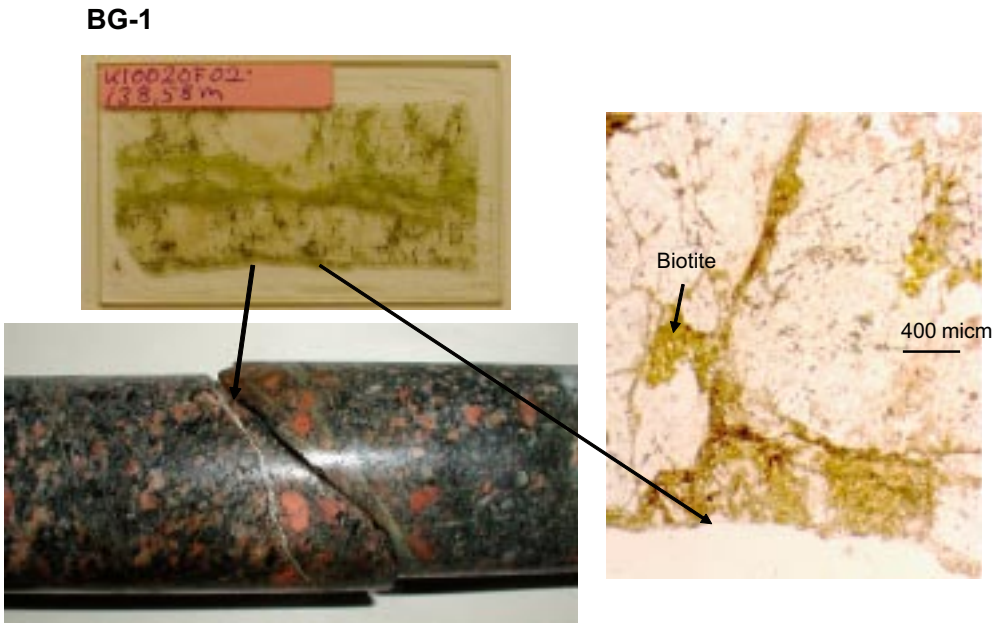

Figure 2-11. *The BG1 intercept in borehole KI0025F02: 1,385 m, Photo of drill core, thin section and microphotograph of part of the same thin section (to the right). The host rock is Äspö diorite.*

The surface is coated with a thin layer of mainly chlorite, calcite in addition to clay minerals, epidote and prehnite. Scattered occurrences of euhedral crystals of calcite and pyrite are also found on the surface. The fracture coating is not continuous and K-feldspar from the host rock is exposed at the fracture edge (cf Figure 2-12).

Figure 2-13 shows SEM photos of the fracture surface BG1. Calcite and pyrite are shown as euhedral crystals on chlorite and clay coatings.

The obtained information from BG1 resulted in the simplified microstructural model and parameterisation given in Table 2-6, in accordance with the detailed descriptions given in Appendices A and B. The wall rock alteration was not very significant but the plagioclase was altered and some red staining was observed and the presence of the thin mylonite and the sealed calcite coating led to the suggested extent of 5 cm for the altered rock layer.

The sorption coefficients proposed for of BG1 are equal to the measured values from the fault gouge material sampled at the intercept with Structure #20 in borehole KI0023B, this since this material showed similar mineralogy to that observed in BG1, cf Table 2-7.

Figure 2-12. *Surface of BG1 in borehole KI0025F02 with thin coating of mainly chlorite, calcite, clay minerals and epidote. The length of the base of the photograph is 46 mm.*

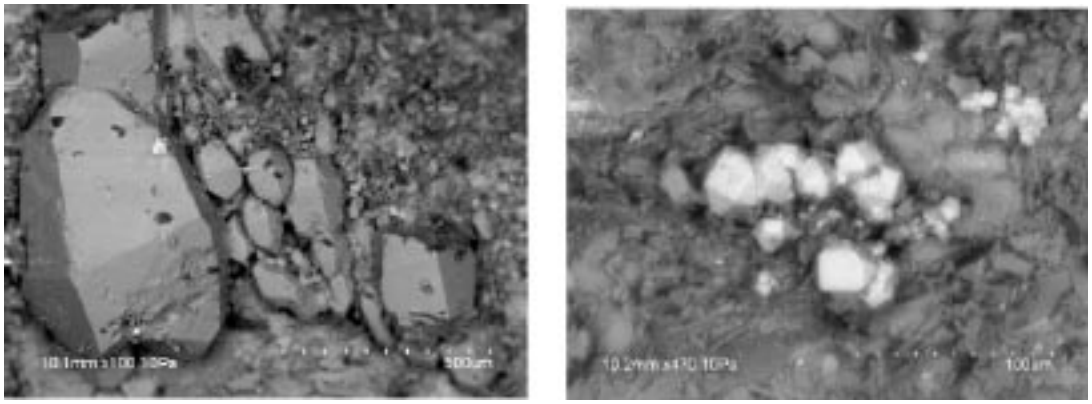

Figure 2-13. *Back-Scatter Electron microscope image of stubby scalenohedral calcite crystals to the left and small euhedral pyrite crystals on fracture surface coated with chlorite and clay minerals to the right.*

Table 2-6. Geometry, porosity and formation factor assigned to rock types making up background fracture BG1.

Rock type	Thickness (cm)	Porosity (%)	Formation factor (−)
Intact wall rock	−	0.3	7.3E–5
Altered zone	5	0.6	2.2E–4
Fracture coating d_c	0.05	5	6.2E–3

Table 2-7. Assigned volumetric sorption coefficient *K*d of fracture coating material of background fracture BG1.

Tracer	K_d (m^3/kg)	± 1 st. dev.
$^{22}Na^+$	2.0E–4	1E–5
$^{133}Ba^{2+}$	2.7E–2	4E–3
$^{54}Mn^{2+}$	1.7E–1	6E–2

From the results presented by /Byegård et al. 1998/, it is estimated that the altered Äspö diorite found in the TRUE-1 Feature A intercept with KXTT2 is the best representative of the fracture rim zone of BG1. However, a drawback in the use of these data is that the tracer distribution ratio in these experiments was only determined for the 1–2 mm fraction. This means that an extrapolation using sorption data from different size fractions (in order to describe the sorption with surface sorption coefficients, K_a and volumetric sorption coefficient, K_d) cannot be performed for this material. An alternative concept has therefore been used which is accounted for in Appendix B. The results are shown in Table 2-8.

As explained in the Section 2.3.1 concerning Structure #19, no further experimental investigations of the porosity and diffusivity parameters have been performed, see also Appendix B. Table B-4 in Appendix B presents the proposed porosities and diffusivity values for different geological materials.

2.3.3 Discussion

Already during the TRUE-1 stage of the tracer experiments it was observed that the parameterisation using sorption and diffusivity values for generic host rock was not sufficient for the modelling the TRUE-1 tracer experiments /Winberg et al. 2000/. It was suggested that: 1) the wall rock close to the fracture edge had properties different from unaltered host rock e.g. different mineralogy and porosity. 2) It was suspected that unconsolidated fracture material with high

Table 2-8. Volumetric (*K*d*x*) and surface sorption (*Ka*x) coefficients proposed for the BG1 rim zone material.

Tracer	$R_{d(1-2mm)}$ altered Äspö diorite /Byegård et al. 1998/	$\left\langle \frac{K_{di}}{R_{d(1-2mm)i}} \right\rangle_i$	K_{dx}	$\left\langle \frac{K_{ai}}{R_{d(1-2mm)i}} \right\rangle_i$	K_{ax}
$^{22}Na^+$	2.9E–6	0.58	1.7E–6	0.24	7.0E–7
$^{133}Ba^{2+}$	1.2E–3		6.9E–4		2.9E–4
$^{54}Mn^{2+}$	Not measured		4.3E–3*		1.8E–3*

*Calculated by multiplying the corresponding value of Ba^{2+} with a factor of 6.3, procedure described in Appendix B.

sorption capacity was lost during the conventional drilling and therefore the retention property of the fracture infilling material was underestimated. These findings led to the microstructural model approach employed for the TRUE Block Scale experiment /Andersson et al. 2002a/, which was further elaborated in the Äspö Task Force Task 6C /Dershowitz et al. 2003/. One improvement since then has been the laboratory sorption measurements carried out on fault gouge and rim zone material from the TRUE block scale structures /Byegård and Tullborg in prep/.

For comparison between the different tracer injections it might be of interest to compare the different structures in which tests with sorbing tracers have been performed in the earlier TRUE tests: Feature A used in the TRUE-1 experiment is featured by ductile deformation later reactivated similar to what is seen Structure #19. However, the dignity (thickness and probably length) of Feature A is however, significantly less that that of Structure #19. Structure #19 and Structure #20 show many similarities, although Structure #20 is characterised by a stronger element of hydrothermal alteration, whereas Structure #19 shows a stronger element of mylonitization. It is noted, however, that this comparison is based on the essentially three intercepts representing the parts investigated by tracer tests, and hence involves an element of speculation. However, the concepts of the microstructural model appear to be applicable to these three structures.

3 Experimental work

3.1 Background

The experimental programme planned to answer the hypotheses set up (cf Section 1.5) included four main components:

1. Optimisation of the instrumentation of the TRUE Blocks scale array based on the decision to focus on Structure #19 and background fracture BG1.
2. A suite of pre-tests (CPT-1 through CPT-4) aiming at finding the best possible test geometry for the tracer tests with sorbing tracers.
3. Tracer tests with sorbing tracers including two test geometries with pumping in Structure #19 and injection in the same structure as well as in the background structure BG1.
4. Laboratory sorption experiments on altered wall rock and fault gouge in order to improve the microstructural model.

3.2 Re-intrumentation of the TRUE Block Scale array

3.2.1 Background

A strategy for the forthcoming tracer tests was suggested at the TRUE Block Scale technical committee meeting in Stockholm late April 2003 The strategy focused on tracer tests over longer distances in Structure #19 and, if possible also in minor fractures connected to, or sub-parallel to #19. The meeting concluded that two of the boreholes, KI0025F02 and KI0025F03, needed to be optimised to better focus on Structure #19.

Besides the need for new packer locations, special consideration had to be taken to the fact that two of the borehole sections in KI0025F03 (P5 and P7) and one in KI0025F02 (P3) earlier have been used for tracer test with radioactive sorbing tracers and most likely was contaminated.

A short-term interference test between the two boreholes was also planned after re-instrumentation of the first borehole (KI0025F03). The purpose was to check if background structures located close to Structure #19 were hydraulically connected between the boreholes.

3.2.2 Instrumentation of borehole KI0025F03

The re-instrumentation focused on Structure #19 at 125 m and “background fracture BG2” close to #19 at 133 m. Sections P5 and P7 was left “untouched” due to radioactive contamination, cf Table 3-1.

The borehole instrumentation, manufactured by Geosigma, was restrained to include a maximum of five sections with possibility to inject and sample tracers (sections marked with C in Table 3-1).

Table 3-1. Old and new instrumentation of borehole KI0025F03.

Old Borehole/section	Borehole length (m)	Structure #	New Borehole/section	Borehole length (m)	Structure #
25F03P1	101.0–141.7	10, 19	25F03R1	135.0–141.7	10
25F03P2	93.5–100.0	?	25F03R2	129.0–134.0 C	BG2
25F03P3	89.0–92.5 C	13	25F03R3	123.0–128.0 C	19
25F03P4	85.0–88.0 C	21	25F03R4	93.5–122.0 C	?
Blind	75.0–84.0		25F03R5	89.0–92.5 C	13
25F03P5	66.5–74.0 C	20	25F03R6	75.0–88.0	21
25F03P6	59.5–65.5 C	22	25F03R7	66.5–74.0 C	20
25F03P7	55.0–58.5 C	23	25F03R8	59.5–65.5	22
25F03P8	51.5–54.0	6	25F03R9	55.0–58.5	23
25F03P9	3.5–50.5	5, 7, 24	Blind	3.5–54.0	5, 6, 7, 24

C = Section equipped for tracer injection/sampling.

3.2.3 Short-term interference test

After re-instrumentation of KI0025F03 and removal of packers in KI0025F02 a double-packer system (5 m section length) with a guard packer close to the tunnel was inserted in KI0025F02 and placed over the background fracture (BG1) at 135–139 m borehole length and at two minor fractures at 165–170 m and at 170–175 m borehole length. Short-term interference tests were performed but no pressure responses in the neighbouring boreholes KI0025F03 and KI0025F could be detected. This result suggests that the background structures BG1 and BG2 are individual fractures rather than interconnected structures.

3.2.4 Instrumentation of borehole KI0025F02

The re-instrumentation was focused on Structure #19 at 132 m borehole length and "background fracture BG1" close to #19 at 138 m. Section P3 was left "untouched" due to radioactive contamination.

The borehole instrumentation, manufactured by SOLEXPERTS, could include a maximum of ten sections with possibility to inject and sample tracers (sections marked with C in Table 3-2).

Table 3-2. Old and new instrumentation of borehole KI0025F02.

Old Borehole/section	Borehole length (m)	Structure #	New Borehole/section	Borehole length (m)	Structure #
25F02P1	135.15-204.2 C	BG1, 10	25F02R1	140.05-204.2 C	10
25F02P2	100.25-134.15 C	19	25F02R2	135.1-139.05 C	BG1
25F02P3	93.40-99.25 C	13, 21	25F02R3	129.2-134.1 C	19
25F02P4	78.25-92.4 C	?	25F02R4	100.25-128.2 C	
25F02P5	73.3-77.25 C	20	25F02R5	93.35-99.25 C	13, 21
25F02P6	64.0-72.3 C	22	25F02R6	78.25-92.35 C	
25F02P7	56.1-63.0 C	23	25F02R7	73.3-77.25 C	20
25F02P8	51.7-55.1 C	6	25F02R8	64.0-72.3 C	22
25F02P9	38.5-50.7 C	7	25F02R9	56.1-63.0 C	23
25F02P10	3.4-37.5 C	5	25F02R10	3.4-55.1 C	5, 6, 7

C = Section equipped for tracer injection/sampling.

3.3 In situ pretests

3.3.1 Objectives

The main objective with the pre-tests was to obtain a test geometry optimised for radioactive sorbing tracer tests. The tests also aimed to improve the hydro-structural model of the TRUE Block Scale site, in particular in the area of Structure #19 which had not been subject to tracer tests in the past.

The test sequence included a series of pressure interference tests combined with tracer dilution tests (CPT-1 through CPT-3) and finally, also tracer tests with non-sorbing tracers (CPT-4a, -4b and -4c). The specific objectives for CPT1–3 were:

- To find the best possible sink for the tests with sorbing tracers.
- To find a set of candidate injection points for the sorbing tracer tests.

By using the selected candidates, CPT-4a and -4b were performed with the specific objectives of:

- Assessing that the selected flow paths gave a tracer mass recovery of < 80%.
- Assessing the tracer residence time for a non-reactive tracer

Finally, CPT-4c was performed with the main objective of assessing the mass recovery for the finally selected flow paths under slightly different boundary conditions than in CPT-4a and -4b.

3.3.2 Performance of the combined tracer dilution tests and interference tests, CPT-1 to CPT-3

Each test (CPT-1 to CPT-3) included measurements in eight borehole sections during a test cycle of four days with a pumping period of 48 hours. The test cycle comprised (sections 2 below refers to consecutive sections tested):

Day 1 – start tracer dilution test under ambient gradient in sections 1–4.

Day 2 – start pumping in selected sink section, tracer dilution test under pumped conditions in sections 1–4.

Day 3 – change of test sections to three new locations (sections 5–8), tracer dilution tests under pumped conditions.

Day 4 – stop of pumping, tracer dilution test under ambient gradient, sections 5–8.

The withdrawal in the selected sinks was established using the maximum sustainable flow rate. The flow was restricted by the dimension of the tubing and the transmissivity of the section.

The pumping and recovery tests were performed as conventional constant rate pressure interference tests, implying that the flow rates and pressures were monitored with a high measurement frequency by the Äspö Hydro Monitoring System (HMS). The equipment used is described in /Andersson et al. 2004/.

3.3.3 Performance of tracer tests CPT-4a to CPT-4c

Tests CPT-4a through CPT-4c were focused on tracer transport and performed by establishing a radially converging flow field with a constant withdrawal rate in borehole section KI0025F03:R3 (Structure #19). The withdrawal rate was established by using the maximum sustainable flow (2.6–2.8 l/min).

Non-sorbing and non-radioactive tracers (fluorescent dyes) were injected either as decaying pulses or by simultaneous injection of water creating a weak dipole flow field. Samples were automatically withdrawn both in the injection and withdrawal sections using techniques and equipment earlier developed in the TRUE Block Scale Project /Andersson et al. 2002b, 2004b/.

The first tracer test (CPT-4a) included three injections with the decaying pulse technique, i.e. without applying any excess pressure. This procedure introduced some tailing in the breakthrough curve due to the relatively slow decay of the input concentration. To remove some of this tailing effect, the injection of tracer solution was terminated by exchanging the tracer solution with unlabelled water soon after breakthrough was noted in the withdrawal section.

Since no excess pressure was applied in CPT-4a, the dilution rate in the injection sections was low and resulted in up to 25% of the tracer mass remaining in the injection sections after several hundreds of hours. This high concentration of tracer in the injection section after such a long time is disadvantageous from a safety aspect when handling radioactive tracers as planned for the sorbing tracer tests. It was therefore decided to repeat some of the pre-tests with an added injection flow rate of 5 ml/min (unlabelled formation water) and to make sure that the recovery did not decrease under these changed conditions.

The tracers used were Uranine (Sodium fluorescein), Rhodamine WT and Amino G Acid with injection concentrations in the order of 500–2,000 ppm, cf Section 3.3.5.

Table 3-3 summarises the test set-ups including the sources and sinks used in the tests. Locations of the boreholes in the TRUE Block Scale array including sink and source sections are shown in Figure 3-1 together with the main interpreted deterministic structures in the investigated rock volume.

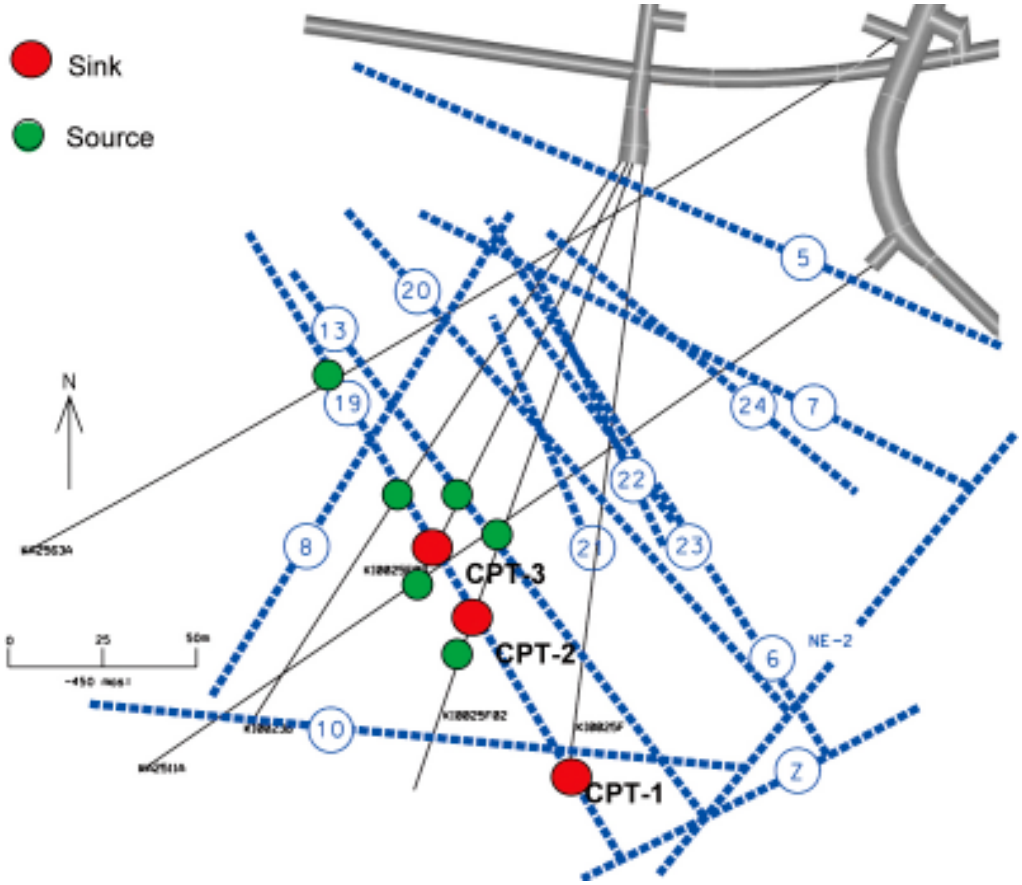

Figure 3-1. *Plan view of hydro structural model based on identified conductive geological structures in the TRUE Block Scale rock volume (horizontal section at Z = –450 m.a.s.l.). Sink (red) and source (green) sections are also marked /from Andersson et al. 2004/.*

Table 3-3. Sources and sinks used for the pre-tests of the TRUE Block Scale Continuation.

Test	Sink	Structure	Source	Structure	Comment
CPT-1	KI0025F:R2	#19	KI0025F02:R3	#19	Tracer dilution/interference test
			KI0025F03:R3	#19	
			KI0023B:P2	#19	
			KA2563A:S1	#19	
			KI0025F02:R2	#BG1	
			KI0025F03:R2	#BG2	
			KI0025F02:R5	#13, 21	
CPT-2	KI0025F02:R3	#19	KI0025F:R2	#19	Tracer dilution/interference test
			KI0025F03:R3	#19	
			KI0023B:P2	#19	
			KA2563A:S1	#19	
			KI0025F02:R2	#BG1	
			KI0025F03:R2	#BG2	
			KI0025F03:R5	#13	
			KI0025F02:R5	#13, 21	
CPT-3	KI0025F03:R3	#19	KI0025F:R2	#19	Tracer dilution/interference test
			KI0025F02:R3	#19	
			KI0023B:P2	#19	
			KA2563A:S1	#19	
			KI0025F02:R2	#BG1	
			KI0025F03:R2	#BG2	
			KI0025F03:R5	#13	
			KI0025F02:R5	#13, 21	
CPT-4a	KI0025F03:R3	#19	KI0025F:R2	#19	Tracer test (radially converging)
			KI0025F02:R3	#19	
			KI0023B:P2	#19	
CPT-4b	KI0025F03:R3	#19	KA2563A:S1	#19	Tracer test (weak dipole, rad. conv.)
			KA2563A:S2	#19	
			KI0025F02:R2	#BG1	
CPT-4c	KI0025F03:R3	#19	KI0025F02:R3	#19	Tracer test (weak dipole)
			KI0023B:P2	#19	
			KI0025F02:R2	#BG1	

3.3.4 Evaluation of pressure responses from CPT-1 through CPT-3

The combined tracer dilution and pressure interference tests CPT-1 through CPT-3 were evaluated both qualitatively and quantitatively using similar procedures as earlier applied in the TRUE Block Scale Project /Andersson et al. 2002ab, 2004b/.

The pressure response matrix for tests CPT-1 to CPT-3 is shown in Table 3-4. The matrix is based on the pressure response diagrams of each test. The colour and letter coding refers to the two indexes s_p/Q (drawdown normalised to pumping rate) and t_R/R^2 (response time normalised to the distance squared) defined in /Andersson et al. 2004b/.

The tests generally show high and fast responses in sections interpreted to include Structure #19, thus confirming the hydro-structural model of the TRUE Block Scale site. The main difference in response pattern is that CPT-1 (sink in KI0025F:R2) gives responses in almost all sections due to the higher withdrawal and thus, larger radius of influence, of the pumping. CPT-2 and CPT-3 give very similar response patterns although some of the responses during CPT-2 were lost due to a major power failure resulting in data losses in some of the boreholes during the test. The effect of the power failure is described in more detail in /Andersson et al. 2004/.

Table 3-4. Pressure response matrix for CPT-1 through CPT-3.

Sink in structure Borehole	Interval (m)	#19 CPT-1	#19 CPT-2	#19 CPT-3	Structure
KA2511A:T1	239–293	B			#10, 11, 18
KA2511A:T2	171–238	B			#19
KA2511A:T3	139–170	B			#?
KA2511A:T4	111–138	B			#20
KA2511A:T5	103–110	B			#16
KA2511A:T6	96–102	B			#6
KA2511A:T7	65–95	B			#?
KA2511A:T8	6–64	B			#4, 7
KA2563A:S1	242–246	G	G	G	#19
KA2563A:S2	236–241	G	G	G	#19
KA2563A:S3	206–208	B	B	B	#13
KA2563A:S4	187–190	B		B	#20
KA2563A:S5	146–186	B			#6, 7
KI0025F:R1	170.5–193.66	B	M	M	Z
KI0025F:R2	165.5–169.5	**S**	G	G	#19
KI0025F:R3	90.5–164.5	E	B	M	?
KI0025F:R4	87.5–89.5	B	B	B	#20, 22
KI0025F:R5	42.5–86.5	B			#6, 7
KI0025F:R6	5–41.5	B			#5
KI0023B:P1	113.7–200.7	B			#10
KI0023B:P2	111.25–112.7	G	E	E	#19
KI0023B:P3	87.20–110.25	B	G	G	?
KI0023B:P4	84.75–86.20	B	B	B	#13
KI0023B:P5	72.95–83.75	B	B	B	#18
KI0023B:P6	70.95–71.95	B	B	B	#21
KI0023B:P7	43.45–69.95	B	B	B	#6, 20
KI0023B:P8	41.45–42.45	B			#7
KI0023B:P9	4.6–40.45	B			#5
KI0025F02:R1	140.05–204.18	B		B	#10
KI0025F02:R2	135.1–139.05	B	B	B	#BG1
KI0025F02:R3	129.2–134.1	G	**S**	E	#19
KI0025F02:R4	100.25–128.2		Tight		
KI0025F02:R5	93.35–99.25	B	B	B	#13, 21
KI0025F02:R6	78.25–92.35		Tight		
KI0025F02:R7	73.3–77.25	B		B	#20
KI0025F02:R8	64.0–72.3	B	B	B	#22
KI0025F02:R9	56.1–63.0			B	#23
KI0025F02:R10	3.4–55.1	B			#5, 6, 7
KI0025F03:R1	135.03–141.72	B	M	G	#10?
KI0025F03:R2	129.03–134.03	B		B	#BG2
KI0025F03:R3	123.03–128.03	G	G	**S**	#19
KI0025F03:R4	93.53–122.03	B		B	#?
KI0025F03:R5	89.03–92.53	B	B	B	#13
KI0025F03:R6	75.03–88.03	B		B	#21
KI0025F03:R7	66.53–74.03	B		B	#20
KI0025F03:R8	59.53–65.53	B	B	B	#22
KI0025F03:R9	55.03–58.53				#23
KA3510A:R1	125–150.06				#?

Index 1 = sp/Q

Excellent
High
Medium
Low
No response

Index 2 = tr/R2

E = Excellent
G = Good
M = Medium
B = Bad

S = Sink

Sink in structure Borehole	Interval (m)	#19 CPT-1	#19 CPT-2	#19 CPT-3	Structure
KA3510A:R2	110–124	B			#15
KA3510A:R3	75–109	B			#?
KA3510A:R4	51–74	B			#6, 8
KA3510A:R5	4.5–50	B			#3, 4, 5

Test CPT-3 was performed in the same geometry as later used for the tracer tests. The test, which was performed by pumping borehole section KI0025F03:R3 (Structure #19), shows pressure responses (> 1 kPa) in a total of 28 borehole sections within and outside the TRUE Block Scale Site over distances up to 70 m from the sink.

The responses presented in Figure 3-2 are clearly separated in three classes. The first, showing high, and in most cases fast, responses, belong to sections associated with Structure #19 and also sections KI0023B:P3, KI0025F:R1 and KI0025F:R3. The second class includes all the remaining sections in the TRUE Block Scale array including the Structure #20-system and the third class shown in Figure 3-2 are the high but slow responding sections including the background structures BG1 and BG2. The magnitudes of the hydraulic responses in Structure #19 are typically between 12–100 kPa whereas responses in Structure #20-system are less than 3 kPa.

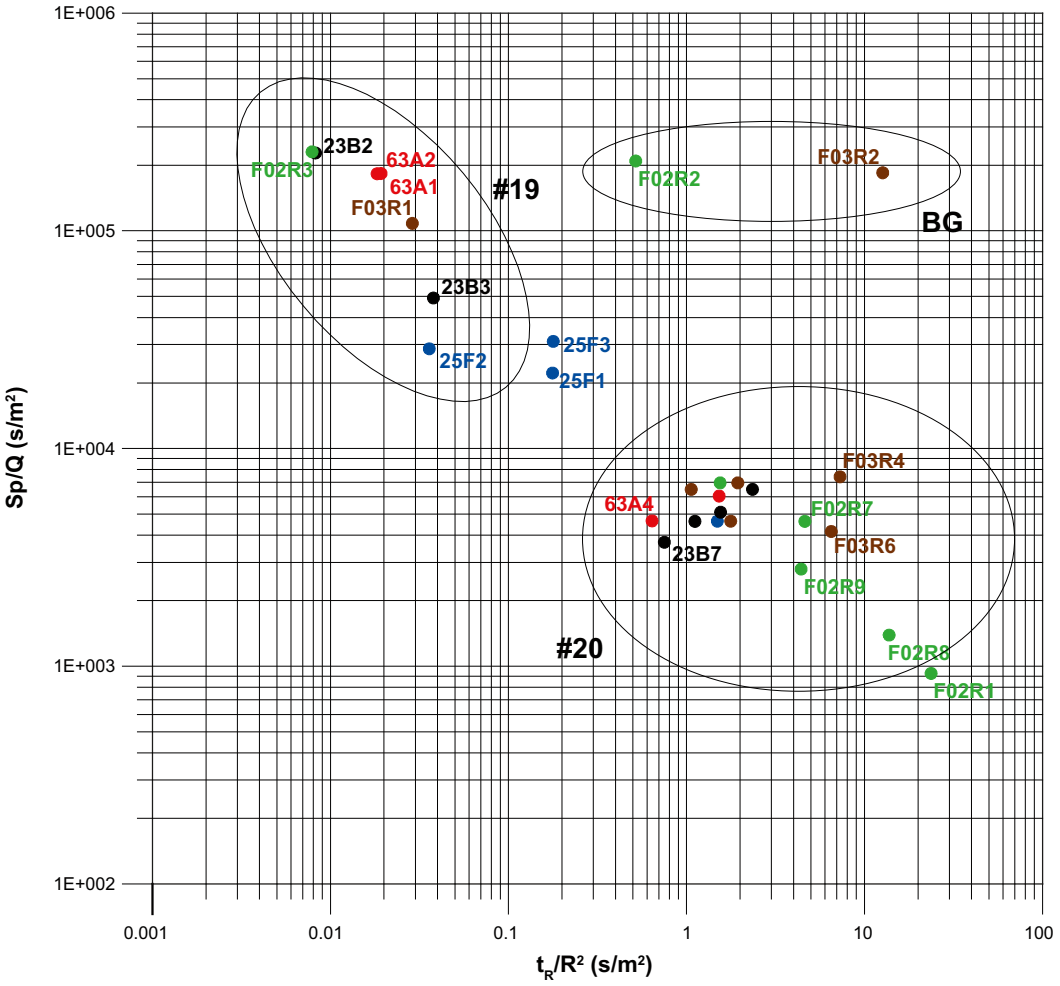

Figure 3-2. *Diagnostic plot of pressure responses during test CPT-3. The encircled areas mark the responses of different structures. Borehole notations are shortened by removing the prefix "KI0025-", KI0023- and"KA25-" from the borehole labels, cf Table 3-2.*

3.3.5 Evaluation of transmissivity

Transmissivity of target structures

The tests CPT-2, CPT-3 and the test of BG1 were evaluated regarding the transmissivity of the sink sections. The test of BG1 was not intended for quantitative evaluation but rather a short-time connectivity test performed during the functionality test of the equipment. cf Section 3.2.4. Only the drawdown periods of the CPT-2 and CPT-3 tests were evaluated since the recovery period was considered to be disturbed and not representative for the formation. Both the drawdown and the recovery periods were evaluated for the test of BG1. The transient analysis of the transmissivity was made using the software AQTESOLV /Ref/. In addition, a steady-state analysis using the Moye's formula (denoted T_M) was performed. The results of the transmissivity evaluations are presented in Table 3-5.

The test CPT-2 as well as test CPT-3 displayed an apparent pseudo-radial flow regime during their respective drawdown periods, see Figure 3-3 and Figure 3-4, respectively. Hence, a model presented by /Dougherty and Babu 1984/ for constant flow rate tests with radial flow, accounting for wellbore storage and skin effects, was used for estimating the transmissivity.

Table 3-5. Results of transmissivity evaluation of tests CPT-2, CPT-3 and short-term test on BG1. Transmissivity regarded as the most representative for the tested section in question are presented in bold.

Test	T_M (m^2/s)	Drawdown period		Recovery period	
		T (m^2/s)	Skin	T (m^2/s)	Skin
CPT-2	$1 \cdot 10^{-7}$	**$5 \cdot 10^{-7}$**	12	–	–
CPT-3	$2 \cdot 10^{-7}$	**$1 \cdot 10^{-6}$**	15	–	–
BG1	**$8 \cdot 10^{-10}$**	–	–	$2 \cdot 10^{-9}$	–2

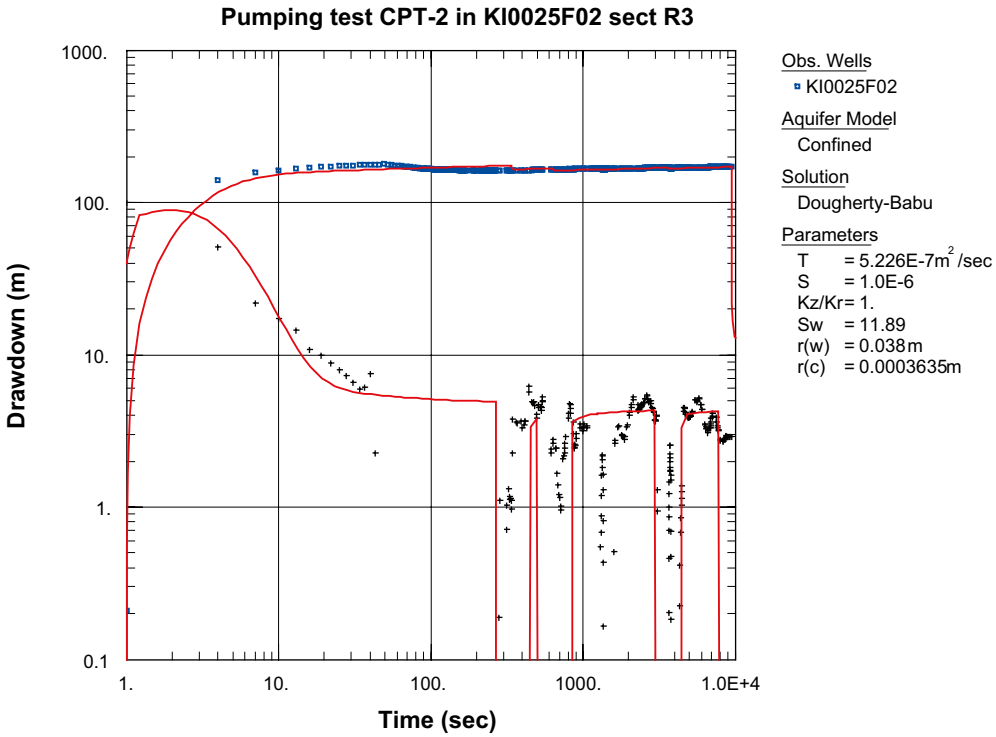

Figure 3-3. *Transient evaluation of the drawdown period of test CPT-2. Log-log plot of drawdown (□) and derivative (+) versus time.*

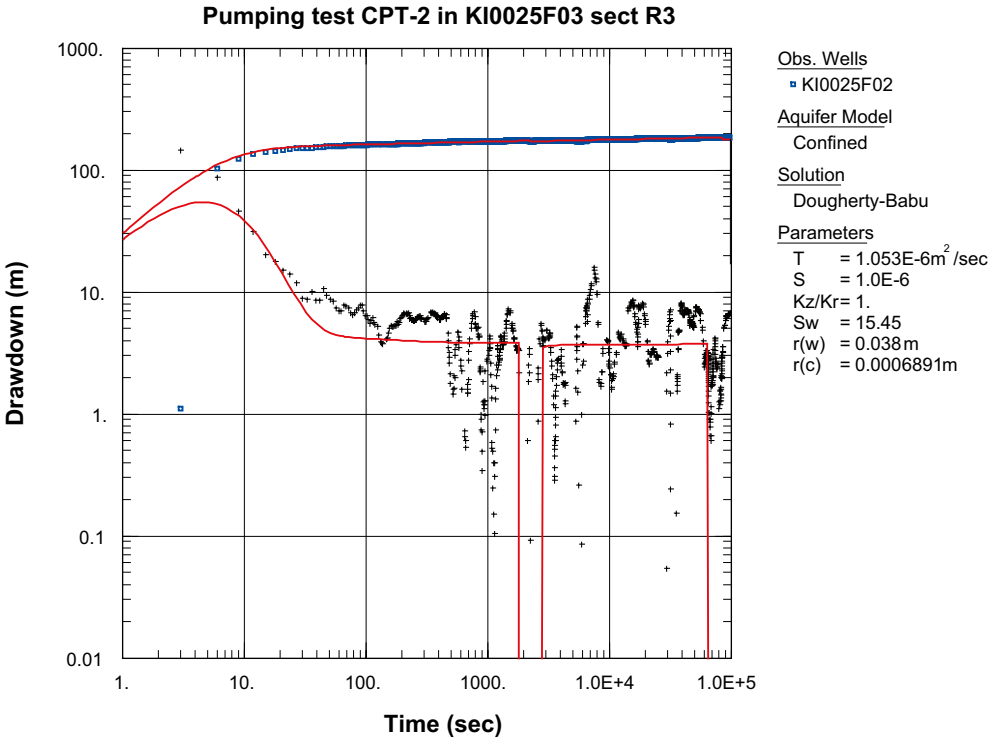

Figure 3-4. *Transient evaluation of the drawdown period of test CPT-3. Log-log plot of drawdown (□) and derivative (+) versus time.*

The evaluation resulted in a rather large skin factor for both tests with an assumed storativity of $1 \cdot 10^{-6}$. T_M does not account for skin effects which may explain why T_M is lower than the transmissivity from the transient evaluation in these cases. For both the CPT-2 and CPT-3 tests, the transient transmissivity was regarded as representative.

During the short-time test of BG1 the pressure response was stabilising rather quickly and only a pseudo-stationary flow was visible during the drawdown period. It was possibly preceded by a short pseudo-spherical flow regime. Consequently, the drawdown period was not evaluated using a transient method. The early phase of the recovery period indicated a pseudo-linear flow regime transitioning into a pseudo-radial flow regime. The latter flow regime was rather short and followed by an increase in the pressure derivative, see Figure 3-5. The period after c 200 s of the recovery may be interpreted as a negative boundary manifested in the formation. However, a negative boundary in this formation is unlikely since the drawdown period clearly was dominated by a pseudo-stationary flow. Instead, it is more likely that this response is due to a yet unexplained disturbance of the formation. A transient evaluation of the recovery period was possible with the Dougherty-Babu model. Still, T_M was considered representative for the tested formation due to the suspected disturbances and because of the rather short period of recovery that was possible for transient evaluation.

Transmissivity – distance analysis

The JNC/Golder team carried out a detailed analysis of transient hydraulic test data to support the evaluation of Structure #19, the focus of planned TRUE Block Scale Continuation BS2B tests with sorbing tracers. This analysis used an approach similar to that developed for Structure #20 during the TRUE Block Scale project /Doe 2002/. The analysis provides insight on conductive geometry for evaluation of tracer tests and structural models.

The hydraulic behaviour of the fracture networks connected to the tested section is expressed through the time variation in the derivative dp/dt. By assuming diffusivity $\eta = 5$ m^2/s, the derivative can be plotted as transmissivity T (m^2/s) vs. distance from the hydraulic signal (metres). This plot is shown in Figure 3-6.

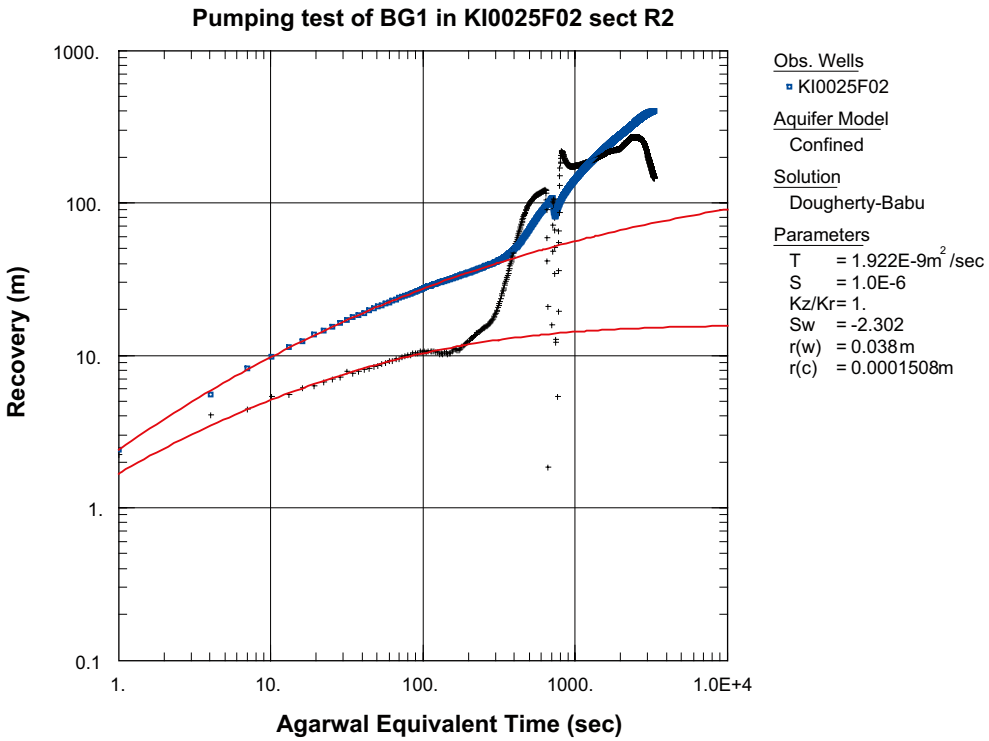

Figure 3-5. *Transient evaluation of the recovery period of the test in BG1. Log-log plot of drawdown (□) and derivative (+) versus time.*

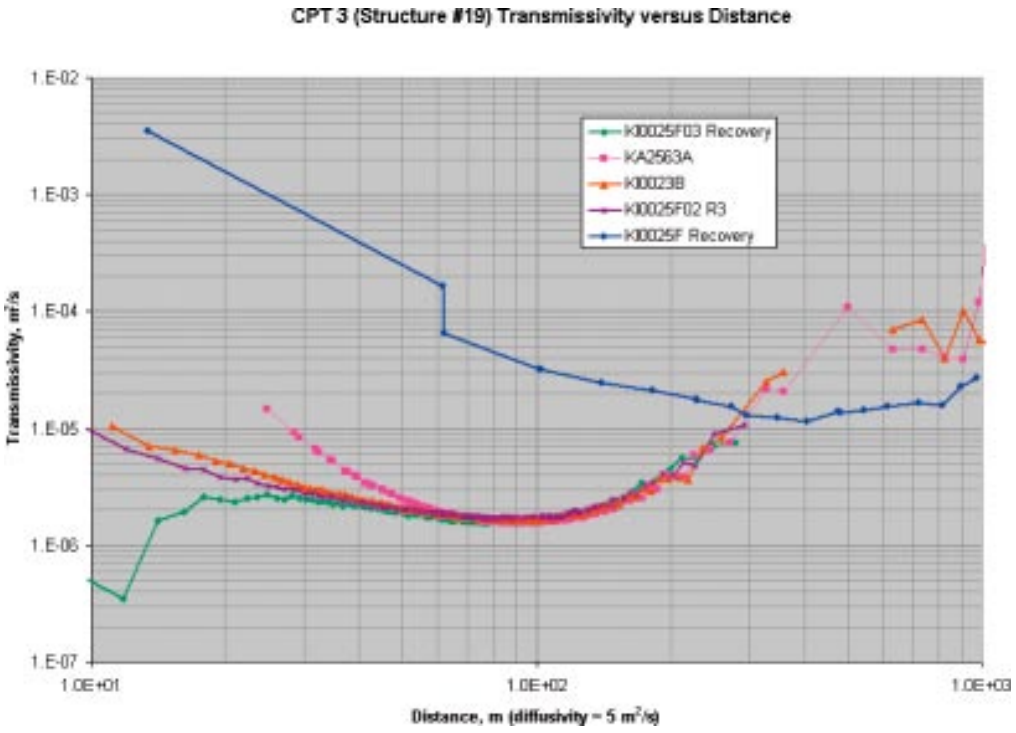

Figure 3-6. *Transmissivity vs. distance plot for CPT-3 pre-test.*

Evaluation of the derivative provides the following observations:

- The local transmissivity around the pumping section in KI0025F03 is low. This may be due to skin effects or local heterogeneity in Structure #19.
- The later time responses are very consistent in monitoring sections in KI0025F02, KI0023B, KA2563A.
- A lower derivative and a higher transmissivity are found near the monitoring section in KI0025F.
- The response shows a partial dimension, which may indicate heterogeneity in the fracture network connected to and comprising Structure #19.

Evaluation of the transmissivity-distance plot (Figure 3-6) provides the following insights:

- The region around the tested section in CPT-3 has similar although heterogeneous properties (local low transmissivity at KI0025F03).
- The KA2563A intercept may be located near a no-flow boundary.
- KI0025F response indicates the presence of a region of higher transmissivity.
- All zones see high transmissivity at late time, possibly the high transmissivity region around KI0025F.
- This high transmissivity region is about 100–200 metres from KI0025F03. This may correspond to the "Z-structure" in the hydrostructural model, or another major bounding feature being constant pressure boundary for Structure #19.

Figure 3-7 shows the comparison between the response seen in CPT-3 against the responses seen in the Structure #20 complex during the TRUE Block Scale project /Andersson et al. 2002a, Doe 2003/. The responses are in a consistent range and magnitude.

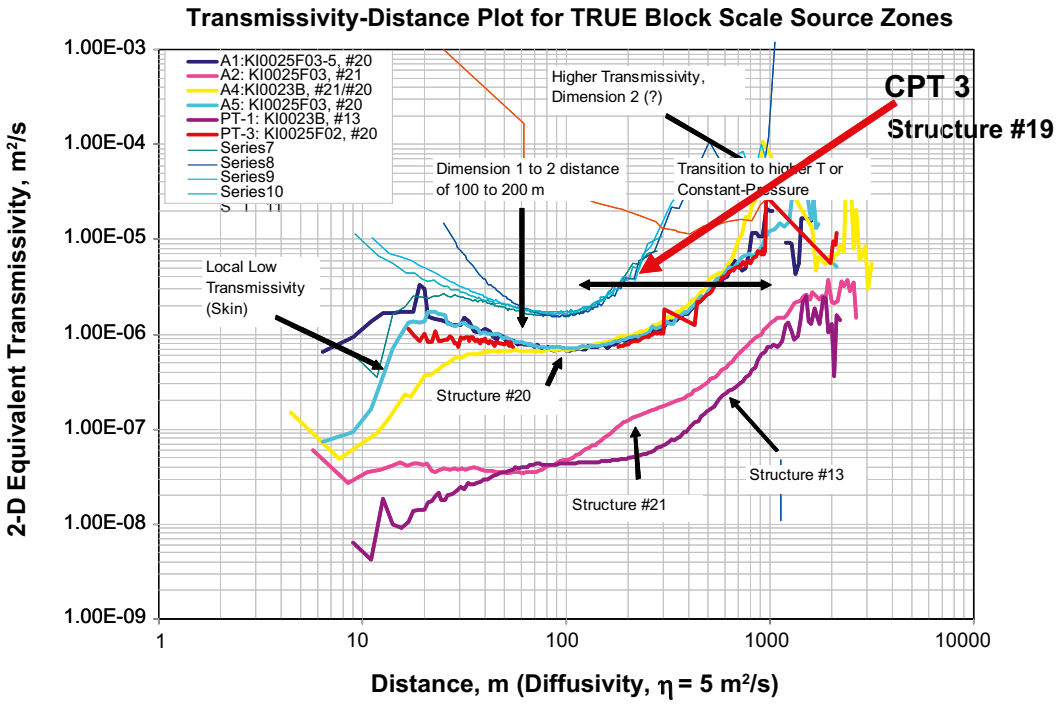

Figure 3-7. *Transmissivity vs. distance plot showing the CPT-3 results draped on the results for the structures (#20, #13, #21) tested during the TRUE Block Scale Project /Doe 2002/.*

The following conclusions were reached regarding the implications of the transmissivity-distance analysis of the CPT-3 test applicable to the Structure #19 region of the hydrostructural model.

- Structure #19 shows consistent behavior with that of Structure #20, although with about a 5 times increase in transmissivity.
- BG1 shows up as a real background structure with lower transmissivity.
- The feature observed to intersect borehole KA2563A is a splay of Structure #19, and not an independent structure.
- The structure intersecting section KI0025F:R1, cf Table 3-4, is probably the large Z structure. This intersection indicates a low transmissivity structure connected to #19 but also to a major structure coupled to a lower hydraulic head.
- There is a potential background fracture in KI0025F:R3. This is important since one of the goals of the project is to obtain test results for a background fracture network.
- The higher flow dimension observed at greater distance in Structure #19 is a possible effect of intersecting fractures.
- The partial dimension observed in CPT-3 indicates a possible heterogeneous network in Structure #19.

Discussion

The results of the evaluation of transmissivity of Structure #19 indicates a transmissivity in the order of $5\ 10^{-7}$ to $1.1\ 10^{-6}$ m^2/s. It should be emphasised that the partial dimension indicated by the transmissivity distance analysis suggests heterogeneity within Structure #19. Hence, the transmissivity values indicated should by no means be regarded as reflecting a structure with a uniform homogeneous transmissivity.

The transmissivity of the background fracture BG1 is found to slightly less than $1\ 10^{-9}$ m^2/s, i.e. close to three orders of magnitude lower than the transmissivity inferred for Structure #19.

3.3.6 Tracer dilution tests

Test CPT-3 included measurements of flow rates using the tracer dilution method in eight selected observation sections. The measurements were performed both under natural gradient and during pumping of section KI0025F03:R3 (Structure #19) in order to study the influence of the pumping, see examples in Figure 3-8. The results presented in Table 3-6 show a distinct increase in all of the tested sections except in KI0025F02:R5 (Structure #13 and #21) where the flow is decreased and in KI0025F02:R2 (BG1) where the flow is constant. The latter flow rate is surprisingly high considering the low transmissivity of the structure. Expected flow rates should be around 10 times lower as in KI0025F03:R2. One possible explanation for this is that the pressure in the borehole interval is lowered as a consequence of a partly clogged filter located at the inlet of the circulation loop close to the upper packer. This lowering of the pressure can be seen in the pressure measurements and amounts to about 25 kPa, thus creating a forced gradient around the borehole resulting in increased flow rates.

3.3.7 Supplementary tracer dilution tests in section KI0025F02:R2 (BG1)

The tracer dilution tests performed (CPT-1 through CPT-3) showed surprisingly high flow rates (35–51 ml/h) in background fracture BG1 (section KI0025F02:R2) and very weak, or even no, responses to the pumping in Structure #19 (Table 3-6). As the transmissivity of BG1 is at least two orders of magnitude lower than Structure #19, one would expect a similar relationship of natural flow through the fractures, unless the hydraulic gradient is significantly higher in BG1.

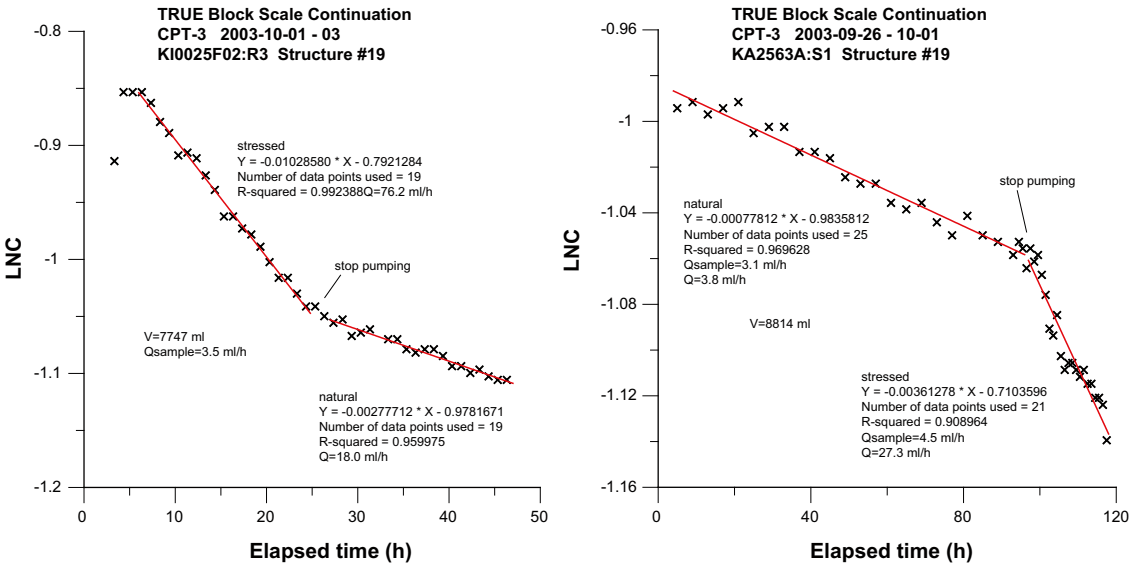

Figure 3-8. *Examples of tracer dilution graphs (Logarithm of concentration versus time) for sections KI0025F02:R3 (Structure #19) and KA2563A:S1 (Structure #19), test CPT-3. Steeper dip of the straight-line fit implies a higher flow rate.*

Table 3-6. Results of tracer dilution tests during CPT-3, using KI0025F03:R3 (Structure #19) as sink.

Test section	Structure #	Section volume (ml)	$Q_{natural}$ (ml/h)	$Q_{stressed}$ (ml/h)	ΔQ (ml/h)
KA2563A:S1	19	8,814	4	27	+23
KI0023B:P2	19	3,621	18	31	+13
KI0025F:R2	19	7,210	22	85	+63
KI0025F02:R2	25	7,141	42	42	± 0
KI0025F02:R3	19	7,747	18	76	+58
KI0025F02:R5	13, 21	7,856	30	18	–12
KI0025F03:R2	25	6,519	6	9	+3
KI0025F03:R3	19	6,343		SINK	
KI0025F03:R5	**13**	**4,912**	**4**	**6**	+2

As the natural flow through the fracture is an important parameter for the interpretation of the tests, a supplementary investigation with the aim to verify and try to explain the high natural flow rate in BG1 was initiated.

The field test was performed in four steps; with and without pumping in KI0025F03:R3 (#19) and with different flow directions during circulation of the tracer solution in the borehole volume. Flow rate from tracer dilution and pressure levels in surrounding borehole sections were measured and any differences would give an insight if leakage or other effects caused by the instrumentation could explain the high natural flow rates. Comparisons with the pressure situation during previous measurements were also made.

The results of the tracer dilution tests (Figure 3-9 and Table 3-7) and the pressure measurements (Figure 3-10) do not give an entirely conclusive picture. It is clear that there is a significant difference in flow rate between the tests but the difference does no seem to originate from which direction of circulation that is applied. Also, pressures in the measured section and in other sections of the borehole are not influenced at all by the circulation, or by changing the direction of circulation.

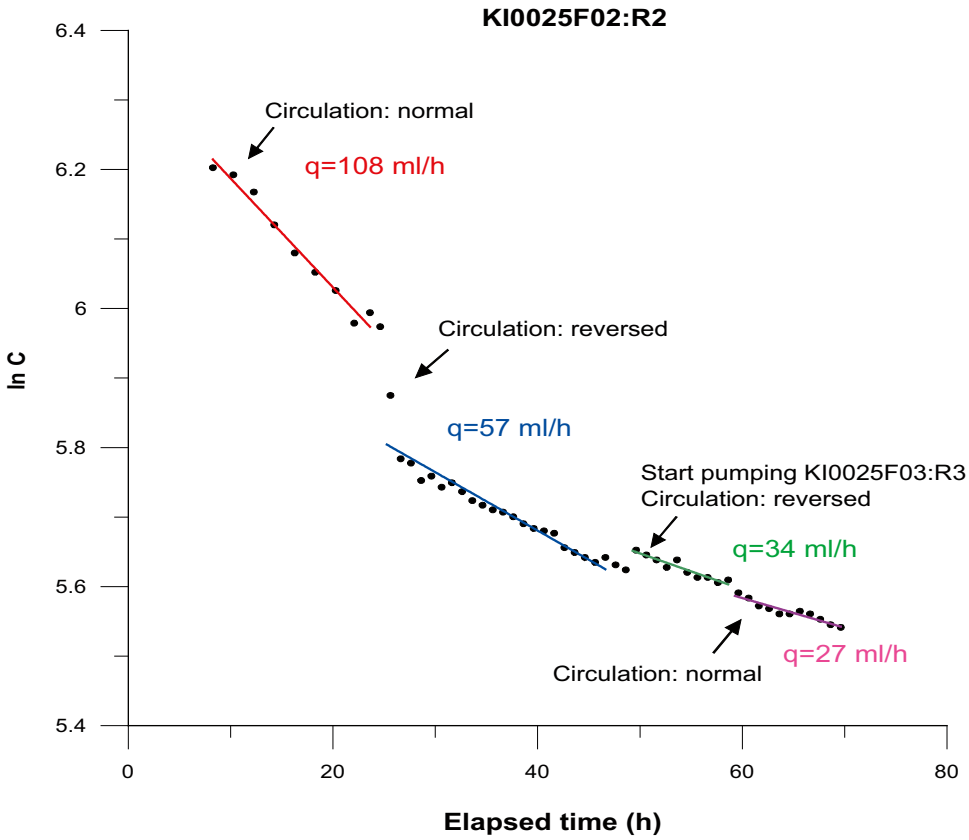

Figure 3-9. *Tracer dilution test in section KI0025F02:R2.*

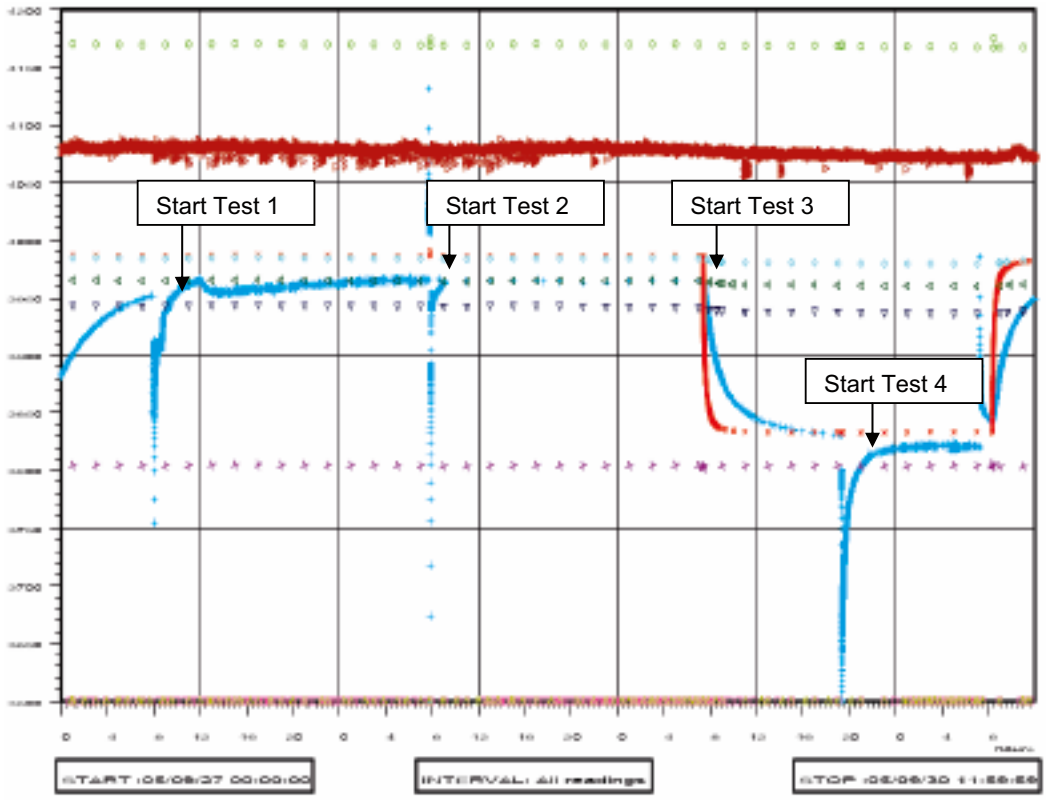

Figure 3-10. *Pressure measurements in borehole KI0025F02 during the tracer dilution tests. The target section R2 in blue and the pumped Structure #19 in red.*

Table 3-7. Summary of tracer dilution tests, pressures and pressure differences during tests performed in KI0025F02:R2 (BG1).

Test #	Experimental conditions	Measured flow rate (ml/h)	Pressure in BG1 (kPa)	Pressure difference #19-BG1
1	Circulation: normal direction No pumping in KI0025F03:R3	108	3,960–3,970 (rising)	33–23 kPa (decreasing)
2	Circulation: reversed direction No pumping in KI0025F03:R3	57	3,970 (stable)	23 kPa (stable)
3	Circulation: reversed direction Pumping in KI0025F03:R3	34	3,830 (transient, sinking)	23–0 kPa (transient,decreasing)
4	Circulation: normal direction Pumping in KI0025F03:R3	27	3,820 (rising)	20–12 kPa (decreasing)

The high flow rate measured in the first test is possibly influenced by transient pressure conditions caused by the installation of the equipment. This is also indicated in the pressure measurements (Figure 3-10) where pressure is still rising after starting the first test. Similar conditions also prevailed during tests CPT-1 through CPT-3, performed in September 2003 where the borehole had been re-instrumented 14 days before the start of CPT-1 and a pressure difference of about 25–30 kPa was measured between Structure #19 and BG1. This pressure difference prevailed throughout the entire test period of CPT-1 through CPT-3. Directly after that, pumping started for CPT-4 and the sorbing tracer tests, continuing until May 2005. Since then, no pressure disturbances have occurred in the borehole and the pressure difference is only about 2 kPa. This suggests that the pressure difference between Structure #19 and BG1 most probably was significantly enhanced during all tracer dilution tests performed creating high flow rates during the dilution tests.

A study of the pressure differences between Structure #19 and BG1 in KI0025F02 (Table 3-7) shows that there is a clear decreasing trend from the first test, starting at 33 kPa pressure difference, towards 12 kPa difference at the end of the last test. This trend follows quite well the decrease in flow rate.

The main conclusions from the tests are:

- There are no indications of leakage in the equipment that could explain the enhanced flow rates.
- The flow rates are in the same order as during previous tests (CPT-1 through CPT-3).
- The comparatively high flow rates measured in BG1 during CPT-1 through CPT-3 and in the current tests are probably due to high hydraulic gradients caused by transient pressure conditions in the borehole.
- Assuming that the head difference measured under undisturbed conditions (2 kPa) prevails, flow rates would possibly be significantly reduced.

3.3.8 Results and interpretation of tracer tests CPT-4a through CPT-4c

Test CPT-4 was divided into three separate batches of tracer injections including three injections in each batch (CPT-4a–c). The last batch of injections, CPT-4c, included re-runs in three of the earlier tested flow paths but with partly changed flow geometry. The tests were performed as cross-hole tracer tests using KI0025F03:R3 (Structure #19) as sink, cf Figure 3-11. The selection of sink was based on the results of CPT-1 through CPT-3 where the selected section gave the best hydraulic and flow responses and also the best possibilities to use different geometries.

The tests were performed in a radially converging flow field with a withdrawal rate of Q = 2.8 l/min at the start of CPT-4a in September 2004 and slowly decreasing to Q = 2.6 l/min until the stop of CPT-4c in March 2004. Some of the injections were also accompanied by net fluid injections into the injection section in order to avoid excessive tailing of the injection function.

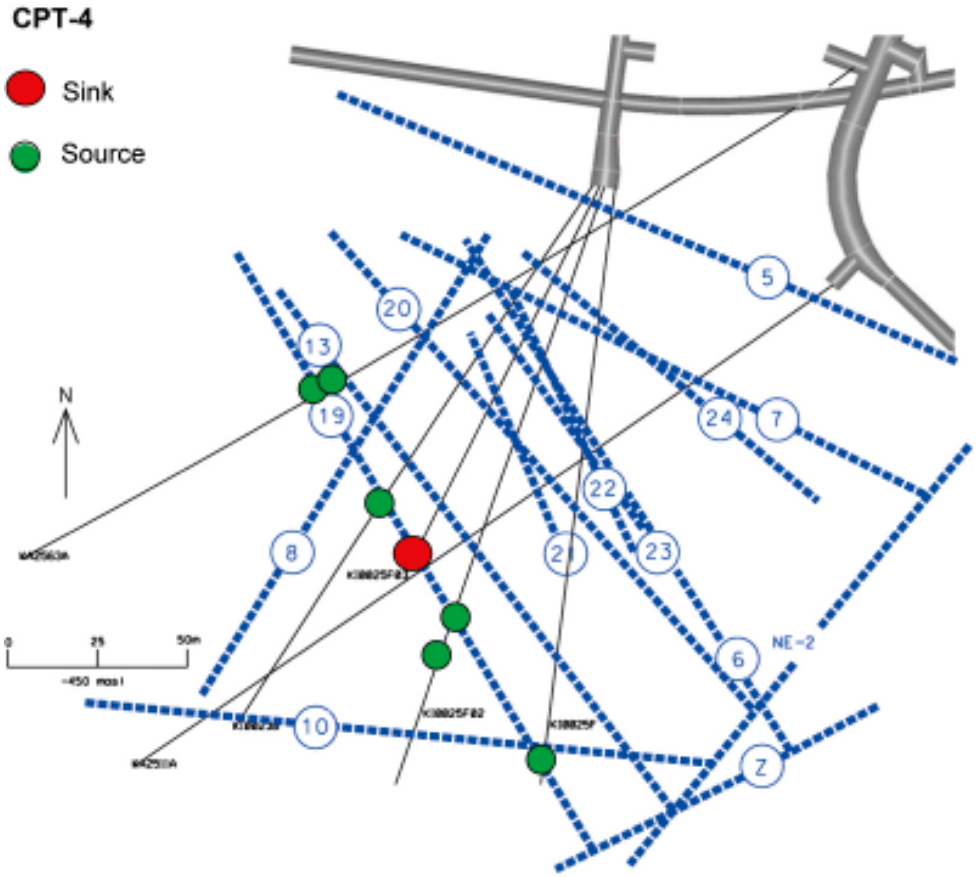

Figure 3-11. *Horizontal section at Z = –450 m.a.s.l. showing the structural model based on identified conductive geological structures in the TRUE Block Scale rock volume and location of pumping (sink) and injection (source) sections employed in pre-test CPT-4.*

The two first batches of tracer injections, CPT-4a and CPT-4b were focused on finding suitable test geometries including injections in Structure #19 and in BG1 whereas the third batch, CPT-4c, focused on using the optimal injection rate and assessing that the tracer recovery exceeded 80%. This mass recovery was necessary to achieve for radiation safety aspects of the tracer tests with radioactive sorbing tracers. A summary of the tracer injections are given in Table 3-6. Details of tracer injections CPT-4a and 4b are given in /Andersson et al. 2004b/.

Test CPT-4c was performed as a decaying pulse with an accompanying injection of water in all three selected injection sections. The main reason for adding extra water to the injection was to shorten the tracer residence time in the injection section.

The injection concentrations of CPT-4c presented in Figure 3-12 and Table 3-8 are the actually measured ones. Based on those, a flow rate was calculated from the dilution of tracer versus time. Notable is that the injection concentration in KI0025F02:R2 (BG1) varies significantly at earlier times due to the relatively poor mixing in the section caused by the clogged filter. This is also reflected by the flow rate calculated from the dilution of tracer versus time where the injection of water was set to (and calibrated to) 2 ml/min while the calculated (mass flux) is only about 0.4 ml/min. For the other two injection sections the calculated flow rates compare better with the actually added (about 4 ml/min compared to 5 ml/min added). This difference has earlier been observed in previous experiments using this set-up and may also be explained by incomplete mixing so that a portion of the unlabelled water added is injected without complete mixing with the rest of the volume in the injection section.

Tracer breakthrough was monitored in KI0025F03:R3 from all three injection points in test CPT-4c, cf Figure 3-13. However, tracer mass recovery was found to exceed 80% only in

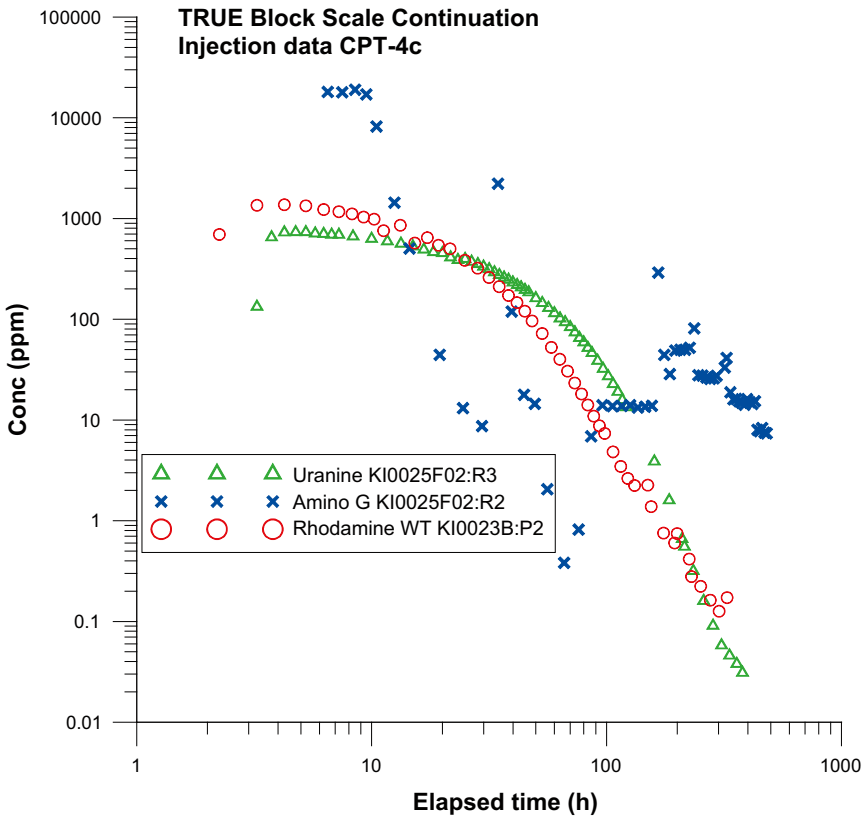

Figure 3-12. *CPT-4c-tracer injection curves (log-log scale).*

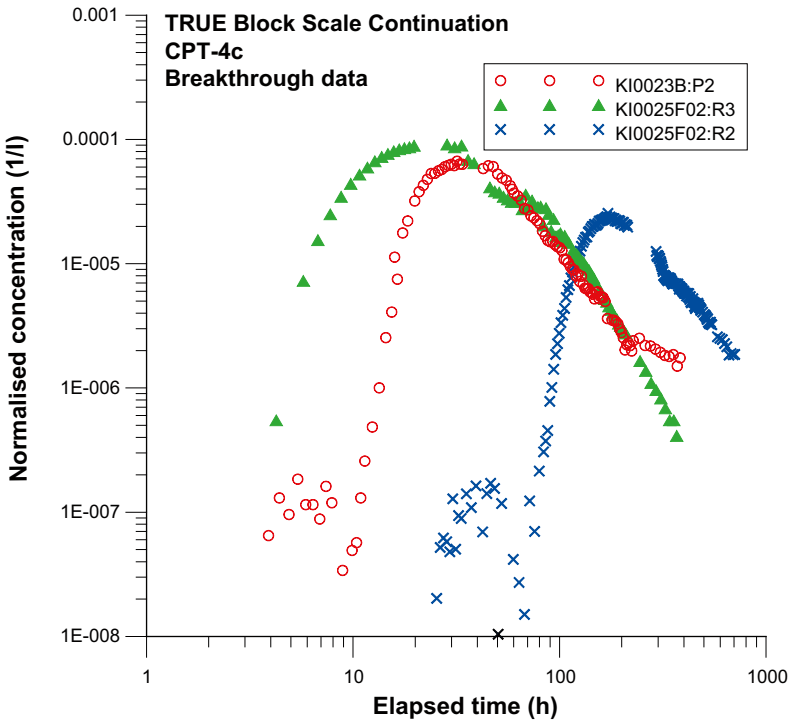

Figure 3-13. *Tracer breakthrough curves for test CPT-4c, injection in KI0023B:P2 (red), KI0025F02:R3 (green) and KI0025F02:R2 (blue), logarithmic time scale. Concentrations are normalised to injected mass.*

Table 3-8. Tracer injection data for tests CPT-4a through CPT-4c (measured values).

Test	Inj. Section	Struct.	Tracer	Max inj. conc. (mg/l)	Inj. rate (ml/h)	Inj. mass (mg)	Section volume (ml)
CPT-4a	KI0025F:R2	#19	Rhodamine WT	1,367	50	12,650	7,210
	KI0025F02:R3	#19	Amino-G Acid	1,647	33	12,400	7,747
	KI0023B:P2	#19	Uranine	414	15	1,300	3,621
CPT-4b	KA2563A:S1	#19	Uranine	888	19	7,830	8,814
	KA2563A:S2	#19	Rhodamine WT	20,000	600	10,900	12,588
	KI0025F02:R2	BG1	Amino-G Acid	1,739	72	15,400	7,141
CPT-4c	KI0025F02:R3	#19	Uranine	733	262	7,290	7,747
	KI0023B:P2	#19	Rhodamine WT	1,370	213	6,300	3,621
	KI0025F02:R2	BG1	Amino-G Acid	18,000	25	17,300	7,141

the injections from KI0025F02:R2 (BG1) and KI0025F02:R3 (#19). Based on this result it was concluded that tracer tests with sorbing tracer was feasible to perform in one fast and less complicated flow path within Structure #19, KI0025F02:R3 to KI0025F03:R3 (path length 19.5 m) and in one slower and more complicated flow path with injection in BG1, KI0025F02:R2 to KI0025F02:R3 (geometrical path length 22 m).

3.4 In situ tests with sorbing tracers

3.4.1 Background and selection of tracers

Based on the results of the pre-tests CPT-1 through CPT-4 a selection of test geometry was done as described in Section 3.3. The outlined test configuration and test equipment was the same as used in the pre-tests with the additional equipment for detection of radioactive tracers. Both injection and sampling systems were equipped with online detectors of gamma radiation. Details of the equipment are given in /Andersson et al. 2004b/.

For the study of the impact of sorption interaction on transport, comparison of the breakthrough of simultaneously injected non-sorbing and sorbing tracers are essential. Furthermore, experiences of earlier sorbing tracer experiments in the TRUE programme have shown that the use of a cocktail of tracers with different degree of sorption strength has been a quite successful concept.

Regarding the sorbing tracers, the same prerequisites as in the earlier TRUE experiments were considered, i.e.:

- Preferentially, elements from the alkali and alkaline earth metal were selected. These elements are considered to interact with the non-mobile phases by a cation exchange mechanism, which is expected to be fast and reversible.
- To avoid non-linear sorption caused by varying chemical concentrations, radioactive tracers were used. Due to the high specific activity of radioactive tracer, these tracers could provide a dynamic range (i.e. injected activity divided by the detection limit activity) only causing a negligible increase of the chemical concentration.
- Radionuclides with its decay associated with γ-radiation were preferred since γ-spectrometry is the most convenient method for measuring and quantify the concentration of radioactive tracers.

Since radioactive tracers were demanded from the reasons mentioned above, it was due to measurement reasons also decided to also use radioactive non-sorbing tracers.

Two different cocktails with radioactive tracers were to be used in the TRUE Block Scale Continuation Tests with sorbing tracers; one for the faster of the two flow paths selected (KI0025F02:R3 → KI0025F03:R3) and one for the slower flow path (KI0025F02:R2 → KI0025F03:R3), cf Table 3-9.

Non-sorbing tracers

The radioactive tracers with its decay associated with γ-radiation that has been used in the TRUE-program so far are $^{82}Br^-$ ($t_{½}$ = 1.47d), $^{131}I^-$ ($t_{½}$ = 8.02d) and $^{186}ReO_4^-$ ($t_{½}$ = 3.72d). All of these tracers are rather short-lived and are therefore, in most tracers tests, not well-suited for studies of the characteristics of the late time arrival ("tailing"). Tritium-labelled water, HTO ($t_{½}$ = 12.3y), is more long-lived non-sorbing tracers that has been frequently used in the TRUE experiments. However, it has the disadvantage of having a decay that shows no detectable γ-radiation which makes the measurement procedures more complicated, e.g. it can not be measured in the on-line measurements.

As been investigated by /Byegård et al. 1999/, the use of metal ion complex (e.g. EDTA and DTPA complexes) offers a great potential and flexibility in half-lives in the choice of radioactive non-sorbing tracers. DTPA complexes of lanthanide ions have with good results been used as tracers in the TRUE program (e.g. /Andersson 1996, Holmqvist et al. 2002, Andersson et al. 2000/, however in their non-radioactive form which demands the use of rather high start concentration (typically in the range of 10,000 ppm). Such high concentrations of complexing agents are obviously not a good choice of non-sorbing tracers in experiments with sorbing tracers; non-metal attached complexing agents may react with the sorbing cations and increase the mobility of these cations. However, the use of complexed radioisotopes allows a significant lower concentration of complexing agent which is not likely to cause this problem.

Limitation of the long term stability of the metal complexes could also be a problem for the use of them as tracers. Based on experiences from laboratory and field investigations /Byegård et al. 1999/, elements in the middle of the lanthanide series complexed with DTPA are indicated to be the best choice of tracers among metal complexes. However, since no experiences exist of low concentration use of these tracers, it can not be recommended to use these tracers as the only non-sorbing from one flow path.

Based on the considerations described above, the selection of non-sorbing tracers in this experiment was:

- $^{131}I^-$ together with ^{160}Tb-DTPA as tracers for the fast flow path i.e. KI0025F02:R3 → KI0025F03:R3.
- HTO together with ^{155}Eu-DTPA as tracers for the slow flow path i.e. KI0025F02:R2 → KI0025F03:R3.

Sorbing tracers

Based on laboratory experiments, e.g. /Byegård et al. 1998/, and earlier experiences from in situ experiments with sorbing tracers in high saline groundwater, e.g. /Winberg et al. 2000, Andersson et al. 2002b/ the cation exchange sorbing tracers can be empirically be divided into different groups regarding their general retention properties:

- Slightly sorbing tracers. Only a very minor retardation compared to the non-sorbing tracers. Examples: Na^+, Ca^{2+} and Sr^{2+}.
- Moderately sorbing tracers. Examples: Rb^+ and Ba^{2+}.
- Strongly sorbing tracers. Example: Cs^+.

Furthermore, the results from the TRUE Block Scale C4 injection /Andersson et al. 2004a/ showed high recovery of the tracer $^{54}Mn^{2+}$. This tracer is far much more influenced by hydrolysis than the other tracers mentioned, and is therefore suspected to be a subject for

surface complexation. The results of the use this tracer showed that the sorption strength of this tracer should be somewhere between Rb^+ and Cs^+.

A complementary laboratory program has been conducted, cf Section 3.5, where the sorption of these tracers on TRUE Block Scale specific material and non-specific fault gouge material has been studied. The tracers above were included in this study, i.e. cation exchange sorbing tracers and also Mn^{2+}.

To fulfil the demand of having tracers of different sorption strength, it was considered as advantageous if one sorbing tracer from each group could be used for each flow path. Based on available isotopes, the following selection was done (see also Table 3-9):

- Slightly sorbing tracers: $^{85}Sr^{2+}$ for the fast flow path (KI0025F02:R3 → KI0025F03:R3) and $^{22}Na^+$ for the slow flow path (KI0025F02:R2 → KI0025F03:R3).
- Moderately sorbing tracers: $^{86}Rb^+$ for the fast flow path and $^{133}Ba^{2+}$ for the slow flow path.
- Strongly sorbing tracers: $^{137}Cs^+$ for the fast flow path and $^{54}Mn^{2+}$ for the slow flow path.

The isotope selection was made in order to assure a sufficient long half-life to allow studies of the late time arrival (tailing) of the tracers. Unfortunately, at the time for the experiment the isotope $^{83}Rb^+$ ($t_{½}$ = 86.2 d) which was used during the earlier TRUE Block Scale Experiment /Andersson et al. 2002b/ was not available from the only known supplier. Therefore, the more short-lived $^{86}Rb^+$ ($t_{½}$ = 18.7 d) had to be used.

All radionuclides, except HTO, were analysed by γ-spectrometry. HTO was analysed by liquid scintillation.

3.4.2 Tracer injections

The injections were performed as decaying pulses with an accompanying injection of non-labelled water in both injection sections. The main reason for adding extra water to the injection was to shorten the tracer residence time in the injection section which is important from a radiation safety aspect when handling radioactive tracers. Long tailing in the injection may also induce tailing in the breakthrough curves which can interfere in the evaluation of the processes.

The measured tracer injection concentrations are presented in Table 3-10, Figure 3-14 and Figure 3-15 for the fast and slow flow paths, respectively. The figures show the data from discrete samples taken in the injection loop. On-line measurements generally gave better data at early times when the sampling values are lacking due to the delay in the sampling system (valves and tubing). The delay, estimated to about 4 hours, represents the time it takes to exchange the tubing volume from the circulation loop to the sampler due to the low sampling flow (2 ml/h). A higher sampling flow would decrease the delay but also decrease the injection rate. However, at larger times the delay is unimportant and sampled values tend to be more reliable as there is a tendency of sorption in the tubing at the on-line detector possibly caused by precipitations. A comparison displaying these effects is shown in Figure 3-16 for $^{85}Sr^{2+}$.

Table 3-9. Tracers used during the TRUE Block Scale Continuation Tests with sorbing tracers (BS2B).

Tracer class	Fast flow path (F02:R3 → F03:R3)	Slow flow path (F02:R2 → F03:R3)
Non-sorbing	$^{131}I^-$	HTO
Non-sorbing metal complex	^{160}Tb-DTPA	^{155}Eu-DTPA
Weakly sorbing	$^{85}Sr^{2+}$	$^{22}Na^+$
Moderately sorbing	$^{86}Rb^+$	$^{133}Ba^{2+}$
Strongly sorbing	$^{137}Cs^+$	$^{54}Mn^{2+}$

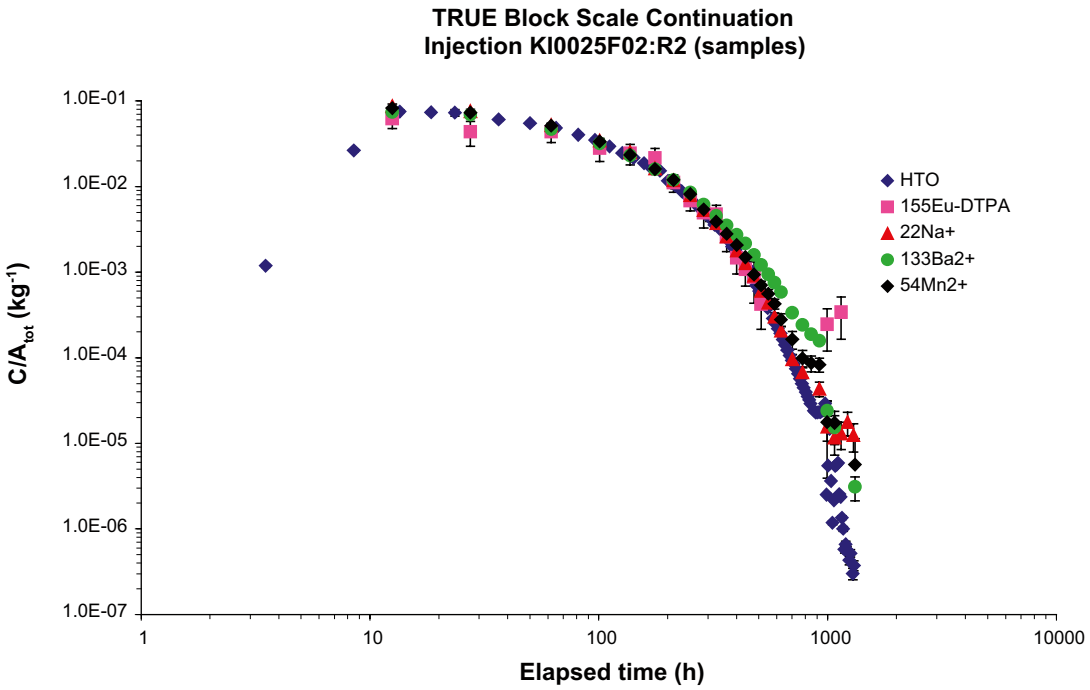

Figure 3-14. *Tracer injection curves (log-log scale) for the injection in KI0025F02:R2 (slow flow path, sample measurements).*

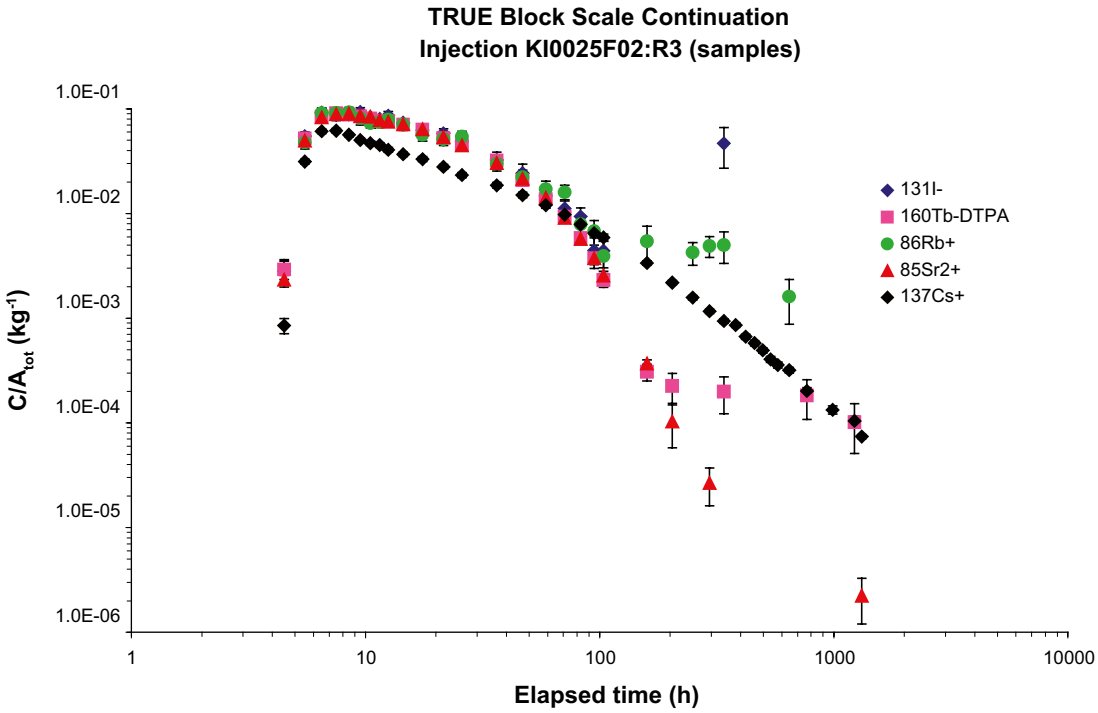

Figure 3-15. *Tracer injection curves (log-log scale) for the injection in KI0025F02:R3 (fast flow path, sample measurements).*

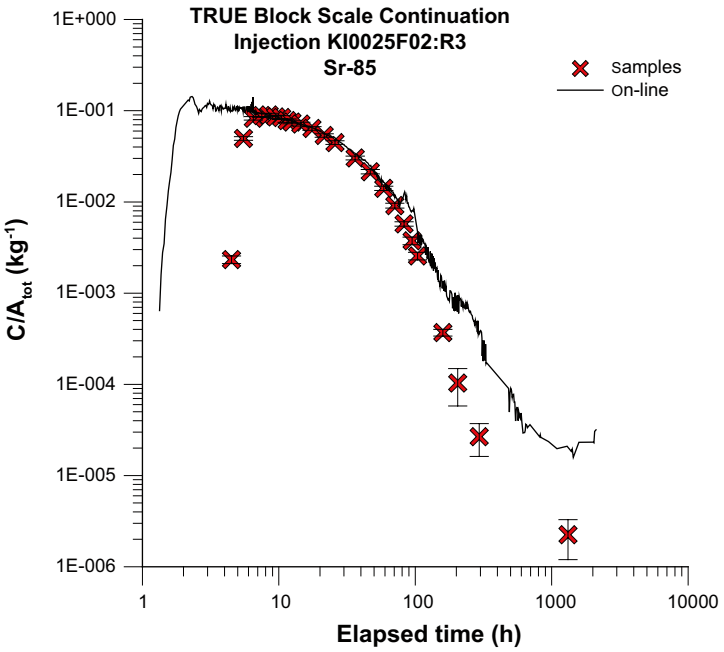

Figure 3-16. *Comparison between on-line measurements and samples for $^{85}Sr^{2+}$ used in the fast flow path (injection in KI0025F02:R3). Error bars represent one standard deviation.*

Table 3-10. Tracer injection data for TRUE Block Scale Continuation, tests with sorbing tracers. Borehole section notation is simplified by removal of the prefix "KI00-" from the borehole labels.

Borehole section	Section volume (ml)*	Inj. rate flow meter (ml/min)	Inj. rate dil.curve (ml/min)	Tracer	$t_{1/2}$	Total inj. amount (MBq)
F02:R3	7,747	5	4.2	$^{131}I^-$	8 d	4.0
(fast path)				^{160}Tb-DTPA	72.3 d	16
				$^{85}Sr^{2+}$	64.9 d	22
				$^{86}Rb^+$	18.7 d	15
				$^{137}Cs^+$	30.2 y	22
F02:R2	7,141	2	1.2	HTO	12.3 y	720
(slow path)				^{155}Eu-DTPA	4.8 y	5.2
				$^{22}Na^+$	2.6 y	15
				$^{133}Ba^{2+}$	10.5 y	18
				$^{54}Mn^{2+}$	312 d	67

Based on the concentrations of the non-sorbing radioactive tracers injected, HTO in KI0025F02:R2 and $^{131}I^-$ in KI0025F02:R3, flow rates were calculated from the dilution of tracer versus time (Table 3-10). The calculated values (1.2 and 4.2 ml/min) are both smaller than the actually added flow (2.0 and 5.0 ml/min). This difference has earlier been observed in previous experiments using this set-up and can be explained by poor mixing such that a portion of the unlabelled water added is injected without complete mixing with the rest of the volume in the injection section. This is particularly evident in KI0025F02:R2 where problems with a clogged filter in the borehole equipment only allowed a mixing rate of 2 litres/hour compared to 10 litres/hour in KI0025F02:R3.

Figure 3-14 shows good agreement between the he measured concentrations (activities) of discrete samples taken from the tracer injection loop for most of the tracers. A small tendency of higher relative concentrations for the sorbing tracers can be noted, especially at longer times. This effect is much more pronounced in the injection interval for the fast flow path (Figure 3-15) where sorption effects are clearly visible for both $^{86}Rb^{+}$ and $^{137}Cs^{+}$.

3.4.3 Tracer breakthrough

Tracer breakthrough in the sink section KI0025F03:R3 (Structure #19) was detected for all tracers injected in the two injection sections, KI0025F02:R3 (Structure #19) and KI0025F02:R2 (BG1), cf Figure 3-17 and Figure 3-18, respectively. The tracer mass recovery was high for the non-sorbing and weakly sorbing tracers, cf Table 3-11 and Table 3-12. Peak arrival times for the non-sorbing tracers in the two flow paths were in the order of 30 and 300 hours, respectively.

Tracer mass recovery was calculated in the same way for all tracers detected in the pumping section. Before the injection a sample of the stock solution was taken and the tracer solution vessel was weighed. After the injection the vessel was weighed again and the tracer concentrations of the stock solution sample were measured to determine the injected mass of the different tracers, cf Table 3-10. The tracer mass recovered in the pumping borehole section was determined by integration of the breakthrough curves for mass flux (Bq/h) versus time (h).

The mass recovery was high for the non-sorbing tracers in both flow paths and similar to the ones obtained in the pre-tests /Andersson et al. 2004b/. Pre-test CPT-4c gave a mass recovery of 84% for the fast flow path and 80% for the slow flow path. This is somewhat lower than the ones reported for the DTPA-complexes in Table 3-11 and Table 3-12 but the sampling time was also about 10 times longer for the latter. The mass recovery for HTO was much lower than expected for unknown reasons.

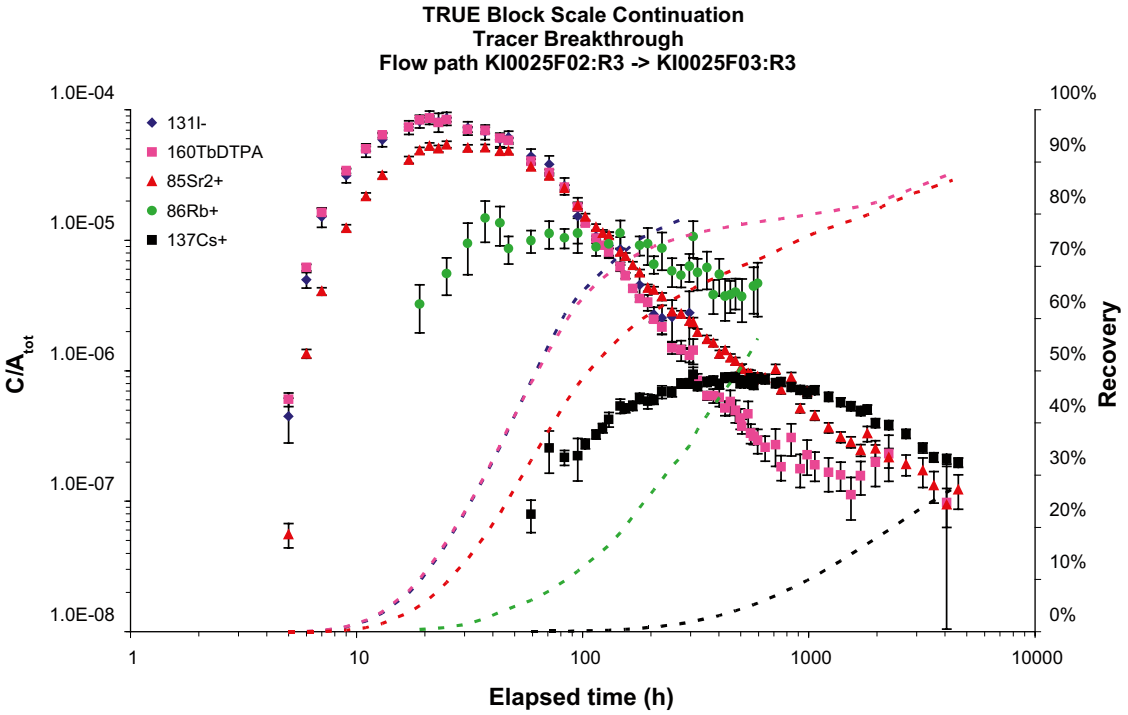

Figure 3-17. *Tracer breakthrough curves and mass recovery for TRUE Block Scale Continuation BS2B tests with sorbing tracers, injection in KI0025F02:R3 (log-log scale). Concentrations are normalised to injected mass. Error bars represent one standard deviation.*

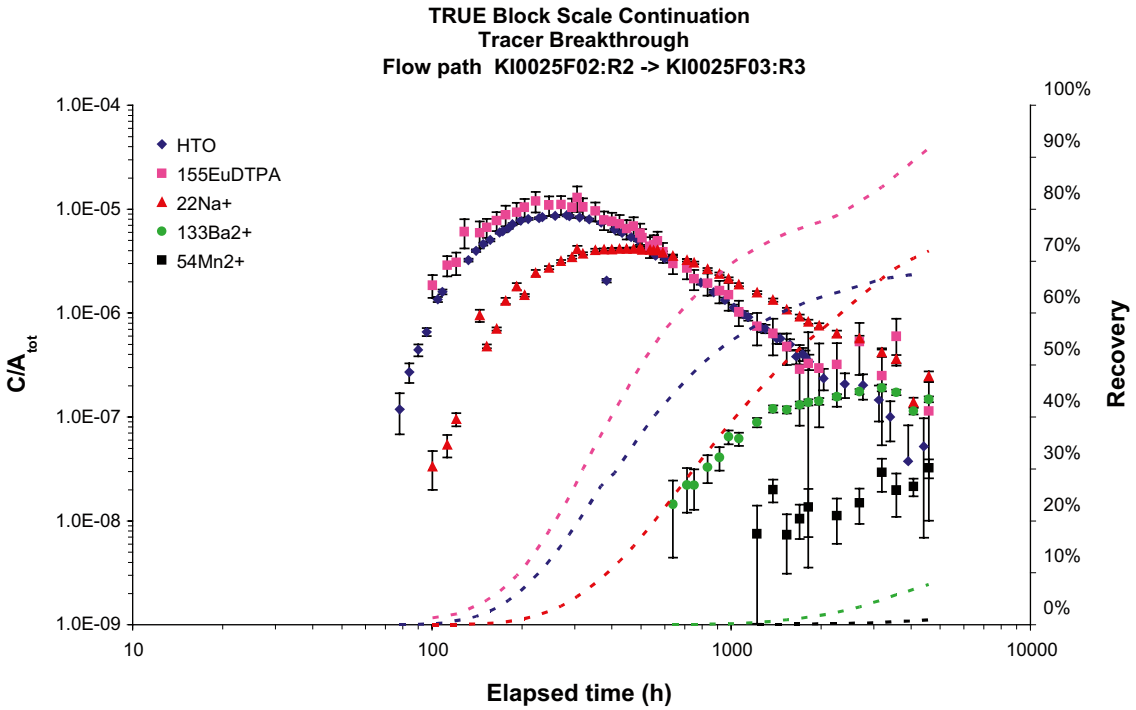

Figure 3-18. *Tracer breakthrough curves and mass recovery for TRUE Block Scale Continuation BS2B tests with sorbing tracers, injection in KI0025F02:R2 (log-log scale). Concentrations are normalised to injected mass. Error bars represent one standard deviation.*

Table 3-11. BS2B, flow path KI0025F02:R3 to KI0025F03:R3 (fast flow path). Tracer travel times, t_5, t_{50} and t_{95} and tracer mass recovery at t_t (t_t is the time for the last sample taken).

Tracer	t_5 (h)	t_{50} (h)	t_{95} (h)	t_t (h)	Recovery (%)
$^{131}I^-$	14	62	–	296	80
^{160}Tb-DTPA	14	63	–	4,075	87
$^{85}Sr^{2+}$	19	107	–	4,327	86
$^{86}Rb^+$	51	490	–	594	56
$^{137}Cs^+$	555	–	–	4,579	28

Table 3-12. BS2B, flow path KI0025F02:R2 to KI0025F03:R3 (slow flow path). Tracer travel times, t_5, t_{50} and t_{95} and tracer mass recovery at t_t (t_t is the time for the last sample taken).

Tracer	t_5 (h)	t_{50} (h)	t_{95} (h)	t_t (h)	Recovery (%)
HTO	183	790	–	4,409	68
^{155}Eu-DTPA	155	500	–	4,577	92
$^{22}Na^+$	300	1,490	–	4,577	72
$^{133}Ba^{2+}$	3,250	–	–	4,577	8
$^{54}Mn^{2+}$	–	–	–	4,577	1

Tracer travel times, t_5, t_{50} and t_{95} (defined as times when 5, 50 and 95% of the recovered mass has arrived in the pumping section at the stop time of sampling, t_t) were calculated and are presented together with the total mass recovery (calculated at the stop time of sampling, t_t) in Table 3-11 and Table 3-12.

3.4.4 Basic evaluation and discussion of results

The basic evaluation of the breakthrough data was done with the same models and concepts as previous tests with sorbing tracers in the TRUE Block Scale, Phase C tests /Andersson et al. 2001, 2004/. The following main results were obtained:

- Experimental data fits relatively well to a one-dimensional advection-dispersion model with matrix diffusion and linear equilibrium sorption. The fit to the models without matrix diffusion is generally less good.
- The following approximate value ranges for R (linear sorption retardation coefficient) for the sorbing tracers were found (in rising order):
  - $^{85}Sr^{2+}$: 1.1–1.25
  - $^{22}Na^{+}$: 1.3–1.5
  - $^{86}Rb^{+}$: 2.9–3.2
  - $^{133}Ba^{2+}$: 4.1–4.5
  - $^{54}Mn^{2+}$: 6.4–7.4
  - $^{137}Cs^{+}$: 12.8–13.2
- The values for $^{54}Mn^{2+}$ are associated with large estimation errors. This is also the case, but to a lesser extent, for $^{86}Rb^{+}$.
- The matrix diffusion effect is probably fairly significant in both of the tested flow paths, based on estimated values of the lumped parameter A /cf Andersson et al. 2004b/. Further evaluation of the effects of matrix diffusion requires estimates of the fracture aperture and the matrix porosity.
- Estimated dispersivity values (generally about 2–3 m) were on the order of one magnitude smaller than the Euclidian transport distance.
- Estimated residence times were about 10–12 hours for the faster flow path, and about 200–220 hours for the slower flow path.
- The evaluation of the faster flow path was found to be very sensitive to the injection input function. An accurate description of the injection function was possible by using the on-line measurements at early stages of the injection.

The results of the modelling show both similarities and differences when compared to the TRUE Block Scale Phase C tests /Andersson et al. 2001/. The main difference is that $^{85}Sr^{2+}$ shows a significantly lower retardation than in the Phase C tests, in fact also lower than for $^{22}Na^{+}$. The flow paths are also significantly different. Phase C (injection C3) was performed in a long and slow flow path (t_0 = 820 h) whereas in this case in a fast flow path (Structure #19, t_0 = 10 h).

4 Modelling

4.1 Introduction and overview

In the current modelling altogether four modelling approaches have been employed. They represent two different categories of modelling tools, one the one hand two site modelling tools; the JNC-Golder and the ANDRA-Itasca discrete channel network models, both sharing an underlying discrete feature representation on which 1D channel networks are draped. The two models can be regarded as tools suitable for application in site investigation modelling in that they can handle both three-dimensional groundwater flow and reactive solute transport. However, the JNC-Golder model with its plug-ins can also be used as a performance assessment model. The other two models, the Posiva VTT streamtube approach and the SKB-KTH/WRE Lagrangian stochastic advection-reaction approach. The latter two models which essentially are describing flow paths lack ain inherent description of groundwater flow. In the case of the SKB KTH/WRE approach this model imports relevant flow statistics from any of the two 3D flow models for its analysis.

In the following sections the theoretical platform for groundwater flow and reactive solute transport are presented followed by summaries of the results of the individual modelling results. The chapter is concluded by a summary compilation of the results of the model predictions of the BS2B tests with sorbing tracers including a comparison with experimental results.

4.1.1 Common conceptual flow model

Groundwater flow is not the main focus of the TRUE Block Scale Continuation project. However, assumptions about the macroscale properties of the flow field are an important aspect of the study of transport and retention. A basic understanding of groundwater flow is therefore a prerequisite for design and planning of a transport experiment, particularly in this case when a previously non-tested part of the TRUE Block Scale volume is addressed. In this context well-performing numerical (or analytical) models of groundwater flow can be an important element in design calculations and model predictions. In the case of TRUE Block Scale Continuation, flow modelling involving the whole TRUE Block Scale rock volume played an important role in assessing the premises for performing large scale tracer tests, cf Section 1.4.

This section attempts to highlight the common basis for "flow" of the various models presented in subsequent sections of this chapter, and also attempts to highlight important differences between the models. The "microscale" properties of the flow field, i.e. the short range variations in aperture (and hence in groundwater velocity) that have a direct bearing on dispersion properties, are however not discussed.

All models include descriptions of groundwater flow which solve for some variant of the classical diffusivity equation:

$$div(K\nabla h) = S_S \frac{\partial h}{\partial t} + q \qquad (4\text{-}1)$$

where

K Hydraulic conductivity tensor [LT^{-1}],

h Hydraulic head [L],

S_s Specific storage [L^2],

q Source term [L^3T^{-1}].

For all models (assuming steady state flow) Equation (4-1) reduces to:

$$div(K\nabla h) = q \tag{4-2}$$

with the same notations as above. Also, since the JNC-Golder and ANDRA-Itasca approaches flow is restricted to multiple one-dimensional (channel) elements, the diffusivity equation is further reduced to:

$$T\frac{\partial^2 h}{\partial x^2} = 0 \tag{4-3}$$

where

T is the integrated hydraulic transmissivity of each pipe [L^3T^{-1}],

x is the coordinate along the pipe [L].

The differences in the approach to modelling of groundwater flow between the various groups can be expressed in terms of "dimensionality" of the elements used to discretise the different types of heterogeneities of fractured crystalline rock, as outlined in Table 4-1.

4.1.2 Common conceptual retention model

Under this heading, all processes relating to transport and retention are considered, including the microscopic, or "local", flow model explicitly used by some groups (see e.g. the Posiva streamtube approach in Section 4.4). In the same manner as in the preceding section, the basic equations that represent the phenomena simulated by the various modelling groups are reviewed. The governing equations are successively "expanded" by adding physical processes one by one, trying to emphasise "common ground" and differences between the groups, in order to provide a better perspective on the work performed and presented in subsequent sections of the report.

Additional discussion of the common framework for solute transport retention employed is found in /Poteri et al. 2002 cf Chapter 6 therein/.

4.1.3 Advection

All models use, either explicitly or implicitly, the assumption that advection is one of the mechanisms for mass transfer. This can be written as:

$$\theta\frac{\partial C}{\partial t} + V_i\frac{\partial C}{\partial x_i} = 0 \tag{4-4}$$

where

C is the solute concentration [ML^{-3}],

t is the time [T],

V_i is the macroscopic velocity in direction i (advective, or Darcy velocity) [LT^{-1}],

θ is the porosity [–],

Indexation implies a summation over the three coordinates in 3D.

Table 4-1. Main entities used to represent the flow domain.

Modelling group/model	Representation of flow domain
ANDRA (Channel Network)	Multiple interconnected 1-D elements
JNC-Golder (Channel Network)	Multiple interconnected 1-D elements
Posiva-VTT (Streamtube)	Non-connected 1-D paths
SKB-KTH/WRE (LaSAR)	Non-connected 1-D paths

Note that deducing the macroscopic velocity in Equation (4-4) from flow computations is not always a straightforward problem. When dealing with fracture flow, a "geometrical" parameter must be inputed that relates flow rates in the fracture with the velocities in Equation (4-4). This is often done by assuming a (transmissivity vs. aperture) relationship.

For all four models (ANDRA-Itasca Channel Network, JNC Channel Network, Posiva streamtube, and SKB LaSAR), advection is only one-dimensional, so the above equation reduces to a scalar one.

4.1.4 Dispersion

Accounting for flow, but this time at the microscopic level, two models (ANDRA-Itasca Channel Network and JNC Channel Network) use a lumped dispersion, thus solving for the following advection-dispersion equation:

$$\theta \frac{\partial C}{\partial t} + V_i \frac{\partial C}{\partial x_i} = \frac{\partial}{\partial x_i}\left(D_{ij} \frac{\partial C}{\partial x_j} \right) \tag{4-5}$$

where D_{ij} is the component of the dispersion tensor [L^2T^{-1}].

More precisely, the Channel Network models (cf Section 4.2 and 4.3) use a longitudinal dispersion only. Also, the porosity θ is equal to unity when considering that flow occurs only in the fracture (Channel Network models), which further simplifies the equation. For a one-dimensional model an example of the simplified equation reads:

$$\frac{\partial C}{\partial t} + V \frac{\partial C}{\partial x} = D_l \frac{\partial^2 C}{\partial x^2} \tag{4-6}$$

where

V is the one-dimensional velocity [LT^{-1}],

x is the single spatial coordinate [L],

D_l is the longitudinal dispersion coefficient [L^2T^{-1}].

The main differences between the four models can already be identified, with two models that essentially do not consider the macroscopic flow field (no attempt is made to predict it) but try to reproduce in somewhat more detail the local transport processes (i.e. the Posiva streamtube approach and the SKB LaSAR approach), and two models forming a midway alternative, i.e. ANDRA-Itasca and JNC-Golder Channel network model, which form a midway alternative between the former two and any type of 3D stochastic continuum approach or discrete feature network models.

Molecular diffusion within the flow domain is taken into account explicitly by Posiva as part of the mechanism for "dispersion". It enables solute to "jump" from one streamline to adjacent ones, therefore smoothing out the variations in transit time between various streamlines. Instead of using a longitudinal dispersion coefficient, the Posiva group therefore directly deduces the distribution of transit times from a hypothesis on the velocity profile along fractures, and the value of molecular diffusion, whereas all other groups implicitly include diffusion through the use of a mechanical dispersion parameter.

4.1.5 Surface sorption

Diffusion within the flow domain is also considered as the mechanism that enables migration of solutes to the surfaces of a fracture, and therefore allowing both sorption onto the surfaces, and further diffusion into the rock matrix. In a first step, taking into account linear equilibrium sorption on the fracture surfaces, adds a retardation factor to the equation. Its form then becomes:

$$R \frac{\partial C}{\partial t} + V \frac{\partial C}{\partial x} = D_l \frac{\partial^2 C}{\partial x^2} \tag{4-7}$$

In the case of a homogeneous channel, the retardation factor R [–] can be related to the surface sorption coefficient, K_a [L], in the following manner:

By definition,

$$R = \frac{m_s + m_a}{m_s} \tag{4-8}$$

where

m_s mass in solution [M],

m_a adsorbed mass [M].

We introduce the adsorbed fraction F [ML^{-2}],

$$F = K_a C = K_a \frac{m_s}{V_w} = \frac{m_a}{S} \tag{4-9}$$

where

S is the surface available for adsorption [L^2],

V_w is the volume of water containing the solute mass [L^3].

Computing the value of m_a from these two equations, and equating them, we get:

$$K_a m_s \frac{S}{V} = m_s (R - 1) \tag{4-10}$$

Therefore

$$R = 1 + K_a \frac{S}{V_w} \tag{4-11}$$

Note that the quantity $\frac{S}{V_w}$ [L^{-1}] is the Flow Wetted Surface (FWS) per unit volume of fluid.

4.1.6 Diffusion and adsorption into the rock matrix

The diffusion and adsorption of solutes into the rock matrix brings in an additional term in the equation for transport in the fracture, while a new equation governs transport within the matrix. Note that all groups consider the transport in the matrix to be only diffusive, and to be one-dimensional, therefore the new equation is of a well known type.

$$R \frac{\partial C}{\partial t} + V \frac{\partial C}{\partial x} = D_l \frac{\partial^2 C}{\partial x^2} + 2 \frac{\theta D_m}{2b} \frac{\partial C_m}{\partial z}\bigg|_{z=0} \tag{4-12a}$$

and

$$R_m \frac{\partial C_m}{\partial t} - D_m \frac{\partial^2 C_m}{\partial z^2} = 0 \tag{4-12b}$$

where

b is the half aperture of the fracture [L],

θ is the porosity of the rock matrix [–],

C_m is the concentration in the rock matrix [ML^{-3}],

D_m is the pore diffusivity into the rock matrix [L^2T^{-1}],

z is the distance normal to the fracture [L],

R_m is the matrix sorption retardation factor [–].

Note that all quantities pertaining to the matrix are given index "m": C_m [ML^{-3}], R_m [–], D_m [L^2T^{-1}] are the concentration, retardation coefficient and diffusion coefficient, respectively, inside the pores of the matrix.

In the same manner as R can be related to the surface sorption coefficient K_a, R_m can be related to the volume sorption coefficient K_d [–]:

R_m is defined similarly by:

$$R_m = \frac{m_s + m_a}{m_s} \tag{4-13}$$

where in this case:

m_s $[M]$ and m_a $[M]$ are the mass in solution and the adsorbed mass in the matrix, respectively.

In this case the adsorbed fraction F_m [–] is defined by:

$$F_m = K_d C_m = K_d \frac{m_s}{V_\phi} = \frac{m_a}{m_{sol}} \tag{4-14}$$

where

V_Φ is the volume of the matrix pore space $[L^3]$,

m_{sol} is the mass of the adsorbing material $[M]$.

We thus have:

$$m_{sol} = \rho V_{sol} = \rho V_\phi \frac{1-\theta}{\theta} \tag{4-15}$$

where

ρ is the density of the solid fraction $[ML^{-3}]$.

Computing m_a by using Equation (4-13), and on the other part by combining Equations (4-14) and (4-15), we get:

$$m_s(R_m - 1) = K_d \frac{m_s m_{sol}}{V_\phi} = K_d m_s \rho \frac{1-\theta}{\theta} \tag{4-16}$$

which yields :

$$R_m = 1 + K_d \rho \frac{1-\theta}{\theta} \tag{4-17}$$

Not all groups are using the full form of Equations (4-12a) and (4-12b). For example, the Posiva-VTT and SKB-KTH/WRE groups do not include the dispersion term $D_l \frac{\partial^2 C}{\partial x^2}$, because it is accounted for in the distribution of transit times.

4.1.7 Heterogeneity

The properties in Equations (4-12a) and (4-12b) may be spatially heterogeneous. Among the many possible types of heterogeneities, two received special attention from some modelling groups in the course of the TRUE Block Scale modelling:

- The “matrix” is constituted of several types of retention zones, with various properties: fault gouge, fault breccia, altered fracture rim zones (Posiva-VTT group).
- The pore diffusion coefficient D_m may depend on the distance from the fracture wall z (SKB-KTH/WRE group).

Accounting explicitly for these yields a slightly different set of equations,

$$R\frac{\partial C}{\partial t} + V\frac{\partial C}{\partial x} = D_l \frac{\partial^2 C}{\partial x^2} + \sum_{i=1}^{N} \frac{\alpha^i \theta^i D_m^i}{b^i} \frac{\partial C_m^i}{\partial z}\bigg|_{z=0} \tag{4-18a}$$

and

$$R_m^i \frac{\partial C_m^i}{\partial t} - \frac{\partial}{\partial z} D_m^i \frac{\partial C_m^i}{\partial z} = 0 \qquad (4\text{-}18b)$$

where

N is the number of retention zones,

i is the index of a retention zone, noted as superscript for all quantities concerned,

α^i is the fraction of the fracture unit area in contact with retention zone "i" ($\Sigma\alpha^i = 1$).

Note that instead of 2 equations, we now have one Equation (4-18a), plus N Equation (4-18b).

4.2 ANDRA-Itasca

4.2.1 Concept and processes included

Structure related data, as well as fracture intersection positions and transmissivities along boreholes are directly included as deterministic information in the model. The rest of the fracture network (i.e. background fractures that do not intersect the boreholes) is represented as a stochastic model with statistical geometrical properties.

The total flow network consists of the union of different "features": the deterministic structures, the conditioned background fractures intersecting the boreholes, and the "purely stochastic" ones in the remainder of the rock. A grid of one-dimensional channels are projected on all these two-dimensional features, intersections between the various features are computed and stored. Such intersections are also considered as conductors, therefore allowing connection of the whole channel network. Any intersection between two features is assigned a conductivity taken from the distribution used for the most transmissive of the two features, and the corresponding section.

Channel conductivities C are generated directly, in order to obtain the given large-scale feature transmissivity. A simple geometrical conceptual model assigns the transport properties. A channel is considered as a flat ribbon, with width w and thickness $2b$. The width w can be deduced from the grid spacing g by consideration of the feature surface area. Assuming that flow covers the whole area, then:

$$w = \frac{g}{2.shapef} \qquad (4\text{-}19)$$

yields the correct total area. In fact, the flow area is not necessarily the same as the area of the feature: on one hand, the sides of the feature are in contact in some parts of the feature area through asperities, and/or filling may prevent flow in some other parts; and on the other hand, the feature may be constituted of several near parallel sub-planes, in which case the "flow area" may actually be larger than the nominal feature area. A single parameter, the "contact fraction" c_f, embodies these variations. The limiting value $c_f = 1$ means that the whole plane of the feature is in contact, and no area is left for flow, while $c_f = 0$ means that the area available for flow is equal to the area of the feature, and $c_f = -1$ corresponds to a feature made of two fully open sub-planes.

Once we know the width of a channel, we obtain its aperture $2b$ in the following way. First, we note that the "local transmissivity" of this ribbon is C/w. We then use a square or cubic law for the variations of local transmissivity with aperture. This brings:

$$2b = \alpha \left(\frac{C}{w} \right)^{1/x} \qquad (4\text{-}20)$$

where α is constant for all the channels in a structure, and x is 2 or 3. For $x = 3$ this equation is the translation of Poiseuille's law in the channel.

For a given channel grid (i.e. fixed *g* and *shapef*, given conductivity distribution), properties x, α and c_f completely describe the geometry of the system with regards to conservative as well as reactive transport. In addition to these parameters, a non-reactive transport model may be completed by the choice of a longitudinal dispersion D_l representing the flow variability at the scale of the channels, i.e. below the length scale defined by the grid. Also, for transport, full mixing is assumed at channel intersections.

Each channel in the flow network can be in contact with one surface retention material and with one matrix type in which tracer may diffuse and be adsorbed. The immobile pore space thickness is considered infinite. This is obviously quite a simplification compared to the conceptual model constructed during the course of the TRUE project. In this conceptual model, the sides of the fracture are often lined with two or more layers of materials with finite thicknesses and contrasted properties. Also, fault gouge in the fracture, while another material lines its sides, often provides two contrasted diffusion domains next to a given flow path, while multiplying the perimeter of the flowing section, with diffusion enabled simultaneously into the sides of the fractures and into "in fracture" fault gouge.

We cannot reproduce the layered nature of the fracture sides. However, we assign one material to every channel in the model. For a given type of feature, (i.e. structure, or background fracture), we distribute the various immobile pore spaces between the channels according to the areas we assume they occupy in this particular feature type.

4.2.2 Calibration process

Calibration of flow properties

The flow calibration is based on the drawdowns observed for tests CPT-1 to CPT-3. We modify the transmissivity of Structure #19 from the given hypothesis, and possibly the distribution of transmissivities of the background fractures. Also, because of the heterogeneity of Structure #19, the actual steady-state drawdown at the pumping point for a given test is mostly representative of the local transmissivities around that point. To take this into account, we add a "skin effect" at each well section represented in the model. This skin effect influences only the near-pumping drawdown.

The transmissivity and small scale heterogeneity of Structure #19 are the main fitting parameters: background fracture properties have essentially no effect on these tests.

The mean transmissivity of Structure #19 is increased from the initial value of 10^{-7} m^2/s to $4\ 10^{-7}$ m^2/s, while widely varying skin effects (from 0.025 to 10) are applied at the boreholes. The observed need to introduce widely different skin factors to account for near-borehole effects in Structure #19 suggests at a large variability of its transmissivity. We therefore also force a high heterogeneity by imposing a variation coefficient of 2 (as well as a minimum equal to 1% of the mean) for the lognormal distribution of channel conductivities in Structure #19.

Calibration of non reactive transport properties

The calibration was based on the CPT-4a, CPT-4b and CPT-4c tests.

Our parameter space for calibration is then composed of the following parameters, both for deterministic structures and background fractures:

- Aperture exponent x,
- Aperture coefficient α,
- Contact fraction c_f,
- Longitudinal dispersivity D_l,
- Matrix effective diffusivity D_e

During the course of the calibration, in order to keep the number of fitting parameters as low as possible, we do not distinguish between structures and background fractures for the values of the aperture exponent x and of the matrix effective diffusivity D_e. Conversely, aperture coefficients, contact fractions and longitudinal dispersivities are allowed to differ between structures and background fractures. Also, we allow the transmissivity of the BG 1 intercept to vary. Our goal here is to reproduce all test results with a unique set of parameters. The final calibrated transport properties are summarised in Table 4-2.

4.2.3 Prediction

Strategy

The transport and retention model is discussed in Section 4.2.1. Each channel in our flow network can be in contact with one surface retention material and with one matrix type in which tracer may diffuse and be adsorbed. The immobile pore space thickness is considered infinite. This is obviously quite simple compared to the conceptual model that has been progressively put together during the course of the TRUE project, where:

1) the sides of the fracture are often lined with two or more layers of materials with finite thicknesses and contrasted properties,
2) fault gouge may be present in the fracture, while another material lines its sides, therefore providing two contrasted diffusion domains next to a given flow path, while multiplying the perimeter of the flowing section, with diffusion enabled simultaneously into the sides of the fractures and into "in fracture" fault gouge.

We cannot reproduce the layered nature of the fracture sides. However, we assign one material to every channel in the model. For a given type of feature, (i.e. structure, or background fracture), we distribute the various immobile pore spaces between the channels according to the areas we assume they occupy in this feature type.

We base the sorption, porosity and diffusivity properties in our model on the values provided in Appendix B.

The amount of fault gouge present in Structure #19 could not be measured directly. Fault gouge was found only in KI0025F02. For the prediction, we chose to consider the presence of only a minimal amount of fault gouge, with 5% of the area of Structure #19 concerned. The remainder of the area of Structure #19 is divided between "Cataclasite/Mylonite", covering 20% of the area of the Structure, and hydrothermally "Altered Diorite", covering the remaining 75%.

Similarly, we consider that background fracture wall rock consist mostly of Altered Diorite, with only 5% of the flow area in contact with fracture filling. Note that the "BG fractures" set of properties below are effectively used for all background fractures, not only BG1.

Table 4-2. ANDRA-Itasca calibrated transport parameters.

Transport property	Value
Aperture exponent x:	2
Aperture coefficient α in structures	0.25 $s^{1/2}$
Aperture coefficient α in background fractures	0.06 $s^{1/2}$
Contact fraction c_f in structures:	–1
Contact fraction c_f in background fractures:	0
Dispersivity D_l in structures:	1 m
Dispersivity D_l in background fractures:	0 m
Matrix effective diffusivity D_e:	$5 \cdot 10^{-11}$ m^2/s

Parameterisation

The assumptions above are summarised in Table 4-3, together with porosities directly taken from Appendix B, and assuming an average rock density of 2,500 kg/m^3. Simplified material names (column "Name" in the table) are assigned for use in Table 4-4 detailing reactive properties.

Diffusivities, K_a's and K_d's are taken directly from the values given, when available. However, sorption properties for a given tracer are given only for the feature in which it is injected. We need in fact a slightly more general model. Tracers injected in BG1 have to travel through Structure #19 too before they reach the sink located in Structure #19, and, less importantly, tracer injected in Structure #19 may travel some part of its path in the background fractures intersecting the structure. The parameter table is therefore completed in an ad hoc manner, based on the concept that 1) background fracture filling and fault gouge may have similar properties, and that altered Äspö diorite close to a background fracture is similar to altered Äspö diorite close to a fault structure. In fact, these assumptions are not critical, since the two paths to be studied are quite independent from each other, as will be seen later.

Table 4-3. Immobile pore space as realised in the model.

	Name	Fraction of area	Porosity (–)	Density (kg/m^3)
BG fractures				
Fracture filling	bg_fil	0.05	0.05	2,500
Altered diorite	bg_rim	0.95	0.006	2,500
Structure #19				
Fault gouge filling	19_gou	0.05	0.20	2,500
Cataclasite/Mylonite	19_cat	0.20	0.01	2,500
Altered diorite	19_dio	0.75	0.006	2,500

Table 4-4. Reactive tracer properties of the different materials and tracers.

Tracer/Micro-structure unit	Diffusivity (D_e) (m^2/s)	K_a (m)	K_d (m^3/kg)
I			
bg_fil	$1.2 \cdot 10^{-11}$	0.	0.
bg_rim	$4.4 \cdot 10^{-13}$	0.	0.
19_gou	$1.1 \cdot 10^{-10}$	0.	0.
19_cat	$9.8 \cdot 10^{-13}$	0.	0.
19_dio	$4.4 \cdot 10^{-13}$	0.	0.
tbDTPA			
bg_fil	$3.0 \cdot 10^{-12}$	0.	0.
bg_rim	$1.1 \cdot 10^{-13}$	0.	0.
19_gou	$2.8 \cdot 10^{-11}$	0.	0.
19_cat	$2.4 \cdot 10^{-13}$	0.	0.
19_dio	$1.1 \cdot 10^{-13}$	0.	0.
Sr			
bg_fil	$5.0 \cdot 10^{-11}$	0.	$1.3 \cdot 10^{-3}$
bg_rim	$1.7 \cdot 10^{-13}$	$1.5 \cdot 10^{-5}$	$2.6 \cdot 10^{-5}$
19_gou	$4.4 \cdot 10^{-11}$	0.	$1.3 \cdot 10^{-3}$
19_cat	$3.9 \cdot 10^{-13}$	$2.2 \cdot 10^{-5}$	$1.4 \cdot 10^{-4}$
19_dio	$1.7 \cdot 10^{-13}$	$1.5 \cdot 10^{-5}$	$2.6 \cdot 10^{-5}$

Tracer/Micro-structure unit	Diffusivity (D_e) (m^2/s)	K_a (m)	K_d (m^3/kg)
Rb			
bg_fil	$1.3 \cdot 10^{-11}$	0.	$1.5 \cdot 10^{-2}$
bg_rim	$4.5 \cdot 10^{-13}$	$1.0 \cdot 10^{-4}$	$4.0 \cdot 10^{-4}$
19_gou	$1.2 \cdot 10^{-10}$	0.	$1.5 \cdot 10^{-2}$
19_cat	$1.0 \cdot 10^{-12}$	$8.0 \cdot 10^{-4}$	$4.0 \cdot 10^{-3}$
19_dio	$4.5 \cdot 10^{-13}$	$1.0 \cdot 10^{-4}$	$4.0 \cdot 10^{-4}$
Cs			
bg_fil	$1.3 \cdot 10^{-11}$	0.	$1.0 \cdot 10^{-1}$
bg_rim	$4.5 \cdot 10^{-13}$	$1.0 \cdot 10^{-3}$	$5.0 \cdot 10^{-4}$
19_gou	$1.2 \cdot 10^{-10}$	0.	$1.0 \cdot 10^{-1}$
19_cat	$1.0 \cdot 10^{-12}$	9.8·10–3	$3.0 \cdot 10^{-2}$
19_dio	$4.5 \cdot 10^{-13}$	1.0·10–3	$5.0 \cdot 10^{-4}$
HTO			
bg_fil	$1.3 \cdot 10^{-11}$	0.	0.
bg_rim	$4.7 \cdot 10^{-13}$	0.	0.
19_gou	$1.2 \cdot 10^{-10}$	0.	0.
19_cat	$1.0 \cdot 10^{-12}$	0.	0.
19_dio	$4.7 \cdot 10^{-13}$	0.	0.
EuDTPA			
bg_fil	$3.0 \cdot 10^{-12}$	0.	0.
Bg_rim	$1.1 \cdot 10^{-13}$	0.	0.
19_gou	$2.8 \cdot 10^{-11}$	0.	0.
19_cat	$2.4 \cdot 10^{-13}$	0.	0.
19_dio	$1.1 \cdot 10^{-13}$	0.	0.
Na			
bg_fil	$8.3 \cdot 10^{-12}$	0.	$2.0 \cdot 10^{-4}$
Bg_rim	$2.9 \cdot 10^{-13}$	$7.0 \cdot 10^{-7}$	$1.7 \cdot 10^{-6}$
19_gou	$7.4 \cdot 10^{-11}$	0.	$2.0 \cdot 10^{-4}$
19_cat	$6.5 \cdot 10^{-13}$	$7.0 \cdot 10^{-7}$	$1.7 \cdot 10^{-6}$
19_dio	$2.9 \cdot 10^{-13}$	$7.0 \cdot 10^{-7}$	$1.7 \cdot 10^{-6}$
Ba			
bg_fil	$5.3 \cdot 10^{-12}$	0.	$2.7 \cdot 10^{-2}$
bg_rim	$1.9 \cdot 10^{-13}$	$2.9 \cdot 10^{-4}$	$2.9 \cdot 10^{-4}$
19_gou	$4.7 \cdot 10^{-11}$	0.	$2.7 \cdot 10^{-2}$
19_cat	4.2·10–13	$2.9 \cdot 10^{-4}$	$6.9 \cdot 10^{-4}$
19_dio	1.9·10–13	$2.9 \cdot 10^{-4}$	$6.9 \cdot 10^{-4}$
Mn			
bg_fil	4.3·10–12	0.	$1.7 \cdot 10^{-1}$
bg_rim	1.5·10–13	$1.8 \cdot 10^{-3}$	$1.8 \cdot 10^{-3}$
19_gou	3.8·10–11	0.	$1.7 \cdot 10^{-1}$
19_cat	3.4·10–13	$1.8 \cdot 10^{-3}$	$4.3 \cdot 10^{-3}$
19_dio	1.5·10–13	$1.8 \cdot 10^{-3}$	$4.3 \cdot 10^{-3}$

Results

The predicted breakthrough curves are presented in Section 4.6. Clearly, as seen in the compilation tables and figures, the ANDRA-Itasca numerical simulations significantly lack retardation. Also, the initial rise of the breakthrough curves is found to be too steep, indicating a lack of dispersivity (or, equivalently, lack of small scale heterogeneity) in the model.

4.2.4 Evaluation of retention properties

This section describes numerical simulations aimed at studying the initial hypotheses as expressed in Section 1.5. This individual work can partly address Hypothesis Ia), "*Microstructural information can provide significant support for predicting transport of sorbing solutes at experimental time scales*", for which a comparison of the various models built by the four project modelling teams will be the best test, and try to gain insights into Hypothesis Ib), "*Transport at experimental time scales is significantly different for faults and joints, due to the indicated differences in microstructure and properties*".

A first step in obtaining a meaningful evaluation is to resolve prediction discrepancies. We had chosen to take into account the presence of only a minimal amount of fault gouge/filling. Clearly, this resulted in a significant lack of retardation. This is taken care of by increasing drastically the amount of fault gouge/fracture filling to be encountered by the tracers. The updated breakthrough curves show an acceptable behaviour relative to measured data. Using the new batch of parameters to simulate the CPT-4a to CPT-4c tracer tests yields fits as good as the ones obtained during calibration. This means that the evaluation parameters we chose provide a consistent model, able to reproduce adequately all observed behaviour – we are probably taking into account enough physical phenomena for the task at hand. However, a negative implication is that very different retardation behaviours can be obtained for two sets of parameters (the "prediction" and the "evaluation" ones), both yielding almost identical responses for the calibration tests simulations.

Discussion

"Average" responses cannot be used to calibrate the model and then predict and evaluate the reactive transport breakthrough curves. One realization of the network must be chosen. Using averages could work for studying paths within a structure, where the variability of the response is moderate, even though the structure itself is quite heterogeneous locally: at the scale studied here (a few tens of meters), flow and transport in a structure are already averaged. This is not quite true when considering the response of the background fractures network. This response is very much reliant on network connections, which are not averaged over a few tens of meters. For example, when generating a number of realizations of the network, a significant portion of them yields an unconnected BG1, preventing any transport simulation. In such instances, the use of averages is meaningless. In other words, the scale of interest here is probably way below the Representative Elementary Volume (REV) for transport in this network, if such a REV exists. Therefore the study of differences between structures and background fractures relies on a "point statistic" (i.e. only one realisation).

Here, a major factor in the behaviour of the reactive tracers at experimental time scales seems to be the filling/fault gouge in fractures and structure. In fact, such material, even if pervasively present in the network, as hypothesised in the evaluation part of this work, would still not be of much consequence for very long time scales, because of its limited thickness. It would essentially act as a thin coating and be saturated fairly rapidly. Therefore, the one part of the system that has most influence on its behaviour at experimental time scales is probably not important for the time scale of interested. This does not augur well of for predicting reactive tracer behaviour at performance assessment time scales.

4.3 JNC-Golder

4.3.1 Concept and processes included

The JNC/Golder model concept was the use of a 500 m scale discrete fracture network (DFN) flow and transport model for the TRUE Block Scale rock block, with steady state flow solved by the finite element method /Miller et al. 2001/, and transport flow solved by the Laplace Transform Galerkin (LTG) method /Dershowitz et al. 1999/.

The underlying *concepts* for this modelling are as follows:

1. It is assumed that flow within fractured rock occurs specifically within fractures as defined by the *hydrostructural model*, and within those fractures within channels, such that the path length through geometry of fractures and channels, rather than the Cartesian distance between injection and pumping locations is of concern for analysis and modelling of transport.
2. It is assumed that the flow field relevant for transport modelling can be approximated as a steady state head derived from measured head data interpolated to the boundaries of the 500 m scale model, combined with the measured drawdown at the pumping borehole. This flow field is solved by the finite element method.
3. It is assumed that each fracture can be approximated by a single, isotropic value of hydraulic (transmissivity m^2/s, storativity), and transport (transport aperture, channel width, immobile zone porosities and sorption coefficients), and that the variation between fractures can be determined from the hydrostructural models, including stochastic distributions of properties
4. It is assumed that at the time and distance scales of these tracer tests, sorbing tracer retention is controlled by the immobile zones as described in the *microstructural models* assigned to every fracture, including structure geologic type (Type 1 fault, Type 2 non fault), and complexity, as described in /Dershowitz et al. 2003/.The effect of complexity, as described in the microstructural model, is assumed to be approximated by applying a multiplicative factor to the area available for diffusion of each immobile zone.
5. It is assumed that the parameter not obtainable from the hydrostructural and microstructural models is the geometry of the flow channels within the fractures. This parameter (channel width) must therefore be obtained from generic assumptions or evaluation of related tracer experiments. In this case, the CPT tracer experiments were used to provide this information.
6. Because the models were constrained by the given hydrostructural and microstructural models, predictions were primarily considered as forward models under alternative assumptions concerning realisations of the DFN, and implementation of channels. However, in the evaluation phase, a range of assumptions were considered to determine which assumptions best matched observed conservative and sorbing tracer breakthroughs.

The processes included in the modelling are as follows:

1. Steady state, laminar flow in channelised fractures.
2. Advective transport including Gaussian longitudinal kinematic dispersion described by a dispersion length α_L, generally estimated at approximately 10% of the path length.
3. Matrix Diffusion, controlled by the product of free water diffusion, porosity, tortuosity, and pathway perimeter.
4. Equilibrium sorption on surfaces in contact with advective flow, controlled by the reactive surface area and sorption coefficient K_a derived from laboratory testing as part of the microstructural model development.
5. Equilibrium sorption in immobile zones, controlled by the diffusion rate to the immobile zone, and the sorption coefficient K_d derived from laboratory testing as part of the microstructural model development.

Colloidal transport, Non-equilibrium sorption, non-Fickian dispersion, turbulent flow, and non-Gaussian dispersion are not considered in the modelling.

4.3.2 Calibration process

The intention of the prediction was to run a forward model simulation, based solely on the hydrostructural and microstructural models as developed by the project. Therefore, calibration was not carried out as part of the prediction. However, because the hydrostructural model did not contain information about channel geometry, and because of the potential role of alternative realisations of background fractures, limited calibration was carried out to compare alternative BS2B predictive models against the non-sorbing pre-test CPT-4c. These alternative predictive models varied the path width and aperture, the algorithm used to generate the channel network within the fracture planes, and the geometry of the DFN for stochastic background fractures. The basic hydrostructural and micro-structural models were kept unchanged.

As part of the evaluation phase considering the BS2B tracer transport results, an additional set of simulations were carried out to consider the role of alternative realisations and channel geometry. From these simulations, it appears that channel width may be the key parameter necessary to better model BS2B sorbing tracer transport.

4.3.3 Prediction

JNC/Golder's procedure for predictive modeling was as follows.

1. Construct the Task 6C hydrostructural model /Dershowitz et al. 2003/ as a three-dimensional discrete feature network (DFN) model using the FracWorks XP software package. This model included all deterministic, semi-synthetic, and background structures.
2. Convert the DFN into a one-dimensional pipe network model, using PAWorks/Genpipe. This pipe network was conditioned to match the connectivity of the DFN model, with pipe properties set to match the apertures and transmissivities of their host fractures. Pipes that did not connect to a head or flow boundary were removed from the system for computational efficiency.
3. Apply the specified steady state flow boundary conditions through the MAFIC software package to obtain a nodal head and flux field. The resulting flow solution assigns an advective transport velocity to all pipes.
4. Convert the full channel network into a smaller mesh of just the "downstream" network of pipes between the defined tracer injection sources and sink. The new mesh is then exported this from PAWorks to the LTG solver. Immobile zone parameters are assigned to pipes based on set membership of their host fractures. Solute transport boundary conditions are also assigned at this stage.
5. Derive advective flow performance metrics (β factor and water residence time distributions) from transport pathways identified in PAWorks through a graph-theory traversal of the channel network.
6. Calculate τ and β values /Poteri et al. 2002/ for the flow pathway that each particle took by dividing the travel time t_w in each pipe by the pipe aperture e, and summing the result over the length of the pipe.
7. Simulate fracture complexity /Dershowitz et al. 2003/ by altering the perimeters of pipes on a set-by-set basis in the LTG input files. Pipes belonging to fractures of Complexity 2 had their pipe perimeter available to transport processes doubled, while pipes belonging to fractures of Complexity 3 had their perimeters tripled. Flow perimeters, and therefore pipe velocities, were left unchanged.
8. Simulate solute transport using FracMan/LTG in the pipe network. This program reports fluxes, concentrations, and cumulative releases at user-specified trace planes and at specified head/flux boundaries (the western edge of the 200 m BS2B experimental volume).
9. Calculate additional performance measure statistics (breakthrough curves, t_5, t_{50}, t_{95}).

Immobile zones transport properties were based on the micro-structural model and the data is mainly taken from Appendix B, together with the microstructural model definitions as provided by /Dershowitz et al. 2003/.

Immobile zones properties are summarised in Table 4-5 and Table 4-6.

Actual node/pipe transport pathways were identified in the BS2B prediction model using both a particle-tracking algorithm and the weighted graph theory traversal within PAWorks. One thousand particles were released into the advection-only flow solution network used to produce the water residence time distribution from each tracer release site.

One limitation to the particle tracking approach within the PA Works software package is that particles can only move along pathways previously identified through the graph theory search; i.e. though the means of the particle travel times are well-constrained, the outliers are sensitive to the number of transport pathways found. For the BS2B simulations, the number of pathways was hard-coded to be 50. In practice, this had little effect on the simulations. For most geometries, there were only 5–6 hydraulically significant pathways. The major difference between pathways was in the selection of in-plane fracture nodes, rather than the selection of alternate fractures.

The breakthrough curves predicted by JNC/Golder of the BS2B sorbing tracer injections are presented in Section 4.6.

4.3.4 Evaluation of retention properties

JNC/Golder carried out an extensive set of simulations to improve the understanding of the retention in both of the BS2B sorbing tracer experiment pathways. These simulations are described in /Fox et al. 2005/ and are characterised by the following changes:

- Improvements to the implementation of the hydrostructural model to remove non-conductive fracture zones.
- Improved meshing of channels onto fracture planes.
- Selective changes to assumed pathway apertures and transmissivities.

Table 4-5. Pore space implementation for Type I structures in the JNC/Golder BS2B model.

Type I Features (faults) Immobile zone	Thickness (m)	Porosity (%)	Formation factor	Density (kg/m³)	Multiplier Applied to path perimeter for diffusion area
Fault gouge	0.003	20	$5.6 \cdot 10^{-2}$	2,755	1x, 2x, 3x based on complexity
Cataclasite	0.01	1	$4.9 \cdot 10^{-4}$	2,914	1x, 2x, 3x based on complexity
Coating	0.0005	5	$6.2 \cdot 10^{-3}$	2,853	1x, 2x, 3x based on complexity
Altered walls	0.15	0.6	$2.2 \cdot 10^{-4}$	2,895	1x, 2x, 3x based on complexity
Fresh rock	1	0.3	$7.3 \cdot 10^{-5}$	2,839	1x, 2x, 3x based on complexity

Table 4-6. Pore space implementation for Type II structures in the JNC/Golder BS2B model.

Type II Features (fractures) Immobile zone	Thickness (m)	Porosity (%)	Formation factor	Density (kg/m³)	Multiplier Applied to path perimeter for diffusion area
Coating	0.0005	5	$6.2 \cdot 10^{-3}$	2,853	1x or 2x based on complexity
Altered walls	0.05	0.6	$2.2 \cdot 10^{-4}$	2,895	1x or 2x based on complexity
Fresh rock	1	0.3	$7.3 \cdot 10^{-5}$	2,839	1x or 2x based on complexity

- Adjustments to the assumed source term masses for Mn and Ba by a scaling factor of 10^{-14} to reflect the actual injection into the model.
- Adjustments to the assumed pathway perimeter available for diffusion to immobile zones.

Each of these changes provided some improvement to the understanding of the BS2B experimental results. However, the reduction of the area (pathway perimeter) available for matrix diffusion provided the most dramatic improvement.

The area available for diffusion in the JNC/Golder blind prediction simulations and in the BS2B evaluation modeling was assumed to be the full pipe perimeter used in the flow solution. This area was made available for all of the immobile zones, such that the total area available for diffusion was equal to the pipe perimeter multiplied by the number of immobile zones. This dramatic reduction of the area available for diffusion is more consistent with the pattern of flow seen in the TRUE-1 Continuation Fault Zones Characterisation epoxy resin injection tests /Hakami and Wang in prep/, in which epoxy resin within fracture planes is shown to be strongly channelised.

For the sensitivity study, the area available for diffusion for each immobile zone was reduced by assuming that a total of 10% of the fracture surface area was available for diffusion, and this area itself was divided among the various immobile zones (i.e. of the 10% perimeter of each pipe, the perimeter available to each immobile zone is an additional fraction, 1/5th for each immobile zone in a Type I structure and 1/3rd for each Type II structure).

Simulation results for this assumption are presented in Table 4-7 and exemplified in Figure 4-1 and Figure 4-2. The match to observed breakthrough is dramatically improved in these simulations, particularly for the more strongly sorbing tracers. This improvement is evident for both the Structure 19 (Flow path I) and Structure BG1 (Flow path II) pathways. These results indicate that the use of channelised pathways at 10% of the fracture surface (or less) is more consistent with tracer transport observations from the BS2B experiment then an assumption of complete channelisation (i.e. access to the full fracture volume).

Table 4-7. Breakthrough time statistics for 10% FWS area transport simulations.

Tracer Breakthrough Times for Flow Path II (BG1-19)

BS2B Experimental Results				
	t5 hours	t50 hours	t95 hours	% Recovery
HTO	183	790	n/r	68%
155Eu	155	500	n/r	92%
22Na	300	1490	n/r	72%
133Ba	3250	n/r	n/r	8%
54Mn	n/r	n/r	n/r	1%

10% of Immobile Zone FWS Area				
	t5 hours	t50 hours	t95 hours	% Recovery
HTO	165	313	613	100%
155Eu	162	315	659	100%
22Na	697	1275	2456	100%
133Ba	n/r	n/r	n/r	< 1%
54Mn	n/r	n/r	n/r	< 1%

Total Time	hrs
HTO	4409
AllOthers	4577

Good Match to Measured Data
O.K. Match to Measured Data
Poor Match to Measured Data

Tracer Breakthrough Times for Flow Path I (19)

BS2B Experimental Results				
	t5 hours	t50 hours	t95 hours	% Recovery
131I-	14	62	n/r	80%
160Tb	14	63	4075	87%
85Sr	19	107	4327	86%
86Rb	51	490	n/r	56%
137Cs	555	n/r	n/r	28%

10% of Immobile Zone FWS Area				
	t5 hours	t50 hours	t95 hours	% Recovery
131I-	12.25	51	606	100%
160Tb	11	40	585	100%
85Sr	9.7	42	231	100%
86Rb	66.5	645	n/r	67%
137Cs	457	1090	n/r	81%

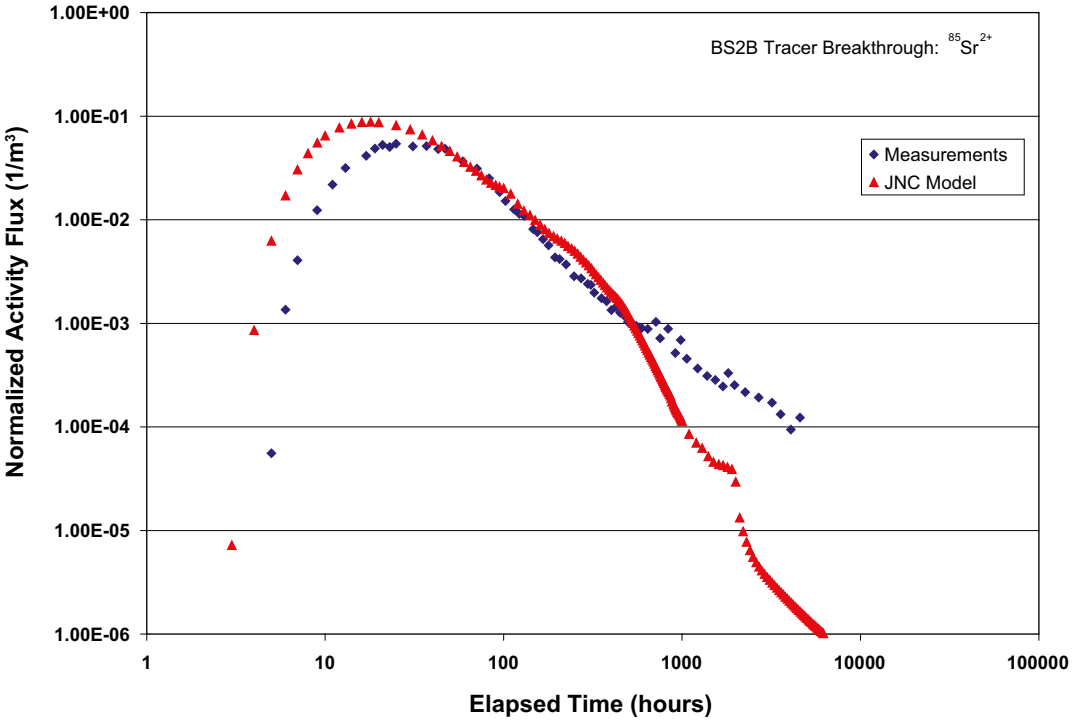

Figure 4-1. *Breakthrough curve for ^{85}Sr, Flow path I (Structure #19), Injection in KI0025F02_R3, 10% FWS.*

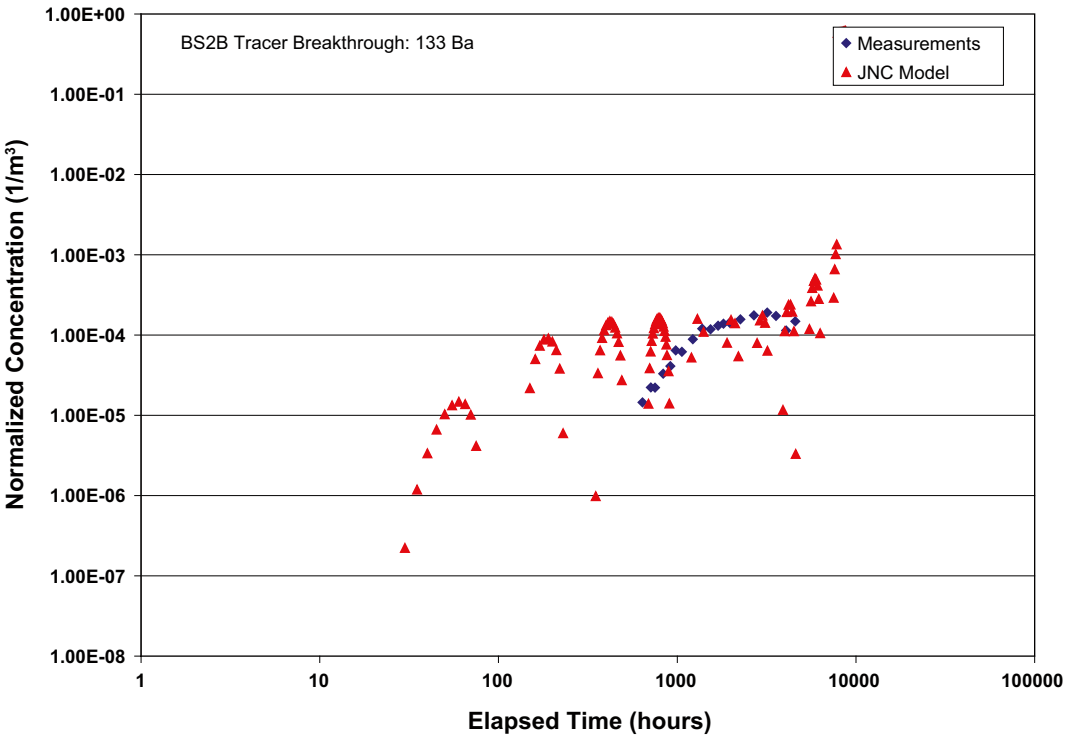

Figure 4-2. *Breakthrough curve for $^{133}Ba^{+}$, Flow path II (BG1), Injection in KI0025F02_R2, 10% FWS.*

4.3.5 Observations based on JNC/Golder Modelling

The following recommendations can be made based on the comparison of predictive simulations to BS2B experimental results, and based on the reconciliation modelling.

1. The stochastic background fracture modeling for the Structure BG1 pathways (Flow path II) clearly illustrated the large range of path lengths and fracture properties that can be encountered on transport pathways that have not been geometrically constrained by extensive site characterization.
2. The variability of Structure BG1 pathway transport simulation results from the Monte Carlo simulation probably correspond to the range of results that could have been found in the tracer experiments on that same pathway. Any conclusions based on these experimental results need to be tempered by the probability that different results (within the range defined by the Monte Carlo simulations) are equally likely to the result observed.
3. Model implementation issues can have a dramatic influence on tracer transport modelling, even within the same assumed hydrostructural and microstructural model. In the predictive and reconciliation modelling, the assumption of parallel diffusion to all immobile zones was particularly important.
4. Further experiments on background fracture pathways are necessary to provide a statistical basis for conclusions.

4.4 Posiva-VTT

4.4.1 Concept and processes included

Both prediction and evaluation models are based on a very simple flow model applied for steady state flow conditions. It is assumed that the distribution of the flow through the main flow channels can be deduced from the results of the tracer dilution tests made prior to the BS2B experiment, but at the BS2B injection locations in Structure #19 and BG1, respectively. The prediction model takes into account only the average flow rate used for the whole transport path (bulk flow). The evaluation model complements this by considering variable flow along the flow paths.

The characteristic of the flow field that is of interest in this modelling is the hydrodynamic control of retention (β). In the present approach β along the flow path is estimated by using entity the $W \cdot L/Q = \beta/2$ (where W is the width, L is the length and Q is the flow rate in the transport channel). Lengths of the transport paths are based on the projected path lengths along Structure #19 and BG1, which is extended to intersect Structure #19. The average Q/W along the transport paths are estimated from the measured flow rates at the injection locations. The Q/W at the injection locations are based on the CPT-3C tracer dilution measurements and they are calibrated using non-sorbing CPT-4C tracer test results. Both of these tests were made under the same pumping conditions as the sorbing BS2B tracer experiment. The BS2B experiment has been carried out as a weak dipole, but it has been deduced that in this case the representative flow conditions (Q/W) along a flow path is mainly determined by the background flow field (that is caused by the pumping at the BS2B extraction borehole and drainage to the tunnels) not by the injection flow rate.

The transport model takes into account advection along the fractures, matrix diffusion and sorption in the immobile pore space. Surface sorption on the fracture walls has not been modelled, but instead, diffusion into the pore space of the fracture coating and sorption inside the pore space of the coating is modelled.

4.4.2 Calibration process

The prediction model was calibrated against the results of the pre-test CPT-4c, which was carried out by employing only non-sorbing tracers. The approach was to try to keep the microstructural model unchanged, i.e. according to the definition of the micro-structural model of the Type 1 and Type 2 fractures. The prediction model is mainly calibrated by fine-tuning the hydrodynamic control of retention of the flow paths (WL/Q). The order of magnitude of the β was set by the dilution flow rate measurements (cf Section 4.4.1) to be about 56,000 h/m for Flow path I and about 167,000 h/m for Flow path II. Calibration using the CPT-4c data resulted in β-values that were 28,000 h/m for Flow path I and 194,000 h/m for Flow path II.

During the calibration it became evident that it was not possible to reproduce the CPT-4c results by keeping both the selected flow field and the given microstructural model. It was decided to retain the order of the magnitude of the flow rates (as measured in the dilution tests) and to change the micro structural model.

Different ways to modify the micro-structural model were investigated. The only way to improve the performance of the model using the given flow field and flow paths was to increase the thickness of the fault gouge in the Type 1 features (Structure #19). This was especially important for the Flow path II, which has a larger β. The main reason that led to the decision to increase the thickness of the fault gouge was that the limited thickness of the fault gouge in the microstructural model did not reproduce the observed tailings of the breakthrough curves. Based on the modelling of the CPT-4c test the predictions of the sorbing BS2B experiment were calculated using a modified microstructural in which the thickness of the fault gouge was increased from 0.3 cm to 3 cm. The calibration also showed that Type 2 fractures along the Flow path II did not have a significant influence on the retention. Therefore, the predictions were calculated using only the contribution of the Type 1 fractures of the Flow path II retention.

The advective delays along the flow paths were also calibrated using the CPT-4c pre-test. The calibration indicated an advective delay of c 6 hours along Flow path I and 120 hours along Flow path II. Estimated advective delays were applied in the predictions of the sorbing BS2B experiment, although the pumping rate was slightly lower in the BS2B experiment than that employed in the CPT-4c test (about 2.5 l/min instead of the 2.8 l/min used in CPT-4c). However, the hydrodynamicl control of the retention (WL/Q or β) was scaled by the change in the pumping rate before the calibrated CPT-4c model was applied in the predictions of the sorbing BS2B experiment.

4.4.3 Prediction

Parameterisation of the predictive modelling is presented in Table 4-8 through Table 4-11. The characterisation of the flow field is quite straightforward, because the underlying flow model is very simple. The flow field is described only by the hydrodynamic control of retention and advective delay.

Description of the immobile zones transport properties applied in the predictions was based on the microstructural model and the data is mainly taken from Appendix B. This dataset does not completely describe the sorption properties of all applied tracers and for all geological materials of the microstructural model. Complementary data were taken from the definition of the Äspö Task Force Task 6C model /Dershowitz et al. 2003/ and, in the case of Mn-54, K_d-values of the fault gouge, cataclasite and altered zone for the Type 1 fractures were estimated from the K_d-values of the Ba-133 using the same ratio between the Mn-54 and Ba-133 K_d-values as the data presented in Appendix B, show for the fracture coating. Similarly, the K_d-value of the Mn-54 for the intact wall rock was estimated from the K_d of the Ba-133 in the intact wall rock using the ratio between the Mn-54 and Ba-133 K_d-values of the altered zone in Type 2 fractures. Applied sorption properties are provided in Table 4-9 and diffusion properties of the tracers are given in Table 4-10.

Physical parameters describing the immobile zones follow the microstructural model. Parameters applied in the predictive modelling are presented in Table 4-11.

Table 4-8. Parameterisation of the flow used in the predictions.

Parameter	Flow path I	Flow path II
Advective delay [h]	6	120
β [h/m]	28,000	194,000

Table 4-9. Sorption properties applied in the predictive modelling. Data are taken from Appendix B, if not otherwise indicated.

	Fracture coating (d_{coat})	Fault gouge (d_{goug}, concept A)	Cataclasite/Mylonite (d_{cata}, 20%)	Altered zone (d_{alt}, #19)	Altered zone (d_{alt}, BG1)	Intact wall rock (d_{rock})
I-131	0	0	0	0	0	0
Tb-160	0	0	0	0	0	0
Sr-85	2.30E–04 [1)]	6.00E–04	1.40E–04	2.60E–05	2.60E–05	4.40E–05 [1)]
Rb-86	5.20E–03 [1)]	2.70E–03	4.00E–03	4.00E–04	4.00E–04	1.00E–03 [1)]
Cs-137	5.20E–02 [1)]	4.00E–02	3.00E–02	5.00E–04	5.00E–04	1.00E–03 [1)]
HTO	0	0	0	0	0	0
Eu-155	0	0	0	0	0	0
Na-22	2.00E–04	1.10E–04 [1)]	1.10E–05 [1)]	1.40E–05 [1)]	1.70E–06	7.10E–06 [1)]
Ba-133	2.72E–02	1.40E–02 [1)]	1.30E–03 [1)]	1.80E–03 [1)]	6.90E–04	8.80E–04 [1)]
Mn-54	1.70E–01	8.75E–02 [2)]	8.13E–03 [2)]	1.13E–02 [2)]	4.30E–03	5.48E–03 [2)]

[1)] Äspö Task Force Task 6C specification /Dershowitz et al. 2003/.
[2)] Calculated based on Ba-133, i.e. the ratio between K_d's of Mn-54 and Ba-133 is same as for fracture coating.

Table 4-10. Diffusivities of the tracers in free water, D_w [m²/s]. Data are taken from Appendix B.

	Fracture coating (d_{coat})	Fault gouge (d_{goug}, concept A)	Cataclasite/Mylonite (d_{cata}, 20%)	Altered zone (d_{alt}, #19)	Altered zone (d_{alt}, BG1)	Intact wall rock (d_{rock})
I-131	2.00E–09	2.00E–09	2.00E–09	2.00E–09	2.00E–09	2.00E–09
Tb-160	5.00E–10	5.00E–10	5.00E–10	5.00E–10	5.00E–10	5.00E–10
Sr-85	7.94E–10	7.94E–10	7.94E–10	7.94E–10	7.94E–10	7.94E–10
Rb-86	2.06E–09	2.06E–09	2.06E–09	2.06E–09	2.06E–09	2.06E–09
Cs-137	2.06E–09	2.06E–09	2.06E–09	2.06E–09	2.06E–09	2.06E–09
HTO	2.13E–09	2.13E–09	2.13E–09	2.13E–09	2.13E–09	2.13E–09
Eu-155	5.00E–10	5.00E–10	5.00E–10	5.00E–10	5.00E–10	5.00E–10
Na-22	1.33E–09	1.33E–09	1.33E–09	1.33E–09	1.33E–09	1.33E–09
Ba-133	8.48E–10	8.48E–10	8.48E–10	8.48E–10	8.48E–10	8.48E–10
Mn-54	6.88E–10	6.88E–10	6.88E–10	6.88E–10	6.88E–10	6.88E–10

Table 4-11. Parameterisation of the immobile pore spaces as given in the micro-structural model, cf Appendix A.

Type 1 (fault) Rock type	Extent [cm]	Porosity [%]	Formation factor [–]
Intact wall rock	–	0.3	7.3E–5
Altered zone	15	0.6	2.2E–4
Cataclasite dcat	1	1	4.9E–4
Fault gouge dg	0.3	20	5.6E–2
Fracture coating dc	0.05	5	6.2E–3
Type 2 (non-fault) Rock type	**Extent [cm]**	**Porosity [%]**	**Formation factor [–]**
Intact wall rock	–	0.3	7.3E–5
Altered zone	5	0.6	2.2E–4
Fracture coating	0.05	5	6.2E–3

The predictions show reasonable fits to the measured breakthrough curves especially for the non-sorbing tracers and in particular for Flow path I. The prediction model is not able to reproduce the early parts of the breakthrough curves, mainly because of the bulk flow model of the advection. For sorbing tracers the predictions show too much retention, so that the discrepancy between the predicted and measured breakthrough curves is largest for the most sorbing tracers. Predictions for Flow path II show incorrect tailings of the breakthrough curves especially for the HTO and Na-22. Predicted breakthrough curves show sharply descending tails indicating saturation of the fault gouge. Measured breakthrough curves show steady power-law tailing. It may also be noted, that in the prediction model the factor of four higher diffusivity of the HTO compared to Eu-155 leads to quite different breakthrough curves. In the case of Eu-155 the fault gouge is only partially saturated while it is almost completely saturated for the HTO. In the measured breakthrough curves this kind of difference between HTO and Eu-155 breakthrough curves is not observed.

The predicted breakthrough curves are presented in Section 4.6.

4.4.4 Evaluation of retention properties

The Posiva-VTT evaluation does not aim at calibration of the properties of the individual tracers to get the best possible fit between the modelled and measured breakthrough curves. Rather, the approach is to critically bring forward the problems and possible contradictions of the possible different explanations. Instead of considering individual tracers, all tracers are studied in parallel to obtain indications of the dynamics of the system.

The evaluation concentrates on the same retention processes that were modelled in the predictive modelling, i.e. sorption and matrix diffusion. All chemical interactions are modelled by linear equilibrium-sorption. As in the predictive modelling, the immobile zones are described by the microstructural model of the pore space that is composed of fracture coating, fault gouge, cataclasite, altered wall rock and intact wall rock.

The same transport model as in the predictive modelling has also been applied in the evaluation. However, the evaluation model has variable flow whereas the predictive modelling was based on the bulk flow.

Three cases have been modelled including both variation of the flow field (in terms of the transport aperture) and of the microstructural model. The following variations were modelled: i) all immobile layers included as given in the definition of the micro-structural model, ii) all immobile layers as in the first case but using changed properties for fault gouge, and iii) only altered zone and intact rock of the microstructural model taken into account.

In all modelling cases the advection is characterised by the same (truncated) Gaussian water residence time distribution. The distribution of the hydrodynamic control of retention (β) is derived from the water residence time distribution dividing the water residence time distribution by the effective transport aperture. For the first two evaluation cases the effective transport aperture is estimated based on the dilution flow measurements (CPT-3) and estimated lengths of the flow paths (the mean of the β-distribution is required to match the estimate based on the flow measurement). The last evaluation case required an increase of the average hydrodynamic control of retention by a factor of 15–40 in order to reproduce the observed retention.

The evaluation indicated that it is possible to explain the measured breakthrough curves by matrix diffusion and sorption. However, the measured breakthrough curves for the both flow paths are typical for the unlimited matrix diffusion. For Flow path II this could mean that the retention is governed by the Type 2 fractures, because the fault gouge in the Type I fractures gets easily saturated (causing deviation in the breakthrough curve from the behaviour of unlimited matrix diffusion). This is exemplified by the third evaluation case that takes into account only altered rock and intact rock as immobile zones. The only problem seems to be that the average hydrodynamic control of retention needs to be over an order of magnitude higher than what the flow measurements indicate. However, it is possible that the estimates of the flow rates applied in the evaluation modelling are too high and that the flow rates at the injection locations of the CPT-3 dilution experiment are much smaller than the measured flow rates /Andersson et al. 2005/. In case of Flow path II, this supports the third evaluation case, which addresses the retention to altered rock. Flow path II includes Type 2 background fractures and this suggests that majority of the retention takes place in them. Based on the poor performance of the tailings of the breakthrough curves in the first evaluation case for Flow path I and, on the other hand, the good performance of the unlimited matrix diffusion model for the Flow path I, it seems that the microstructural model may require updating. The first evaluation case addresses the microstructural model using average flow conditions taken from the CPT-3 dilution experiment. The resulting tailings of the modelled breakthrough curves show saturation of the major retention zones that has not been observed in the experimental results.

4.5 KTH-WRE

4.5.1 Concept and processes

Flow and transport take place in two flow paths in BS2B test. Flow path I is in a single Type 1 (fault) structure (Structure #19) with a Euclidean length of approximately 20 m. Flow path II starts from the background fracture BG1 and ends in Structure #19 with a comparable Euclidean distance.

We assume advection only in fractures, while local dispersion is neglected. We account for hydrodynamic dispersion caused by velocity variation between trajectories. The hydrodynamic dispersion is characterised by the joint distribution of β and τ, g(β,τ). We further account for retention processes in rock matrix, including sorption on fracture surface characterized by K_a, diffusion/sorption in rock matrix characterized by parameter κ. The parameter κ defined as $\kappa = \theta\sqrt{D(1+\frac{K_d\rho}{\theta})}$ is governed by the porosity θ, diffusivity D and the sorption coefficient K_d.

The sorption into the fault gouge material is not explicitly accounted for, but viewed as being part of the equilibrium surface sorption.

The Lagrangian Stochastic Advection Reaction (LaSAR) framework /Cvetkovic et al. 1999/ is applied for the predictions and evaluations of BS2B tests.

The relation between β and τ is assumed to be deterministic and linear, i.e. $\beta = k\tau$. Thus the entire distribution of β is replaced by the distribution of τ and the parameter k. The parameter k is referred as the flow-wetted surface per unit volume of water /Andersson et al. 1998/.

The travel time distribution $g(\tau)$ was determined by deconvoluting the breakthrough curves (BTC) of the conservative tracer, while accounting for the diffusion into the rock matrix. The actual form of $g(\tau)$ is assumed to be inverse-Gaussian /Cvetkovic and Cheng 2002/. Using $g(\tau)$, the BTCs of sorbing tracers are modelled by accounting for the retention processes. The parameter groups $\psi = k\kappa$ and $\xi = kK_a$ are calibrated using the measured BTCs of sorbing tracers until a best fit is obtained for each tracer. The two procedures are iterative until satisfactory fittings are obtained consistently for all tracers injected in the same flow path.

A comprehensive description of the theory, prediction and evaluation procedures is given in /Cvetkovic et al. 2000, Cvetkovic and Cheng 2002, Cheng and Cvetkovic 2005/.

4.5.2 Calibration and evaluation strategies

The predictions of the BTCs for the BS2B tests have been conducted by calibrating the measured BTCs of the preparatory conservative tracer tests performed in the same flow paths, CPT-4c (Flow path I) and CPT-4b (Flow path II) /Andersson et al. 2004b/.

In the predictions, the water residence time distribution $g(\tau)$ was determined by deconvoluting the BTC of Uranine from the CPT-4c test for Flow path I and the BTC of Amino G acid from the CPT-4b test for Flow path II. The first two moments of the water residence time and the parameter $\psi = k\kappa$ are calibrated for each flow path /Cheng and Cvetkovic 2005/. We then estimated k and κ based on the obtained ψ, and further estimated the porosity θ, by assuming Archie's law $F = 0.71\theta^{1.58}$ from the obtained κ /Cheng and Cvetkovic 2005/. We assumed that the estimated θ value is applicable for all tracers in the same flow path. Note that the calibrations of the blind predictions could be only made on BTCs of conservative tracers used in the pre-tests.

The evaluations of the BTCs of BS2B tests were conducted by calibrating on the measured BTCs. We determined $g(\tau)$ by deconvoluting the BTC for conservative tracer in the same flow path, i.e. the BTC of I-131 for Flow path I and the BTC of HTO for Flow path II. The actual form of $g(\tau)$ was assumed to be the same as for the predictions with an inverse-Gaussian distribution. The first two moments of the water residence time distribution are calibrated for each flow path. We then calibrated the two parameter groups $\zeta = kK_a$ and $\psi = k\kappa$ on the measured BTC data for sorbing tracers using the deconvoluted first two moments of $g(\tau)$ from the conservative tracer along the same flow path. Note that the calibrations were made on the BTCs of all tracers from the BS2B tests in the evaluations. The aim of the calibrations was not just to fit the measured curves, but rather find the consistent explanations for all tracers in the same flow path and possible reasons of the difference between two flow paths.

4.5.3 Prediction

The prediction results generally matched the measured BTCs well for the first flow path, but overestimated the retention for Rb-86 (Figure 4-3 and Figure 4-4). For the second flow path, the retention for all tracers has been underestimated (Figure 4-5 and Figure 4-6). The parameters used in the predictions are summarised in Table 4-12 through Table 4-16 (as predicted). The temporal moments obtained by calibrating on the CPT-4c and CPT-4b tests are presented in Table 4-12. The parameter k is also presented in Table 4-12.

Due to the short residence time scale in Flow path I, we expect that the retention occur mainly in the rim zone immediately adjacent to the open fracture. For the task of predicting sorbing tracer BTCs in Flow path I, we assume that the rim zone would be representative for estimating the retention parameters, thus effective K_a and K_d values should be based only on rim zone of Structure #19 for Flow path I. We therefore assumed that the effective K_d and K_a values obtained from the fracture rim zone (the upper limits data provided in Appendix B applicable for the

prediction of the BTCs for Flow path I (Table 4-14 and Table 4-15). Flow path II has nearly the same Euclidean distance as for Flow path I. However, the mean travel time for Flow path II is much longer than that for Flow path I, indicating a possible stronger overall retention from the background fracture BG1. The BG1 (and possible additional background fractures making up the flow path) thus appears to be responsible for most of the overall retention for Flow path II. For the purpose of the blind prediction of the BTCs in Flow path II, we therefore assumed that effective K_d and K_a values obtained from the BG1, cf Appendix B, are applicable for the prediction of the BTCs for Flow path II (Table 4-14 and Table 4-16). The actual procedure of determining K_d and K_a values is presented in /Cheng and Cvetkovic 2005/.

4.5.4 Evaluation of retention properties

The evaluations were performed by assuming effective (uniform) retention parameters and also by accounting for depth-wise heterogeneity of retention parameters. Since the mass recovery of Mn-54 was only about 1%, the evaluation of Mn-54 is not pursued further in our analysis.

In the first step, we assume effective (constant) retention parameters; the evaluations were conducted by calibrating on the measured BTC data of all tracers in the same flow path. An effective (uniform) porosity was assumed applicable for all tracers (whether conservative or sorbing). The slope k was kept the same as for the prediction, i.e. k = 13,000 m^{-1} for Flow path I and k = 17,000 m^{-1} for Flow path II, consistent with the effective apertures. The evaluations were performed by iterative procedures described in Section 4.5.2 until consistent results were obtained for all tracers along the same flow path. The effective retention parameters obtained in the evaluations are summarised in Table 4-12 through Table 4-16 (denoted as "Fitted"). The evaluation results indicate that the underestimation or overestimation of the retention in the predictions are probably due to underestimation or overestimation of the sorption processes in the rock matrix, as represented by K_d.

The estimation of the retention parameters were also made by accounting for the in-depth heterogeneity of the retention parameters following the definition of two structure types from Task 6C /Dershowitz et al. 2003/. The two geological structure types (1 and 2) are quantified in terms of the thickness and retention parameters (porosity, K_d) of each geologically defined retention zone /Dershowitz et al. 2003/. For the purpose of the current project, the Type 1 and Type 2 structures are being defined in consistency with those of the Task 6C model /Dershowitz et al. 2003/, although with some slight modifications of the thickness of the retention zones and distribution of the retention zones, cf Appendix A and /Cheng and Cvetkovic 2005/.

The in-depth heterogeneity was accounted for in terms of the performed penetration analysis. By calculating the penetration depth into the rock matrix by way of diffusion for the individual tracers we could obtain the effective retention parameters /Cheng and Cvetkovic 2005/. The retention parameters thus obtained are presented as "Estimated" parameters in Table 4-13 to Table 4-15.

The retention parameters from the predictions, evaluations through the calibration procedure (Fitted) and by the penetration analysis (Estimated) are compared in Table 4-12 through Table 4-16. The K_d values differ by a factor of 3 to 12, while the values of the parameter group κ are relatively close to each other, within a factor of 2. The parameter group κ which summarise the retention properties of the different rock materials can be inferred reasonably well from the microstructure data, i.e. independently of the tracer test results.

The K_a values were kept the same as used for the predictions (from Appendix B), for all tracers except for the weakly sorbing tracers Na-22 in Flow path II since good predictions were obtained. The predicted BTC of Na-22 underestimated the measured BTC. This is probably due to an underestimation of both K_a and K_d for Na-22.

Table 4-12. Summary of SKB KTH/WRE temporal moments from prediction and evaluation.

Path	< τ > (hour)		σ_T^2 (hour^2)		K (m^{-1})	
	Pred.	Fitted	Pred.	Fitted	Pred.	Fitted
I	14	12	160	200	13,000	13,000
II	200	270	15,000	25,000	17,000	17,000

Table 4-13. Comparison of the κ parameters evaluated by the SKB KTH/WRE team.

Tracer	Predicted κ [m h$^{-1/2}$]	Fitted κ [m h$^{-1/2}$]	Estimated κ [m h$^{-1/2}$]
Na-22	2.3E–6	6.0E–6	2.6E–6
Sr-85	3.1E–5	5E–5	6.8E–5
Ba-133	2.7E–5	4.7E–5	3.3E–5
Rb-86	2.2E–4	1.5E–4	4.8E–4
Cs-137	5.3E–4	1.1E–3	5.5E–4

Table 4-14. Comparison of SKB KTH/WRE predicted, evaluated and estimated K_d.

Tracer	Sr-85 TRUE BS2B (Path I)	Na-22 TRUE BS2B (Path II)	Ba-133 TRUE BS2B (Path II)	Rb-86 TRUE BS2B (Path I)	Cs-137 TRUE BS2B (Path I)	Mn-54 TRUE BS2B (Path II)
Predicted K_d (m^3/kg)	4.9E–5	1.7E–6	6.9E–4	1.1E–3	6.4E–3	4.3E–3
Evaluated K_d (m^3/kg)	1.4E–4	2.1E–5	2.1E–3	5E–4	2.6E–2	–
Estimated K_d (m^3/kg)	1.5E–4	1.7E–6	6.9E–4	3.7E–3	1.2E–2	–

Table 4-15. Comparison of SKB KTH/WRE predicted, fitted and estimated porosity θ.

Tracer	Flow path Porosity θ(%)		
	Pred.	Fitted	Estimated
I-131 (Path I)	2.56	2.6	2.1
HTO (Path II)	0.43	0.42	0.51
Na-22 (Path II)	0.43	0.42	0.47
Sr-85 (Path I)	2.56	2.6	3.6
Ba-133 (Path II)	0.43	0.42	0.55
Rb-86 (Path I)	2.56	2.6	3.2
Cs-137 (Path I)	2.56	2.6	1.8

Table 4-16. Comparison of SKB KTH/WRE predicted and evaluated K_a.

Tracer	Sr-85 TRUE BS2B (Path I)	Na-22 TRUE BS2B (Path II)	Ba-133 TRUE BS2B (Path II)	Rb-86 TRUE BS2B (Path I)	Cs-137 TRUE BS2B (Path I)	Mn-54 TRUE BS2B (Path II)
Predicted K_a (m)	1.64E–5	7.0E–7	2.9E–4	2.4E–4	2.8E–3	1.8E–3
Evaluated K_a (m)	1.64E–5	3.1E–5	2.9E–4	2.4E–4	2.8E–3	–

For Flow path II, the estimated porosity is much smaller (0.43%) and the mean travel time is much longer (270 h) compared to those estimated for Flow path I (2.6% and 12 h) from the evaluations. This may reveal the difference between faults (Structure #19) and joints (BG1). We inferred the parameter κ as shown in Table 4-17 /Cheng and Cvetkovic 2005/ for Structure #19 and BG1. The background structure BG1 flow path appears to have lower retention properties compared with Structure #19 as quantified by the effective parameter group κ. The difference for the parameter group κ is a factor of 2–9.

The tracers Na, Sr and Ba have K_d values (inferred) close to those obtained in the previous TRUE tests, i.e. within a factor of about 2. The tracers Rb and Cs have lower K_d values (inferred) compared to those obtained in the previous TRUE tests, the difference being within a factor of 5–10.

4.6 Predictive modelling

The modelling groups were asked to provide predictions of the outcome of the BS2B reactive tracer tests, given the results of conservative tracer tests along the same flow paths (Pre-tests CPT-4a through CPT-4c) and preceding interference and tracer dilution tests (CPT-1 through CPT-3), cf Chapter 3. All modelling groups involved (ANDRA-Itasca, JNC-Golder, Posiva-VTT and SKB-KTH/WRE) had prior experience in modelling solute transport related to Äspö conditions, either through the preceding TRUE Block Scale experiments set in the same rock volume /Poteri et al. 2002/ or activities related to modelling work as part of the Äspö Task Force on modelling of groundwater flow and solute transport. The latter included modelling the site scale transport experiment LPT-2 /Gustafson and Ström 1995/ as part of Äspö Task Force Tasks 1–2 and modelling of detailed scale transport in an interpreted single fracture related to the TRUE-1 experiments /Winberg et al. 2000/. The latter as part of Äspö Task Force Task 4 /Elert 1999, Elert and Svensson 2001, Marschall and Elert 2003/. Additional tasks addressed within the Äspö Task Force include Task 5 (on coupling between hydrogeology and hydrogeochemistry) /Bath and Jackson 2003, Rhén and Smellie 2003/ and Task 6 and extrapolation of site scale models to PA time scales /Hodgkinson and Black 2005, Black and Hodgkinson 2005/.

Although a defined dataset, cf Appendices A and B, for model prediction was provided prior to the BS2B predictions the modelling groups were free to use their own experience and judgement is selection/assignment of the parameters that would go into their respective model predictions. Furthermore, based on the kinship between the investigated TRUE-1 Feature A, experience gained from evaluation of in situ retention parameters from TRUE-1 was used for the prediction of the TRUE Block Scale BS2B experiment wit sorbing tracers.

By comparing the conceptual positions taken by the groups, cf Chapter 4 and Appendices C1 through C4, and input data used in the predictions with the corresponding evaluated (calibrated) parameter groups and parameters presented in Chapter 5, a representation is provided of the evolution of understanding of transport/retention during the project.

Table 4-17. Inferred κ [m $h^{-1/2}$] for Structure #19 and BG1 [for κ (#19) = 13,000 1/m and κ (BG1) = 17,000 1/m].

Tracer	Structure #19 (Path I) κ [m $h^{-1/2}$]	Path II κ [m $h^{-1/2}$]	Structure BG1	Ratio of κ
Na-22	3.9E–5	**6E–6**	4.9E–6	8
Sr-85	**5E–5**	8.4E–6	7.0E–6	7
Ba-133	3.3E–4	**4.7E–5**	3.7E–5	9
Rb-86	**1.5E–4**	1.0E–4	9.9E–5	2
Cs-137	**1.1E–3**	4.0E–4	3.8E–4	3

In the following sections a brief overview of the different tracer test phases which form the basis for the predictions and the results of the model predictions of the BS2B test are presented and discussed.

4.6.1 Overview of performed characterisation and tracer tests

The TRUE Block Scale Continuation BS2B experiment with sorbing tracers was preceded by two site characterisation stages:

- Characterisation and experiments conducted as part of the TRUE Block Scale project, summarised by /Andersson et al. 2002ab/.
- Cross-hole interference and tracer dilution pre-tests CPT-1 through CPT-3 /Andersson et al. 2004b/, see also Chapter 3.
- Tracer pre-tests CPT-4a through CPT-4c using conservative tracers /Andersson et al. 2005/, see also Chapter 3.

The main objective of the CPT-1 to CPT-3 pre-tests was to obtain a basis for selecting a test geometry, sink and source sections, optimised for the BS2B radioactive sorbing tracer tests. The tests also aimed to improve the hydrostructural model of the TRUE Block Scale rock volume, in particular the area including Structure #19, which has not been subject to tracer tests in the past.

The objectives of the CPT-4a and CPT-4b tests, once the test geometry was established, was to assess tracer residence times for non-reactive tracers and to safeguard that the selected flow paths gave tracer mess recoveries > 80%. The CPT.4c test was performed with the main objective of assessing the mass recovery of the selected flow paths for the BS2B test under slightly different boundary conditions compared with CPT-4a and CPT-4b.

4.6.2 Outcome of predictive modelling

The modelling groups were given access to the results of TRUE Block Scale experiment, relevant information on the microstructural model and its parameterisation (cf Appendices A and B), the BS2B pre-tests (cross-hole interference pre-tests, tracer dilution tests and results of relevant non-sorbing tracer tests performed in the flow paths at relevant pump rates). They were then asked to predict the reactive tracer breakthrough and associated mass recovery of the BS2B tests with sorbing tracers.

Table 4-18 and Table 4-19 present the arrival times for 5%, 50% and 95% of the tracer mass for the injections in Flow paths I and II, respectively, assuming that the calculations are driven to 100% recovery. This means that a comparison of predicted and measured mass recovery is futile. However, for completeness the measured mass recovery at the time of termination of the sampling is given.

The predicted and measured breakthrough and cumulative mass arrivals are plotted in Figure 4-3 through Figure 4-6.

An overview of the results for the non-reactive tracers for the two flow paths, Figure 4-3 and Figure 4-5, suggests that two of the modelling teams (Posiva-VTT and ANDRA-Itasca) introduce too much retention resulting in a shift of the breakthrough curves (BTC) compared with the experimental data for Flow path I (Figure 4-3). This pattern is consistent for Posiva-VTT also for Flow path II, but not so for ANDRA-Itasca. The predictions of other two teams are better behaved, at least for Flow path I, and in terms of time. An inconsistency is noted for the non-reactive JNC-Golder predictions in that the peak is well reproduced for Tb-160 but not so for I-131 in Flow path I. In the case of the SKB-KTH/WRE non-reactive predictions, those for Flow path I are slightly delayed, whereas those for Flow path II are slightly too early. The above

findings are a bit surprising given that the information used for calibration of non-reactive transport of the two flow paths included the CPT-4c tests which were run in the same configuration and at essentially the same pump rate, cf Chapter 3. Still, it is noted that the above differences (in terms of arrival time) are contained within a factor of 5, i.e. the differences are not that great.

When considering successively more sorbing tracers it is noted that increasing sorbtivity and geometrical complexity (Flow path II) adds more spread in the predictions. For the low to intermediate sorbing Strontium (Flow path I, cf Figure 4-3) the differences are comparable to the non-reactive tracers. In case of Na-22 (Flow path II, cf Figure 4-5) the spread is much larger, where both SKB-KTH/WRE and ANDRA-Itasca predict too early first arrival. Posiva-VTT consistently predicts delayed arrivals for these two tracers.

When evaluation the predictions of the intermediate to highly sorbing Rb-86 (Flow path I, cf Figure 4-4) the spread is larger amongst the modelling teams. However, the shape of the breakthrough is well reproduced by the SKB-KTH/WRE and JNC-Golder teams, although in both cases underpredicting the elongated "peak" of the BTC. In the case of the corresponding Ba-133 in Flow path II (Figure 4-6), the experimental BTC is flanked in time by the four predictions, peaks relatively well captured.

In the case of the highly sorbing tracers, the SKB-KTH/WRE prediction for Cs-137 captures well the overall breakthrough, both time-wise and in terms of the peak. The ANDRA prediction lack significant retention as already pointed out in Section 4.2.3. In this case also the JNC-Golder team overpredict the arrival time similar to Posiva-VTT.

Two types of differences may explain the range of responses obtained by the modelling groups. If one assumes that the differences between the conceptual models employed by the groups are negligible, the variations in modelled responses must be due to the use of widely varying input parameters (their magnitude and distribution). Unlike the predictions made for the TRUE Block Scale experiment /Poteri et al. 2002/, the current geometrical conceptual model include two distinctly different fracture types and also a mapping of variability in complexity /Dershowitz et al. 2003/. A discussion of the implications of the numerical implementation of the microstructural models is provided in Section 5.3.2. It is noted that the ANDRA-Itasca team acknowledges introducing too small amounts of fault gouge along their simulated flow paths. Similarly the JNC-Golder team introduced too high "complexity" along their flow paths, resulting in to high β, and hence to high retention at least for the highly sorbing tracers. The Posiva-VTT team overemphasised the importance of fault gouge, resulting in delayed tracer breakthroughs. Mapping of the "effective" material retention group κ, cf Section 5.3.1, is not trivial because it involves the effects of the conceptualisation (including description of flow employed by the modelling teams, cf Section 5.3.3) and the retention properties (κ) in union. An example of back-calculated effective κ from the evaluation of the BS2B test is given in Figure 5-15 allowing comparison with the pure retention property κ's evaluated by the different modelling teams.

In summary, a full comparison of the prediction results of the modelling teams in relation to the input parameter data has to take into account the conceptualisation of the studied system (flow field and micro-structure/immobile zones, their distribution and parameterisation). To the extent models with similar input data produce equitable output, the underlying conceptualisation of the flow field and description of immobile pore space (number of immobile zones, geometry and parameter values) produce a net effect which is nearly the same. In Section 5.3.3, attempts are made to evaluate the relative effects of the flow field on the evaluated retention. In Section 6.3 the results of the predictive modelling are discussed in the light of the results presented in Section 5.3.

Table 4-18. Measured and predicted characteristic times and mass recoveries, Flow path I, injection in KI005F02:R3 with pumping in KI0025F03:R3. Times T_{xx} in hours, Recovery in % of total injected mass.

Tracer	Measured	Measured	SKB	JNC	Posiva	ANDRA
I-131	T_5	14	16	55	22	21
	T_{50}	62	56.2	555	66	44
	T_{95}	–	493.7	1,300	453	125
	Recovery	80 (296 h)	NA	NA	NA	NA
Tb-160-DTPA	T_5	14	14.9	15	17	21
	T_{50}	63	48.1	60	49	44
	T_{95}	–	441.2	330	461	125
	Recovery	87 (4,075 h)	NA	NA	NA	NA
Sr-85	T_5	19	18.9	30	32	22
	T_{50}	107	73.3	275	110	47
	T_{95}	–	1,140	1,400	3,562	130
	Recovery	86 (4,327 h)	NA	NA	NA	NA
Rb-86	T_5	51	101	235	161	36
	T_{50}	490	1,157	2,650	761	71
	T_{95}	–	53,600	7,650	13,874	273
	Rec	56 (594 h)	NA	NA	NA	NA
Cs-137	T_5	555	418	1,350	1,230	145
	T_{50}	–	6,030	4,250	9,030	290
	T_{95}	–	310,000	8,250	190,000	> 1,000
	Rec	28 (4,579 h)	NA	NA	NA	NA

Table 4-19. Measured and predicted characteristic times and recoveries for Flow path II, injection in KI0025F02:R2 and pumping in KI0025F03:R3. Times T_{xx} in hours, Recovery in % of total injected mass.

Tracer	Measured	Measured	SKB	JNC	Posiva	ANDRA
HTO	T_5	183	74	185	311	76
	T_{50}	790	227	450	750	150
	T_{95}	–	1,934	1,100	1,697	530
	Recovery	68 (4,409 h)	NA	NA	NA	NA
Eu-155-DTPA	T_5	155	68	220	209	73
	T_{50}	500	185	510	497	136
	T_{95}	–	708	1,300	2,634	336
	Recovery	92 (4,577 h)	NA	NA	NA	NA
Na-22	T_5	300	76	300	379	83
	T_{50}	1,490	242	675	1,244	173
	T_{95}	–	2,416	1,800	3,995	2,100
	Recovery	72 (4,577 h)	NA	NA	NA	NA
Ba-133	T_5	3,250	869	4,650	9,581	870
	T_{50}	–	7,463	7,400	56,000	2,150
	T_{95}	–	290,000	8,700	305,000	> 10,000
	Recovery	8 (4,577 h)	NA	NA	NA	NA
Mn-54	T_5	–	4,741	> 8,770	50,395	4,700
	T_{50}	–	42,630	> 8,770	296,000	> 10,000
	T_{95}	–	1.6E6	> 8,770	2.04E6	> 10,000
	Recovery	1 (4,577 h)	NA	NA	NA	NA

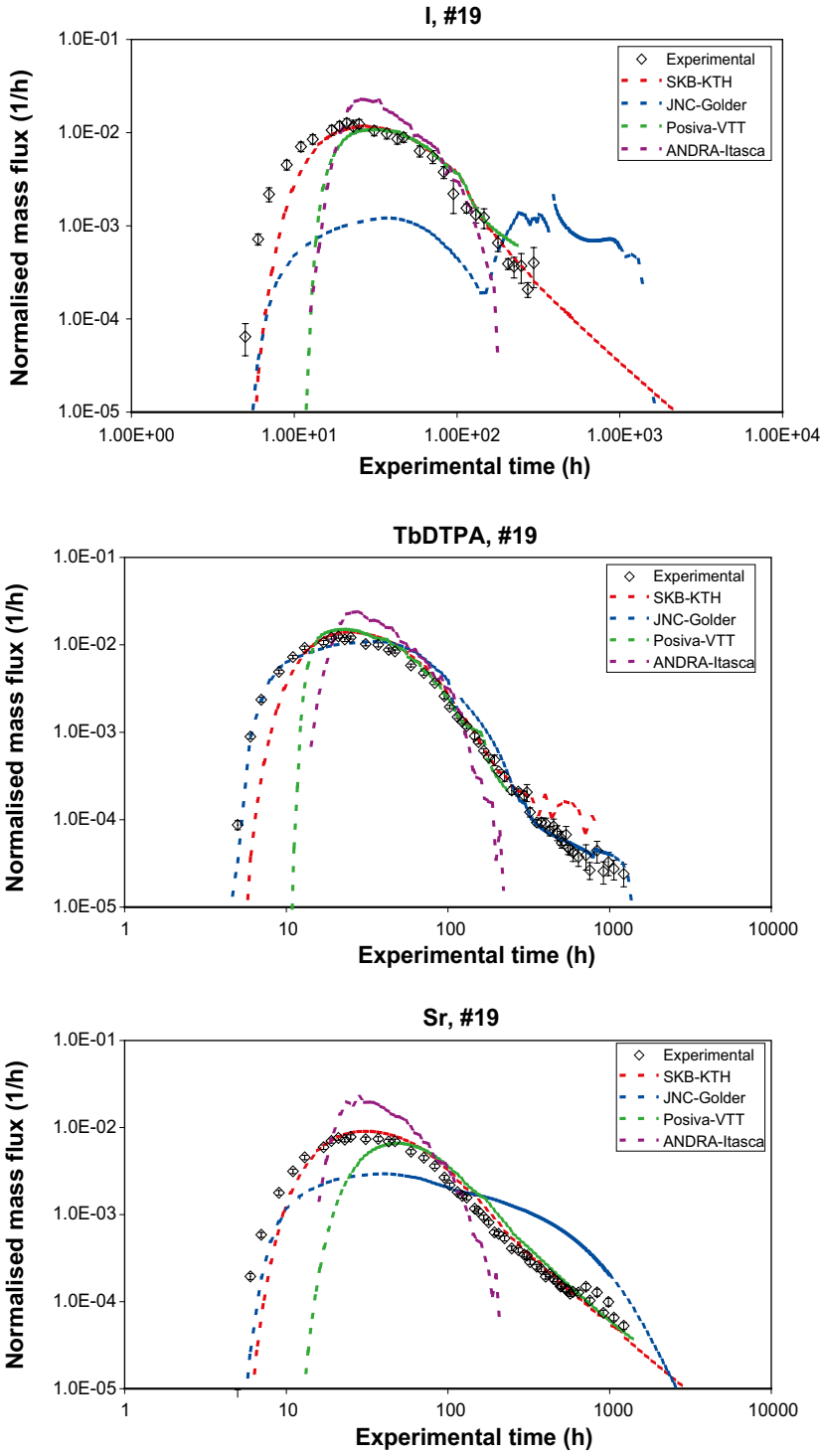

Figure 4-3. *Flow path I – Predicted and measured breakthrough of I-131, Tb-160-DTPA and Sr-85.*

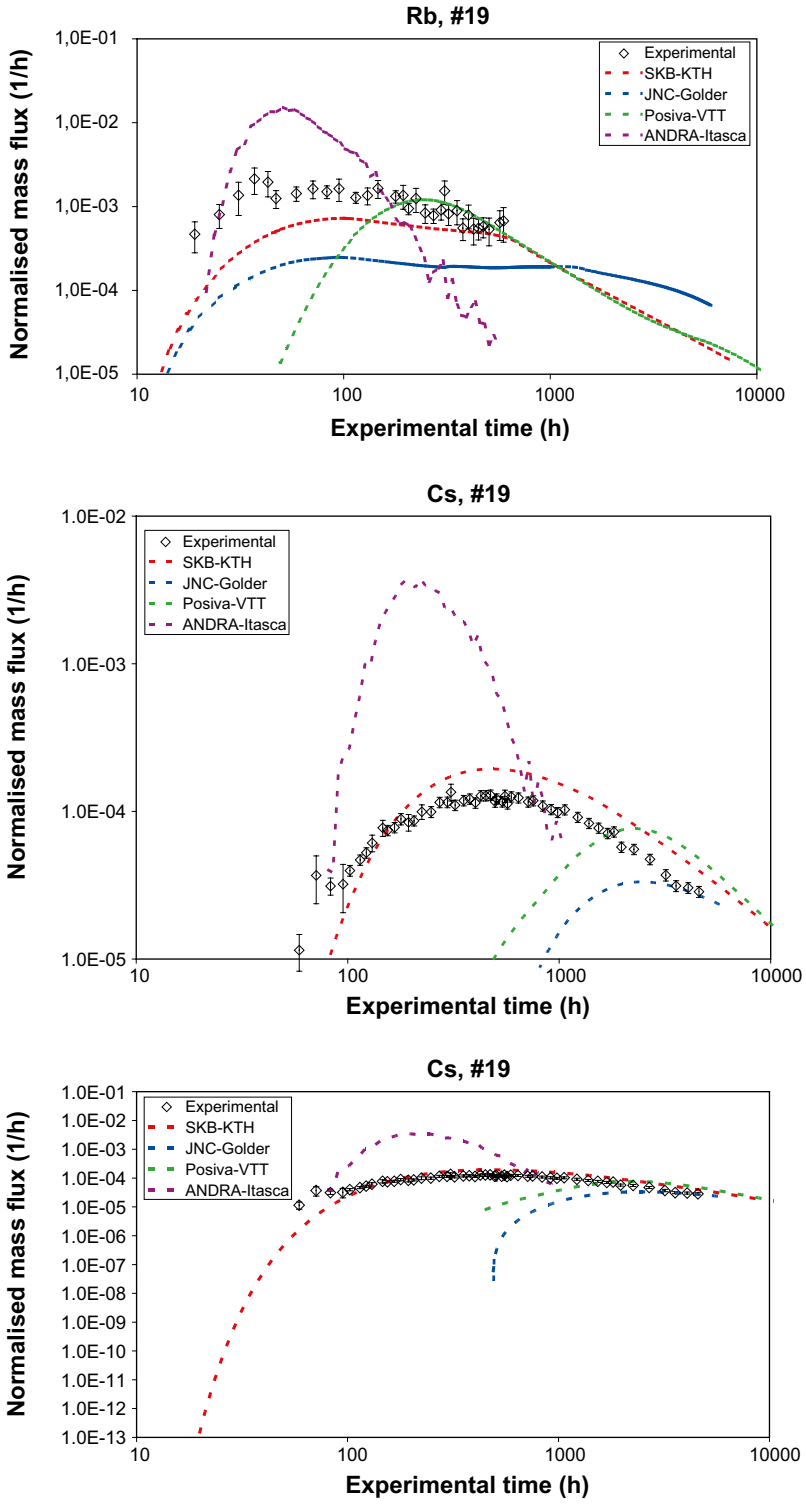

Figure 4-4. *Flow path I – Predicted and measured breakthrough of Rb-86 and Cs-137, including a blow-up of the Cs-137 predictions.*

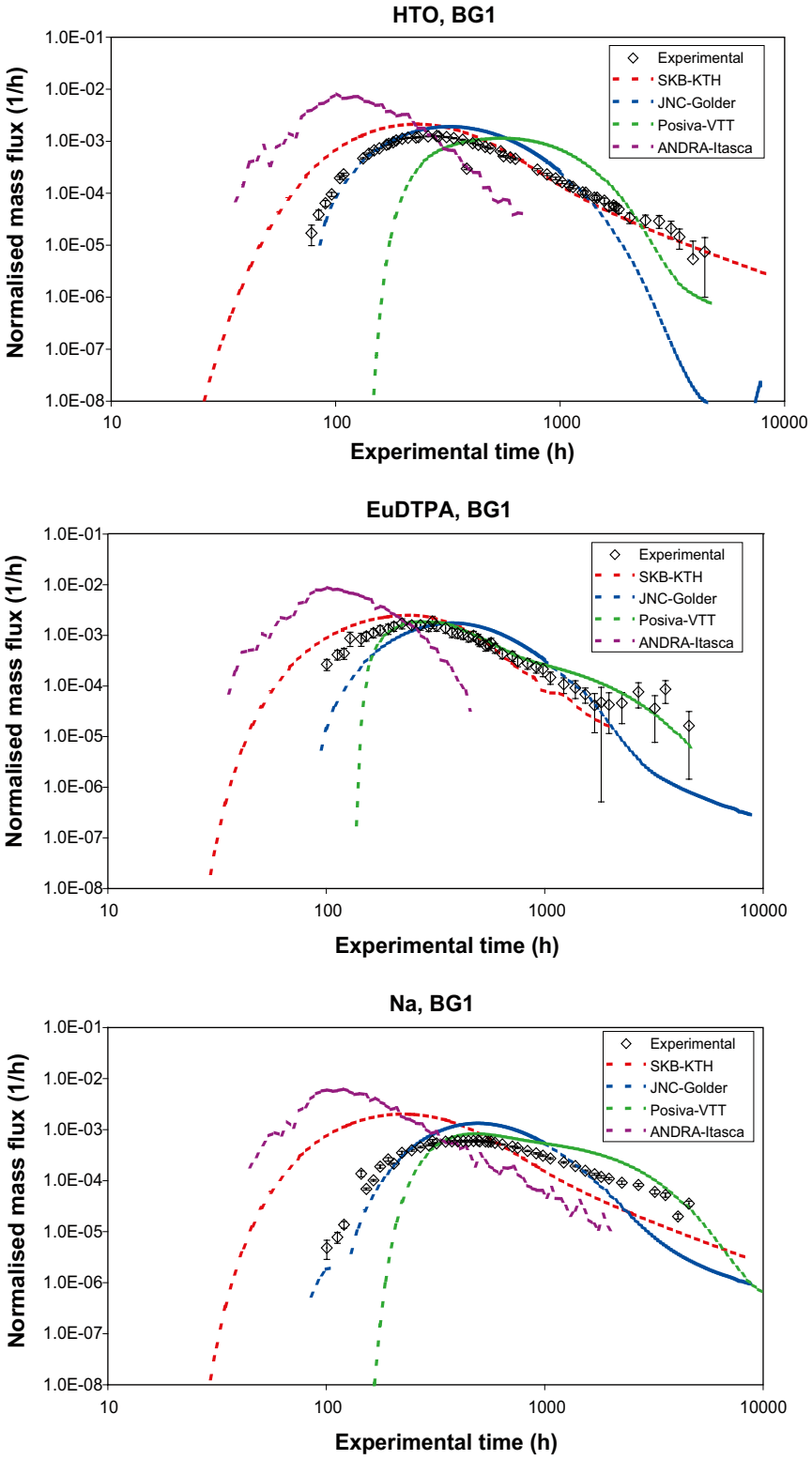

Figure 4-5. *Flow path II – Predicted and measured breakthrough of HTO, Eu-152-DTPA and Na-22.*

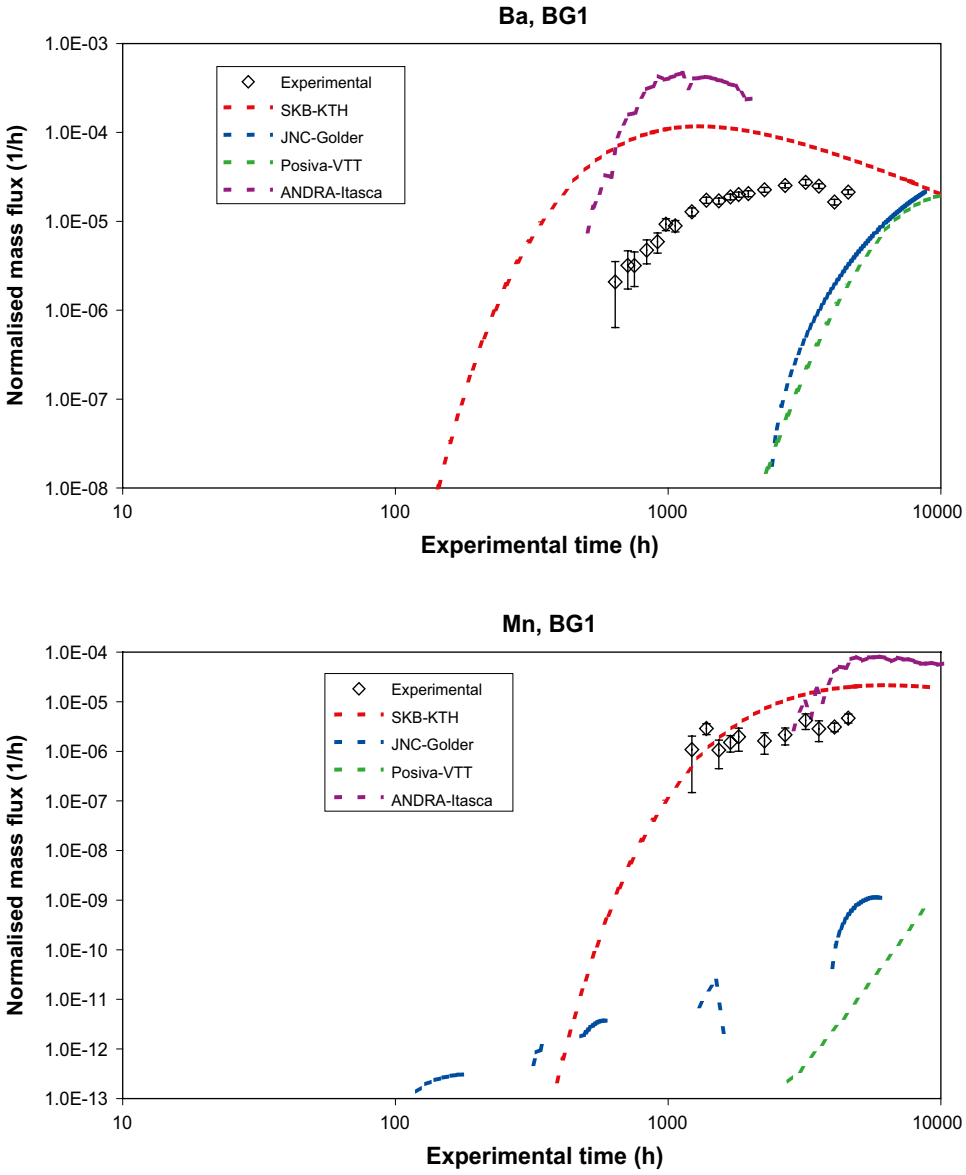

Figure 4-6. *Flow path II – Predicted and measured breakthrough of Ba-133 and Mn-54.*

5 Evaluation

5.1 Overview of evaluation process

In the following subsections a treatise is provided of the important aspects of evaluation which also provides elements of intercomparison of results from the various models. Section 5.5 provides illustrations of the flow paths explored. Of particular interest is the visualisations of the more complex Flow path II which involves background fracture BG1. Section 5.3 reviews aspects of interest in assessing the immobile zone retention properties of the two flow paths. In this context also the hydrodynamic control on radionuclide retention is discussed. Results from the four modelling concepts are compared and discussed. Section 5.4 reviews the validity of the developed hydrostructural model in the light of the experimental results and modelling performed.

5.2 Assessment of path geometries and characteristics

In this section, we study the properties of the paths followed by the tracers between the two injection sections and the pumping section in Structure #19 (flow paths I and II, respectively), by looking at the relationship between the explicit representation of structures and background fractures on one side, and the determination of the transport paths on the other side, in the ANDRA/Itasca and JNC/Golder models. Only these two models represent background fractures explicitly.

5.2.1 Flow path I

Flow path I is represented as obtained by the ANDRA/Itasca team. Despite the explicit representation of the background fractures around Structure #19, as shown in Figure 5-1, the tracer stays within Structure #19, with only a minimal number of background fractures participating in the transport path. In fact, the part of the few background fractures involved in transport is mostly their intersections with Structure #19, as illustrated in Figure 5-2, where the underlying pipe network used for the simulations is represented. Figure 5-3 shows, in the pipe transport network, the ratio of the total mass injected supported by each channel, in log scale. The tracer paths are fairly concentrated, despite the not-so-small injection flow rate. In summary, Flow path I behaves as though Structure #19 was isolated, with very little interference from the background fractures network.

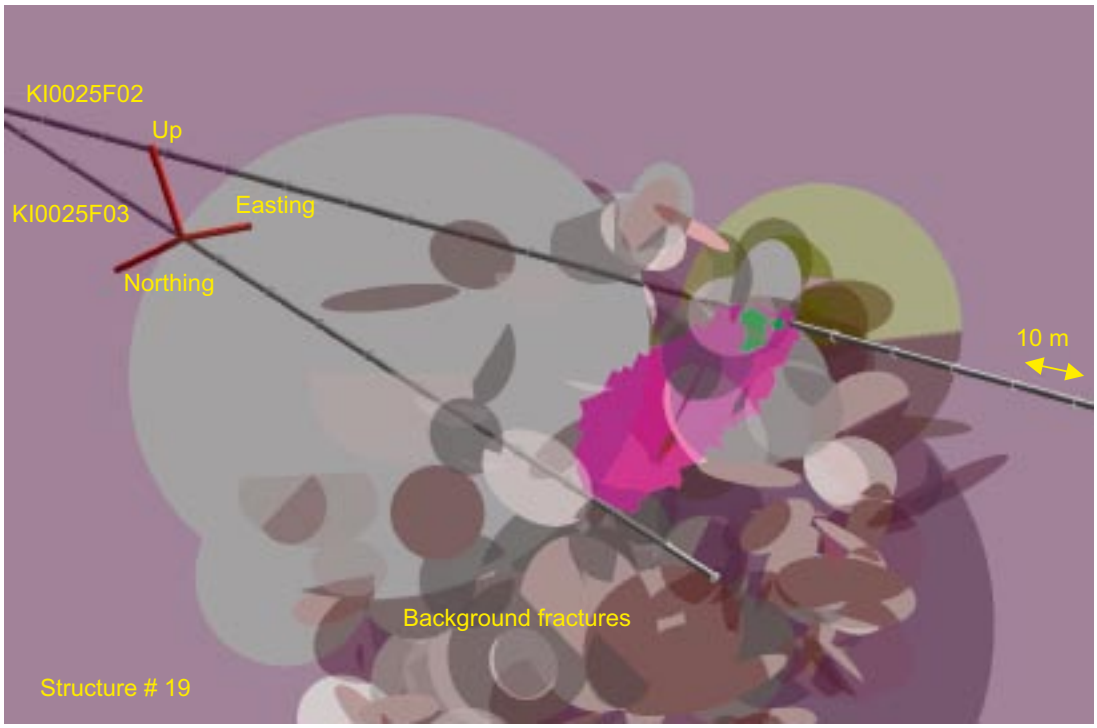

Figure 5-1. *BS2B test, injection in Structure #19 – Flow path I. View of the transport path within Structure #19 ("plume" indicated in pink), and of the background fractures (semi-transparent). Result from the ANDRA/Itasca model.*

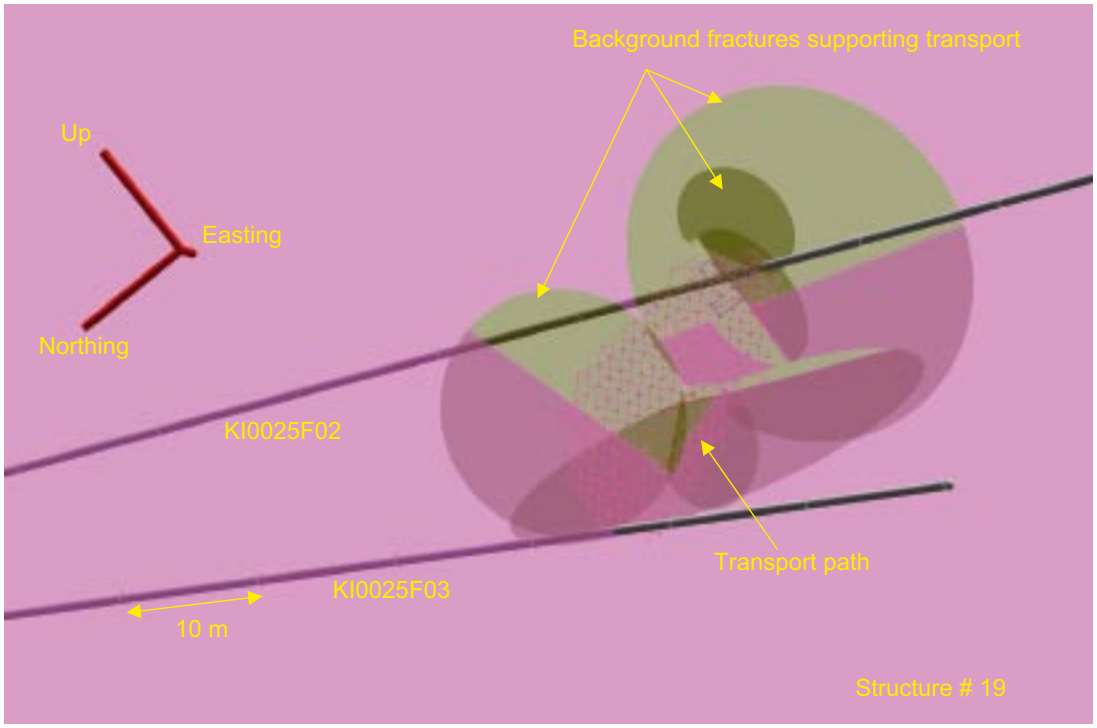

Figure 5-2. *BS2B test, injection in Structure #19 – Flow path I. Close-up view of the transport path within Structure #19 (channels within Structure #19 in pink), and of the background fractures supporting transport (semi-transparent). Result from the ANDRA/Itasca model.*

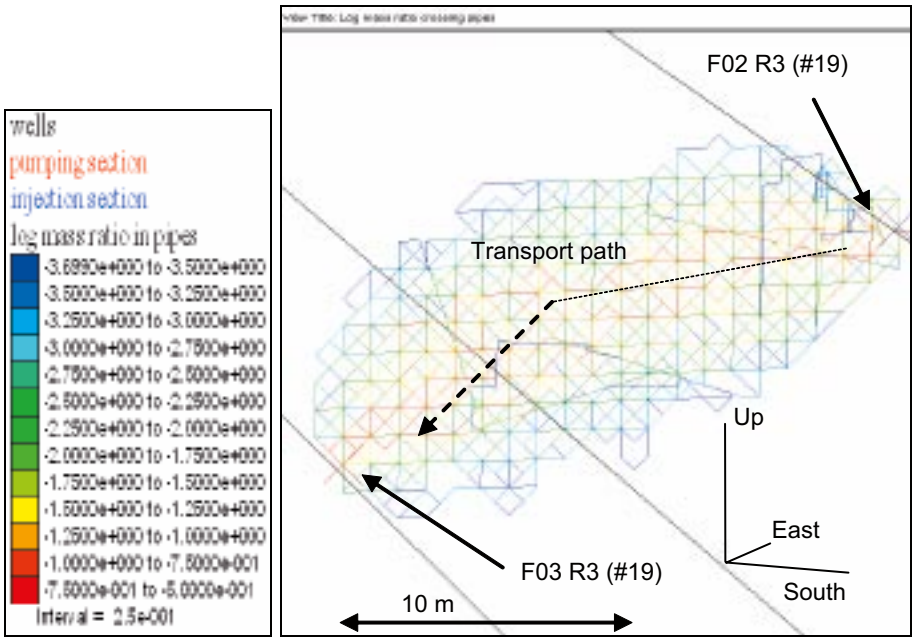

Figure 5-3. *BS2B test, Iodine injection, Flow path I. Log of mass ratio travelling through each channel along the transport path. Result from the ANDRA/Itasca model.*

5.2.2 Flow path II

Flow path II is first illustrated Figure 5-4 and Figure 5-5 as obtained from the JNC/Golder model. Only a few background fractures support the flow path (Figure 5-4a). The transport channels on these fractures are fairly short and stay confined in the interval between the injection and pumping sections, as illustrated by Figure 5-4b and Figure 5-5a. Also, it can be noted from Figure 5-5b that the tracer travels directly to the pumping point, with very little distance travelled in Structure #19, as can be seen readily from Figure 5-5. The BG-1 fracture does not connect directly to Structure 19, so that all transport paths follow at least two background fractures.

The following figures were obtained from the ANDRA/Itasca model. While Figure 5-6 shows a general view, including background fractures, Figure 5-7 outlines from two different viewpoints the three features that make up the main transport path in this model: BG1 (yellow colour), a large background fracture (blue colour), then Structure #19 (pink colour). Figure 5-8 shows the part of these "main transport path" features that was effectively sampled by the tracer. Figure 5-9 is a close-up, with the same view angle as the inlet in Figure 5-7, in which secondary transport paths and the background fractures that support these paths are illustrated.

We observe the "main path" along one large background fracture (due south-east, see Figure 5-8), then back to KI0025F03 along Structure #19. The more direct "secondary paths" use background fractures sub-orthogonal to Structure #19. From Figure 5-8, it is clear the total area covered by the tracer is quite large, with most of the BG1 fracture invaded.

Figure 5-10 shows the ratio of the total mass injected supported by each channel, in log scale: most of the tracer follows the "main path" described before: flow along the large background fracture and back along Structure #19. The colour scale is the same as for Figure 5-3, that gives the same quantity for path I. The tracer paths are more spread here, despite the lower injection flow rate, because of the tightness of the BG1 fracture. Essentially, flow from the injection point is first radial in this fracture, until the intersection to the large background fracture is encountered.

a)

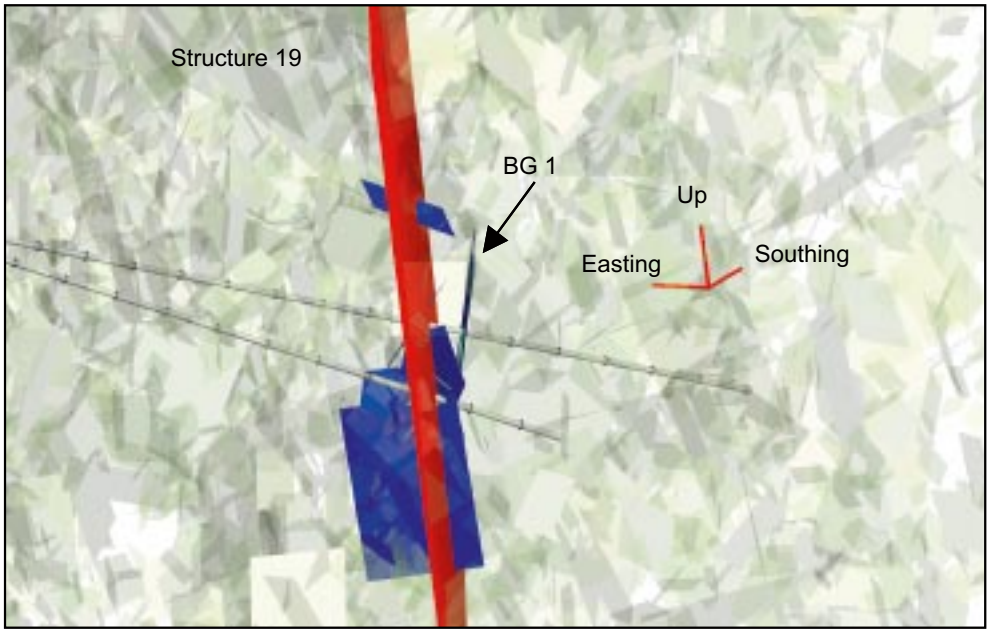

b)

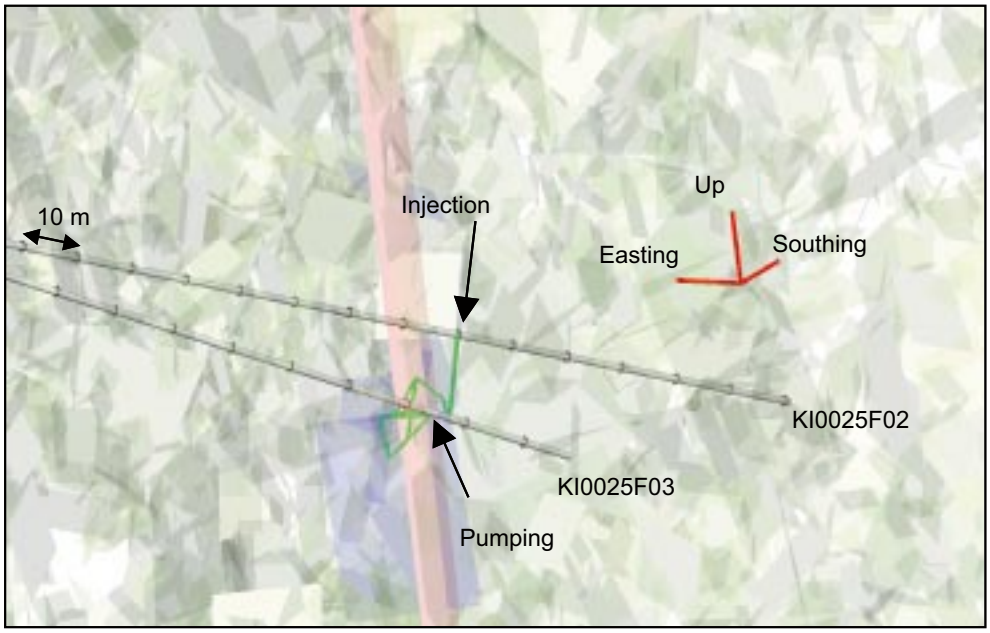

Figure 5-4. *BS2B test, injection in fracture BG1 – Flow path II. a) View of the Structure #19 (in red), and of the background fractures supporting transport (in blue). Other background fractures are made transparent. b) Zoomed view of the channels supporting the transport, in green. Structure #19 and background fractures are made transparent. Scale given by tick marks on boreholes. Result from the JNC/Golder model.*

a)

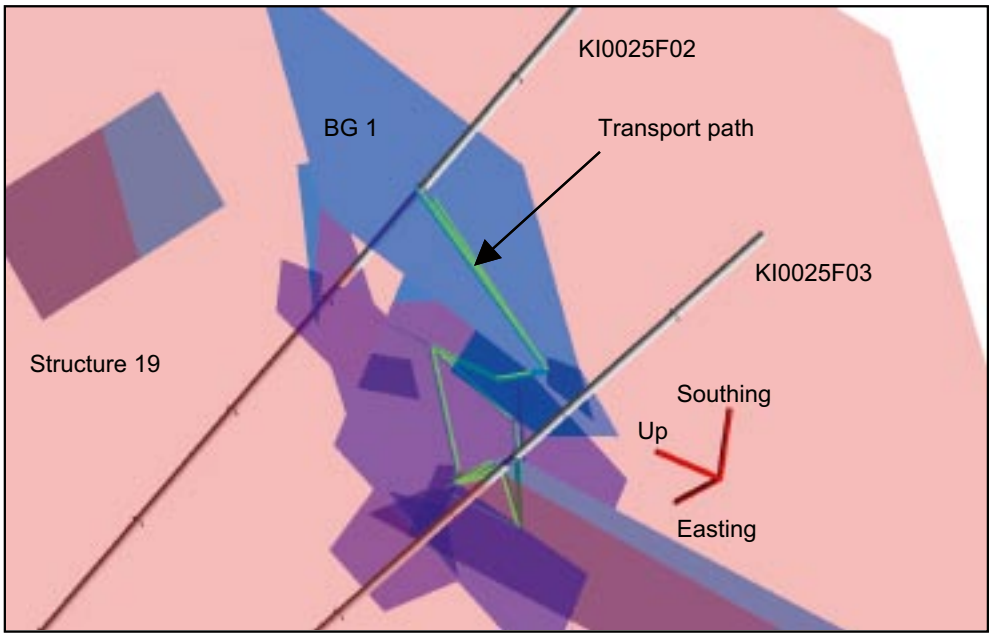

b)

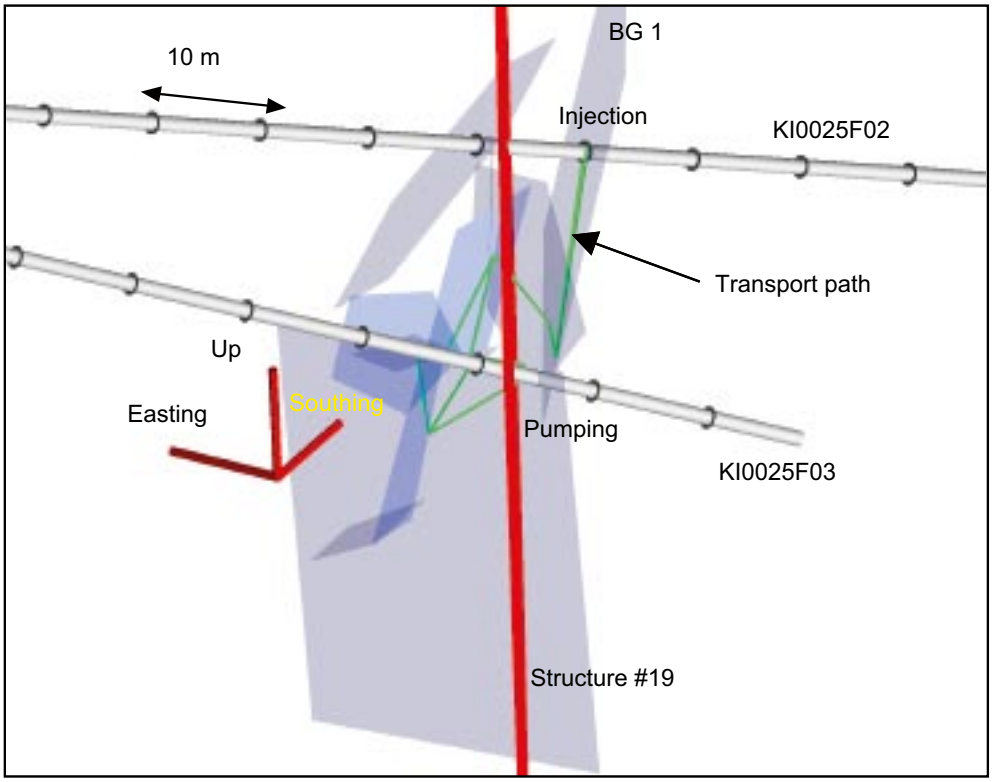

Figure 5-5. *BS2B test, injection in fracture BG1 – Flow path II. View of the channels supporting the transport, in green, of the background fractures supporting these channels, in blue, and of Structure #19, in pink/red. a)View across Structure #19, b) view parallel to Structure #19. Tick marks on bore-holes show 10 m scale. Results from the JNC/Golder model.*

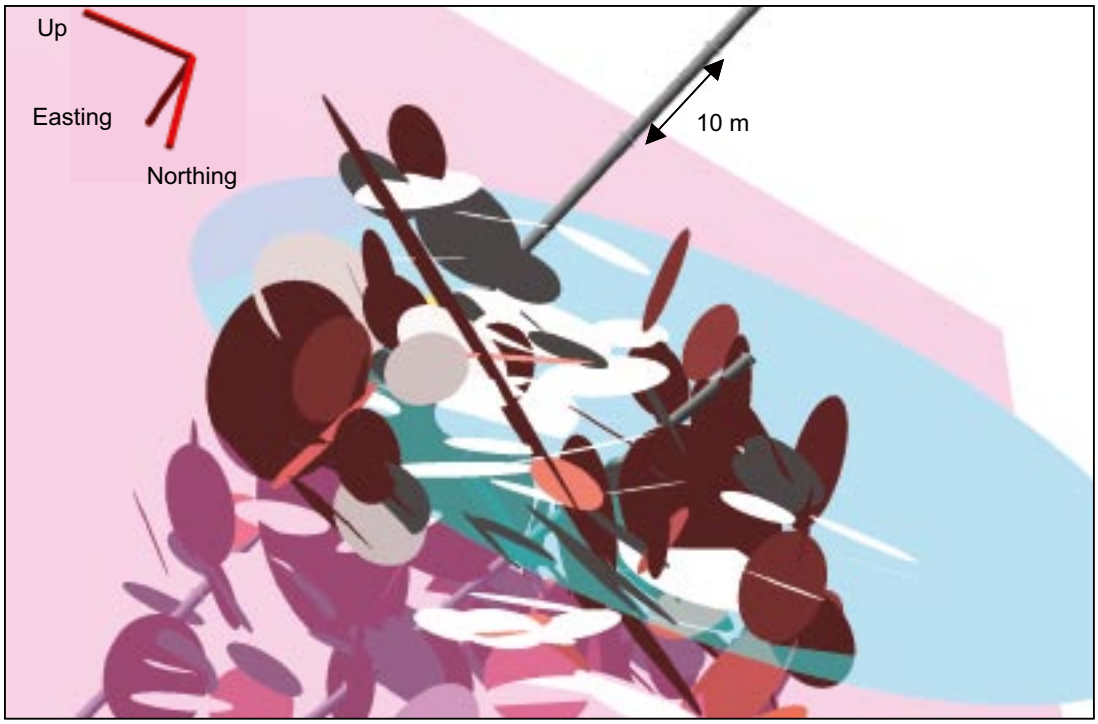

Figure 5-6. *BS2B test, injection in fracture BG1 – Flow path II. All fractures. Structure #19 is shown in pink. Scale given by 10 m spaced tick marks along boreholes. Same view angle as Figure 5-5. Result from the ANDRA/Itasca model.*

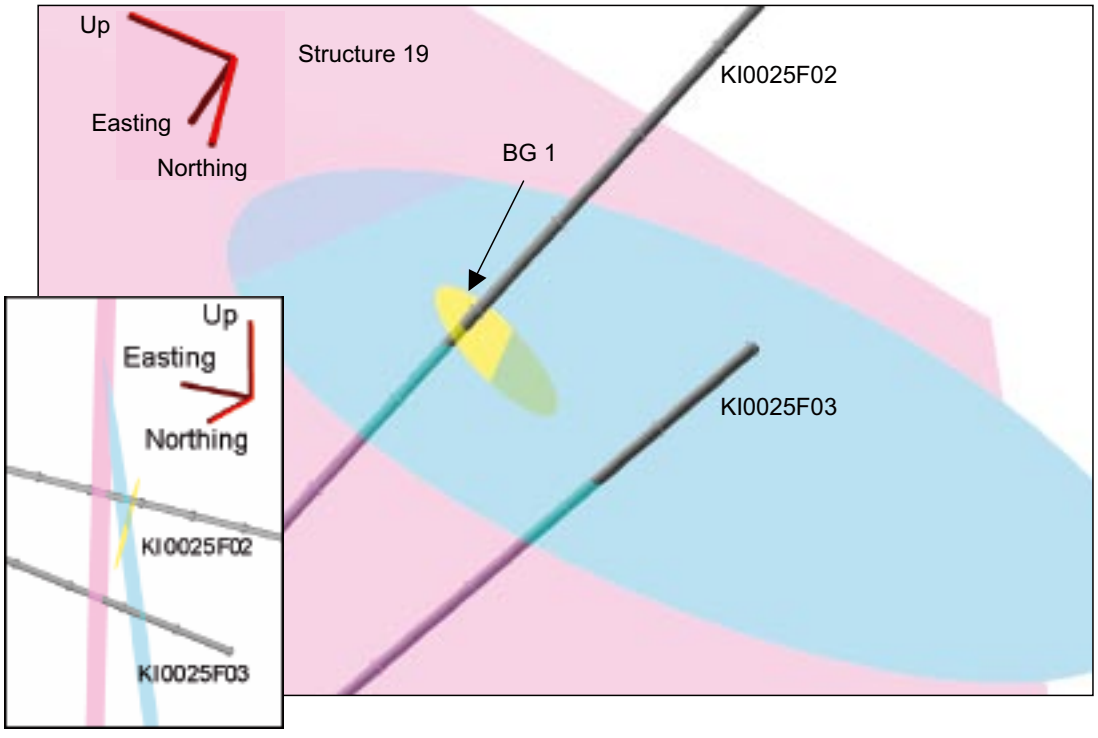

Figure 5-7. *BS2B test, injection in fracture BG1 – Flow path II. Structure 19 (in pink), BG1 (in yellow), and main transport-supporting background fracture (in blue). Inlet shows another viewpoint, same as in Figure 5-8. Result from the ANDRA/Itasca model.*

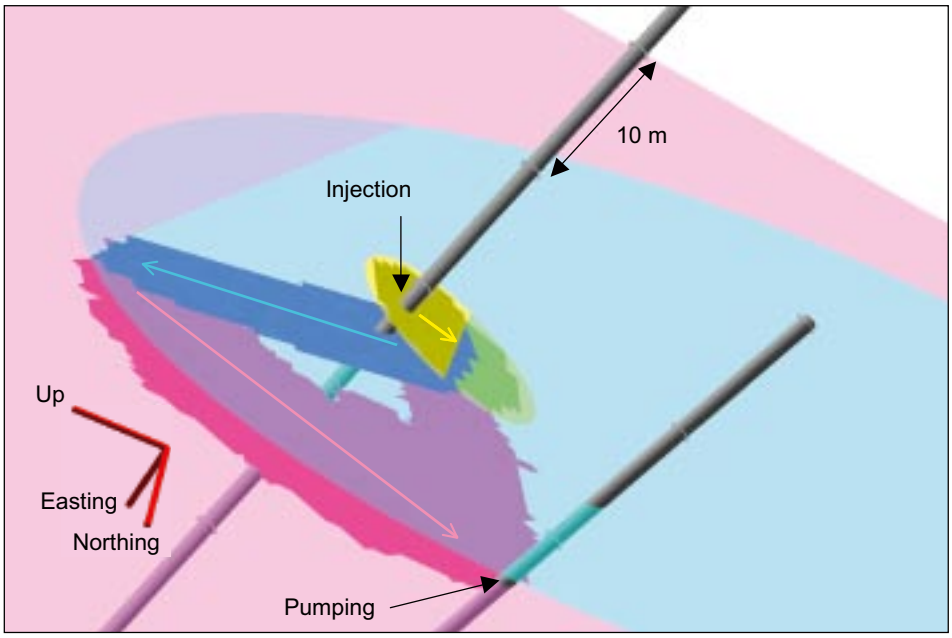

Figure 5-8. *BS2B test, injection in fracture BG1 – Flow path II. Main transport path. Solid colours represent part of fracture/structure effectively touched by the tracer. Coloured arrows show the direction of flow. Result from the ANDRA/Itasca model.*

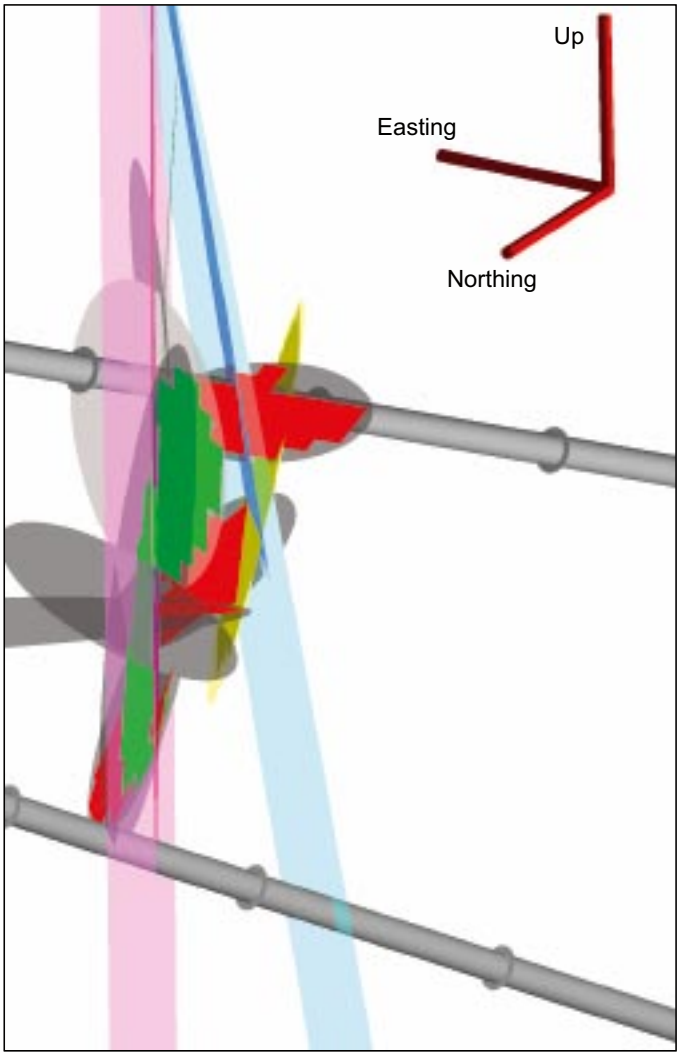

Figure 5-9. *BS2B test, injection in fracture BG1 – Flow path II. Close-up on secondary transport paths (red and green). The background fractures supporting these secondary paths are shown in grey. Result from the ANDRA/Itasca model.*

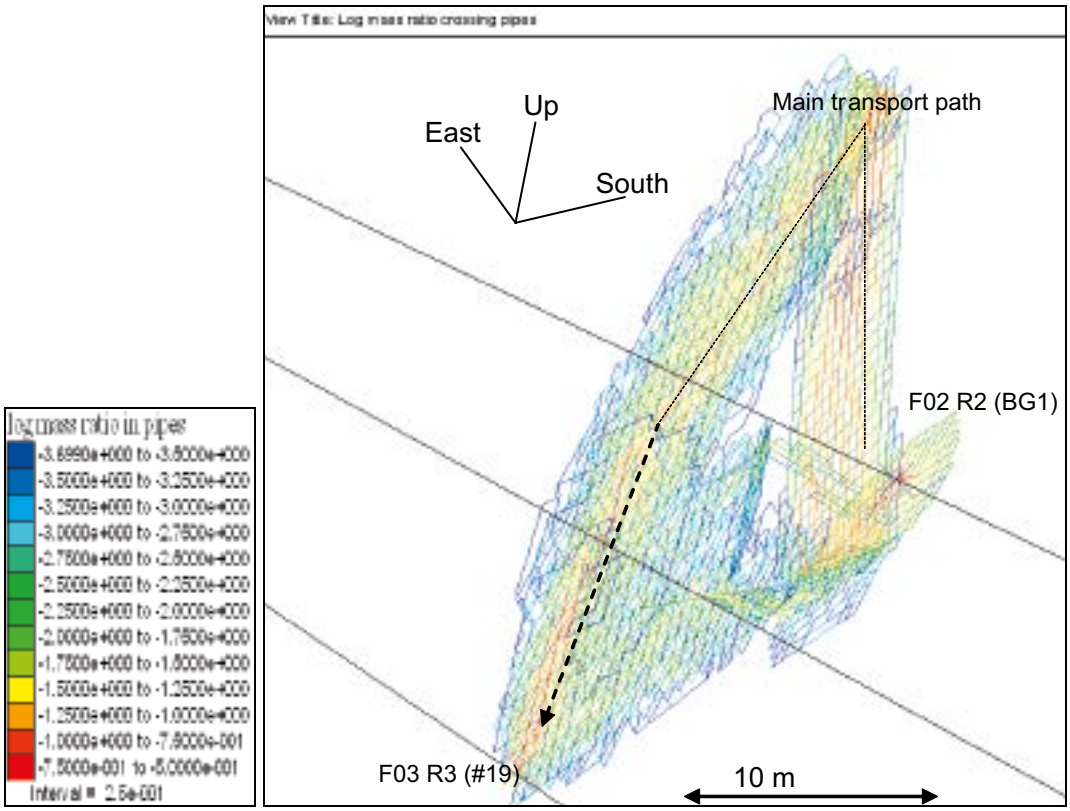

Figure 5-10. *BS2B test, HTO injection, Flow path II. Log of mass ratio travelling through each channel along the transport paths. Result from the ANDRA-Itasca model.*

5.2.3 Flow paths dimensions

By monitoring the displacements of all particles during simulations, the ANDRA/Itasca team was able to study in detail the geometry of their paths from injection to pumping. For each particle, the total path length, the length of the part of the path situated in Structure #19 and in background fractures were recorded. For Flow path I (injection in Structure #19), the mean path length is 29 m, and the path is completely situated in the structure. For Flow path II (injection in background fracture BG 1), the mean path length is much larger – 71 m. On the average, 29 m of Flow path II are travelled in background fractures and 42 m are travelled in Structure #19.

The transport paths obtained by the ANDRA/Itasca and JNC/Golder teams for Flow path II are quite contrasted. While both teams use fracture networks where BG1 does not connect directly to Structure #19, the role of Structure #19 in the transport is minimal in the JNC/Golder model and important in the ANDRA/Itasca model, for which it plays the role of an extended, large conductivity, fast flow sink. The role of Structure #19 in the ANDRA/Itasca model is exemplified in Figure 5-11, which shows the order of magnitude differences in the flow rates experienced by the 3 parts of the main flow path.

Values obtained for path widths are discussed in the following paragraphs and are summarised in Table 5-1.

The ANDRA/Itasca team obtained parameter values that yielded contrasted effective apertures in the order of 0.1 mm for Structure #19 and 0.01 mm for the background fractures. It was also noted that very heterogeneous properties were needed to reproduce the observed effective diffusion. These values yield large path widths, in the order of 2–3 m for Flow path I (see Figure 5-3) and 5–10 m for Flow path II (Figure 5-10). Note that within these widths, the tracers were shown to travel mostly within the centre of the path.

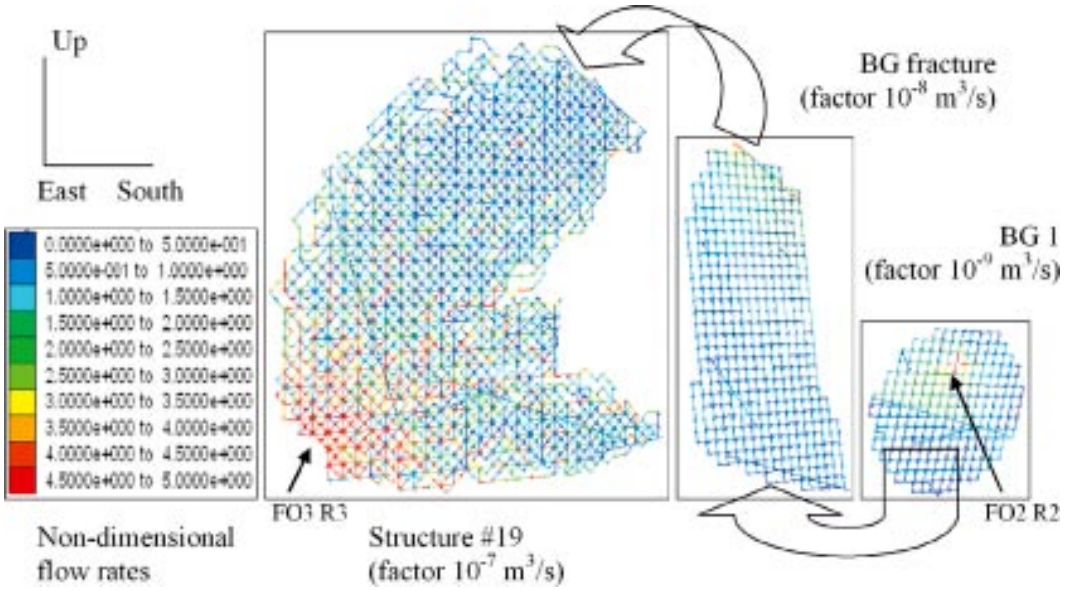

Figure 5-11. *BS2B test, injection in fracture BG1, Flow path II. Flow rates in the main parts of the flow path. Flow rate in each plot is the product of the colour scale by the indicated factor.*

The SKB KTH-WRE team back-calculated the width of the stream tubes from the values of the effective parameters, considering lengths of 20 m for Flow path I and 50 m for Flow path II. Effective apertures of 0.15 mm for Flow Path I and 0.12 mm for Flow path II were obtained from the slope of the (β vs. τ) relationship for each path. This yielded widths of 7 cm for Flow path I and 2 m for Flow path II. Note that the latter was considered unrealistic in the framework of the simple streamtube approach.

The Posiva-VTT team also gave a geometrical interpretation of the effective properties of the transport channels, considering lengths of 20 m for Flow path I and 40 m for Flow path II. Two cases were considered for the flow field. A first one yielded widths of 21 cm for Flow path I and 67 cm for Flow path II, while the estimate for the second case was in the order of 10 m for both paths.

5.3 Assessment of immobile zone retention properties

This section aims to determine effective immobile retention zone properties for the BS2B flow paths. Assessment of the effective immobile zone retention properties is based on results of the four different BS2B models/approaches as outlined in Chapter 4. The main emphasis is on the retention caused by matrix diffusion that is dependent on both on the properties of the flow field and the corresponding immobile zones along the flow path/-s. This means that the properties of

Table 5-1. Path widths obtained from the models employed in the evaluation.

	Flow path I width, m	Flow path II width, m
ANDRA/Itasca	2–3	5–10
JNC/Golder	–	–
SKB/KTH	0.07	2
Posiva/VTT	Low: 0.2	Low: 0.7
	High:10	High:10

immobile zones need always to be assessed in conjunction with assumptions regarding the flow field and flow path. In this section the interpretation of the properties of the immobile zones is also coupled to a reasonable flow field.

5.3.1 Effective immobile zone retention property

In a case of homogeneous and infinite immobile zone the retention by matrix diffusion is governed by a grouped parameter

$$B = \kappa\ \beta\ = \varepsilon \sqrt{D_p R_p}\ \frac{t_w}{b} \qquad (5\text{-}1)$$

where $\kappa\ = \varepsilon \sqrt{D_p R_p}$ determines the immobile zone properties and $\beta = t_w/b$ determines the flow field. In the case of a homogeneous immobile zone it is straightforward to define that the immobile zone retention properties are specified by κ. For a heterogeneous immobile zone this is not that obvious and the structure of the heterogeneity may also influence the retention properties. We may conceptualise the possible types of the heterogeneity into two groups:

- *Heterogeneity parallel to the fracture plane* (e.g. along the flow field). In this case it is possible to find an equivalent or effective value of κ that gives the correct retention for the flow path. The effective κ can be calculated as an average along the flow path of local κ's weighted by local β's. In this case the effective immobile zone property is well defined in a sense that it does not vary if β is scaled. In practice the scaling of β would mean e.g. that the same pathway is examined using different total flow rates (i.e. the overall magnitude of β is changed but the profile of β along the flow path is maintained, this means that weighting of the local κ's remains unchanged).
- *Heterogeneity in the direction of the matrix diffusion* (usually perpendicular to the fracture plane). In this case it may not be possible to find a single effective κ that describes the whole breakthrough curve. The effective immobile zone retention property depends also on the overall level of β and characteristic retention properties may change significantly if the level of the overall β is changed. Usually, the immobile zone retention properties are divided into the small scale heterogeneity that cause equilibrium type of behaviour and large scale heterogeneity that cause kinetic behaviour, and that could be approximated by an effective κ. This way it is possible to provide an effective immobile zone retention property that is valid for a given range of β. Experimental time scale of the tracer experiment have also an influence on the observed effective retention properties. The effective porosity will be dependent upon the tracer (or rather its K_d), because during the fixed experimental time scale the breakthrough curves of different tracers will convey information on the different penetration depths. The effective immobile zone retention property $\gamma = \varepsilon \sqrt{D_p R_p}$ can be represented by an "effective" porosity assigned with typical nuclide dependent data. In that case, if the porosity has a decreasing trend in the rim zone in the direction of matrix diffusion then the resulting "effective" porosity will depend on the tracer in the experimental time scale (see an example of the specific estimates in Table 4-15). This is an artefact of the fixed experimental time scale. In principal, penetration does not depend on the sorption properties of the tracer.

Background information on the fractures in the TRUE Bloc Scale rock volume underlies the importance of the heterogeneity. Classification of the fractures in different fracture types explicitly shows the differences in the heterogeneity of the immobile zone retention properties.

5.3.2 Major retention zones

A microstructural model of the immobile zones has been developed for the fractures of the BS2B block, cf Section 2.3. Two major fracture types have been identified. The fracture types have very distinct microstructural models. Type 1 fractures are of fault type that exhibit a high degree of heterogeneity and also include layers of porous geological materials. Type 2 fractures

are non-fault type fractures. Type 2 fractures are not as heterogeneous as Type 1 fractures and the volumes (thicknesses) of the high porosity geological materials are much smaller than for Type 1 fractures.

From a tracer retention point of view the different immobile layers show quite different characteristics. Some of the immobile layers are rather thin and they probably get saturated by the tracer. In many cases the contribution of these layers to the tracer retention can be described through equilibrium retention. Many of the models used in the BS2B evaluation also represent the thinnest layers of immobile pore space by the equilibrium sorption (cf Table 5-2). More detailed descriptions of the fracture types in given in Section 2.3.

The microstructural model of the immobile pore space does not directly specify how the different immobile layers are distributed along the flow path or fracture surface. This information can in part be deduced, in a statistical form, from the property denoted complexity factor and is provided for the hydraulic features in the BS2B volume (cf section 2.2 and Appendix A). The distribution of the different immobile layers along the flow path has a direct, but non-unique, influence on the effective immobile zone retention property of the whole transport path. The distribution of the different immobile zones can be regarded as heterogeneity that is parallel to the fracture plane (cf first bullet of Section 5.3.1).

Different modelling approaches utilise the complexity factor in different ways. The ANDRA-Itasca model applies the coverage of the immobile layers along the flow path as a calibration tool. For the initial BS2B prediction, the JNC-Golder team applies the full complexity model, as specified in the Task 6C hydrostructural report /Dershowitz et al. 2003/. Fracture complexity is simulated by increasing the perimeter (and therefore the surface area) for each transport pathway by a multiple of the assigned fracture complexity. In the final JNC-Golder evaluation model, all structures are assigned a complexity factor of 1 (no additional surface area). Full coverage of the immobile zones is assumed in every fracture (parallel diffusion). The Posiva-VTT model does not apply the complexity factor but instead assumes full coverage of the immobile layers in each fracture. The SKB-KTH/WRE team uses directly an effective property to replace the multiple immobile zones. SKB-KTH/WRE has also checked that there is a good agreement between the applied effective properties and the corresponding properties calculated from the microstructural model.

Table 5-2 shows the modelling approaches and how the immobile zones are conceptualised in the four modelling approaches. Most of the approaches apply equilibrium type of sorption to model the thinnest immobile zones. Differences between the models in describing the heterogeneity of the immobile zones are also illustrated in Figure 5-12.

The ANDRA-Itasca and SKB-KTH/WRE models do not apply directly the layered structure of the multiple immobile zones as defined in the microstructural model cf Section 2.3. Instead, the immobile zones are arranged in parallel along the flow paths, the distribution and thickness of the immobile zones may vary and this is also applied for the model calibration.

The difference in the breakthrough time history for this approach relative to the actual layered microstructural model depends on the flow conditions. It is possible that one of the immobile zones acts as the main retention zone. Thinner immobile zones become more or less saturated, but the main retention zone still behaves as if it is infinitely thick. Under these kinds of conditions it is possible to represent the layered structure by an appropriate equilibrium sorption coupled with a matrix diffusion process assigned to an infinite immobile zone. The effective immobile zone retention property can be calibrated by introducing a few different immobile zones and adjusting the relative distribution of them.

The measured breakthrough curves for the two tested flow paths show behaviour that can be explained by effective immobile zone retention property of a single infinite immobile layer. This implies that immobile zones arranged either in series or in parallel can be applied to model the tracer transport.

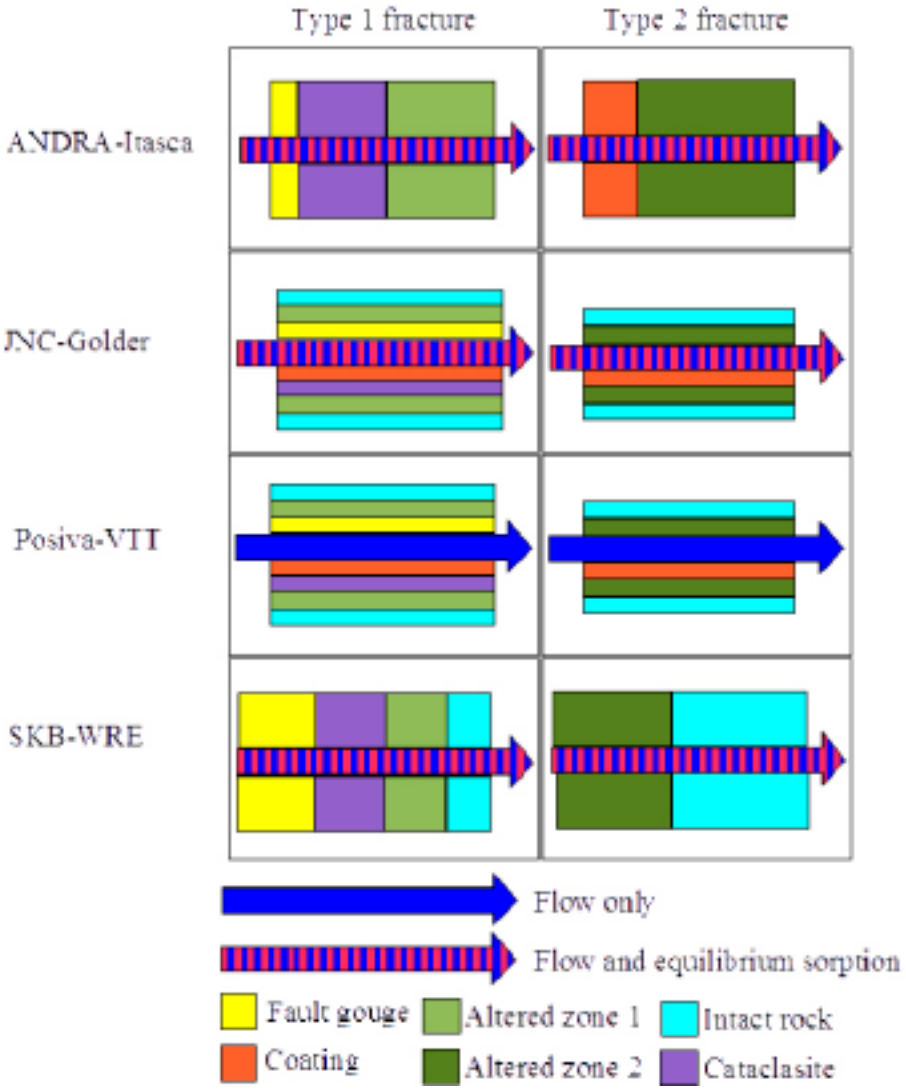

Figure 5-12. *Illustration of the immobile zones applied in the different modelling approaches. ANDRA-Itasca and SKB-KTH/WRE have implemented the microstructural model as parallel diffusion processes. JNC-Golder and Posiva-VTT have implemented the microstructural model by modelling fault gouge and fracture coating in parallel and others in series (same as in the microstructural model). Colour coding of the immobile layers is the same as in Figure 5-15.*

Table 5-2. Modelling approaches used in the prediction and evaluation of the BS2B tests.

Model	Advection	Solute transport	Immobile zones included
ANDRA-Itasca	Numerical DFN, Particle tracking	Numerical	Fault gouge, Cataclasite, Altered zone Coating represented by surface sorption Immobile pore spaces in parallel
JNC-Golder	Numerical DFN, Particle tracking	Numerical (Laplace Transform Galerkin Program, LTG)	Fault gouge, Cataclasite, Altered zone, Intact zone Coating represented by surface sorption Immobile pore spaces in parallel and in series
Posiva-VTT	Single Streamtube (truncated) Gaussian distribution of the WRT	Analytical	Coating, Fault gouge, Cataclasite, Altered zone, Intact zone Immobile pore spaces in parallel and in series
SKB-KTH/WRE	Ensemble of streamlines Inverse Gaussian WRT	Analytical	Fault gouge, Cataclasite, Altered zone, Intact zone Coating represented by surface sorption Immobile pore spaces in parallel

5.3.3 Flow paths

The flow paths tested by the BS2B sorbing tracer test (cf Section 5.2) have distinctly different immobile zone properties. This offers a way to use the deduced effective immobile zone retention properties to identify the major retention zones, and in that way also the dominating fracture types of the different pathways.

Tracer injection and extraction points for Flow path I are both in a Type 1 fracture (Structure #19). It is thus quite likely that this flow path is dominated by Type 1 fractures. The CPT hydraulic interference tests (cf Section 5-4 and Figure 3-12) support the interpretation that the sink and source of Flow path I indeed are connected by Structure #19.

Contrary to this, the injection point of Flow path II is in a Type 2 fracture (denoted BG1) whereas the pumping point is in a Type 1 fracture (Structure #19). It seems clear that Flow path II contains both Type 1 and Type 2 fractures, but there is no direct way to measure how much of the total flow path is along Type 1 or Type 2 fractures, respectively. There is strong hydraulic connection between Structure #19 and BG1 (established by the CPT2 pre-test). On the other hand, advective water residence times for Flow path II are much longer than for the Flow path I (cf Section 5.4.2, Table 3-11 and Table 3-12] and the modelled water residence time distribution (WRT) in Figure 5-13). Based on this evidence and results of other supporting experiments it is concluded in Section 5-4 that it is likely that the Flow path II contains a (small) number of background fractures connecting BG1 to Structure #19.

Flow modelling indicates that the uncertainty in the geometry of Flow path II is much greater than for Flow path I. This is reflected by the importance of the background fractures in explaining the water residence time distribution along the Flow path II and correspondingly large variability between DFN realisations (this should refer to appropriate figure/table in Section 5-2).

Advective water residence time distributions of the four evaluation models are presented in Figure 5-13 (i.e. non-diffusive, non-reactive BTCs for a Dirac pulse injection). There are rather large differences between the models. The Posiva-VTT model is based on short water residence time and minor amount of dispersion, i.e. it is more like a bulk flow. The other models, especially the numerical DFN model of the ANDRA-Itasca, show longer residence times and a much larger element of dispersion.

Most of the models describe Flow path I as showing a few hours of advective residence time and Flow path II as characterised by about 150 hours mean advective residence. All models show clear differences in the advective transport between Flow path I and Flow path II. The Euclidian distance from the injection point to the sink is about the same for both flow paths, but the models indicate an order of magnitude higher advective water residence times in Flow path II. Given that the Cartesian distances are essentially equitable this suggests that Flow path II in reality is geometrically much more complex than Flow path I.

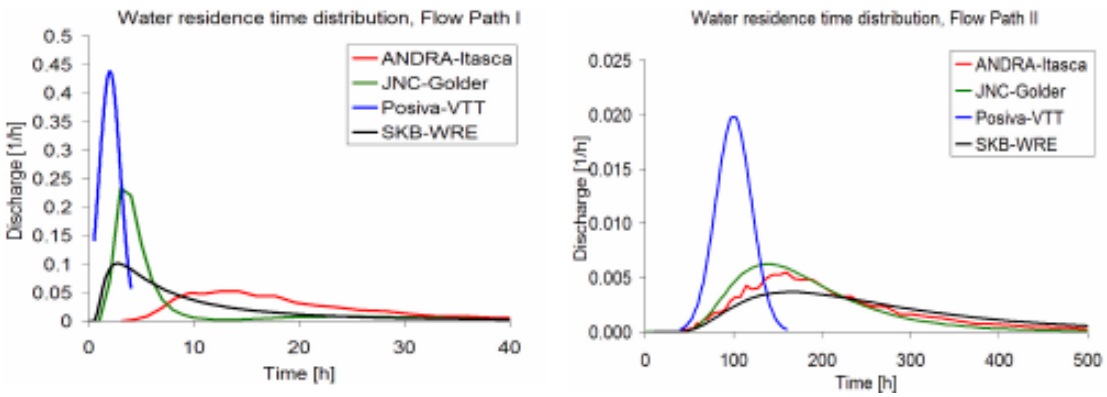

Figure 5-13. *Advective water residence time distributions of the different evaluation models.*

5.3.4 Effective immobile zone retention properties along the tested flow paths

The main emphasis is here put on the retention caused by the matrix diffusion. Therefore, this section does not give full attention to the equilibrium type of retention that is caused e.g. by saturated thin layers of the immobile pore spaces.

The approach is first to look at the hydrodynamic control of retention (β) in different models in order to confirm consistency of the flow description between the models. Then the applied immobile zone retention properties (κ) for the different flow paths are compared.

Figure 5-14 shows the mean β along the two flow paths as applied in the respective evaluation models. Along both flow paths the hydrodynamic control of retention is fairly consistent between most of the models. The deviations from the general characteristics are small β for Flow path I in case of the Posiva-VTT model and small β for Flow path II in the case of the JNC-Golder model. The average level of the β parameter is almost two orders of magnitude higher for Flow path II than it is for Flow path I. The three order difference in transmissivity between the Structure #19 and BG1 described in Section 3.3.5 would suggest an even larger difference in β. This circumstance may be explained additional fractures making up Flow path II together with BG1 exhibit higher transmissivities than BG1.

Different modelling approaches implement the heterogeneity of the immobile pore space by employing varying assumptions, e.g. the number and properties of the immobile zones vary between the different models. Most of the models do not directly show the effective immobile zone retention property of their model. However, all evaluation models are able to give reasonable breakthrough curves compared to the measured ones. It can be deduced that the retention time caused by the matrix diffusion need to be similar amongst the models; within the variability caused by the differences in the advective residence time distribution (retention time is defined as a product of the hydrodynamic control of retention and effective immobile zone retention property $t_{ret} = B^2 = \kappa^2 \beta^2$, cf Equation (5-1). The variability between the models in advective residence times is in the order of 10 hours for the Flow path I and about 50 hours for the Flow path II. This variability can be considered to be small, because the peak arrival times of the sorbing tracers are tens of hours for the Flow path I and several hundreds of hours for

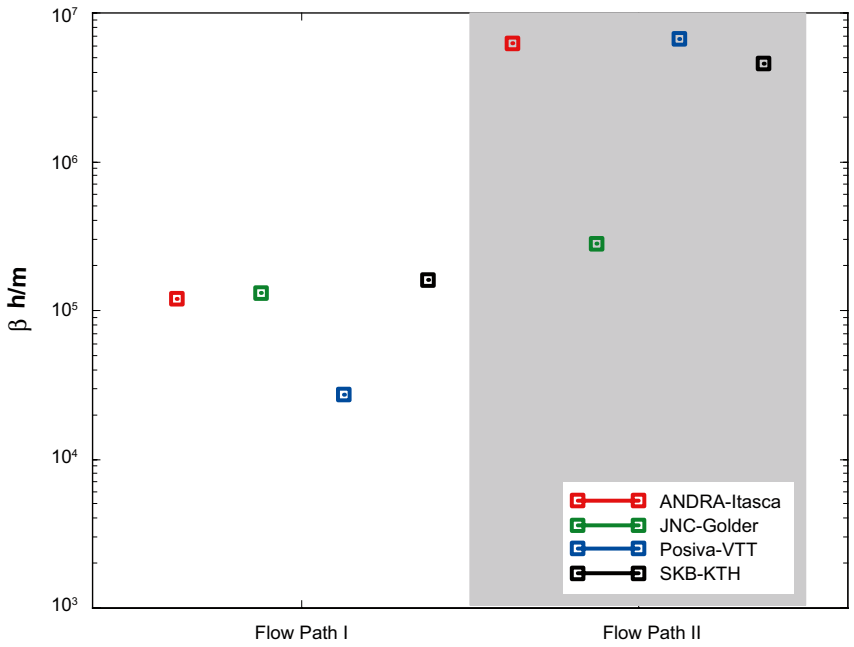

Figure 5-14. *Hydrodynamic control of the retention in the different evaluation models (mean β).*

the Flow path II. It is noted that the advective water residence time distribution and equilibrium sorption are not important when the matrix diffusion retention time is large enough, e.g. for strongly sorbing tracers.

The discussion above means that the matrix diffusion retention time (t_{ret}) and the hydrodynamic control of retention (β, cf Figure 5-14) are generally equal in the different models. This implies that the effective immobile zone retention properties of the flow paths (as expressed by the parameter κ) in the four models also need to be quite similar.

The immobile zones that contribute to the effective immobile zone retention properties in different models are shown in Figure 5-15. Each immobile zone implemented in the model is represented by its κ-value (cf e.g. Equation (5-1)). Figure 5-15 does not separate different implementations of the immobile zones. It shows the range of the immobile zones available for tracers in four models. All models employ more or less the full range of the immobile zones that are provided by the microstructural model, i.e. the κ's span over two orders of magnitude. However, it should be noted that a high κ alone does not provide the retention capacity, but also the volume of the immobile pore space need to be sufficiently large.

The effective immobile zone retention properties along the two flow paths and for most of the tracers were calculated by SKB-WRE. Figure 5-15 shows the estimated effective κ as red pentagrams. In addition, Table 5-3 compares the effective immobile zone retention property (effective κ) for the different flow paths. There seems to be a clear difference between the Flow path I (first five tracers, from Tb to Cs) and the Flow path II (last five tracers, from Eu to Mn). Flow path I shows effective immobile zone retention properties that are close to the properties specified for the cataclasite in the microstructural model. Contrary to this, Flow path II shows effective immobile zone retention properties close to those of the altered zone. This finding is also supported by the nature of the flow paths. It is known that the injection and extraction points of the Flow path I both are in the Structure #19. This is a complex fault type feature that is composed of multiple immobile zones and also high porosity immobile zones are available (fault gouge). The injection point in Flow path II is in a simple non-fault type fracture. Results of both the numerical flow modelling and the modelled advective water residence time distributions (Figure 5-13) suggest that this flow path is geometrically more complex and dominated by background fractures.

Numerical estimates based on the SKB-KTH/WRE evaluation model for the effective immobile zone retention properties are presented in Table 5-3. In this table we also compare the difference in the estimated contributions to the effective retention property of Structure #19 and background fracture (BG). The comparison shows a factor in the range 2–9 stronger retention in Structure #19. The effective κ's suggest that the retention along the Flow path II

Table 5-3. Comparison between inferred κ [m $h^{-1/2}$] for Structure #19 and background fractures (BG). Effective κ presented in Figure 5-15 are printed using bold face. The table is based on the results of the SKB-KTH/WRE evaluation model, cf Section 4.5 and /Cheng and Cvetkovic 2005/.

	Evaluation of the breakthrough curves				Penetration profile and microstructural model	Evaluation vs. penetration profile
Tracer	Flow path I (= Structure #19 contribution) κ[m $h^{-1/2}$]	Flow path II κ[m $h^{-1/2}$]	Estimated BG contribution κ[m $h^{-1/2}$]	Ratio of κ (Structure #19/ BG)	κ[m $h^{-1/2}$]	Ratio of κ (penetration profile/ evaluation)
Na-22	3.9E–5	**6E–6**	4.9E–6	8	2.6E–6	0.43
Sr-85	**5E–5**	8.4E–6	7.0E–6	7		
Ba-133	3.3E–4	**4.7E–5**	3.7E–5	9	3.3E–5	0.7
Rb-86	**1.5E–4**	1.0E–4	9.9E–5	2		
Cs-137	**1.1E–3**	4.0E–4	3.8E–4	3		

is associated with immobile zones that are typical for the non-fault type background fractures and the contribution of the fault type Structure #19 to the effective retention property along this flow path is very limited. Table 5-3 shows also SKB-KTH/WRE estimates of the effective κ that are based on the penetration profile and microstructural models of the features investigated by BS2B. Results indicate consistency between the effective properties evaluated from the breakthrough curves and those calculated based on the basis of the microstructural model.

5.3.4 Discussion

The evaluation models show that it has been easier to estimate the effective immobile zone retention properties for Flow path I. The reason for this could be that the spatial β-κ correlation is simpler along this flow path, possibly because it contained mainly in one fracture type. Flow path II is composed of a more complicated network of fractures that have very different immobile zone retention properties. This means that in the case of Flow path II it is critical to estimate correctly how the flow is divided between different fracture types. In particular, the retention time and the corresponding effective immobile zone retention property (κ) along the Flow path II is determined by the division of the total β between BG1 (and other background fractures) and Structure #19, respectively.

Still, although Flow path II is more complicated the different modelling approaches make quite similar conclusions about its immobile zone retention properties:

ANDRA-Itasca modelling concludes that transport in Flow path II is clearly dominated by the properties of the background fractures. The reason for this seems to be that the majority of the β accumulates in the background fractures and only a small part of the total β is contributed by Structure #19. However, the same network statistical properties can produce network realisations and associated pathways with widely different transport and retention properties.

JNC-Golder modelling concludes that there are indications of smaller effective immobile zone retention properties along Flow path II than along Flow path I. The difference in the measured breakthrough curves seems to be even stronger than what is suggested by the microstructural model. Their modelling also shows that the assumption of channelling to reduce the percentage of the fracture surface available for diffusion to approximately 5–10% provided much better results.

Posiva-VTT modelling shows that the thickness of the major immobile retention zones of the both flow paths needs to be several centimetres Especially, for Flow path II, which has smaller flow rate, this indicates that the observed retention time cannot accumulate in the Structure #19. Structure #19 includes immobile pore spaces of high porosity but limited volume, which should show up at the breakthrough curves. The present understanding of the flow field along Flow path II, based on e.g. dilution flow measurements, indicates that it is possible to accumulate the observed retention time in the background fractures.

SKB-KTH/WRE modelling takes into account the altered zone and cataclasite to be the kinetic retention zones. Fracture coating and fault gouge are modelled indirectly through equilibrium sorption. SKB-KTH/WRE works out the effective immobile zone retention material properties of the flow paths. Also these results indicate that the background fractures dominate retention along Flow path II, i.e. the effective immobile zone retention material properties of the whole flow path are close to those of altered zone. In addition, it is demonstrated that the effective κ values for both Flow path I and Flow path II can be inferred reasonable well from the microstructural model (assuming that the Flow path II is dominated by background fractures). The SKB-KTH/WRE modelling also shows that the flow field, i.e. β's (that need to be coupled with the given effective immobile zone properties (κ's)) are reasonable and consistent with the tracer dilution flow data. SKB-KTH/WRE have also calculated that the average porosity of the immobile zone along Flow path I corresponds to about 2% and it is about 0.5% along Flow path II, assuming Archie's law

The following general conclusions on immobile zone retention can be stated:

- The basis for the estimation of the effective immobile zone retention property (κ), and in that way for prediction of solute transport, is provided by the knowledge of the microstructural model. However, a detailed microstructural model is probably more important for estimation of the effective κ in the in situ experimental time scale than it will be for the PA time scales.
- For the flow path through background fractures the same network statistical properties can yield realisations with pathways with widely different transport and retention properties
- Transport is significantly different for structures and background fractures. This is indicated by the effective immobile zone retention property of Flow path I (dominated by fault type fractures) and Flow path II (dominated by background fractures). The SKB-KTH/WRE evaluation shows a factor 2–9 stronger effective immobile zone retention properties (κ) in Structure #19 compared with BG1.
- The BS2B tracer tests provide an excellent support for the current understanding of the transport in PA scale. This while Flow Paths I and II offer a unique opportunity to compare the immobile zone retention properties between a flow path along background fractures and along a fault. PA usually assumes, although so far without direct experimental evidence, that the part of the flow path that goes along the background fractures dominates the retention. This is now demonstrated being the case for the BS2B experiment, (cf Figure 5-15).

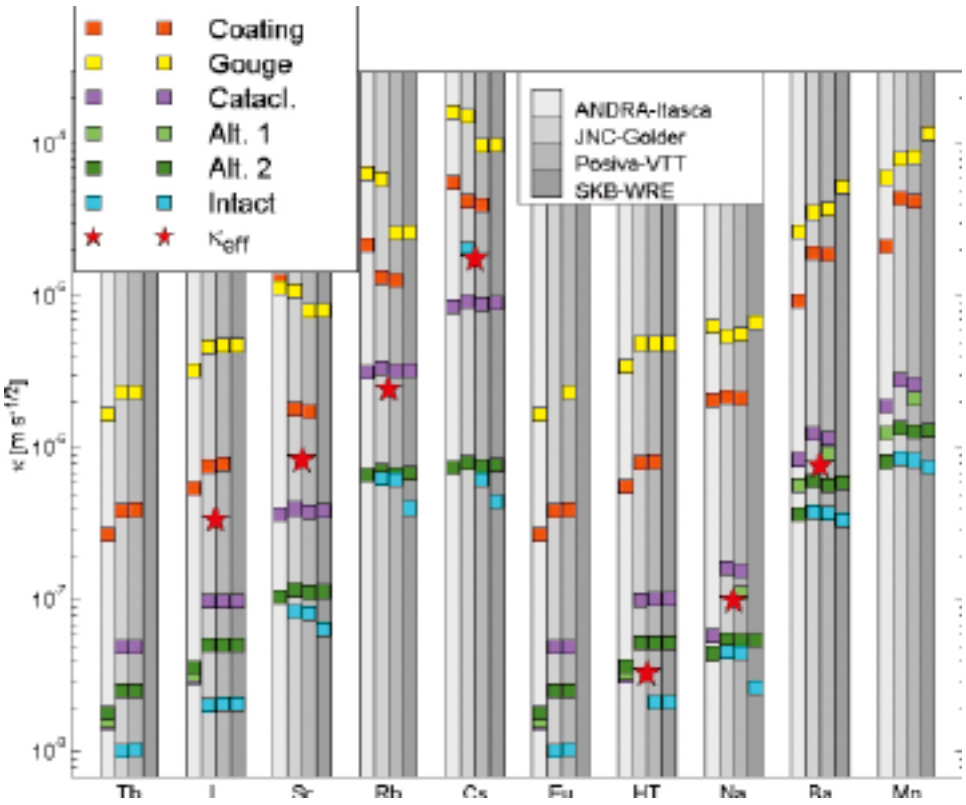

Figure 5-15. *Immobile zone retention properties (κ's) for the four different modelling approaches. The background colours indicate modelling team according to the legend. The coloured squares in the figure show the κ's applied in different models (Alt. 1 means altered zone in Type 1 fracture, Alt. 2 means altered zone in Type 2 fracture). Evaluated effective κ for some the tracers are indicated by red pentagrams (cf Table 5-3). The first five tracers (from left) are for the Flow path I and the last five tracers are for the Flow path II, respectively.*

5.4 Assessment of hydrostructural model

As described in Section 5.2, the pathways taken by flow are very important in understanding transport and retention in fractured rock. Unlike a homogeneous porous medium, in a fractured rock, the tracer transport pathway is controlled not only by the flow field, but also by the geometry of the fractures. Experiments performed within the TRUE Block Scale project /e.g. Andersson et al. 2002b/ and the current TRUE Block Scale Continuation projects have clearly demonstrated that locations that are not hydraulically connected by fracture networks do not provide flow or solute transport pathways.

The hydrostructural model, cf Section 2.2, which defines the geometry of the fractures which in turn control transport path geometry, is therefore critical to the understanding of transport in fractured rock. The geometry of the BS2B tracer tests are illustrated in plan view in Figure 3-1 and Figure 3-11 with illustrations in 3D of flow paths provided in Section 5.2.

5.4.1 Structure #19

Flow path I is defined between an injection point in a borehole intersection identified as being part of "Structure #19" and a pumping section also defined as being part of "Structure #19".

The following evidence was used to derive the location and properties of "Structure #19" during the TRUE Block Scale project:

1. Fracture intersections observed in BIPS logs, with similar orientations in several intersecting boreholes (Figure 2-5).
2. Geophysical evidence of a structure at this general location from cross-hole seismic surveys, cf Section 3.2.4 in /Andersson et al. 2002a/.

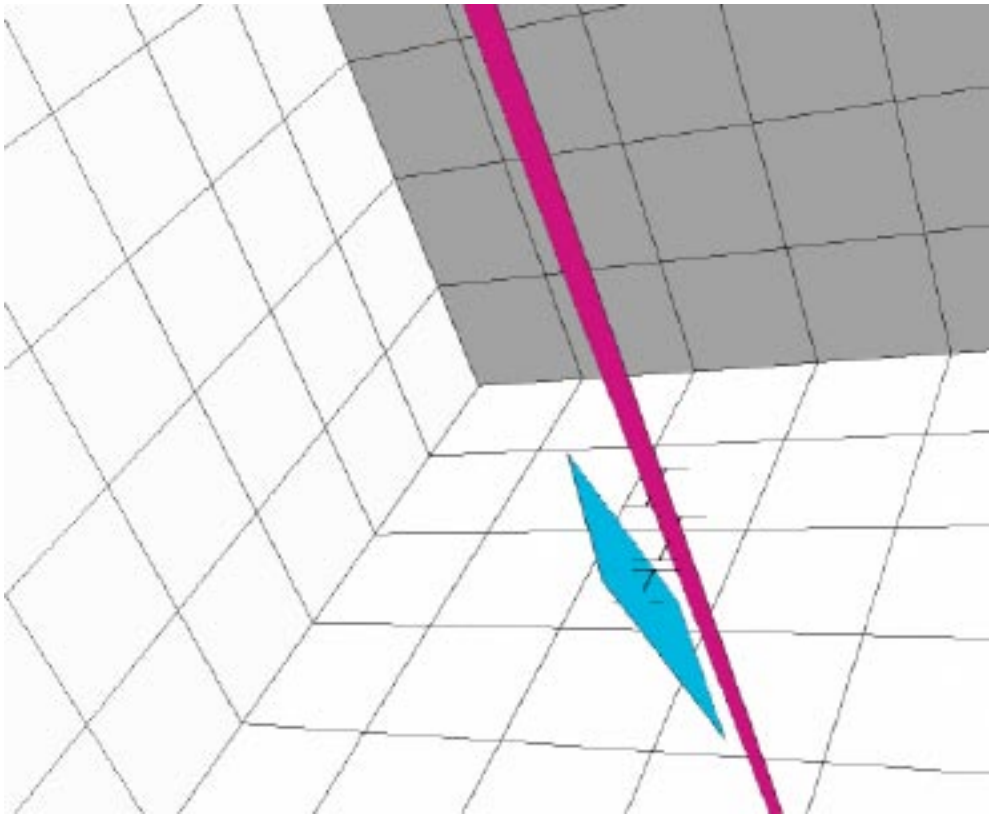

Figure 5-16. *Structure BG1 (teal), Structure #19 (purple), and the BS2B borehole test sections. View is looking to the northwest from the southeast corner of the 500 m scale TRUE Block. Note the lack of a direct intersection between BG1 and #19.*

3. Drilling response data with responses measured in packed-off intervals containing Structure #19 whilst drilling new boreholes, cf Sections 3.5, 4.3, 4.4 and 4.5 in /Andersson et al. 2002a/. Targeted hydraulic interference measurements with sinks established in Structure #19 were not conducted as part of the TRUE Block Scale Project. However, using data from UCM and Posiva flow loggings a hydraulic linkage of the five borehole intercepts was made possible, cf Section 3.3.

The hydrostructural model of Structure #19 is essentially confirmed by the results of BS2A and BS2B hydraulic tests and tracer tests between sections located at the interpreted location of "Structure #19", cf Section 3.3. In particular

- The CPT-3 hydraulic inference test results (Figure 3-6 and Figure 3-7) clearly show evidence that Structure #19 is acting as a planar, effectively homogeneous conductive structure, over a distance in excess of some 100 metres. Flow in Structure #19 is essentially radial at intermediate distances, and is similar for the different observation borehole sections. This behaviour is similar to that for Structure #20 investigated in the TRUE Block Scale project (Figure 3-7), although Structure #19 exhibits a slightly higher transmissivity. From a hydraulic point of view, this evidence refutes the concept that these structures could be adequately represented by 3D heterogeneous porous media, unless such media were discretised to approximate 2D planar (DFN) components.
- The CPT-4 and BS2B tests with conservative tracers were carried out between borehole sections intersecting the interpreted Structure #19 have advective travel times (Table 3-11) and dispersion values, cf /Andersson et al. 2004b, 2005/ which consistent with flow in a single, planar structure.
- The magnitude of the effective solute retention values from the BS2B sorbing tracer experiments (Table 5-3) are consistent with those that would be expected for transport on a fracture plane in contact with the immobile zones defined in the microstructural model and the given flow situation.

This evidence tends to confirm that the procedure developed in the TRUE Block Scale project to identify conductive structures of scale 50+ metres has been successful in this case. The hydrostructural model was useful in defining the geometry for the BS2B sorbing tracer tests, achieving tracer recoveries acceptable for regulatory agencies.

5.4.2 Background fracture BG1

The background fracture BG1 was the location of the injection in Flow path II. The designation "background fracture" is made because of lack of direct evidence of this fracture in other neighbouring boreholes. The evidence for the existence of this fracture is limited to a single flow log in KI0025F02 and the corresponding BIPS log (Figure 2-6). Due to the lack of evidence of BG1 in additional boreholes, it is not possible to definitively assign a fracture size. Furthermore, in our experience in the TRUE Block Scale project, the local fracture intersections (in boreholes) have orientations which are generally 10 to 30 degrees off from the average orientation of the assigned plane based on multiple borehole intercepts. Consequently, the hydrostructural model geometry of BG1 is very uncertain.

The questions that can be posed concerning the hydrostructural model for Structure BG1 include the following:

a) Does BG1 extend continuously all the way to the pumping section of KI0025F03:R3 (including Structure #19), such that Flow path II could be considered as a single "background fracture" pathway?

b) Does BG1 intersect Structure #19, making Flow path II a two fracture network, and if so, where?

c) What is the size of BG1, and how much of Flow path II, from KI0025F02:R2 to KI0025F03:R3 (Structure #19), follows along BG#1?

d) How many (background) fractures make up Flow path II?

e) Is BG1 a fracture of type 2 with a limited number high porosity immobile zones, as indicated by the microstructural model?

Since there is no geological/geophysical information available to answer these questions, we must rely on the indirect evidence from the hydraulic tests and tracer tests. They provide the following evidence:

- The CPT-2 pre-test investigated hydraulic connections between the intervals containing BG1 and Structure #19 along KI0025F02, over a Cartesian distance of 5.4 m. A strong hydraulic response was seen, a normalised drawdown dh/Q of approximately 10^5 s/m^2.
- The CPT-3 pre-test investigated hydraulic connections between the KI0025F02:R2 interval containing BG1 and the KI0025F03:R3 interval containing Structure #19. A strong normalised drawdown dh/Q of approximately 10^5 s/m^2 was also seen for this connection.
- The tracer test CPT-4b (Q = 2.4 l/min pumping) showed a conservative tracer travel time t_5 of around 170 hours from BG1 in KI0025F02 to Structure #19 in KI0025F03 The BS2B conservative tracer travel time t_5 for a similar pumping rate (2.8 to 2.5 l/m pumping) showed a conservative tracer (Eu and HTO) travel time t_5 of 150 to 183 hours.

Based on the above evidence based on hydraulic and conservative tracer tests, it can be hypothesised that there are fractures connecting from BG1 to the nearby (5.4 m away) Structure #19. This would be consistent both with the similar hydraulic response and the similar conservative tracer transport times. This could be achieved within the existing hydrostructural model by including BIPS log fractures observed in KI0025F02, as shown in Figure 2-6. The orientation of these fractures in the BIPS log is such that these fractures provide a direct connection between BG#1 and Structure #19.

However, the comparison between tracer testing results for Flow paths I and II provide a completely different conclusion.

- The advective travel time on Flow path I is approximately 10% of that for Path II (Table 3-11 and Table 3-12). Therefore, if there were fractures making a direct connection, then the flow on the 5 m Cartesian distance between BG#1 and Structure #19 would require an unrealistically large transport aperture to achieve this longer travel time.
- The effective immobile zone solute retention material properties are distinctly lower for Flow path II as compared to Flow path I (Table 5-3). This indicates that Flow path II can not include a significant length on Structure #19.

The conclusion from this is that the hydrostructural model for BG#1, as shown above in Figure 5-16, is consistent with the available data. With reference to the questions posed above:

a) A fracture BG1 extending all the way to the pumping section of KI0025F03:R3 in Structure #19 would be consistent with tracer test results.

b) BG1 must connect to Structure #19 since there was a strong hydraulic response noted in CPT2. The most likely way for this connection to occur is through background fractures which are not seen in boreholes, i.e. stochastic background fractures. The stochastic background fracture (-s) connecting BG1 to Structure #19 at KI0025F02 may not be part of Flow path II because of the difference in the flow field between CPT-2 and CPT-3.

c) Very little of Flow path II can be along Structure #19 due to the distinctly different immobile zone solute retention properties. BG1 can therefore either be of a scale greater than 20 m radius (to approach KI0025F03), or else Flow path II must be made up of either a large number of stochastic background fractures, or a stochastic background fracture of this particular length scale.

d) While the effective dispersion length back-calculated for Flow path II is relatively small (1.4–5.3 m) /Andersson et al. 2005/, it is more likely that Path II contains a small number of connected background fractures.

e) The lower immobile zone retention observed for Flow path II supports the hypothesis that BG#1 is a “Type 2” fracture with limited high porosity immobile zones, cf Section 5.3.4.

The points above essentially confirm the hydrostructural model derived for BG#1, and employed in the predictive modelling. The differences between predictive and evaluation modelling are within the range of the geometrical uncertainty related to BG1 within the hydrostructural model.

From the above discussion, it is important to note that the hydrostructural model for BG1 from the single-hole BIPS and flow logs were associated with significant uncertainty, but in the end were found to be useful all the way through a complex set of hydraulic and tracer experiments. This emphasises the value and merit of geologic characterisation, and the use of hydrostructural models based on such data, provided uncertainty is properly accounted for and incorporated in the analysis.

5.4.3 Stochastic background fractures

The Andra and JNC/Golder DFN modelling included populations of statistically generated background fractures (Figure 5-4 through Figure 5-9). The questions addressed were:

a) how important are these stochastic background fractures for the transport pathways I and II,

b) how well have the TRUE Block Scale experiments confirmed the existence of these fractures.

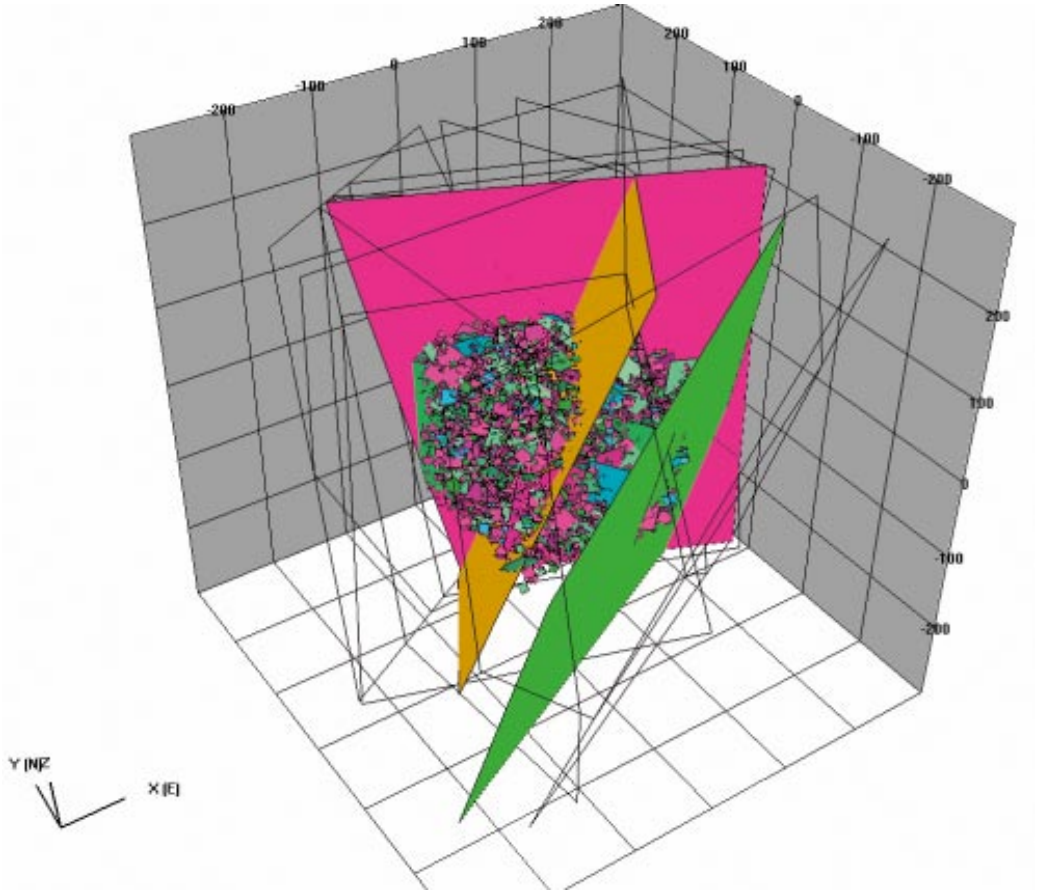

Figure 5-17. *Baseline DFN Model. View is to the northeast, looking towards the Äspö HRL tunnel. The wire frame fractures represent the structures which provide connection to the hydraulic boundaries for the 500 m model.*

The results show that the stochastic background fractures are not overly important for Flow path I since this path is dominated by the deterministic Structure #19. Similarly, the evaluation of Flow path II emphasises the role of the background fracture, and more so the effects of a series of interconnected background fractures.

5.4.4 Hydrostructural model framework

The TRUE Block Scale Continuation hydrostructural model includes a number of structures beyond Structure #19 and BG#1, which were evaluated as part of the TRUE-BSC experiment. In particular, these structures influenced (a) the head field in the rock block, (b) the transient response in hydraulic interference tests, and (c) solute recovery in CPT experiments.

Points to be made: 1) the existence of nearby high K/high porosity structures to the east and west is confirmed. 2) the locations of these structures is consistent with what was assumed from TRUE Block Scale characterisation 3) The experiment did not depend on a reduction in the (currently huge) uncertainty about these structures, 4) The experiment did not significantly reduce this uncertainty.

6 Discussion of important findings

In the following sections the important findings of the TRUE Block Scale Continuation Project are reviewed. In Chapter 7 the conclusions of the project are drawn.

6.1 Possibility to conduct experiments over longer distances

As deliberated in Section 1.4, a comprehensive effort has been made by the project (and the JNC-Golder team in particular) to assess the prospects for testing and analysis of longer flow paths, including those involving low-transmissive background fractures. Various difficulties foreseen (e.g. hydraulic short-circuiting) and the possible increase of the number of injection points in background fractures were analysed in a quantitative fashion. Although the ambition was to explore longer fracture network flow paths, the results convincingly showed that tests involving long complex flow paths would result in transport times well beyond the time frames of the planned BS2B tracer tests. Furthermore, the projected tracer mass recoveries would not be sufficiently high to allow use of radioactive sorbing tracers in the analysed flow paths. Instead, the focus for the planned experimental activities was shifted to the inner parts of the TRUE Block Scale rock volume. The selected main feature for experimentation (Structure #19) is intercepted by most boreholes, with good hydraulic connectivity, enabling variable injection and pumping points. Furthermore, the selected locality is unaffected by the identified short circuiting, and allow opportunity for possible injection in background fractures connected to the major structure. Given that the experimental focus was directed to a structure and environs yet untested with cross-hole tracer experiments allowed for a test of the prediction capability of sorbing tracer transport and retention as established on the basis of the established geological know how to date.

6.2 In situ experiments

The series of tracer experiments conducted, the CPT-1 through CPT-4 pre-tests /Andersson et al. 2004b/ and the BS2B tracer tests /Andersson et al. 2005/ have performed well and have overall confirmed the hydrostructural model of Structure #19. The identification of an injection point with acceptable tracer mass recovery in a background fracture also opened up for tests in a flow path involving a background fracture, and ultimately for a comparison between a pure fault type (Type 1) flow path (Flow path I) in Structure #19 with a flow path (Flow path II) involving injection in a background fracture (BG1) in direct, or indirect, contact with Structure #19. The experimental results have enabled address of retention in a non-fault (background fracture) flow path compared to that in fault type flow path, cf further discussion in Sections 6.4 through 6.8.

6.3 Model predictions

The model predictions of the outcome of the BS2B sorbing tracer tests, cf Section 4.6, should primarily be regarded as a receipt of our capability to transfer our geological understanding and associated assignment of retention properties to another, previously untested part of the TRUE Block Scale rock volume. Overall the predictions of transport in Flow path I compare well with the experimental outcome, whereas the picture is more erratic in the case of the background fracture flow path (Flow path II). This largely reflects the level of information available for the two flow paths. Flow path I is essentially constrained geometrically by the global geometry of Structure #19, although flow paths extending outside the bounds of Structure #19 cannot

be excluded. Furthermore, the microstructural model for this structure has a strong kinship with the previously investigated Feature A /Winberg et al. 2000/ and Structure #20 /Andersson et al. 2002ab, Poteri et al. 2002/. In the case of Flow path II the uncertainties of the applicable microstructural model are probably significantly smaller, given that the structure is interpreted as a non-complex non-fault fracture. However, the uncertainty about the true nature and intricacy of the geometry of this flow path, see also Section 6.4, is significantly higher, in part explaining the outcome of the predictions relative to this flow path.

6.4 Geometries of transport paths

As reasoned in Section 6.3, the geometry of Flow path I is relatively well constrained, although the distribution of flow paths over the plane of Structure #19 is not known deterministically. The uncertainty in the geometry of Flow path I is assumed less than for Flow path II. In the latter case we will never establish the exact nature of the number of fractures making up the flow path and their interrelations.

An attempt is made in Section 5.2 to visualise the two flow paths on the basis of select realisations from the two discrete channel network models employed by ANDRA-Itasca and JNC-Golder, respectively. Irrespective of the unknown nature of the exact geometry of the two flow paths, the unified analysis of the breakthrough curves from the two injections therein can be used to assess the relative retention between the two flow paths, cf Section 6.5. Still, the discrete channel network models demonstrate that, at the scale of the tracer test, the same network statistics can yield realisations with highly dissimilar pathways.

6.5 Immobile zone retention properties

The retention properties of Flow path II (involving fracture BG1) are evaluated indirectly, by inferring retention properties of Flow path I (Structure #19) from the breakthrough curve of the injection in Flow path I, and then using that result to deduce retention properties of Flow path II. It is noted that the retention material parameter group of Flow path II is considerably lower than that for Flow path I, and its back-calculated effective material property group κ_{eff} is found to be equivalent to intact to altered Äspö granite, cf Figure 5-15, whereas the effective material property group κ_{eff} of Flow path I, for the experimental times scales considered, is reflecting more the retention properties of fracture coating to cataclasite materials.

The evaluated hydrodynamic control parameter of Flow path II is close to two orders of magnitude higher than that for Flow path I, cf Figure 5-14. This is consistent with smaller flow rate (longer residence times) and longer flow path length inferred from the hydrostructural model (Section 6.7), and the geologic designation of BG1 as a non-fault (background) fracture. The evaluation results provide a clear indication that although the immobile zone retention properties are weaker in Flow path II, the overall retention (taking effects of both κ and β into account) is stronger for Flow path II than for Flow path I due to the higher hydrodynamic control parameter β evaluated to Flow path II.

All model approaches demonstrate that the implementation of the microstructural model is important for the resulting effective immobile zone retention properties. Differences in this implementation introduce uncertainty in the evaluated parameterisation of the flow field and immobile zone retention properties. In the modelling results this is evident in a larger spread in the evaluated retention properties of the more complex flow path (involving Type 2 fractures), because retention is significantly different in the Type 1 structures than in the Type 2 background fractures.

6.6 Assessment of background fracture retention properties

An interesting outcome of the BS2B experiments and their evaluation may alleviate the burden of characterising retention properties in networks of background fractures and structures. These two populations (i.e. background fractures and larger (deterministic) structures) can be studied independently of each other: on the one hand, a path originating and finishing in the same structure will be extremely unlikely to leave the particular structure, because of the higher conductivity of the structure, and will therefore be essentially insensitive to background fracture network properties. On the other hand, we can use a structure as a "sink" for a path originating in a background fracture. While permitting acceptable recoveries, travel is so much faster in the structure, that we can disregard the part of the transport path in the structure, and consider only reactive transport in the background fractures network. Therefore, the TRUE Block Scale continuation tests have confirmed the feasibility of testing retention of background fractures.

6.7 Assessment of hydrostructural model

The hydrostructural model at Structure #19 is substantially confirmed by the results of BS2 hydraulic and tracer tests between sections located at the interpreted location of Structure #19.

The hydraulic inherence tests (pre-tests) /Andersson et al. 2004/ clearly show evidences of Structure #19 acting as a planar effectively homogeneous conductive structure. Flow in Structure #19 is essentially radial at intermediate distances, and is similar for the different borehole intersections. This behaviour is comparable to that of Structure #20, investigated in the TRUE Block Scale project /Andersson et al. 2002a/.

The conservative tracer tests /Andersson et al. 2004, 2005/ carried out between boreholes intersecting what is interpreted as Structure #19 show advective travel times and evaluated dispersion values consistent with flow in a single, planar structure over the distance in question.

The magnitude of the effective solute retention values from the BS2B sorbing tracer experiments, see Section 5.3, are consistent with those that would be expected for transport on a fracture plane in contact with the immobile zones as inferred for the microstructural models of the fracture types on the basis of performed laboratory experiments, cf Table 6-1.

The evidence for the existence of background fracture BG1, that constitutes the point of injection for Flow path II, is limited to a single flow log and a BIPS log. Since BG1 is only known in one borehole, it is not possible to definitively assign a size to this fracture. It is expected that the local fracture orientation determined from the single borehole intersection may differ 10 to 30 degrees compared to the average orientation of the BG1 actual fracture plane. Consequently, the hydrostructural model is very uncertain concerning BG1 and the associated Flow path II.

Only very small portions of Flow path II can be along Structure #19 due to the distinctly different immobile zone solute retention properties. BG1 may therefore either be of the scale of greater than 20 m radius (to approach borehole KI0025F03), or Flow path II must be made up of either a large number of stochastic background fractures, or a stochastic background fracture of this scale. The DFN-based channel network realisations analysed suggest that the true length of Flow path II may vary between 50 to 70 metres, being made up of multiple background fractures.

Table 6-1. Summary of involved structures and dominant fracture types in the investigated flow paths.

Flow path	BG1	Structure #19	Dominant fracture type
I		X	Type 1
II	X	x	Type II

The weaker immobile zone retention observed on Flow path II supports the hypothesis that BG1 (and possible additional fractures connecting to Structure #19) is a Type 2 fracture with limited high porosity immobile zones.

These results indicate that assessment of transport properties needs to be made as a combination of discrete fracture network analysis to evaluate the pathway geometry, and immobile zone geochemical experiments to assess the retention properties of fractures and fracture populations.

6.8 Revisiting the stated hypotheses

As discussed in Section 1.5, of the palette of hypotheses originally discussed for the TRUE Block Scale Continuation project, only two can be regarded to be covered by the final experimental scales and associated analysis. These are;

- *Hypothesis Ia) Microstructural (i.e. detailed geological, mineralogical and geochemical) information can provide significant support for predicting transport of sorbing solutes at experimental time scales,*

As outlined in the preceding sections, the combined efforts of geological and mineralogical know how and experience, as expressed in the developed hydrostructural and microstructrural models, have helped make relatively accurate predictions of the outcome of the performed tracer test (Section 6.3). It should of course be acknowledged that the export and projection is not long in spatial scale. The investigated structure is at Äspö HRL, and less than 100 m away from the experimental focus of TRUE Block Scale. The real test of exporting geological information comes when applying the findings of the TRUE programme to transport problems elsewhere, e.g. in conjunction with the ongoing site investigations in the Simpevarp and Laxemar areas /SKB 2006/.

- *Hypothesis Ib) Transport at experimental time scales is significantly different for faults (significant alteration, brecciation and fault gouge) and joints (with or without alteration), due to differences in microstructure and associated properties.*

High hopes were originally placed on the possibility to conduct sorbing tracer experiments in an isolated single background fracture. This turned out futile, but we were still left with an injection point in a low-transmissivity non-fault background fracture in hydraulic contact with the sink in the larger fault type Structure #19. We show successfully how the joint analysis of the breakthrough data from the two flow paths can be used to verify the retention material properties of background fractures as suggested by the parameterised microstructural model for Type 2 fractures. Moreover, we demonstrate that the background fracture Flow path II still exhibits a higher overall retention (taking both κ and β into account) while the hydrodynamic control parameter β of Flow path II is found to be close to two orders of magnitude higher compared to Flow path I, consistent with smaller flow rate (longer residence times) (Section 6.5) in Flow path II, and that the parameter κ is about one order of magnitude higher in Flow path I compared with Flow path II.

7 Conclusions

In the following the main conclusions of the TRUE Block Scale project are summarised:

- The lower immobile zone retention material properties assigned to background fractures compared to those assigned to the fault-type Structure #19 have been verified by means of back-calculations. The evaluated structure flow path (Structure #19) retention material properties, as expressed by the κ parameter, are about one order of magnitude higher than for the background fracture flow path. This finding is consistent with the developed microstructural models. It is noted that the observed difference is applicable to experimental time scales while at longer time scales the retention capacity of the fault type fractures may become saturated.
- The overall retention (taking effects of both κ and β into account) in the background fracture Flow path II is found to be about one order of magnitude higher than for Flow path I. This finding is attributed to the fact that that the flow rate is significantly lower compared with Flow path I, resulting in longer residence times.
- The presented results are consistent with Flow path I being contained in a planar structure with immobile zones assigned according to the microstructural model. Similarly, the results suggest Flow path II is being made up of a set of background fractures, including BG1.
- The uncertainty associated with the analysis and interpretations has been evaluated quantitatively, demonstrating that the uncertainty in the hydrodynamic (pathway length and velocity) parameter group β is higher than that for the retention (physical and geochemical) parameter group κ. This analysis supports the development of more realistic hydrostructural models with uncertainty represented through discrete fracture network (DFN) simulations for radionuclide transport in crystalline rock.
- The analysis (prediction and evaluation) made of the TRUE Block Scale Continuation tracer tests demonstrates clearly that a good geological basis (as expressed in the developed hydrostructural and microstructure models) is important for understanding sorbing tracer transport in fractured crystalline rock.

The quantitative analysis pertaining to the background fracture Flow path II suggests that background fracture flow paths, although with poor material retention properties, may contribute significantly to retention because of the low flow rates expected in them. Given that the current results are based on one sole experimental result there exists a need to further substantiate the present findings.

It is noted that the presented evaluation is focused sloley on the TRUE Block Scale Continuation Experiments. The final joint evaluation of TRUE-1, TRUE Block Scale and TRUE Block Scale Continuation is still to be carried out.

8 References

Andersson P, 1996. TRUE 1st stage tracer test program. Experimental data and preliminary evaluation of the TRUE-1 radially converging tracer test. Äspö Hard Rock Laboratory Progress Report HRL-96-24.

Andersson J, Elert M, Hermanson J, Moreno L, Gylling B, Selroos J-O, 1998. Derivation and treatment of the flow wetted surface and other geosphere parameters in the transport models FARF31 and COMP23 for use in safety assessment. SKB R-98-60, Svensk Kärnbränslehantering AB.

Andersson P, Wass E, Holmqvist M, 2000. TRUE Block Scale. Tracer Test Stage. Tracer tests, phase B. Äspö Hard Rock Laboratory International Progress Report IPR-00-29, Svensk Kärnbränslehantering AB.

Andersson P, Byegård J, Holmqvist M, Skålberg M, Wass E, Widestrand H, 2001. TRUE Block Scale tracer test stage. Tracer tests, phase C. Äspö Hard Rock Laboratory International Progress Report IPR-01-33, Svensk Kärnbränslehantering AB.

Andersson P, Byegård J, Dershowitz W, Doe T, Hermanson J, Meier P, Tullborg E-L, Winberg A, 2002a. TRUE Block Scale Project. Final report. 1. Characterisation and model development. SKB TR-02-13, Svensk Kärnbränslehantering AB.

Andersson P, Byegård J, Winberg A, 2002b. TRUE Block Scale Project Final Report 2. – Tracer tests in the block scale. SKB TR-02-14, Svensk Kärnbränslehantering AB.

Andersson P, Gröhn S, Nordqvist R, Wass E, 2004. TRUE Block Scale Continuation, BS2 Pretests. Crosshole interference, dilution and tracer tests, CPT-1 CPT-4. SKB International Progress Report IPR-04-25, Svensk Kärnbränslehantering AB.

Andersson P, Byegård J, Tullborg E-L, Doe T, Hermanson J, Winberg A, 2004a. In situ tracer testst to determine retention properties of a block scale fracture network in granitic rock at the Äspö Hard Rock Laboratory, Sweden. J. Cont. Hydrology, vol 70, pp 271–297.

Andersson P, Byegård J, Nordqvist R, Wass E, 2005. TRUE Block Scale Continuation. BS2B tracer tests with sorbing tracers. Äspö HRL International Progress Report IPR-05-01, Svensk Kärnbränslehantering AB.

Bath A, Jackson C P, 2003. Review of Task 5. Äspö HRL International Progress Report SKB IPR-03-10, Svensk Kärnbränslehantering AB.

Bear J, 1972. Dynamics of fluids in porous media, American Elsevier Publishing Co., New York, New York.

Billaux D, 2005. Analysis of Reactive Transport in a Fault Structure and Associated Background fractures. TRUE Block Scale Continuation project. Äspö HRL International Progress Report IPR-05-37, Svensk Kärnbränslehantering AB.

Black J, Hodgkinson D, 2005. Review of Task 6C. SKB R-05-33, Svensk Kärnbränslehantering AB.

Byegård J, Johansson H, Skålberg M, Tullborg E-L, 1998. The interaction of sorbing and non-sorbing tracers with different Äspö rock types: sorption and diffusion experiments in the laboratory scale. SKB TR-98-18, Svensk Kärnbränslehantering AB.

Byegård J, Skarnemark G, Skålberg M, 1999. The stability of some metal EDTA, DTPA and DOTA complexes: Application as tracers in groundwater studies. J Radioanalytical and Nuclear Chemistry, vol 241, no 2, pp 281–290, August 1999.

Byegård J, 2002. Tracer Retention Understanding Experiments. Continued sampling and tracer measurements in the TRUE-1 experiment and TRUE Block Scale experiment, Phase C. Äspö Hard Rock Laboratory International Progress Report IPR-02-69, Svensk Kärnbränslehantering AB.

Byegård J, Tullborg E-L, in prep. Sorption experiments and leaching studies using fault gouge and rim zone materials from the Äspö Hard Rock Laboratory. TRUE-1 Continuation project. Äspö HRL International Progress Report in prep, Svensk Kärnbränslehantering AB.

Cheng H, Cvetkovic V, Selroos J-O, 2003. Hydrodynamic control of tracer retention in heterogeneous rock fractures. Water Resour. Res., 39, 1130–1139.

Cheng H, Cvetkovic V, 2005. Evaluation of the BS2B sorbing tracer tests using the LASAR approach. TRUE Block Scale Continuation Project. Äspö HRL International Progress Report IPR-05-39, Svensk Kärnbränslehantering AB.

Cvetkovic V, Selroos J-O, Cheng H, 1999. Transport of reactive tracers in rock fractures, J. Fluid Mech., 378, 335–356.

Cvetkovic V, Cheng H, Selroos J-O, 2000. Evaluation of Tracer Retention Understanding Experiments (first stage) at Äspö. International Cooperation Report, ICR-00-01, Svensk Kärnbränslehantering AB.

Cvetkovic V, Cheng H, 2002. Evaluation of block scale tracer retention understanding experiments at Äspö HRL. Äspö Hard Rock Laboratory. International Progress Report IPR-02-33, Svensk Kärnbränslehantering AB.

Cvetkovic V, Haggerty R, 2002. Tansport with multiple-rate exchange in disordered media. Phys. Rev. E 65, 051308.

Cvetkovic V, 2003. Significance of diffusion limitations and rim zone heterogeneity for tracer transport through fractures at the Äspö site. TRUE Block Scale Continuation project. Äspö HRL International Progress Report IPR-03-43, Svensk Kärnbränslehantering AB.

Cvetkovic V, Painter S, Outters N, Selroos J-O, 2004. Stochastic simulation of radionuclide migration in discretely fractured rock near the Äspö Hard Rock Laboratory. Water Resour. Res., 40, W02404, doi:10.1029 /2003WR002655.

Cvetkovic V, Cheng H, Widestrand H, Byegård J, Winberg A, Andersson P, in manuscript. Sorbing tracer experiments in a crystalline rock fracture at Äspö (Sweden): 1. Experimental results, conceptual model and effective parameter estimation. Paper submitted to Water Resources Research.

Darcel C, 2003. Assessment of the feasibility of tracer tests with injection in “background fractures” using a model based on a power law fracture length distribution. TRUE Block Scale Continuation project. Äspö HRL International Progress Report IPR-03-41, Svensk Kärnbränslehantering AB.

Dershowitz W, Shuttle D A, Foxford T, Eiben Th, 2000. PAWorks: Pathways Analysis for discrete fracture networks with LTG solute transport: User Documentation. Version 1.62. Golder Associates Inc., Seattle.

Dershowitz B, Klise K, 2002. Evaluation of fracture network transport pathways and processes using the Channel Network approach. Äspö Hard Rock Laboratory. International Progress Report IPR-02-34, Svensk Kärnbränslehantering AB.

Dershowitz W, Winberg A, Hermanson J, Byegård J, Tullborg E-L, Andersson P, Mazurek M, 2003. Task 6C. A Semi-synthetic Model of Block Scale Conductivite Structures at the Äspö HRL. SKB, International Progress Report, IPR-03-13, Svensk Kärnbränslehantering AB.

Doe T, 2002. Generalized dimension analysis of build-up and pressure interference tests. TRUE Block Scale Project. Äspö HRL International Progress Report IPR-02-70, Svensk Kärnbränslehantering AB.

Dougherty D E, Babu D K, 1984. Flow to a partially penetrating well in a double-porosity reservoir, Water Resour. Res., 20 (8), 1116–1122.

Elert M, 1999. Evaluation of modelling of the TRUE-1 radially converging tests with conservative tracers. The Äspö Task Force on Modelling of Groundwater Flow and Transport of Solutes. Tasks 4C and 4D. SKB TR-99-04, Svensk Kärnbränslehantering AB.

Elert M, Svensson H, 2001. Evaluation of modelling of the TRUE-1 radially converging tests with conservative tracers. The Äspö Task Force on Modelling of Groundwater Flow and Transport of Solutes. Tasks 4E and 4F. SKB TR-01-12, Svensk Kärnbränslehantering AB.

Fox A, Dershowitz W, Ziegler M, Uchida M, Takeuchi S, 2005. BS2B Experiment: Discrete Fracture and Channel Network Modeling of Solute Transport Modeling in Fault and Non-Fault Structures. TRUE Block Scale Continuation Project. Äspö HRL International Progress Report IPR-05-38, Svensk Kärnbränslehantering AB.

Gustafson G, Ström S, 1995. Evaluation of report on Task No 1, the LPT2 large scale field experiments. The Äspö Task Force on Modelling of groundwater flow and transport of solutes. Äspö HRL International Cooperation Report ICR-95-05, Svensk Kärnbränslehantering AB.

Hakami E, Wang W, in prep. Characterisation and quantification of samples of in situ resin-impreganted rock using image analysis. Fault rock zone characterisation, TRUE-1 Continuation project. Äspö HRL International Progress Report (in prep), Svensk Kärnbränslehantering AB.

Hodgkinson D, Black J, 2005. Review of Tasks 6A, 6B and 6B2. SKB TR-05-14, Svensk Kärnbränslehantering AB.

Holmqvist M, Andersson P, Byegård J, Trick T, Fierz T, Eichinger L, Scholtis A, 2002. TRUE Block Scale Project. Detailed Characterisation satge. Test of new possible non-reactive tracers. Experimental description and evaluation. Äspö Hard Rock Laboratory International Progress Report IPR-02-71, Svensk Kärnbränslehantering AB.

Jakob A, Mazurek M, Heer W, 2003. Solute transport in crystalline rocks at Äspö – II: Blind predictions, inverse modelling and lessons learnt from test STT1. J Cont Hydrology 61, 175–190.

Kornfält K-A, Wikman H, 1988. The rocks of the Äspö island. Description of the detailed maps of solid rocks including maps of 3 uncovered trenches. Äspö Hard Rock Laboratory, Progress Report PR 25-88-12, Svensk Kärnbränslehantering AB.

Maersk Hansen L, Staub I, 2004. Overcoring (300 mm) of impregnated fault rock zones at chainages 2/430, 2/545, 2/163 and 1/1600. Fault rock characterisation, TRUE-1 Continuation project. Äspö HRL International Progress Report IPR-04-10, Svensk Kärnbränslehantering AB.

Marschall P, Elert I, 2003. Overall evaluation of the modelling of the TRUE-1 tracer tests – Task 4. The Äspö Task Force on Modelling of Groundwater Flow and Transport of Solutes. SKB TR-03-12, Svensk Kärnbränslehantering AB.

Mazurek M, Jakob A, Bossart P, 2003. Solute transport in crystalline rocks at Äspö – I: Geological basis and model calibration. J Cont Hydrology 61, 157–174.

Miller I, Lee G, Dershowitz W, Sharp G, 2001. MAFIC Matrix/Fracture Interaction Code with Solute Transport. User Documentation, Version 1.5. Golder Associates Inc, Seattle.

Poteri A, Billaux D, Cvetkovic V, Dershowitz B, Gómez-Hernández J-J, Hautojärvi A, Holton D, Medina A, Winberg A, 2002. TRUE Block Scale Project. Final Report – 3. Modelling of flow and transport. SKB TR-02-15, Svensk Kärnbränslehantering AB.

Poteri A, 2003. Retention processes discrimination for various assumptions of fracture heterogeneity. TRUE Block Scale Continuation project. Äspö HRL International Progress Report IPR-03-42, Svensk Kärnbränslehantering AB.

Poteri A, 2005. Evaluation of the BS2B sorbing tracer tests using the Posiva streamtube approach. TRUE Block Scale Continuation project. Äspö HRL International Progress Report IPR-05-36, Svensk Kärnbränslehantering AB.

Poteri A, 2006. Evaluation of the BS2B sorbing tracer tests using the Posiva streamtube approach. TRUE Block Scale continuation project. SKB, International Progress Report, IPR-05-36, Svensk Kärnbränslehantering AB.

Rhén I, Gustafsson G, Stanfors R, Wikberg P, 1997b. Äspö HRL-Geoscientific evaluation 1997/5. Models based on site characterization 1986–1995. SKB TR 97-06, Svensk Kärnbränslehantering AB.

Rhén I, Smellie J, 2003. Task 5 summary report. SKB TR-03-01, Svensk Kärnbränslehantering AB.

SKB, 2006a. Preliminary site description, Laxemar subarea – version 1.2, SKB R-06-10, Svensk Kärnbränslehantering AB.

Sudicky E A, 1989. The Laplace transform Galerkin technique: A time-continuous finite element theory and application to mass transport in groundwater. Water Resour. Res., 25(8), pp 1833–1846.

Sudicky E A, 1990. The Laplace transform Galerkin technique for efficient time-continuous solution of solute transport in double-porosity media, Geoderma, 46, pp 209–232.

Sudicky E A, McLaren R, 1992. The Laplace transform Galerkin technique for large-scale simulation of mass transport in discretely fractured porous formations, Water Resour. Res., 28(2), 499–514.

Wahlgren C-H, Hermanson J, Curtis P, Forssberg O, Drake H, Tullborg E-L, 2005. Geological description of rock domains and deformation zones in the Simpevarp and Laxemar subareas. Preliminary site description, Laxemar subarea, version 1.2. SKB R-05-69, Svensk Kärnbränslehantering AB.

Widestrand H, Byegård J, Cvetkovic V, Tullborg E-L, Winberg A, Andersson P, Siitari-Kauppi M, in manuscript. Sorbing tracer experiments in a crystalline rock fracture at Äspö (Sweden):2. Micro-scale characterization of retention properties. Paper submitted to Water Resources Research.

Winberg A, 1997. Test plan for the TRUE Block Scale Experiment. Äspö Hard Rock Laboratory. International Cooperation Report ICR 97-02, Svensk Kärnbränslehantering AB.

Winberg A, Andersson P, Hermanson J, Byegård J, Cvetkovic V, Birgersson L, 2000. Final report of the first stage of the tracer retention understanding experiments. SKB TR-00-07, Svensk Kärnbränslehantering AB.

Winberg A, Andersson P, Poteri A, Cvetkovic V, Dershowitz W, Doe T, Hermanson J, Gómez-Hernández J J, Hautojärvi A, Billaux D, Tullborg E-L, Holton D, Meier P, Medina A, 2002. TRUE Block Scale Project. Final report – 3. Synthesis of flow, transport and retention in the block scale. SKB TR-02-16, Svensk Kärnbränslehantering AB.

Åhäll K-I, 2001. Åldersbestämning av svårdaterade bergarter i sydöstra Sverige. SKB R-01-60. Svensk Kärnbränslehantering AB (in Swedish).

Appendix A

Assignment of distribution of geological structure type, complexity and parameters of the micro-structural model applicable to the predictive modelling of the BS2B sorbing experiment

TRUE Block Scale Continuation

Eva-Lena Tullborg, Terralogica AB

Jan Hermanson, Golder Associates AB

2004-06-15

Comments to the structure table

- Type 1 and Type 2 refers to Task 6C definition /cf Dershowitz et al. 2003/.
- **Complexity factor** indicates the number of conducting fractures in the structure.
- The micro-structural table (Table 1) below gives details for the Type 1 and Type 2 structures. Note that some thicknesses have been changed compared with the Task 6C definition. See also associated PowerPoint presentation.
- Width: is the width in centimetres of the tectonised/altered section of the zone. One intercept of Structure #22 and one intercept of Structure #20 (KI0025F) are so close that the altered parts overlap.
- Observe that the previously notation "Structure #25" (subsequently renamed to "BG1") is no longer valid! Instead the intercept in borehole KI0025F02 L = 138.5 (N30W/76NE) which is used as one injection point the ongoing BS2B Sorbing experiment is from now on named "BG1" (Background fracture 1).
- In borehole KA2563A a hydraulically conductive splay associated with Structure #19 is recorded at L = 245.5 (N55W/54 NE) (denoted "#19 Splay" in the table below) whereas the hydraulically active structure intercept interpreted at L = 237.85 m is interpreted as the main intercept with Structure #19, although being less conductive than "#19 Splay".

Table A-1. Detailed assignment of a) distribution of structure types and associated complexity to the deterministic structure of the TRUE Block Scale structures. Update made using the Task 6C assignment /Dershowitz et al. 2003/ as a base.

Structure	Number of intercepts	Distribution of structure types and complexities		
#5	4	100% Type 2 Complexity: 2 Width 5–12 cm		
#6	5	40% Type 1 Compexity 1 Width:5–20 cm	20% Type 1 Complexity 2 Width: 20 cm	40% Type 2 Compexity 2 Width:10 cm
#7	5	60% Type 1 Compexity 3 Width 30–60 cm	20% Type 1 Compexity 2 Width 15	20% Type 2 Compexity 2 Width 5
#8	2	50% Type 1 Compexity 3 Width:60 cm	50% Type 2 Complexity 2 Width 35	
#10	2	50% Type 2 Compexity 3 Width:20 cm	50% Type 2 Compexity 2 Width:15 cm	
#13	4	75% Type 1 Complexity 2 Width 15–20 cm	25% Type 2 Complexity 1 Width 15 cm	
#19	5	60% Type 1 Complexity 2 Width 20–100 cm	20% Type 1* Complexity 3 Width 100 cm	20% Type 2 Complexity 1 Width 10
#19 Splay	1	100% Type 2 Complexity 1 Width: 5 cm		
#20	5	60% Type 1 Complexity 3 Width 25–40	20% Type 1 Compexity 2 Width 30 cm	20% Type 1 Compexity 1 Width 100 cm*
#21	3	33% Type 1 Compexity 2 Width 15 cm	66% Type 2 Compexity 2 Width 25–10 cm	
#22	3	33% Type 1 Compexity 3 Width 55 cm	33% Type 1 Compexity 2 Width 100 cm*	33% Type 1 Compexity 1 Width 15 cm

Structure	Number of intercepts	Distribution of structure types and complexities		
#23	2	100% Type 2 Compexity 1 Width:5 cm		
#24	4	25% Type 1 Compexity 2 Width 20 cm	25% Type 1 Compexity 1 Width 10 cm	50% Type 2 Compexity 1 Width 5 cm
BG1 NB. No structure!	1	100% Type 2 Complexity 1 Width 5 cm		
#Z	1	100% Type 1 Compexity 3 Width 600 cm		

Micro-structural model

The microstructural models for Geological Structure Type 1 and Type 2 are quantified in terms of the thickness of each of the geometrically defined (immobile) zones, and the porosity and formation factor of those zones. Since both Type 1 and Type 2 structures can be made up of multiple discrete features, the representative thickness provided of each of the zones is per feature. Larger structures tend to be made up of more features, and will consequently have a greater total thickness of each zone. In addition, the thickness of each zone can be scale dependent. The properties of the Geological Structure Type 1 and Type 2 are provided in Table A-2, Table A-3 and Table A-4, respectively. Note that two different tables are given for type 1 structures. Table A-3 should be used for Zone Z.

Table A-2. Properties of Geological Structure Type 1 (Fault).

Rock type	Thickness (cm)	Porosity (%)	Formation factor (−)
Intact wall rock	−	0.3	7.3E–5
Altered zone	15	0.6	2.2E–4
Cataclasite/Mylonite d_{cm}	1	1	4.9E–4
Fault gouge d_g	0.3	20	5.6E–2
Fracture coating d_c	0.05	5	6.2E–3

Table A-3. Properties of Geological Structure Type 1 (Fault) to be used for #Z.

Rock type	Thickness (cm)	Porosity (%)	Formation factor (−)
Intact wall rock	−	0.3	7.3E–5
Altered zone	25	0.6	2.2E–4
Cataclasite/Mylonite d_{cm}	2	1	4.9E–4
Fault gouge d_g	0.5	20	5.6E–2
Fracture coating d_c	0.05	5	6.2E–3

Table A-4. Properties of 100-m Scale Geological Structure Type 2 (Non-fault).

Rock type	Thickness (cm)	Porosity (%)	Formation factor (−)
Intact wall rock	−	0.3	7.3E–5
Altered zone	5	0.6	2.2E–4
Fracture coating d_c	0.05	5	6.2E–3

Appendix B

Proposed sorption, porosity and diffusivity properties for the prediction modelling of the TRUE Block Scale Continuation BS2B sorbing tracer experiment

Johan Byegård, Geosigma AB

Eva-Lena Tullborg, Terralogica AB

2004-07-08

B1 Non-sorbing tracers

Dual sets of non-sorbing tracers were used for each injection in the BS2B sorbing experiments. For the injection in KI0025F02:R3 (#19), the tracers $^{131}I^-$ and $^{160}TbDTPA^{2-}$ were used. For the injection in KI0025F02:R2 (BG1), HTO and $^{155}EuDTPA^{2-}$ were applied as non-sorbing tracers.

B2 Sorption

B2.1 Structure #19

B2.1.1 Fault gouge material

Investigations of the different borehole intercepts with Structure #19 yielded significant amount of gouge material only for the KI0025F02 intercept. The results of the mineralogical analysis /Andersson et al. 2002a Table 7-3/ indicate high amounts of e.g. smectite (15%) and chlorite (30%). Based on literature data for cation exchange capacities, one would thus on the basis of this intercept expect high sorption coefficients for the sorbing tracers used in the TRUE Block Scale experiment.

However, no presence of significant amounts of gouge material could be found in the other intercepts with Structure #19. This could be interpreted as a presence of fault gouge material only in minor portions of the #19.

A contradictory observation is, however, that the most successful triple-tube drilling within the block was performed in the case of borehole KI0025F02. This could be an indication that the smectite/chlorite-rich fault gouge material actually is present in all parts of Structure #19 but could (based on the absence of fully successful triple-tube drilling in the other boreholes) only be successfully sampled at the KI0025F02 intercept.

An attempt to sample gouge material from the #19 intercept in borehole KI0025F was done by careful scraping off material from the surface of the fracture sample. Small amounts were obtained; not sufficient to be used for sorption experiments, but enough for mineralogical analyses. The analyses indicated that this fault gouge material had a different composition compared to the corresponding material from the KI0025F02 intercept; no smectite was present and mixed layer-clay was found instead.

Based on these facts, two alternative concepts for material property assignment to fault gouge material are proposed in the case of Structure #19:

A. Assigning the fault gouge material properties according only to the material sampled at the KI0025F02 intercept, i.e. based on the only #19 gouge material studied in the laboratory sorption experiment. The uncertainties given are based on the counting statistics in the measurements of a single sample (2σ confidence interval).

B. Assigning material properties to fault gouge materials as an ensemble average of the results from all the gouge materials analysed in the laboratory sorption experiments sampled from structures of the same magnitude/dignity as Structure #19. These samples are from Structures #19 (KI0025F02 intercept), #20 (KI0023B intercept) and #22 (KI0025F02 intercept). An average value is provided together with the interval observed in the laboratory experiments.

Table B-1. Assignment of volumetric sorption coefficient K_d according to the two outlined concepts A and B.

Tracer	Concept A K_d (m³/kg)	±	Concept B K_d (m³/kg)	Interval
$^{85}Sr^{2+}$	6.0E–4	3E–5	1.3E–3	(6.0–21)E–4
$^{86}Rb^{+}$	2.7E–3	9E–4	1.5E–2	(2.7–27)E–3
$^{137}Cs^{+}$	4.0E–2	1E–3	1.0E–1	(4.0–14)E–2

It is further noted that the fracture coating in accordance with the Type 1 structure in /Dershowitz et al. 2003/ is assigned equivalent properties as the fault gouge material described above.

B2.1.2 Fracture rim zone material

The fracture rim zone of Structure #19 has been categorised to consist of ~ 80% of "strongly hydrothermally altered rock" (represented by the intercept in KI0023B) and ~ 20% of "mylonitic and cataclasitic wall rock, in Äspö diorite" (represented by the intercept in borehole KI0025F). These two rock materials have been subject to sorption experiments giving the following results for the tracers used in the TRUE Block Scale Continuation experiment.

B2.2 Background fracture BG1

For estimating the material properties for the BG1 fracture, the only available source of information at present stage are BIPS images. From the images, it has been estimated that the fracture is located in weakly altered Äspö diorite. From general experiences of fractures of this magnitude, it has also been interpreted that an ~ 5% porous 0.5 mm (total) thick facture coating is present in the fracture, consisting of chlorite, calcite and illite.

Further analyses of BG1 will be available later when a closer inspection of the drill core will be done. From the minute data available at this stage, the material properties are estimated as follows:

- The fracture coating is assigned sorption properties based on the results of the laboratory sorption experiments using the fault gouge material sampled in borehole KI0023B (L = 69.9 m, Structure #20). The mineralogy of this material is estimated to consist of 20% illite, 20% chlorite and 25% calcite, which is the composition most similar to that of the BG1 fracture coating described above.
- The fracture rim zone material is assigned material properties from the laboratory experiments studying the sorption properties of altered Äspö diorite (TR-98-18).

Table B-2. Assignment of surface sorption coefficient K_a relevant to fracture rim zone material of Structure #19.

	Strongly hydrothermally altered rock (80%)				Mylonitic and cataclasitic wall rock, in Äspö diorite (20%)			
Tracer	K_a (m)	±	K_d (m³/kg)	±	K_a (m)	±	K_d (m³/kg)	±
$^{85}Sr^{2+}$	1.5E–5	5E–6	2.6E–5	1.5E–5	2.2E–5	9E–6	1.4E–4	2E–5
$^{86}Rb^{+}$	< 1E–4		< 4E–4		< 8E–4		< 4E–3	
$^{137}Cs^{+}$	1.0E–3	4E–6	< 5E–4		9.8E–3	5E–4	< 3E–2	

Table B-3. Assigned volumetric sorption coefficient K_d of fracture coating material of background fracture BG1.

Tracer	K_d (m³/kg)	± 1 st. dev.
$^{22}Na^{+}$	2.0E–4	1E–5
$^{133}Ba^{2+}$	2.7E–2	4E–3
$^{54}Mn^{2+}$	1.7E–1	6E–2

B2.2.1 Fracture coating material

As mentioned above, the source for the sorption coefficient of BG1 is the results of sorption experiment using the fault gouge material sampled at the intercept of Structure #20 in borehole KI0023B.

B2.2.2 Fracture rim zone material

From the results presented by /Byegård et al. 1998/, it is estimated that the altered Äspö diorite found in the Feature A intercept with KXTT2 is the best representative of the fracture rim zone of BG1. However, a drawback in the use of these data is that the tracer distribution ratio in these experiments was only determined for the 1–2 mm fraction. This means that an extrapolation using sorption data from different size fractions (in order to describe the sorption with surface sorption coefficients, K_a and volumetric sorption coefficient, K_d) cannot be performed for this material.

An alternative concept has therefore been used. Using the data from the recently performed laboratory sorption experiment /Byegård et al. 2004/, the following calculations have been done:

$$K_{\mathbf{d}x} = \left\langle \frac{K_{\mathbf{d}\,i}}{R_{\mathbf{d\,(1-2mm)}i}} \right\rangle_i \cdot R_{\mathbf{d(1-2mm)}x} \qquad (1)$$

where

K_{dx} mass sorption coefficient for the altered Äspö diorite.

$\left\langle \frac{K_{\mathbf{d}\,i}}{R_{\mathbf{d\,(1-2mm)}i}} \right\rangle_i$ average value for the ratios of the K_d-values and the distribution coefficients for the 1–2 mm size fraction. The data source is based the sorption of Ba^{2+} on all the six rim zone materials included in the on-going investigation /Byegård et al. 2004/.

$R_{d(1–2mm)x}$ measured distribution coefficient for altered Äspö diorite /Byegård et al. 1998/.

Similarily, the surface distribution coefficients (K_{ax}) for the altered Äspö diorite have been calculated according to:

$$K_{\mathbf{a}x} = \left\langle \frac{K_{\mathbf{a}\,i}}{R_{\mathbf{d\,(1-2mm)}i}} \right\rangle_i \cdot R_{\mathbf{d(1-2mm)}x} \qquad (2)$$

where

K_{ax} surface sorption coefficient for the altered Äspö diorite.

$\left\langle \frac{K_{\mathbf{a}\,i}}{R_{\mathbf{d\,(1-2mm)}i}} \right\rangle_i$ average value for the ratios of the K_a-values and the distribution coefficients for the 1–2 mm size fraction. The data source is based the sorption of Ba^{2+} on all the six rim zone material included in the on-going investigation /Byegård et al. 2004/.

Furthermore, the situation is complicated by the fact that no measured sorption coefficients are available for Mn^{2+} on fracture rim zone material. It has therefore been decided to use the ratio in measured K_d-values for Mn^{2+} and Ba^{2+} on fault gouge material sampled at the intercept of Structure #20 in borehole KI0023B for the calculation of the sorption coefficients for Mn^{2+} of altered Äspö diorite. This means that the K_a- and K_d-values for Ba^{2+} are multiplied with a factor (i.e. 0.17/0.027 = 6.3) to obtain the corresponding values for Mn^{2+}.

Table B-4. Volumetric (*Kdx*) and surface sorption (*Kax*) coefficients proposed for the BG1 rim zone material.

Tracer	$R_{d(1-2mm)}$ altered Äspö diorite /Byegård et al. 1998/	$\left\langle \frac{K_{di}}{R_{d(1-2mm)i}} \right\rangle_i$	K_{dx}	$\left\langle \frac{K_{ai}}{R_{d(1-2mm)i}} \right\rangle_i$	K_{ax}
$^{22}Na^{+}$	2.9E–6	0.58	1.7E–6	0.24	7.0E–7
$^{133}Ba^{2+}$	1.2E–3		6.9E–4		2.9E–4
$^{54}Mn^{2+}$	Not measured		4.3E–3*		1.8E–3*

*Calculated by multiplying the corresponding value of Ba^{2+} with a factor of 6.3, procedure described above.

B3 Porosity and diffusivity

No further experimental investigations of these parameters have been performed.

Based on the concept proposed and described for the Task 6C concept /Dershowitz et al. 2003/, general values for porosities are proposed for the different materials. Formation factors are calculated using the combination of Archies law and tabulated water diffusivities for the different tracers.

Table B-5. Proposed porosity and diffusivity values for different geological materials.

		Fracture coating (BG1)	Fault gouge (#19)	Cataclasite (#19)	Altered Zone (#19 and BG1)
	Porosity (%)	5	20	1	0.6
	Formation factor	6.2E–3	5.6E–2	4.9E–4	2.2E–4
Tracer	D_w (m²/s)	D_e (m²/s)	D_e (m²/s)	D_e (m²/s)	D_e (m²/s)
$^{131}I^{-}$	2.00E–9	1.2E–11	1.1E–10	9.8E–13	4.4E–13
$^{160}TbDTPA^{2-}$	5E–10	3.0E–12	2.8E–11	2.4E–13	1.1E–13
$^{85}Sr^{2+}$	7.94E–10	5.0E–12	4.4E–11	3.9E–13	1.7E–13
$^{86}Rb^{+}$	2.06E–9	1.3E–11	1.2E–10	1.0E–12	4.5E–13
$^{137}Cs^{+}$	2.06E–7	1.3E–11	1.2E–10	1.0E–12	4.5E–13
HTO	2.13E–9	1.3E–11	1.2E–10	1.0E–12	4.7E–13
$^{155}EuDTPA^{2-}$	5E–10	3.0E–12	2.8E–11	2.4E–13	1.1E–13
$^{22}Na^{+}$	1.33E–9	8.3E–12	7.4E–11	6.5E–13	2.9E–13
$^{133}Ba^{2+}$	8.48E–10	5.3E–12	4.7E–11	4.2E–13	1.9E–13
$^{54}Mn^{2+}$	6.88E–10	4.3E–12	3.8E–11	3.4E–13	1.5E–13

Appendix C1

Theoretical basis of the ANDRA/Itasca Modelling

C1.1 Overview

3FLO has been developed by Itasca, since the early nineties, as a support for groundwater flow and reactive mass transport modelling. *3FLO* is an object-oriented program (C^{++}) sharing a common platform with other Itasca codes. *3FLO*'s major features are described in Figure C1-1.

The Itasca programming language, named *FISH*, greatly enlarges *3FLO*'s functionality. *FISH* can be used, for example, to modify the domain discretization, run the code until user-defined convergence criteria are met, define new variables and functions, implement conditional boundary conditions or element properties, generate specific input/output, customize particle tracking.

3FLO solves groundwater saturated/unsaturated flow and reactive mass transports equations over an anisotropic heterogeneous three-dimensional domain.

C1.2 Saturated/unsaturated flow modelling

3FLO is based on the finite element method and uses the Galerkin (combined with a conjugated gradient technique, pre-conditioned by an incomplete Cholevski decomposition) or the mixed-hybrid elements approach. The mixed-hybrid elements present the advantage, over the Galerkin formulation, of respecting the flow field continuity at the elements faces.

Three-dimensional flow in unsaturated media is based upon *the Richards equation* which is solved with a Picard numerical scheme using pressure as primary variable. Saturation is therefore also written in terms of pressure. Several models are available for linking pressure with saturation and relative permeability: *Genuchten-Mualem*; *Haverkamp* or *Brooks-Corey*.

Three types of element geometries are currently available in *3FLO*: pipes (2 nodes elements), tetrahedrons and hexahedrons.

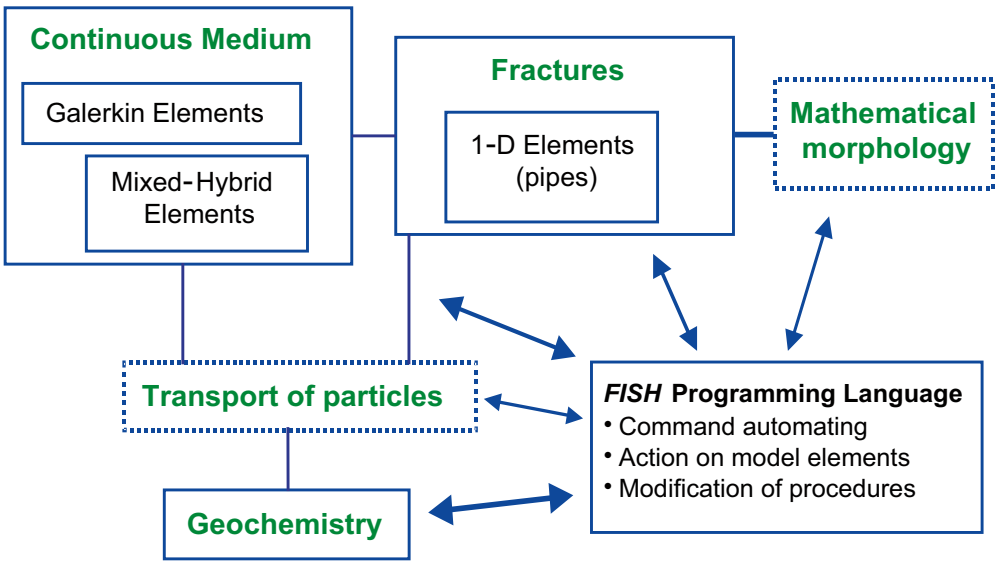

Figure C1-1. *Main features of 3FLO.*

C1.3 Mass transport modelling

A Lagrangian numerical method, named "particle following", is implemented to simulate 1d advective and diffusive transport in fractures, coupled with retention phenomena, i.e. adsorption on fracture walls as well as diffusion and retention in the rock matrix.

The method is based on the following hypothesises:

- transversal diffusion across 1D conduits is negligible,
- molecular diffusion and dispersion in the fracture insure a complete mixing of the solute in the transversal direction,
- transport is 1d. Flow in fractures is simulated as flow in a network of 1d pipes,
- complete mixing occurs at intersections.

In the fracture:

$$\theta \frac{\partial c}{\partial t} = -\frac{V}{R_a}\frac{\partial c}{\partial x} + \frac{1}{R_a}\frac{\partial}{\partial x}\left(D_L \frac{\partial c}{\partial x}\right) + 2\frac{\theta_m \cdot D_m}{2b \cdot R_a}\frac{\partial c_m}{\partial z}\bigg|_{z=b} \qquad \text{(C1-1)}$$

$$R_a = 1 + \frac{K_a}{b}$$

with the following notations:

θ	[–]	Porosity
c	[ML^{-3}]	Concentration
V	[LT^{-1}]	Darcy velocity
R_a	[–]	Retardation factor accounting for adsorption on fracture walls
D_L	[L^2T^{-1}]	Longitudinal dispersion in the fracture ($D_L = \alpha_L \cdot u_r$,α_L: [L] dispersivity, and u_r: [LT^{-1}] velocity, $u_r = V/\theta$)
K_a	[L]	Sorption coefficient on fracture walls
b	[L]	Half-aperture
c_m	[ML^{-3}]	Concentration in the matrix
θ_m	[–]	Porosity of the matrix
D_m	[L^2T^{-1}]	Diffusion coefficient in the matrix
D_e	[L^2T^{-1}]	Effective diffusion in the matrix ($D_e = \theta_m \cdot D_m$)

In the matrix:

$$R_m \frac{\partial c_m}{\partial t} + \lambda c_m = D_m \frac{\partial^2 c_m}{\partial z^2}$$

$$R_m = 1 + \rho_m \cdot K_d / \theta_m = 1 + \rho \cdot K_d (1 - \theta_m)/\theta_m$$

with the following notations:

c_m	[ML^{-3}]	Concentration in the matrix
R_m	[–]	Retardation factor accounting for sorption
D_m	[L^2T^{-1}]	Diffusion coefficient in the matrix
K_d	[L^3M^{-1}]	Sorption coefficient in the matrix
ρ	[ML^{-3}]	Density of the solid fraction in the matrix $\rho_m = (1 - \theta_m)\,\rho$
ρ_m	[ML^{-3}]	Effective density in the matrix

The "time domain random walk" method used is a Lagrangian type method. The residence time for a particle in a part of the fracture (1d pipe) is taken from a lognormal distribution with known mean and variance. In the case of no correlation between matrix residence time and fracture residence time, the global residence for a particle in the system is simply the sum of Δt_m (time in matrix, including diffusion and sorption processes), and Δt_l (time in pipe, including advection, diffusion, and wall adsorption processes). The correlation is then accounted for.

The total time in the matrix is:

$$\Delta t_m = \left(\frac{a \cdot t_0}{R_l \cdot erfc^{-1}(Z_0^1)} \right)^2 \qquad \text{(C1-2)}$$

$$\text{where } t_0 = \frac{R_a}{u_l} \cdot \Delta x, \quad a = \frac{\sqrt{\alpha \cdot D_e}}{2b} \cdot \Delta x \text{ et } \alpha = \theta_m + \rho_m \cdot K_d \qquad \text{(C1-3)}$$

with the following notations:

u_l	[LT^{-1}]	Velocity in the pipe ($u_l = \frac{V}{\theta}$)
a	[T^{-1}]	
Δx	[L]	Length of the transport path
α	[–]	Capacity factor integrating matrix retention properties
t_0	[T]	Travel time for pure advection
Z_0^1	[–]	Random number drawn from a uniform distribution between 0 and 1

The mean and variance of the lognormally distributed residence time in a pipe are:

$$m_t = \frac{R_a}{u_l^2} \left(u_l + \frac{\partial D_L}{\partial x} \right) \Delta x \qquad \text{(C1-4)}$$

$$\sigma_t^2 = 2 \cdot \frac{R_a^2}{u_l^3} \cdot D_L \cdot \Delta x \qquad \text{(C1-5)}$$

Taking into account the influence of matrix diffusion on the residence time in the pipe, the parameters of the pipe residence time are modified, obtaining mean m'_t and standard deviation σ'_t as given by:

$$m'_t = \frac{R_a}{u^{*2}_l} \left(u_l^* + \frac{\partial D_L^*}{\partial x} \right) \Delta x \qquad \text{(C1-6)}$$

$$\sigma'^2_t = 2 \cdot \frac{R_l^2}{u_l^3} \cdot D_L^* \cdot \Delta x \qquad \text{(C1-7)}$$

with:

$$u_l^* = R_{diff} \cdot u_l$$
$$D_L^* = f(u_l^*) \text{ or } D_L \qquad \text{(C1-8)}$$

$$R_{diff} = 1 + \beta \sqrt{\sigma_t} \left(\left[\frac{\exp(-\xi^2)}{\sqrt{\pi} \cdot erfc(\xi)} \right] - \xi \right) \qquad \text{(C1-9)}$$

$$\text{with } \xi = \frac{\beta \cdot t_0}{\sqrt{\sigma_t}} \text{ and } \beta = \frac{\sqrt{\alpha \cdot D_e}}{2 \cdot b \cdot R_a} = \frac{\sqrt{\alpha \cdot \theta_m \cdot D_m}}{2 \cdot b \cdot R_a} \qquad \text{(C1-10)}$$

Appendix C2

Theoretical basis of JNC/GOLDER modelling

The goal of the JNC/Golder modeling team during the BS2B prediction effort was to apply the knowledge gained from past tracer tests (TRUE Block Scale C1 to C4, Task 6D, Task 6E, and the BS2B pre-tests CPT 1–4) to an updated version of the Task 6C hydrostructural model to produce a block-scale transport model able of adequately predicting the results of the BS2B sorbing tracer tests. This modeling effort focused on understanding solute retention processes in the geologically complex zones at the interface between flowing fractures and the rock matrix.

C2.1 Implementation of the BS2B channel network (CN) model

All of the background fractures and deterministic structures of the Task 6C /Dershowitz et al. 2003/ semi-synthetic hydrostructural model were used to construct the BS2B base DFN. The inclusion of additional larger-scale fractures generated during Task 6C, but not included in the final 500 m scale model, was necessary to provide adequate connections to external head boundaries to produce a stable steady-state flow solution, cf Chapter 3.

C2.1.1 Geometrical description of the discrete fracture network

The JNC/Golder BS2B blind prediction DFN model was largely based on the Task 6C DFN, such that the modeled DFN looked the same as that described in /Andersson et al. 2002a/. However, due to file formats requirements imposed by the PAWorks software package, it was necessary to transform the model from Äspö local coordinates (positive x points east) into FracMan local coordinates (positive x points south). Each fracture was represented by a polygon, whose extent and orientations are specified by nodal coordinates at the vertices and by a normal vector to the fracture plane.

The discrete fracture network was reduced to a three-dimensional network of one-dimensional, rectangular cross-section pipe elements (a ‘channel network’) utilizing the PAWorks software suite. The discretization process is described in detail in Section 4.2. Samples of the resulting network are illustrated in Figure C2-1 and Figure C2-2.

C2.1.2 Geometrical description of pore space

The pore space models used for “Type 1” and “Type 2” structures are illustrated in Figure 2-2 and Figure 2-3. Pore spaces representing fault gouge, cataclasite/mylonite, fracture mineral coatings, altered wall rock, and fresh wall rock (Äspö diorite) were implemented as PAWorks/LTG immobile zones /Dershowitz et al. 2000/. In PAWorks/LTG, immobile zones simulate mechanical and chemical transport processes by applying retardation factors to solute transport based on the zone properties. Fundamentally, mass is not ‘lost’ from a model to immobile zones; it is merely slowed down to a point where it does not reach the specified sinks during the time frame of the simulation. The basic conceptual model behind the PAWorks/LTG implementation of immobile zones is illustrated in Figure C2-3.

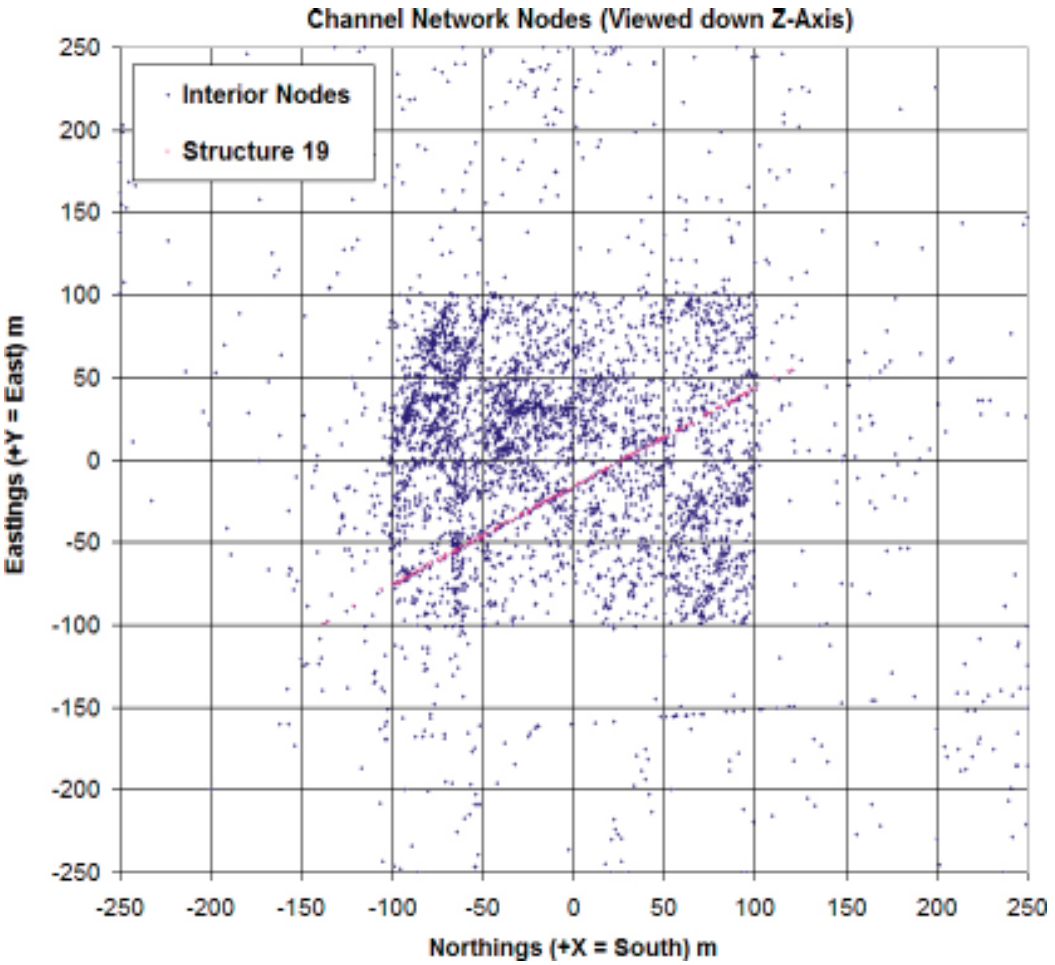

Figure C2-1. *TRUE Block Scale BS2B channel network model. Blue dots are nodes representing pipe endpoint connections in the model; the pink dots are nodes representing pipes along Structure #19. The model is expressed in FracMan coordinates; the Äspö HRL tunnel is in the upper left corner of the map.*

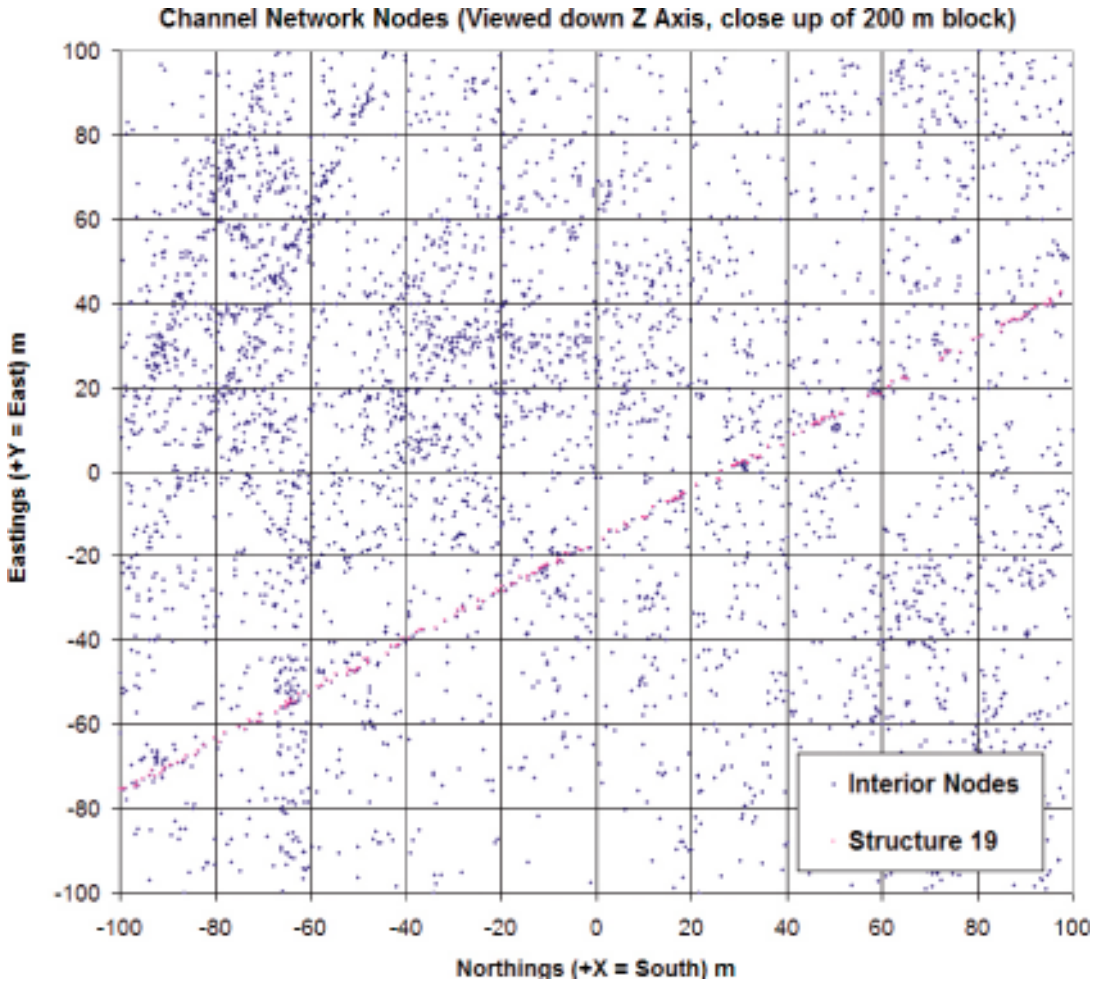

Figure C2-2. *500-m TRUE Block channel network model, zoomed in on the 200-m BS2B experimental volume. Blue dots are nodes representing pipe endpoint connections in the model; the pink dots are nodes representing pipes along Structure #19. The model is expressed in FracMan coordinates; the Äspö HRL tunnel is in the upper left corner of the map.*

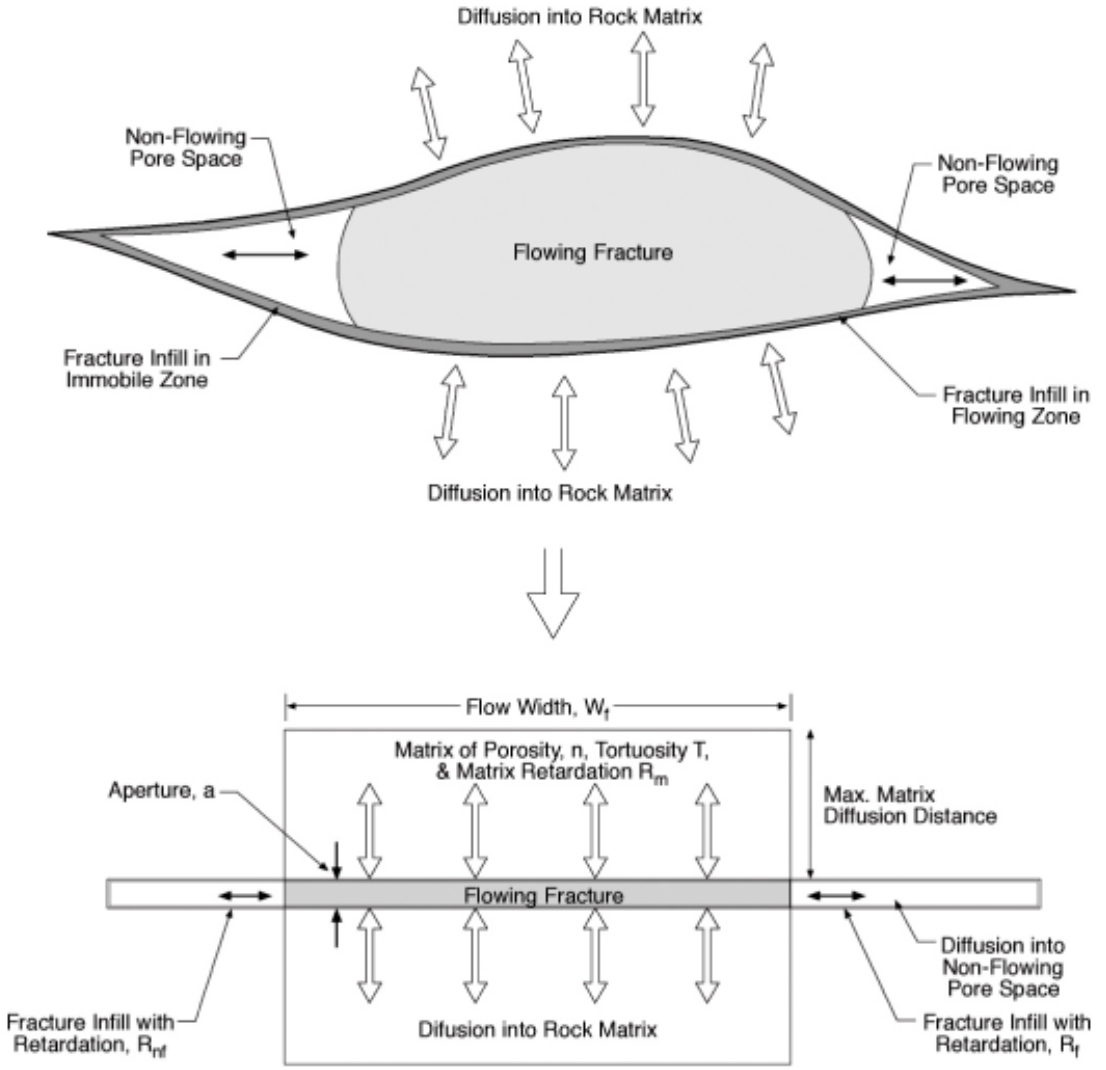

Flow Area = $W_t \cdot a$

Matrix Diffusive Area/Unit Length = 2 W_t, where W_t is transport width, $W_t <= W_t$

Non-Flowing Diffusive Area/Unit Length = 2a

NOT TO SCALE

Figure C2-3. *Implementation of pore space as parallel immobile zones in PAWorks and LTG channel-network modelling. Figure taken from the PAWorks/LTG users manual, version 1.62 /Dershowitz et al. 2000/.*

C2.2 Flow model

Flow was modeled using the FracMan/MAFIC code. The MAFIC flow model is described in /Miller et al. 2001/. In the MAFIC conceptual model, each of the fracture intersections are considered to be line segments ("traces"). These segments, along with the edges of the polygonal fractures, are then used to discretize the fractures to either 1D or 2D finite elements. When discretizing a DFN to 2D elements, the fractures are transformed into triangular finite elements conditioned to match the edges of the fracture and the intersection traces. When discretizing a DFN to 1D (pipe) elements, the pipes are defined to provide connections between the intersection traces, maintaining the same flow area between the fracture traces (Figure C2-4). The discretization process is described in detail by /Dershowitz et al. 2000/.

C2.2.1 Processes considered

The flow model considered only advective flow, modeled as Darcy flow through rectangular cross-section pipes or triangular finite elements.

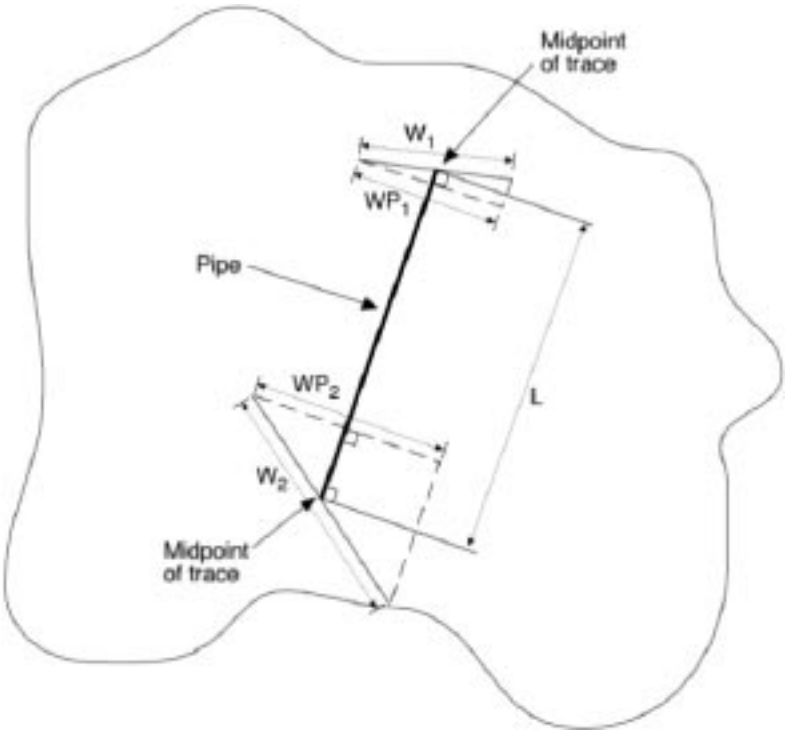

Figure C2-4. *Implementation of rectangular pipe elements between fracture intersection traces.*

C2.2.2 Mathematical description

The mathematical description of flow modeling in MAFIC is taken from /Miller et al. 2001/. Using continuum principles of mass balance, the diffusivity equation that describes flow can be written as /Bear 1972/:

$$\frac{\partial}{\partial x_i}[\frac{\rho}{\mu}k_{ij}(\frac{\partial P}{\partial x_i}+\rho g\frac{\partial z}{\partial x_j})] = \rho(\alpha+\phi\beta)\frac{\partial P}{\partial t} - q \qquad \text{(C2-1)}$$

where

x_i Coordinate directions (L)

ρ Fluid density (M/L^3)

μ Fluid viscosity (M/LT)

k_{ij} Permeability (absolute) (L^2)

P Fluid pressure (M/LT^2)

g Gravitational acceleration (L/T^2)

z Vertical direction (upward) (L)

α Pore compressibility (LT^2/M)

Φ Porosity

β Fluid compressibility (LT^2/M)

q Source term (M/T)

t Time (T)

For nearly incompressible fluid (e.g. water), and for flow in two dimensions (e.g. in a fracture), the mass-conservation of Equation (C2-1) can be simplified to a volume-conservation equation:

$$S\frac{\partial h}{\partial t} - K\overline{\nabla}^2 h = q \qquad \text{(C2-2)}$$

where

S Fracture Storativity (dimensionless)

h Hydraulic head (L)

T Fracture Transmissivity (L^2/T)

q Source/Sink Term (L/T)

t Time (T)

$\overline{\nabla}^2$ Two-dimensional Laplace Operator

C2.2.3 Numerical implementation

MAFIC uses a Galerkin finite element solution scheme to approximate the solution for Equation (C2-1). The finite element approximation to the diffusivity equation in two dimensions is given by:

$$\sum_{m=1}^{N}\left[\int_R (T_{nm}\overline{\Delta}\xi_n \bullet \overline{\Delta}\xi_m dR)h_m\right] + \sum_{m=1}^{N}\left[\int_R (S_{nm}\xi_n\xi_m dR)\frac{dh_m}{dt}\right] = \int_R q\xi_n dRn = 1,2,...N \qquad \text{(C2-3)}$$

where

T Fracture transmissivity (L^2/T)

S Fracture storativity (dimensionless)

q Source flux, volume per unit area (L/T)

ξ Linear or quadratic basis function

R Element area (L^2)

h Nodal hydraulic head (L)

t Time (T)

N Number of nodes

For the present study, flow modeling was carried out using a three-dimensional network of rectangular cross-section pipe elements generated from the base discrete-fracture network model.

C2.2.4 Flow model parameters

Flow modeling was carried out assuming steady-state conditions, with the injection and pumping rates specified in Chapter 3, and the head boundary conditions as calibrated for the 500 m TRUE Block Scale volume (see Chapter 3).

For steady state flow modeling, the only important parameters are fracture transmissivity (m^2/s) and aperture. These values were specified for each fracture as provided in the Task 6C report /Dershowitz et al. 2003/, except for Structure BG1, where transmissivity was altered to attempt to match previous (CPT-4c) tracer test results. The distributions of values for fracture transport aperture and transmissivity are described in Chapter 5.

C2.3 Transport model

Solute transport was simulated using the Laplace Transform Galerkin method, as implemented in PAWorks/LTG /Dershowitz et al. 2000/. Radionuclide transport occur within a three-dimensional channel network composed of one-dimensional pipe elements, with multiple immobile zones working in parallel to simulate rock and structural interactions.

C2.3.1 Processes considered

Solute transport modeling with the PAWorks and LTG packages considers the following processes:

- advection,
- dispersion (longitudinal only),
- diffusion (to immobile zones),
- sorption (in immobile zones),
- surface sorption (onto fracture mineral coatings).

For these simulations, radionuclide decay, and non-equilibrium chemical processes were not considered.

C2.3.2 Mathematical description

This section describes the mathematical basis of the FracMan/PAWorks Laplace Transform Galerkin (LTG) solute transport model. This section of text was taken from the PAWorks/LTG manual /Dershowitz et al. 2000/. The model topology is illustrated in Figure C2-5.

The LTG transport solution is carried out assuming steady-state flow. A second-order approach is used to describe the diffusive mass transfer of a solute between the groundwater in a pipe and the multiple immobile porosity zones attached to it. The advective-dispersive transport of solute species (index *n*) in a pipe network is given by:

$$A\left[R_n(\ell)\frac{\partial C_n}{\partial t}+q(\ell)\frac{\partial C_n}{\partial \ell}-\frac{\partial}{\partial \ell}D_{l_n}(\ell)\frac{\partial C_n}{\partial \ell}+R_n(\ell)\lambda_n C_n-R_{n-1}(\ell)\lambda_{n-1}C_{n-1}\right]$$
$$\pm\sum_{\ell'}\dot{M}\,\delta(\ell-\ell')+\sum_{\ell^*}Q(C_n-C_n^*)\delta(\ell-\ell^*)+\sum_{im=1}^{IM}P_{im}\theta_{im}D_{im}\frac{\partial C_n^{im}}{\partial w}\Big|_{w=0}=0 \qquad \text{(C2-4)}$$

where

n	nuclide index [–]
im	Immobile zone class number (note: if desired im can equal 0) [–]
IM(ℓ)	Total number of immobile zones attached to pipe ℓ [–]
A(ℓ)	Pipe cross-sectional area [L^2]
Rn(ℓ)	Retardation factor [–]
$q(\ell)$	Specific discharge (≡ Pipe velocity v) [L/T]
$D_{\ell_n}(\ell)$	Dispersion coefficient = $\alpha v + D_n^o$ [L^2/T]
α	Pipe longitudinal dispersivity [L]
D_n^o	Free-solution diffusion coefficient [L^2/T]
λ_n	Decay constant [1/T]
$\dot{M}$(t)	Internal solute mass source/sink [M/T]
Q	External fluid source/sink [L^3/T]
$\delta(\ell-\ell')$	Dirac delta [1/L]
$\delta(\ell-\ell^*)$	Dirac delta [1/L]
P_{im}	Block surface area per unit length of matrix (equivalent to the effective perimeter of immobile zone im) [L]
D_{im}	Matrix effective diffusion coefficient [L^2/T]
θ_{im}	Immobile zone porosity for immobile zone im
Cn	Pipe concentration [M/L^3]
C_n^*	Concentration of injectate in external fluid source [M/L^3]
C_n^{im}	Immobile zone concentration [M/L^3]
ℓ	Distance along interconnected pipe network [L]
ℓ'	Location of solute mass source/sink [L]
ℓ^*	Location of external fluid source/sink [L]
w	Distance perpendicular to plane of fracture [L]
t	Time [T]

It should be noted that if there is no flow along a particular pipe within the network (i.e. *q(l) = 0)*, then the model allows for diffusive transport along the length of this pipe. It should also be pointed out that if fluid is withdrawn at a resident concentration, $C_n^* = C_n$, then the term involving Q in (Equation (C2-4)) vanishes. If the injectate concentration $C_n^* = 0.0$, then this term accounts for the dilution effect of the injection of solute-free water.

The initial concentrations of all species within the domain are assumed to be zero. Boundary conditions may be either of the Dirichlet-type where the input concentration history of each species is a specified function of time, or of the Cauchy-type where the advective input mass flux can be prescribed as a function of time at the origin of a pipe on the boundary of the domain. Mathematically, these boundary conditions are described by:

Dirichlet: $Cn = C_n^o(t)$ on Γ (C2-5)

Cauchy: $A(\ell)q(\ell)C_n^o(t) = A(\ell)\left[q(\ell)C_n(\ell,t) - D_{\ell_n}(\ell)\frac{\partial C_n}{\partial \ell}\right]$ on Γ (C2-6)

where C_n^o is the specified concentration for species n. LTG also allows the concentration or flux rate (e.g. mol/yr) to be specified at an interior point.

Immobile zone

In order to represent the diffusive exchange of solute mass between the pipes and any on the immobile zones (index *im*) attached to them, LTG uses a second-order approach described by:

$$\theta_{im}(im,\ell)R_n^{im}(im.\ell)\frac{\partial C_n^{im}}{\partial t} - \frac{\partial}{\partial w}\theta_{im}(im,\ell)D_{im}\frac{\partial C_n^{im}}{\partial w} \quad \text{(C2-7)}$$
$$+ \theta_{im}(im,\ell)R_n^{im}(im,\ell)\lambda_n C_n^{im} - \theta_{im}(im,\ell)R_{n-1}^{im}(im,\ell)\lambda_{n-1}C_{n-1}^{im} = 0$$

where

$\theta_{im}(_{im},\ell)$ Immobile zone porosity for immobile zone "*im*" attached to pipe "ℓ" [–]

$R_n^{im}(^{im},\ell)$ Immobile zone retardation factor for immobile zone "*im*" attached to pipe "ℓ" [–]

C_n^{im} Concentration in matrix [M/L^3]

D_{im} Matrix effective diffusion coefficient [L^2/T]

$D_n^0\,\tau$

D_n^o Free-solution diffusion coefficient [L^2/T]

τ Tortuosity [–]

If a particular immobile zone is fluid-filled, such as within an immobile water zone attached to a pipe within a fracture plane, then the immobile zone porosity, θ_{im}, would equal unity.

C2.3.3 Numerical implementation

The LTG method /Sudicky 1989, 1990, Sudicky and McLaren 1992/ is a numerical solution procedure where the Laplace transform is first applied to the governing equation, and the transformed equation is then solved numerically using the Galerkin finite element procedure (or alternatively any other discretization method such as finite differences). Finally, upon a solution for the nodal Laplace-space solution, the time-domain solution is recovered by a numerical inversion of the Laplace transformed nodal solution.

Let the Laplace transform of a function *f(t)* be defined according to:

$$\bar{f}(p) = \int_0^\infty f(t)e^{-pt}\,dt \quad \text{(C2-8)}$$

where p is the Laplace-transform parameter. Applying this to Equation (C2-7) for the im^{th} immobile zone and following algebraic manipulations, one obtains:

$$g_n\overline{C}_n = -qA\frac{\partial \overline{C}_n}{\partial \ell} + A\frac{\partial}{\partial \ell}D_{\ell_n}\frac{\partial \overline{C}_n}{\partial \ell} + AR_{n-1}\lambda_{n-1}\overline{C}_{n-1} + \sum_{im=1}^{IM}\sum_{k=1}^{n-1}G_{nk}^{im}\overline{C}_n \quad \text{(C2-9)}$$

The *k* summation in Equation (C2-9) is summing the nuclide's predecessors, where nuclide *1* is the first species in the chain, and nuclide *n–1* is the direct parent.

In Equation (C2-9):

VSA Volume per surface area [L]

p Laplace transform parameter

$$g_n = \left[AR_n(p+\lambda_n) + \sum_{im=1}^{IM} V_{im}\theta_{im}D_{im}\frac{Z_n^{im^2}}{VSA_{im}}B_n^{im}(Z_n^{im}) \right] \quad \text{(C2-10)}$$

$$G_{n,k}^{im} = -V_{im}\theta_{im}D_{im}\sum_{\ell=k}^{n} E_{n,k}^{\ell,im}\frac{Z_\ell^{im^2}}{VSA_{im}}B_\ell^{im}(Z_\ell^{im}) \quad \text{(C2-11)}$$

$$E_{n,k}^{\ell,im} = \frac{\prod_{p=k}^{n-1}(\lambda_p R_p^{im})}{\prod_{\substack{p=k \\ p\neq\ell}}^{n}\left[R_p^{im}(p+\lambda_p) - R_\ell^{im}(p+\lambda_\ell)\right]} \quad \text{(C2-12)}$$

$$\phi_n^{im} = \sqrt{\frac{(p+\lambda_n)R_n^{im}}{D_{im}}} \quad \text{(C2-13)}$$

$$Z_n^{im} = \phi_n^{im} VSA_{im} \quad \text{(C2-14)}$$

For a "slab" geometry for a matrix block $B_n^{im}(Z_n^{im})$ and VSA are defined by:

$$B_n^{im}(Z_n^{im}) = \frac{\tanh(Z_n^{im})}{Z_n^{im}} \quad \text{(C2-15)}$$

VSA The volume to surface area ratio is equal to half the total slab width, 2dmax

VSA d_{max}

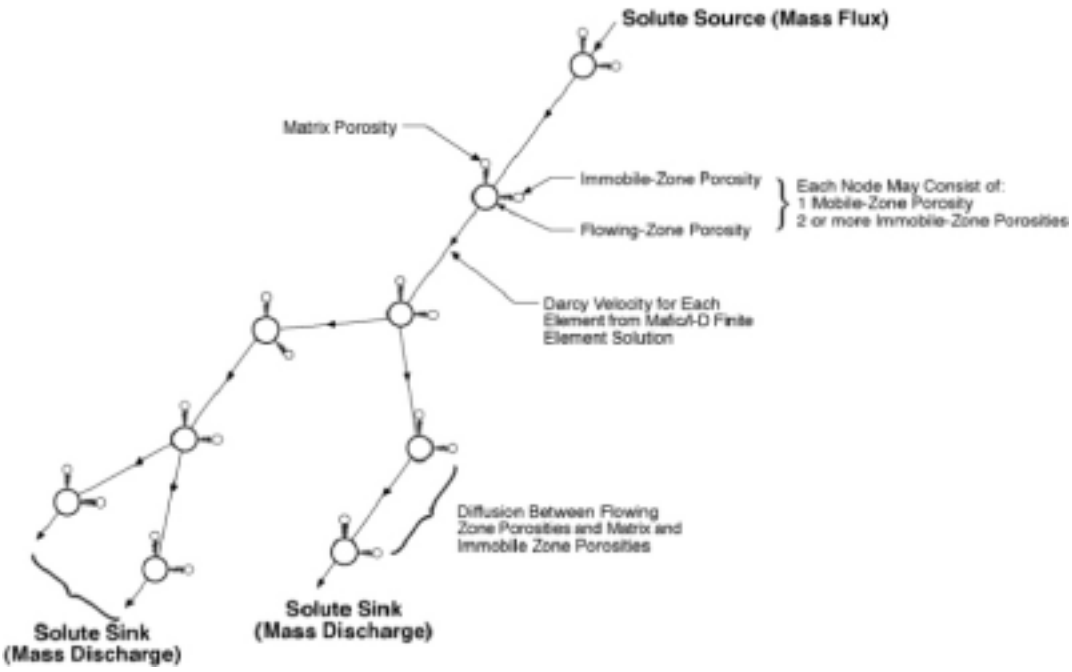

Figure C2-5. *Topology of LTG transport solution.*

Appendic C3

Implementation of the Posiva-VTT model

C3.1 Background

Posiva-VTT model is based on an analytical approach that takes into account the layered structure of the immobile pore spaces as specified in the BS2 microstructural model. The focus of the modelling is on the transport modelling. Flow properties and visited fractures are deduced from the configuration of the experiments, using the Task 6C semi-synthetic fracture network model and by modelling of the pre-tests, like the tracer dilution tests and the tracer test CPT-4c.

Essentially, the model is composed of one-dimensional flow path coupled to one-dimensional matrix diffusion process between the immobile pore spaces and the flow channel.

C3.2 Conceptual model and underlying assumptions

Transport channel is represented by one-dimensional streamtube that carries the flow. Tracer particles may interact with the immobile pore space that surrounds the transport path by diffusing to the immobile pore space. Tracer particles may also sorb in the immobile pore space.

The transport model applies following assumptions:

- All particle pathways will go to the sink. This means that influence of the background flow field is negligible for the tracer recovery and all tracers will eventually give 100% recovery.
- The flow field near the injection borehole adapts itself to the background flow field. This means that the hydrodynamic control of retention can be deduced from the tracer dilutions tests performed in the same experimental configuration and pump rate as the BS2B experiment. This is used as guidance for the calibration of the β in the evaluation model.
- In the prediction model the flow field is characterised by a plug flow. Evaluation model applies Gaussian distribution for the water residence times and hydrodynamic control of retention.
- Concentration of the tracer in the flow channel is well-mixed.
- Sorption is linear equilibrium sorption that is characterised by the tracer K_d.
- Surface sorption on the fracture walls is not taken into account.
- Radioactive decay is not taken into account.

Figure C3-1 illustrates the conceptual model applied in the modelling.

C3.3 Flow model

C3.3.1 Hydrodynamic control of retention

The prediction model is based on a very simple flow model that is applied for the steady state flow conditions. It is assumed that the flow rate through the main flow channel can be deduced from the results of the tracer dilution tests performed at the BS2B injection locations in Structure #19 and BG1, respectively. A significant simplification in the prediction model is that only the average flow rate (bulk flow) is applied. Variable flow is taken into account only in the evaluation model.

Hydrodynamic control of the retention (β) is represented by the entity $W \cdot L/Q = \beta/2$, where W is the width, L is the length and Q is the flow rate in the transport channel. Flow conditions at the injection locations in the field are used for estimation of the average Q/W along the transport

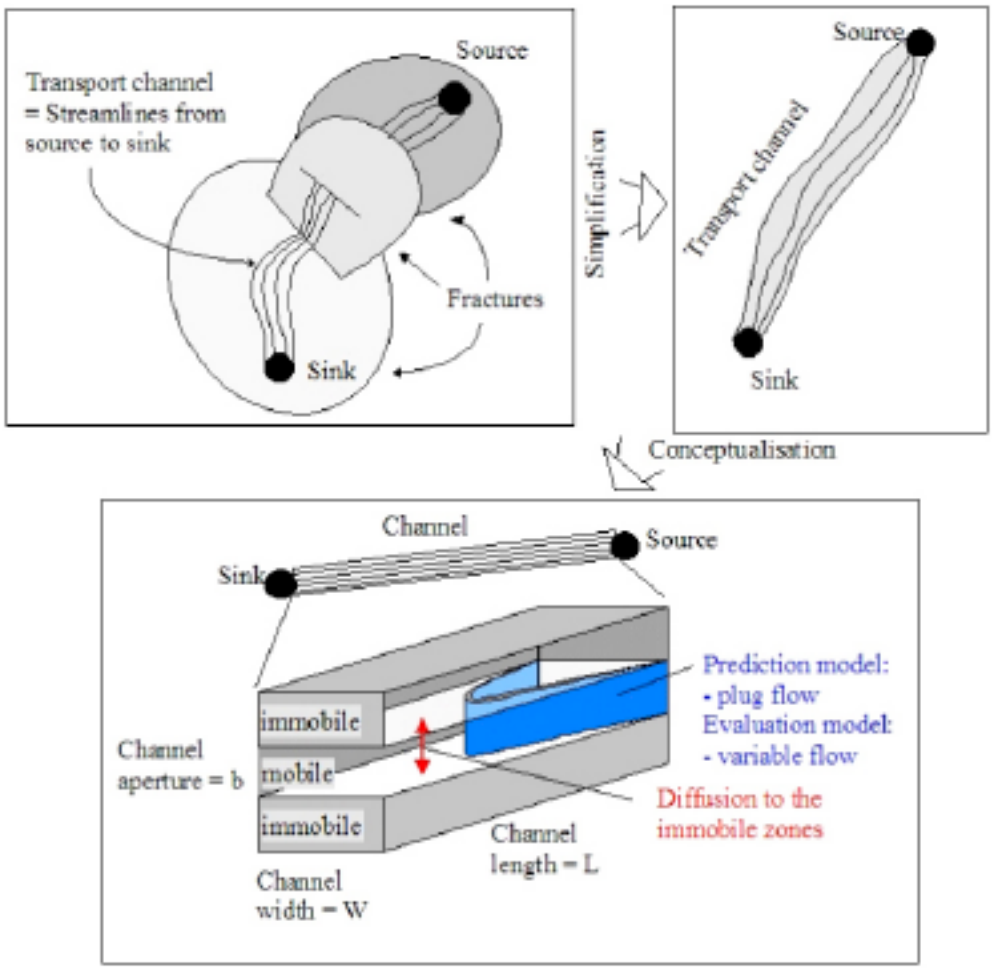

Figure C3-1. *Illustration of the conceptual model applied in the BS2B modelling.*

paths. The quotient Q/W at the injection locations are taken from the tracer dilution measurements that are made under the same pumping conditions as the BS2B experiment (CPT-3c dilution tests). It is assumed that the measured Q/W is representative for the flow conditions along the whole flow path.

C3.3.2 Flow paths

The length of the Flow path I is estimated by the Euclidian distance from the source to the sink. Flow path I runs in its entirety along a Type 1 fracture (Structure #19). The length of the Flow path II is estimated by extending the fracture intersected by the injection borehole (BG1) to intersect with the structure that intersects the sink (Structure #19).

The geometry of the flow model is characterised by the lengths and effective widths of the flow paths I and II. The effective width of the flow path is deduced from the β of the flow path. Both predictive and evaluation models have applied path length of 20 m for the Flow path I and 40 m for the Flow path II. Widths of the flow paths have been estimated for the different alternative evaluation models. The effective widths of the flow paths are 0.2–8 m for the Flow path I and 0.7–10 m for the Flow path II. The resulting path widths are controlled by the retention properties along the path and they vary quite a lot depending on the corresponding effective immobile zone retention properties.

C3.4 Transport model

C3.4.1 Processes considered

Transport model takes into account advection along the fractures, matrix diffusion and sorption in the immobile pore space. Surface sorption on the fracture walls is not modelled, but the diffusion into the pore space of the fracture coating and sorption in the pore space of the coating are directly modelled. In the prediction model there is no variable advection inside the transport path. Variable advection is included only to the evaluation model.

C3.4.2 Mathematical description

Transport of the tracers is described by applying the advection – matrix diffusion equation

$$R_a \frac{\partial c_f}{\partial t} + v\frac{\partial c_f}{\partial x} - 2\frac{D_e}{2b}\frac{\partial c_m}{\partial z}\bigg|_{z=0} = 0$$
$$R_p \frac{\partial c_m}{\partial t} - D_p \frac{\partial^2 c_m}{\partial z^2} = 0 \qquad \text{(C3-1)}$$

where v is the flow velocity, D_e is the effective diffusion coefficient from fracture to the immobile zone, D_p is the pore diffusivity in the immobile zone, $2b$ is the fracture aperture and R_a is the retardation coefficient of the surface sorption (R_a = 1 for all tracers in this modelling, i.e. surface sorption is not taken into account). Equation (C3-1) is solved analytically for a homogeneous and limited thickness immobile zone /Poteri 2006/.

C3.4.3 Adapting transport model to the current problem

Fractures in the BS2B block has been classified to two different fracture types according to the microstructural model of the immobile zones. The model applied in the transport calculations follows the definition of the layered structure of the immobile zones. Figure C3-2 illustrates the conceptual model of the transport channel and the immobile zones that is applied in the transport calculations.

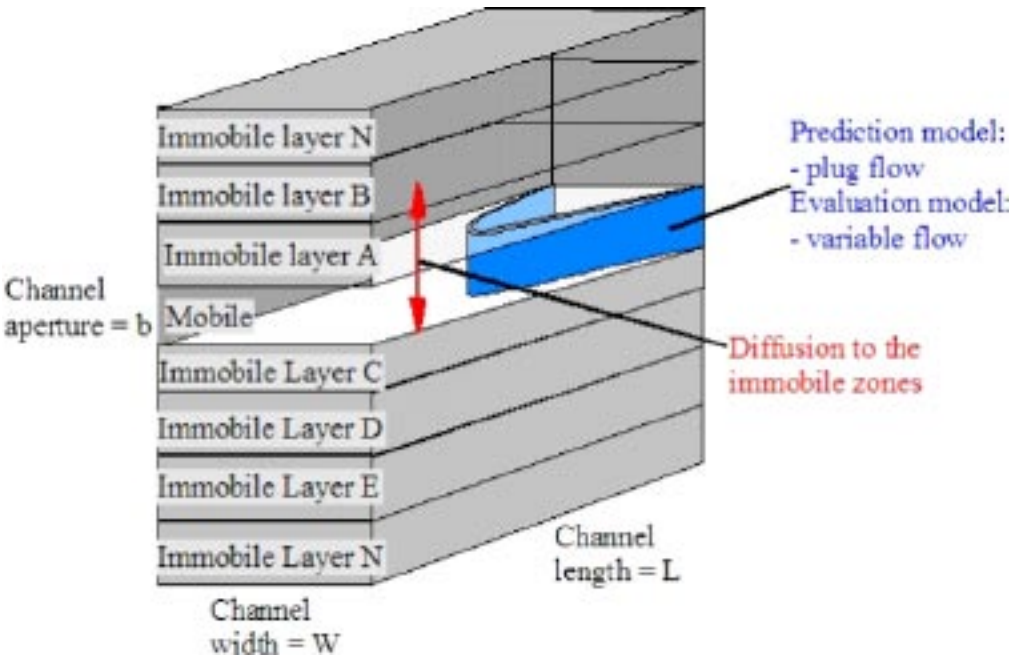

Figure C3-2. *Conceptual model of the transport path applied in the BS2B experiment. The number and properties of the immobile layers depends on the fracture type according to the microstructural model of the TRUE Block Scale fractures.*

Solute transport through the system of layered immobile zones is calculated by constructing an equivalent system of successive flow paths that have homogeneous and limited thickness immobile regions and applying analytical solution of the Equation (C3-1). An equivalent system of successive flow paths can be found if the immobile zone retention property (i.e. γ) is smaller for the layers that are deeper in the rock matrix than for the layers that are closer to the fracture /Poteri 2006/. This is the case for the microstructural model of the TRUE Block Scale site (Type 1 and Type 2 features) and for the tracers applied in the BS2B tests.

C3.4.4 Numerical implementation

Equation (C3-1) is solved using an analytical model that is based on a one-dimensional lattice walk. The interaction of the solute particles between the mobile and immobile pore space is described by a waiting time distribution applied for the grid points /Cvetkovic and Haggerty 2002/. The waiting time distribution at the grid points is calculated directly from the diffusion of the solute particles between the mobile and immobile zones.

C3.5 Input parameters and data used

C3.5.1 Flow and transport data

Flow rates through the transport channels are not determined by applying flow modelling. They are deduced from the results of the tracer dilution tests performed in the same experimental configuration as the BS2B experiment. The prediction model is based on the average flow rate (bulk flow) through the transport paths. The evaluation model takes into account variable flow along the flow paths by utilizing Gaussian water residence time distribution.

Flow field is characterised by distributions of the water residence times and hydrodynamic control of retention (β, cf Equation (5-4)). β is important for the estimation of the retention times, especially for the sorbing tracers. Approximate value of the βs are based on the results of the tracer dilution experiments and estimated lengths of the transport paths. The approximate value of β is based on the identity $W \cdot L/Q = \beta/2$, where W is the width, L is the length and Q is the flow rate in the transport channel. This gives for the Flow path I, $WL/Q = 0.1 \times 22$ m/(68 ml/h) = 28,000 h/m, and for the Flow path II, $WL/Q = 0.1 \times 20$ m/(42 ml/h)+0.1×20 m/(68 ml/h) = 83,000 h/m (here also the contributions of the WL/Q along BG1 and Structure #19 are indicated). Correspondingly, we get β = 56,000 h/m for the Flow path I and β = 170,000 h/m for the Flow path II.

The calibrated parameter values that have been applied in the modelling for the flow field are presented in Table C3-1. The calibration is made using results of the dilution tests and pre-tests of the BS2B tracer experiment (prediction model) or as a part of the BS2B tracer test evaluation.

Majority of the parameters specify the properties of the immobile pore space and chemical interactions (K_d) of the different tracers for the different immobile layers. Parameterisation of the immobile layers and tracer sorption properties has been provided as a part of the BS2B microstructural model /Dershowitz et al. 2003/. Other Äspö Hard Rock Laboratory related data sources have been applied for the tracers that lack of data in the microstructural model. Input parameters applied both in the prediction and evaluation models are presented below in Tables C3-2 and C3-3. Thicknesses of the various retention zones, their assigned porosities and formation factors are given in Tables A-2 and A-4, cf Appendix A.

Table C3-1. Properties of the flow field in the prediction and evaluation models.

Parameter		Flow path I	Flow path II
Prediction	**Advective delay**	6 h	120 h
	β	28,000 h/m	194,000 h/m
Evaluation	**Advective delay**	Gaussian distribution mean = 2.0 h, std = 1.0 h	Gaussian distribution mean = 100 h, std = 20 h
	β [h/m]	Gaussian distribution mean = 270,000 h/m std = 130,000 h/m	Gaussian distribution mean = 440,000 h/m std = 89,000 h/m

Table C3-2. Compilation of sorption properties applied in the prediction and evaluation models. Data are compiled from Appendix B, if not otherwise indicated.

	Fracture coating (d_{coat})	Fault gouge (d_{goug}, concept A)	Cataclasite/ Mylonite (d_{cata}, 20%)	Altered zone (d_{alt}, #19)	Altered zone (d_{alt}, BG1)	Intact wall rock (d_{rock})
I-131	0	0	0	0	0	0
Tb-160	0	0	0	0	0	0
Sr-85	2.30E–04 [1)]	6.00E–04	1.40E–04	2.60E–05	2.60E–05	4.40E–05 [1)]
Rb-86	5.20E–03 [1)]	2.70E–03	4.00E–03	4.00E–04	4.00E–04	1.00E–03 [1)]
Cs-137	5.20E–02 [1)]	4.00E–02	3.00E–02	5.00E–04	5.00E–04	1.00E–03 [1)]
HTO	0	0	0	0	0	0
Eu-155	0	0	0	0	0	0
Na-22	2.00E–04	1.10E–04 [1)]	1.10E–05 [1)]	1.40E–05 [1)]	1.70E–06	7.10E–06 [1)]
Ba-133	2.72E–02	1.40E–02 [1)]	1.30E–03 [1)]	1.80E–03 [1)]	6.90E–04	8.80E–04 [1)]
Mn-54	1.70E–01	8.75E–02 [2)]	8.13E–03 [2)]	1.13E–02 [2)]	4.30E–03	5.48E–03 [2)]

[1)] Task 6C specification /Dershowitz et al. 2003/.

[2)] Calculated based on Ba-133, i.e. the ratio between K_d's of Mn-54 and Ba-133 is same as for fracture coating.

Table C3-3. Tracer diffusivities in free water, D_w [m^2/s]. Data are compiled from Appendix B.

	Fracture coating (d_{coat})	Fault gouge (d_{goug}, concept A)	Cataclasite/ Mylonite (d_{cata}, 20%)	Altered zone (d_{alt}, #19)	Altered zone (d_{alt}, BG1)	Intact wall rock (d_{rock})
I-131	2.00E–09	2.00E–09	2.00E–09	2.00E–09	2.00E–09	2.00E–09
Tb-160	5.00E–10	5.00E–10	5.00E–10	5.00E–10	5.00E–10	5.00E–10
Sr-85	7.94E–10	7.94E–10	7.94E–10	7.94E–10	7.94E–10	7.94E–10
Rb-86	2.06E–09	2.06E–09	2.06E–09	2.06E–09	2.06E–09	2.06E–09
Cs-137	2.06E–09	2.06E–09	2.06E–09	2.06E–09	2.06E–09	2.06E–09
HTO	2.13E–09	2.13E–09	2.13E–09	2.13E–09	2.13E–09	2.13E–09
Eu-155	5.00E–10	5.00E–10	5.00E–10	5.00E–10	5.00E–10	5.00E–10
Na-22	1.33E–09	1.33E–09	1.33E–09	1.33E–09	1.33E–09	1.33E–09
Ba-133	8.48E–10	8.48E–10	8.48E–10	8.48E–10	8.48E–10	8.48E–10
Mn-54	6.88E–10	6.88E–10	6.88E–10	6.88E–10	6.88E–10	6.88E–10

Appendix C4

Implementation of the LaSAR framework

The objectives of KTH/WRE modelling work are (1) to make predictions of the breakthrough curves using information from the micro-characterization, laboratory program and the knowledge obtained from the previous TRUE tests (e.g. TRUE-1, TRUE Block Scale), and (2) to provide estimates of the effective retention parameters by assuming the best fit between measured and modelled BTCs.

C4.1 Immobile zone and retention parameters

C4.1.1 Pore space

For the purpose of the TRUE Block Scale Continuation project, Type 1 and Type 2 structures have been defined in consistency with those in the Task 6C model /Dershowitz et al. 2003/, with certain modifications of the thickness of the retention zones, cf Appendix A, and distribution of the retention zones.

The microstructural models for Geological fracture types (Type 1 and Type 2) are quantified in terms of the thickness of each of the geometrically defined (retention) zones, and the porosity and formation factor of those zones. The properties of the Geological fracture Type 1 and Type 2 are provided by, cf Appendix A.

Compared with the Task 6C model /cf Tables 2-1 and 2-2 in Dershowitz et al. 2003/, the retention zones in the BS2B model, cf Tables A-2 and A-4 in Appendix A, are thinner for all zones, except for fracture coating.

Type 2 fracture

It is assumed that the altered zone of 5 cm is evenly distributed on both sides of the fracture adjacent to the rock matrix, i.e. 2.5 cm on each side. Outside the altered zone is the intact rock matrix (Figure C4-1).

Table C4-1 summarises the porosity profile for Type 2 fractures at different depths in the rock matrix, as deduced from Appendix A (Table A-4). The porosity is generally decreasing with depth into the rock matrix.

Type 1 fractures

Two retention zones (cataclasite and fault gouge) are located behind the fracture coating in the microstructural model of Type 1 fracture. We assume that the cataclasite is distributed along 50% of the length of the flow path and the fault gouge along the other 50% of the length. However, they are not assumed to be monotonously distributed along respective sides of the fracture, but alternatively distributed on both sides as is shown in Figure C4-2. The altered zone (7.5 cm thick) is still evenly distributed on both sides of the rock matrix. The intact rock zone is behind the altered zone on both sides (not shown in Figure C4-2).

Table C4-1. Porosity profile at different depths for Fracture Type 2 (based on /Tullborg and Hermanson 2004/, cf Appendix A).

Rock type	Depth from surface (mm)	Porosity (–)
Fracture coating	0–0.25	0.05
Altered zone	0.25–25.25	0.006
Unaltered	25.25–	0.003

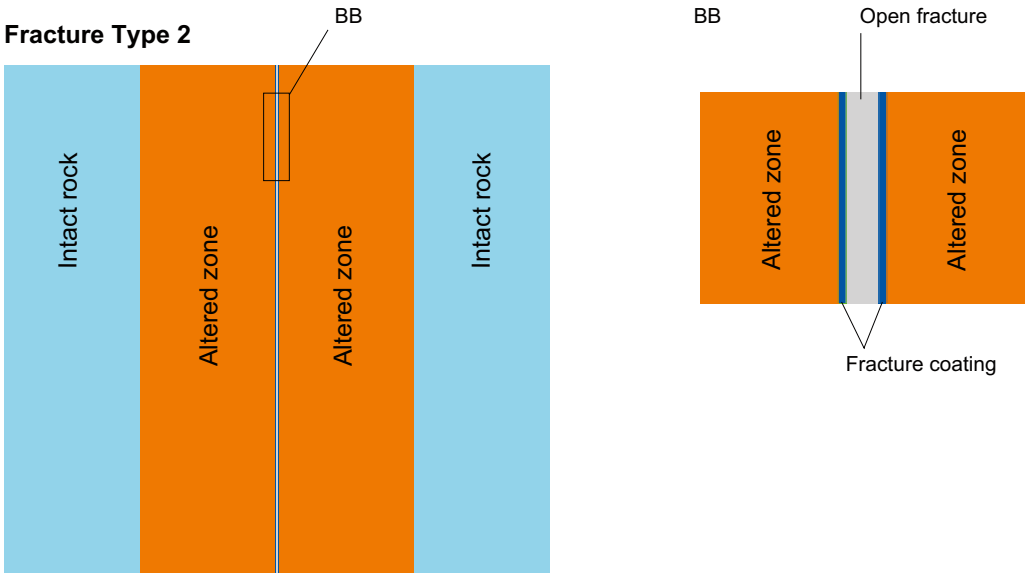

Figure C4-1. *Distribution of the retention zones in Fracture Type 2. Fracture coating is viewed as fracture surface.*

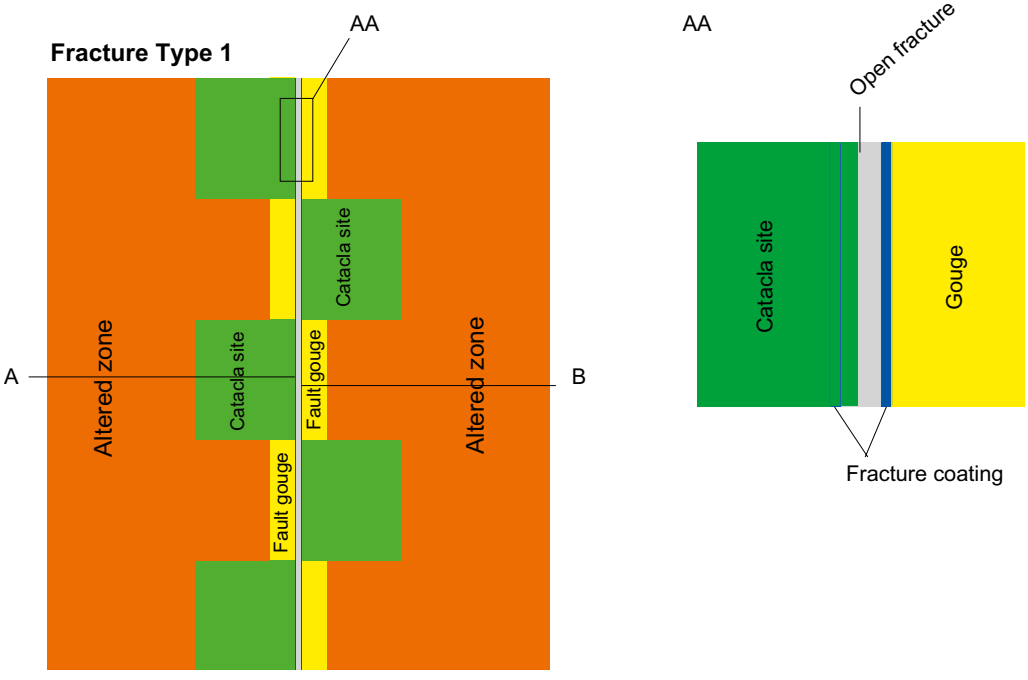

Figure C4-2. *Distribution of the retention zones in Fracture Type 1. Part A: Cataclasite+altered zone+intact rock. Part B: Fault gouge+altered zone+intact rock Fracture coating is viewed as fracture surface.*

As is shown in Figure C4-2, the immobile zone in fracture Type 1 is divided into two parts consisting of different retention zones on both sides of an open fracture. In the middle lies the open fracture with the fracture coatings. The first part of the immobile zone (part A in Figure C4-2) contains the following retention zones: the cataclasite, the altered zone and the intact rock. The second part (part B in Figure C4-2) contains the retention zones of the fault gouge, the altered zone and the intact rock. From the data shown in Table A-2 the porosity profile at different depths within the rock matrix is given by Table C4-2 for Part A and by Table C4-3 for Part B.

Table C4-2. Porosity profile at depth for Fracture Type 1, Part A in Figure C4-2.

Rock type	Depth from surface (mm)	Porosity
Fracture coatings	0–0.25	0.05
Cataclasite	0.25–10.25	0.01
Altered zone	10.25–85.25	0.006
Intact rock	85.25–	0.003

Table C4-3. Porosity profile at depth for Fracture Type 1, Part B in Figure C4-2.

Rock type	Depth from surface (mm)	Porosity
Fracture coatings	0–0.25	0.05
Fault gouge	0.25–3.25	0.20
Altered zone	3.25–78.25	0.006
Intact rock	78.25–	0.003

C4.1.2 Fracture surface

The fracture coating is in immediate contact with the groundwater, and is to be viewed as equivalent to the fracture surface (K_a). The thin fracture coating is assumed to be evenly distributed on both sides of the fracture for both types of structures (Figures C4-1 and C4-2).

C4.1.3 Fracture rim zone

From the laboratory program, the rim zone material of Structure #19 consists of approximately 80% of "strongly hydrothermally altered rock" and of 20% of "mylonitic and cataclasitic wall rock, in Äspö diorite", cf Appendix B. The gouge material also exists in Structure #19 as has been shown by the laboratory experiments, cf Appendix B. These are consistent with the definition of Type 1 structure. We therefore assume the K_d values of the tracers in Flow path I presented in Table C4-4 are also applicable for the corresponding retention zones in the microstructural model of Type 1 structure (Table C4-5).

The rim zone material of BG1 defined by the laboratory experiments is the altered Äspö diorite which is consistent with Type 2 structure of the microstructural model. We therefore assume the K_d data of the rim zone material of BG1 shown in Table C4-4 are valid for the altered rock in Type 2 structure (Table C4-5).

Table C4-4. Compilation of K_d values for the gouge material and the rim zone material (based on results provided in Appendix B.

Tracer	Gouge	Structure BG1 Rim zone		Structure #19 Rim zone			
	K_d (m^3/kg)	Altered rock		Cataclasite (20%)		Altered rock (80%)	
		K_d (m^3/kg)	K_a (m)	K_d (m^3/kg)	K_a (m)	K_d (m^3/kg)	K_a (m)
$^{85}Sr^{2+}$	6.0E–4	–	–	1.4E–4	2.2E–5	2.6E–5	1.5E–5
$^{86}Rb^{+}$	2.7E–3	–	–	4E–3	< 8E–4	4E–4	< 1E–4
$^{137}Cs^{+}$	4.0E–2	–	–	3E–2	9.8E–3	5E–4	1.0E–3
$^{22}Na^{+}$	2.0E–4	1.7E–6	7.0E–7	–	–	–	–
$^{133}Ba^{2+}$	2.7E–2	6.9E–4	2.9E–4	–	–	–	–
$^{54}Mn^{2+}$	1.7E–1	4.3E–3	1.8E–3*	–	–	–	–

C4.1.4 Parameters

Porosity and formation factor

Table B–5 in Appendix B presents porosity and formation factor data for the different rock materials. The formation factors are calculated using Archie's law, $F = 0.71 \cdot \theta^{1.58}$.

Diffusivity

Given the formation factor F, the effective diffusivity is calculated by $D_e = D_w \cdot F$ where D_w ($L^2\ T^{-1}$) is the diffusivity of the tracer in bulk water. The calculated D_e values for different tracers in contact with the different rock materials are summarised in Table B-5 in Appendix B.

The sorption coefficient in matrix K_d

The K_d values are summarised in Table 1-8. Note that these K_d values may differ from the values given in Task 6C /cf Table 2-6 in Dershowitz et al. 2003/. There are no data available for intact rock material in Appendix B. The K_d data provided in the Task 6C model /Dershowitz et al. 2003/ are larger than the K_d values for the altered zone as is shown in Table 1-8 which is unlikely. We therefore assume that the intact rock has the same K_d values as that for the altered zone shown in Table 1-8. The K_d data for the intact rock may also be obtained from the MIDS data of the TRUE-1 project /Byegård et al. 1998/. By using different sets of the K_d data will probably affect the final results only marginally.

Table C4-5. Compilation of K_d values for different rock materials in contact with the TRUE Block Scale groundwater (based on tabulations in Appendix B).

Tracer	Structure	Gouge θ = 0.2 K_d (m^3/kg)	Cataclasite θ = 0.01 K_d (m^3/kg)	Altered zone θ = 0.006 K_d (m^3/kg)	Intact rock θ = 0.003 K_d (m^3/kg)
$^{85}Sr^{2+}$	#19	6.0E–4	1.4E–4	2.6E–5	2.6E–5
$^{86}Rb^{+}$	#19	2.7E–3	4E–3	4E–4	4E–4
$^{137}Cs^{+}$	#19	4.0E–2	3E–2	5E–4	5E–4
$^{22}Na^{+}$	BG1	–	–	1.7E–6	1.7E–6
$^{133}Ba^{2+}$	BG1	–	–	6.9E–4	6.9E–4
$^{54}Mn^{2+}$	BG1	–	–	4.3E–3	4.3E–3

*The density ρ is assumed to be 2,700 kg/m^3 for all zones.

Surface sorption coefficient K_a

K_a values obtained from the fracture rim zone material (Table 1-6) are assumed to be applicable for the fracture surface sorption and are summarized in Table 1-9.

Table C4-6. Compilation of K_a values for the rim zone material based on data presented in Appendix B.

Tracer	Structure	Rim zone K_a (m)
$^{85}Sr^{2+}$	#19	1.6E–5
$^{86}Rb^{+}$	#19	2.4E–4
$^{137}Cs^{+}$	#19	2.8E–3
$^{22}Na^{+}$	BG1	7.0E–7
$^{133}Ba^{2+}$	BG1	2.9E–4
$^{54}Mn^{2+}$	BG1	1.8E–3*

C4.2 Transport model

C4.2.1 Processes considered

We consider the following mass transfer processes in our modelling:

- Dispersion of tracers in the fracture due to velocity variation (characterised by τ and β distribution).
- Unlimited diffusion (D) into the rock matrix and linear equilibrium sorption (K_d) inside the rock matrix (κ).
- The fracture coating in the micro-structural model is considered to be equivalent to the fracture surface, and sorption on the fracture surface is assumed to be at equilibrium (K_a).

C4.2.2 Mathematical description

In the LaSAR framework, the advective transport is coupled with related retention processes and solved in the Lagrangian domain. The retention processes include matrix diffusion/sorption and fracture surface sorption. The basic solution of this transport model is

$$\gamma(t,\tau;\beta) = \frac{H(t-\tau)B}{2\sqrt{\pi}\,(t-\tau-A)^{3/2}} \exp\left[-\frac{B^2}{(t-\tau-\beta A)}\right] \qquad \text{(C4-1)}$$

where

$$B = \sum_{j=1}^{M} \beta_j \kappa_j\,; \qquad \beta_j = \frac{l_j}{V_j b_j}\,; \quad \tau_j = \frac{l_j}{V_j} \qquad \text{(C4-2)}$$

$$A = \sum_{j=1}^{M} K_a^j \beta_j\,; \qquad \kappa_j \equiv \theta_j \left[D_j \left(1 + \frac{\rho_b K_d^j}{\theta_j}\right)\right]^{1/2} \qquad \text{(C4-3)}$$

and γ [1/T] is the probability density function of the residence time for a single tracer particle travelling from the injection to the pumping boreholes coupled with the processes of advection, diffusion and sorption. γ is conditioned on the parameter A and B; and H is Heaviside step function.

The index "*j*" designates either the *j*th fracture (if the particle is transported through a series of fractures), and/or the *j*th discretization segment in a single heterogeneous fracture; *M* is the total number of segments, which could also extend through a series of heterogeneous fractures; and ρ_b is the density of the rock matrix. All of the parameters are in general segment-dependent, they all therefore have the index "*j*".

Note that Equations (C4-1) to (C4-3) are applicable to a single trajectory (e.g. the *i*th trajectory). We have a number of trajectories (*N* trajectories in this simulation).

In Equation (C4-1) two grouped quantities *B* and *A* govern the value of γ. The grouped quantity *B* is further determined by β and κ if the retention parameters are uniform (θ and K_d in the present work). Here β is purely a flow dependent quantity. Since $\kappa = \theta\sqrt{D(1+\frac{\rho K_d}{\theta})}$ by definition and is a parameter describing the diffusion and sorption in the rock matrix, the effect of aperture variation on matrix diffusion/sorption is accounted for by the product $\beta\kappa$. On the other hand, the effect of aperture variation on surface sorption is described by the parameter *A* that is determined by the product βK_a in Equation (C4-1).

Dispersive effects

The effects of hydrodynamic dispersion on solute transport are accounted for by the statistical properties of the random variables τ and β. The solution γ in Equation (C4-1) applicable to a single trajectory will depend on (or is conditioned to) the random values of τ and β if the retention parameters are uniform.

Let $g(\tau, \beta)$ denote the joint probability density function (PDF) of τ and β at a pumping section or a control plane (CP). This PDF can in principle be computed using particle tracking (Monte Carlo) simulations /e.g. Cvetkovic et al. 1999/. If $g(\tau, \beta)$ is known, and γ is available in a closed form, the solute discharge, *Q* (or the breakthrough curve, BTC), at the pumping section (or CP) can be evaluated as:

$$Q(t) = \int_0^t \phi(t-t')dt' \int_0^\infty d\beta \int_0^\infty \gamma(t', \tau; \beta) g(\tau, \beta) d\tau \qquad \text{(C4-4)}$$

where $\phi(t)$ is the injection function. There is, however, a strong correlation between τ and β as shown by numerical simulations in generic configurations /e.g. Cvetkovic et al. 1999, 2004, Cheng et al. 2003/. We can, therefore, assume a deterministic relation between τ and β, and ascribe the variation of β to PDF of the residence time for pure advection, $g(\tau)$. The remaining problem is then to determine $g(\tau)$. If $g(\tau)$ is known, the solute discharge *Q* is evaluated as:

$$Q(t) = \int_0^t \phi(t-t')dt' \int_0^\infty \gamma\left[t', \tau; \beta(\tau)\right] g(\tau) d\tau \qquad \text{(C4-5)}$$

where $\beta(\tau)$ is a deterministic functional relation between τ and β. For the present work, a linear β and τ relation is assumed.

ISSN 1404-0344
CM Digitaltryck AB, Bromma, 2007